




DOCTORAL THESIS IN ASTROPHYSICS

Sorbonne Université

École doctorale 127: Astronomie et Astrophysique d'Île-de-France

Institut d'Astrophysique de Paris

A study of the thermal emission of rocky planets with JWST: The case of the TRAPPIST-1 planets

---

Presented by:

Alice MAUREL

Supervised by:

Jean-Philippe Beaulieu

Pierre Drossart

Martin Turbet

Presented and publicly defended on the *29/09/2025*
in front of the following jury:

Nicolas Cowan	Associate Professor, McGill University	Referee
Emily Rauscher	Associate Professor, U. of Michigan	Referee
Emeline Bolmont	Professor, Université de Genève	President
Brice-Olivier Demory	Professor, University of Bern	Examiner
Sandrine Guerlet	Chargée de recherche, LMD, CNRS	Examiner
Franck Selsis	Directeur de recherche, LAB, CNRS	Examiner
Jean-Philippe Beaulieu	Directeur de recherche, IAP, CNRS	Supervisor
Pierre Drossart	Directeur de recherche émérite, IAP, CNRS	Supervisor
Martin Turbet	Chargé de recherche, LMD, LAB, CNRS	Supervisor

Abstract

Planets around other stars offer amazing possibilities for planetary science - from the discovery of new, original worlds, to population studies on thousands of individuals, they allow us to detach from a Solar-system centered vision. Among them, rocky temperate exoplanets have a special status: harder to detect and characterize, they also possess the highest potential for harboring remotely detectable life forms. Because of their size and the detection bias towards planets close to their stars, one must turn to the coolest and smallest stars, M-dwarfs, to detect temperate rocky exoplanets, that are thus often tidally locked. The TRAPPIST-1 system, with its seven temperate rocky planets, offers unique possibilities for the study of this kind of object.

So far, no atmosphere has been conclusively detected on rocky planets, despite the numerous observations made possible by the James Webb Space Telescope. Indeed, the traditional method, transmission spectroscopy, is contaminated by the inhomogeneities of the star that, for now, strongly limit the conclusions that can be made from observations. Another possibility to detect an atmosphere is to look for planet's emission. Indeed, when the planet passes behind the star (secondary eclipse), the drop of luminosity corresponds to the thermal emission contribution of the dayside of the planet. Secondary eclipses have been observed for several rocky exoplanets, including TRAPPIST-1 b and c. Emission can also be observed by a phase curve, during a full orbit of the planet, allowing access to the nightside emission. A phase curve of TRAPPIST-1 b and c have been observed, making them the coldest planets to be observed with this technique.

My PhD was aimed at interpreting all these observations. I used atmospheric models to produce synthetic observables and compare them to the data available. I took advantage from both a fast, 1D model and a complex 3D GCM to explore possible atmospheres on TRAPPIST-1 b and c.

For each planet, I studied several types of atmospheres and their compatibility with the observational data. It allowed me to highlight various 3D effects that cannot be taken into account in 1D, like altitude-dependent heat redistribution and atmospheric collapse. I showed that TRAPPIST-1 b is either a bare rock, or possesses a thin atmosphere with few absorbing and/or condensible gases, or holds an atmosphere with a thermal inversion and aerosols, although this last case is very unlikely. TRAPPIST-1 c is different. It could also be a bare rock, but different models of atmospheres with CO_2, SO_2 or a thermal inversion better explain the data. It is thus not possible to conclude. Besides, we showed that current available emission observations are not informative about the external planets.

Finally, this thorough study of individual planets is key to build an observing strategy for observations, notably by assessing how informative observations in emission can be.

After introducing the context of this work (Chapter 1) and describing the methods I used (Chapter 2), this thesis details the possible atmospheres of TRAPPIST-1 b (Chapter 3) and TRAPPIST-1 c (Chapter 4), and some work on the outer planets (Chapter 5). Finally, I propose a general conclusion to my work (Chapter 6), as well as a few perspectives (Chapter 7).

Résumé (français)

Les milliers d'exoplanètes détectées à ce jour nous permettent de voir plus loin que le système solaire, grâce à la découverte de mondes exotiques, mais aussi au travail statistique permis par le grand nombre de ces objets. Parmi eux, les exoplanètes rocheuses tempérées intéressent beaucoup : bien qu'elles soient plus difficiles à détecter et à caractériser, ce sont elles qui ont le plus de potentiel pour accueillir une forme de vie détectable depuis la Terre. À cause de la petite taille de ces planètes et des biais observationnels qui rendent beaucoup plus facile de détecter une planète tout près de son étoile, ce sont autour des étoiles les plus petites et les plus froides, les naines M, que les exoplanètes tempérées ont été découvertes jusqu'ici. Le système TRAPPIST-1, avec sept exoplanètes rocheuses tempérées, offre des possibilités uniques pour l'étude de ce type d'objets.

Pour l'instant, il n'y a pas encore eu de détection claire d'atmosphère sur une exoplanète rocheuse, malgré les nombreuses tentatives déjà réalisées par le télescope spatial James Webb depuis le début de ses opérations à l'été 2022. En effet, la méthode classique, la spectroscopie de transit, souffre de contamination par les inhomogénéités à la surface de l'étoile, qui limitent fortement l'exploitation de ce type d'observations. Mais il est aussi possible de détecter des atmosphères en étudiant l'émission des exoplanètes. Ainsi, quand la planète passe derrière l'étoile (éclipse secondaire), elle engendre une baisse de luminosité correspondant à l'émission thermique du côté jour de la planète. Des éclipses secondaires ont été observées pour quelques exoplanètes, notamment les deux plus chaudes du système TRAPPIST-1, b et c. L'émission des exoplanètes peut aussi être mesurée à travers une courbe de phase, tout au long de l'orbite de la planète. Cela a été fait pour TRAPPIST-1 b et c, faisant de ces planètes les plus froides à avoir été observées avec cette technique à ce jour.

Dans ce contexte, le but de ma thèse était d'interpréter ces observations. Pour cela, j'ai eu recours à des modèles d'atmosphères pour produire des observables synthétiques et les comparer aux données récoltées. J'ai utilisé les avantages respectifs d'un modèle 1D, rapide et simple, et d'un modèle de circulation générale 3D (GCM), plus complexe et précis, pour explorer différentes possibilités d'atmosphères autour de TRAPPIST-1 b et c.

Pour chacune de ces planètes, j'ai étudié plusieurs types d'atmosphères et leur compatibilité avec les observations. Cela m'a permis de repérer divers effets 3D qui ne peuvent pas être prédits en 1D, comme la dépendance en altitude de la redistribution de chaleur ou l'effondrement atmosphérique dû à la condensation de ses composants. J'ai montré que TRAPPIST-1 b est soit une planète rocheuse nue, soit possède une atmosphère très mince pauvre en gaz absorbants et/ou condensables, soit pourrait posséder une atmosphère avec une inversion thermique et des aérosols, bien que ce dernier cas semble peu probable. TRAPPIST-1 c est différente. Elle peut être planète rocheuse nue, mais différents modèles d'atmosphères avec du CO_2, du SO_2 ou une inversion expliquent mieux les données. Il n'est donc pas possible de conclure. Par ailleurs, les observations en émission actuelles ne permettent pas non plus de conclusion pour les planètes externes. Enfin, cette étude détaillée de planètes individuelles est utile pour la mise en place de stratégies d'observations, notamment car elle permet d'évaluer dans quelle mesure les observations en émission peuvent être informatives sur la présence d'atmosphères.

Après avoir introduit le contexte de mon travail (Chapitre 1) et décrit les méthodes utilisées (Chapitre 2), cette thèse détaille mes résultats sur les atmosphères possibles de TRAPPIST-1 b (Chapitre 3) et TRAPPIST-1 c (Chapitre 4), ainsi qu'un travail sur les planètes externes du système (Chapitre 5). Enfin, je propose une conclusion générale à mon travail (Chapitre 6), ainsi que quelques perspectives (Chapitre 7).

Acknowledgments/Remerciements

I would like to express my gratitude to those who have supported and accompanied me during this PhD. It turns out that I mainly interacted with french-speaking people, so I prefer to write most of this in French.

Merci à mes trois encadrants, Martin, Pierre et Jean-Philippe. J'ai eu beaucoup de chance de vous avoir tous les trois, vous avez été complémentaires dans vos domaines d'expertise comme dans votre type d'encadrement. Pierre et Jean-Philippe, merci de m'avoir apporté un regard extérieur, votre enthousiasme par rapport à mon travail m'a souvent fait du bien. Martin, merci d'avoir été autant présent, disponible et motivé par notre travail. Merci d'avoir partagé ta passion, ton talent et ta rigueur avec moi. Tu m'as montré une belle facette de la recherche scientifique.

Thank you to the members of my jury, Emily Rauscher, Nic Cowan, Brice-Olivier Demory, Sandrine Guerlet, Franck Selsis, and Emeline Bolmont. I appreciate the interest you have shown in my work, your interesting questions and discussions. Merci particulièrement à Sandrine, Emeline et Franck qui m'ont un peu suivie dans mon parcours et ont souvent eu des paroles encourageantes.

J'ai quelques autres collègues à remercier particulièrement. Clément, pour ton soutien et tes conseils précieux, que tu donnes à tou.te.s les doctorant.e.s qui en ont besoin à l'IAP. Alexandre, pour ton aide sur les codes, mais aussi les gâteaux, la bienveillance - tu es clairement le highlight du LAB. Jérémy, merci pour ton aide que j'ai vraiment vécue comme un sauvetage, mais aussi merci pour ta confiance, ton respect, et pour ces discussions qui m'ont fait sentir d'égal à égal alors que j'avais peu d'expérience. Enfin, merci Elsa, on s'est rencontrées en novembre 2023 je crois, mais j'ai l'impression qu'on est amies depuis bien plus longtemps. Ça a été extrèmement précieux de travailler avec toi.

Je souhaite remercier les membres du bureau de la SF2A, notamment des commissions Transition Environnementale et Femme et Astronomie. Les discussions sociétales pendant les journées SF2A de Strasbourg et Marseille m'ont fait beaucoup de bien et redonné de la motivation pour travailler dans ce domaine, en sachant que je n'étais pas seule à me préoccuper de ces questions. De même, je remercie la SFE pour l'organisation des RED, et pour faire vivre la communauté exobiologie en France. Enfin, merci à l'ED 127, qui fait beaucoup d'efforts pour que nos thèses se passent dans de bonnes conditions. De manière générale, je suis reconnaissante envers la communauté exoplanètes pour sa bienveillance.

Merci à mes camarades de thèse, de l'IAP où j'ai passé la plupart de mon temps, du LMD et du LAB. Merci à celleux qui ont mis de l'énergie pour rendre ces labos accueillants. Merci à Émilie, la meilleure grande soeur de thèse qu'on puisse espérer.

Ori, Juliette et Valentine, nos verres plus ou moins réguliers m'ont fait un bien fou, et je penserai à vous pour votre dernière année.

Merci à l'équipe médiation de la Cité des Sciences, qui m'a offert de nombreux précieux moments de décompression, de recul. En fait, merci à tout le public avec qui j'ai interagi, surtout les enfants, qui m'ont permis de trouver plus de sens à mon travail. Je remercie d'ailleurs les profs qui m'ont encouragée tout au long de mon parcours, depuis mon enfance à moi.

Il est temps de passer aux personnes qui m'ont entourée au-delà du cercle professionnel. Merci à ma famille, qui m'a supportée et pris soin de moi pendant mes nécessaires moments de pause, de plus en plus rares vers la fin. Merci d'être venu.e.s me voir au planétarium, puis à la soutenance. Flora, Papa, Maman, merci de partager avec moi l'amour des sciences naturelles, et pour tout le reste qu'on partage aussi. J'ai une pensée spéciale pour mes grand-parents maternels qui nous ont quitté.e.s. J'aurais tellement aimé vous voir dans la salle pour ma soutenance.

Merci à mes camarades des femrev grâce à qui le militantisme a représenté mes moments de joie et d'évasion. Merci à mes colocs au sens large, celleux qui ont habité avec moi et les auto-proclamés satellites. Heureusement que j'avais tout ce monde à rejoindre après le travail. Merci pour l'énergie, la joie, l'écoute, le soin, les weekends colocs, les déguisements d'aliens et les soirées films. Merci à mes ami.e.s un peu plus loin, qui m'ont aussi fait tenir le coup.

We have found nothing you can sell. We have found nothing you can put to practical use. We have found no worlds that could be easily or ethically settled, were that end desired. We have satisfied nothing but curiosity, gained nothing but knowledge.

Becky Chambers, *To be taught, if fortunate*

Contents

1 Introduction **1**
1.1 A short introduction to astrobiology . . . 1
1.2 Rocky planets in the era of JWST . . . 6

2 Methods **15**
2.1 Observational data . . . 16
2.2 Modeling atmospheres . . . 20
2.3 Computing observables . . . 26
2.4 Comparing observations and models . . . 27

3 TRAPPIST-1 b **30**
3.1 Introduction . . . 31
3.2 Methods . . . 33
3.3 Results . . . 38
3.4 Discussions . . . 51
3.5 Conclusion . . . 53
3.6 Appendix . . . 54

4 TRAPPIST-1 c **64**
4.1 Introduction . . . 65
4.2 Methods . . . 66
4.3 Results . . . 68
4.4 Discussions . . . 72
4.5 Conclusion . . . 73
4.6 Appendix . . . 74

5 TRAPPIST-1 external planets **83**
5.1 Emission observation of TRAPPIST-1 e . . . 84
5.2 Emission of external planets from available emission data . . . 85

6 Conclusions **91**
Planets of the TRAPPIST-1 system . . . 91
What can we learn from emission observations of rocky planets ? . . . 92

7 Perspectives **94**
7.1 TRAPPIST-1 system . . . 94
7.2 Future observations . . . 95
7.3 Population level studies for rocky exoplanets . . . 96
7.4 Comparison between models and observations . . . 97
7.5 Improvements of the methodology . . . 100

Bibliography **102**

Appendices **110**

A Gillon & Ducrot et al. 2025 **111**

B Outreach **185**

1. Introduction

Contents

1.1 A short introduction to astrobiology . . . 1
1.1.1 Life on Earth . . . 1
1.1.2 Detection of extraterrestrial life . . . 4
1.1.2.1 Solar system . . . 4
1.1.2.2 Exoplanets . . . 5
1.1.3 Conclusion . . . 5
1.2 Rocky planets in the era of JWST . . . 6
1.2.1 Context . . . 6
1.2.1.1 Before JWST . . . 6
1.2.1.2 JWST . . . 7
1.2.2 Transit spectra and stellar contamination . . . 9
1.2.3 Observations in emission . . . 9
1.2.4 Cosmic shoreline . . . 11
1.2.5 The TRAPPIST-1 system . . . 13
1.2.6 Conclusion . . . 14

1.1 A short introduction to astrobiology

This section is mostly based on the RED (Rencontres Exobiologie pour Doctorant·e·s) astrobiology one-week introductory course that I followed in March 2024.
Astrobiology is the study of life in the universe. In this sense, it includes not only the research on extraterrestrial life, but also the question of the emergence of life on Earth (Cottin et al. 2017). In this section, I propose a short introduction to this field.
An important feature of astrobiology is its multidisciplinarity. It gives the opportunity to work together between biologists, chemists, geoscientists, astrophysicists, astrochemists... and it thus requires an effort of communication between the disciplines, different from the usual model of highly specialized, compartmentalized scientific research.

1.1.1 Life on Earth

Before talking about extraterrestrial life, let us stay on Earth, and try to understand what all living organisms that we know have in common.

Our shared features: composition Earth biosphere is constituted of millions of species, displaying an extraordinary diversity. However, all living beings are based on organic chemistry: carbon-based molecules that react in a solvent, water (Cockell 2020). Carbon can easily form molecular bonds with many other

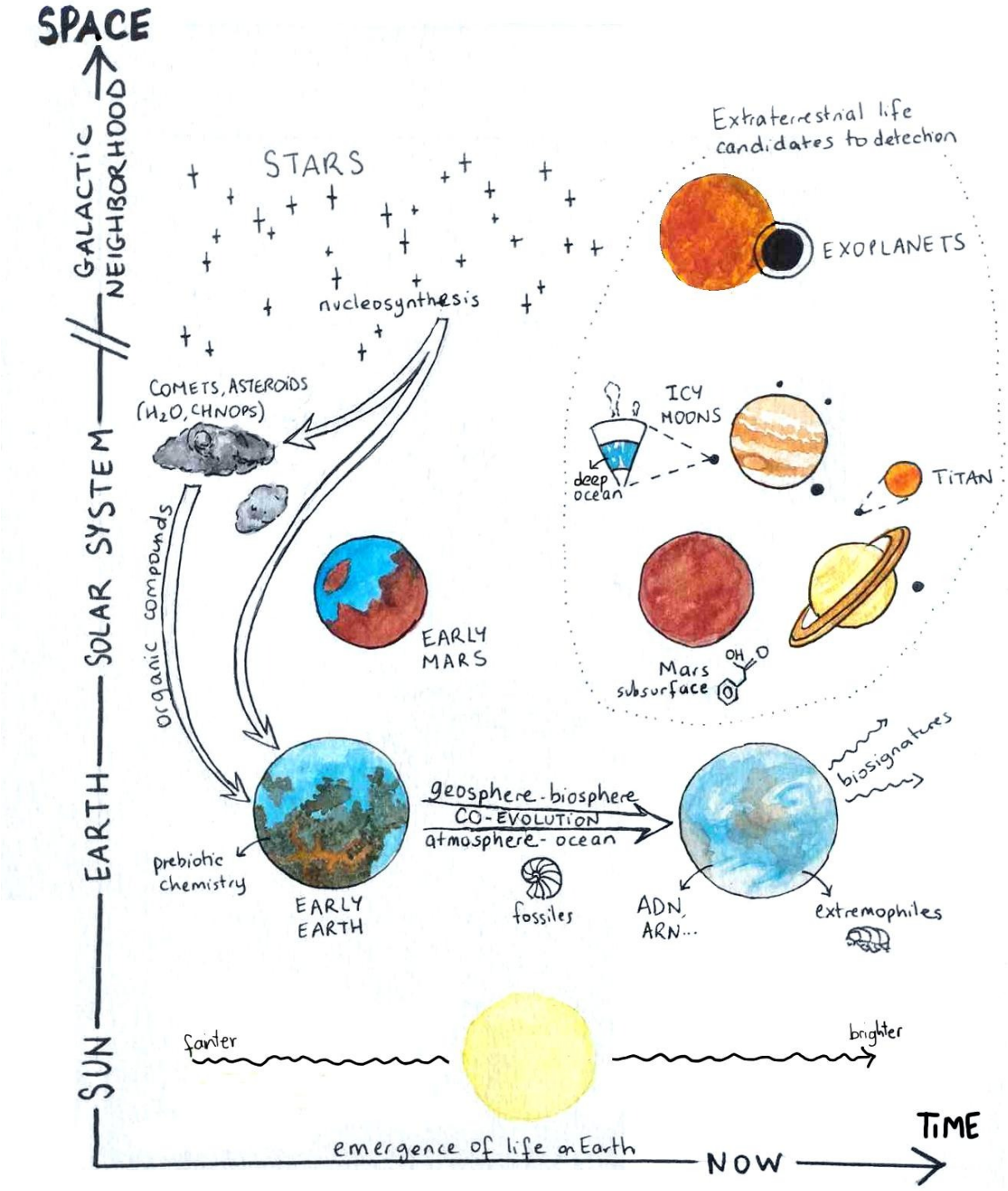

Figure 1.1: A scheme of the exobiology research field. Credits: Alice Maurel and Lo Conche

atoms, allowing for a rich range of chemical reactions that do not require a lot of energy (Horowitz 1986). Liquid water's polarity, temperature and viscosity make it an excellent solvent for organic chemical reactions (Cottin et al. 2017). Carbon and the other atoms that are present in organic chemistry (nitrogen, oxygen, phosphorus, sulfur) are quite common elements in the universe. They are products of the nucleosynthesis happening inside the stars (Krijt et al. 2023).
These elements are joint into different kind of molecules, often referred as building blocks for life (Cottin et al. 2017): amino acids, lipids, nucleic acids, carbohydrates (sugars), and phosphorus, which in turn assemble into functional components: proteins for metabolism, DNA and RNA for information coding, and the membrane, to isolate the cell from the environment.
Chemists are able to recreate these building blocks by chemical reactions in laboratory. However, they need particular conditions to happen. On Earth, two main kinds of environments are candidates for the natural synthesis of these molecules: early Earth atmosphere (which suppose to know/make assumptions on its composition...), and hydrothermal vents in the deep oceans (Cottin et al. 2017). Finally, through the analysis of meteorites, we know that comets and asteroids constitute exogenous sources of a large diversity of organic molecules, although their synthesis in space is still not fully understood (Cottin et al. 2017).

From chemistry to biology What distinguishes life from abiotic chemistry is the selectivity. Where abiotic chemistry constitutes all the range of possible reactions, biological systems select molecules for their function (Peretó 2012). To understand this transition from abiotic to biological, prebiotic chemists use two different approaches: "top-down", and "bottom-up".
The top-down approach consists in studying the basis of living organisms (proteins, DNA/RNA and cell) and trying to find chemical ways to synthesize them within the same solution. With the bottom-up approach, on the other hand, prebiotic chemists study the evolution from abiotic to prebiotic chemistry by bringing together a large diversity of organic components in water and adding an energy source, to facilitate the selection of chemical reactions in order to synthesize more complex molecules, like the famous Miller experiment (Miller 1953).
Research in prebiotic chemistry shows that the transition from abiotic to life should not be seen as a sudden event but as a continuity, with the progressive emergence of more complex and selective chemistry (Cottin et al. 2017).

Limits of life on Earth Earth is a habitable planet, but some parts of it are more welcoming than others. Although we humans can only survive under a narrow range of conditions, some archaea and bacteria called extremophiles thrive in very different environments (Merino et al. 2019). Studying these organisms allow to broaden our definition of habitability on Earth, and therefore elsewhere (especially in the solar system). Besides, environments that we call extreme now are closer to Early Earth conditions. Biologists study extremophiles *in situ*, in order to see where and how they thrive and grow, but also in laboratory to set further the limiting conditions of life (in these cases, organisms merely survive, waiting for more friendly conditions). Temperature, pH, salinity, pressure are among the physical and chemical conditions tested. The most studied extreme environments on Earth are hot springs, the deep sea, deserts, and subsurface environments (Merino et al. 2019).

Is our planet special ? For now, Earth is the only planet on which we have detected life. Among its different characteristics, it is difficult to know which ones are necessary for the emergence of life. Here we present a few characteristics of our planet. Earth is a rocky planet, around a G-type star. Statistics of observed exoplanets show us this is not a unique setup (Bryson et al. 2021). Earth contains a fair amount of water, which is a very common molecule in the universe. Our planet is situated at the right distance to its star to have liquid water at its surface (the so-called Habitable Zone, e.g., Kasting et al. 1993; Kopparapu et al. 2013)[1]. It possesses a moon, like most other planets of the solar system, but this

[1]Note that it does not guarantee the existence of surface oceans, as the planet may not contain water, and the temperature of a planet depends also on the atmosphere and surface albedo. More precisely, there are three stable states of current Earth: Earth as we know it, a snowball-Earth where all water constitutes ice caps reflecting a large part of the sunlight, and a hot Earth with all water in the atmosphere acting as a greenhouse gas Turbet et al. (2021).

moon is very large, and have stabilizing effects on the orbit and spin of the planet. This characteristic is quite rare if we refer to the solar system (and there is no exomoon detected so far), and it could have played a role in conditions for life to emerge (Ward & Brownlee 2000). Another unique feature of Earth in the solar system is plate tectonics. Plate tectonics exchanges matter, energy and heat, creates continents, recycles volatiles on geological timescales, all of this being especially helpful for the emergence of life. Volcanoes and geophysical activity are common in other bodies of the solar system, but the horizontal convective movement of plate tectonics is only known on Earth[2]. In summary, our planet has some special characteristics among the solar system bodies, but it is difficult to assess their rarity around other stars. Moreover, we know that life happened on Earth, but from our perspective, and, with no other example, it is delicate to estimate which of Earth properties are necessary, helpful or even inconvenient for the emergence of life (Kasting 2001).

Now comes the question of the presence of life elsewhere. On one hand, emergence of life on Earth is still not really understood, and is the result of complex chemistry. Our existence may be the result of an extraordinary improbable chain of coincidence. On the other hand, our galaxy counts hundreds of billions of stars, and exoplanet detections show that they are common objects. Moreover, life adapted to an extreme diversity of environments on Earth, far beyond the common understanding of "habitable worlds". Looking for evidence of life outside of Earth is thus a key goal for astrobiologists. However, it comes with a lot of scientific and technical challenges.

1.1.2 Detection of extraterrestrial life

A definition Now that we described life as we know it, we can start wondering what we are looking for when we search for life beyond Earth. Trying to detach from the terrestrial specificities and generalize our understanding of "life", astrobiologists usually agree on the NASA definition: *Life is a self-sustaining chemical system capable of Darwinian evolution*. With this definition, life does not require *a priori* liquid water, or carbon-based molecules, and leaves space for imagining another biochemistry. Some would argue that it is still too Earth-centered, but as we will see, the exact definition is not really the central problematic of the search of life beyond Earth.

1.1.2.1 Solar system

The solar system allows for in-situ exploration through spatial missions. From precise measurements to samples, solar system science can rely on very rich data compared to exoplanets. Here we will focus on the most promising solar system bodies regarding astrobiology.

Mars Mars is Earth's neighbor. It is also rocky, but smaller (one tenth of the mass of Earth). Because of the numerous missions and observations of the planet, it is the most studied object in terms of habitability, although the question of climate history, past oceans and geological evolution is still a subject of debate. There is ample evidence for the presence of liquid water on its surface around 3-4 billions of years ago (Fassett & Head 2008), suggesting that the planet possessed a greenhouse-efficient atmosphere, heating the planet and increasing pressure enough to allow for liquid water at the surface. Today, the planet is dry, with a 6 mbar atmosphere of mainly CO_2, and the only water detected is in vapor and solid form. However, it is possible that some liquid water is present in the form of liquid brine (McEwen et al. 2011). In this case, maybe some life form emerged when there were oceans on Mars (Poulet et al. 2005), and is still persisting today (Wassmann et al. 2012). It is also possible that life existed and is now extinct, but that there are some traces that can be found. This is why Mars is one of the main targets of astrobiology in the solar system.

From Mars to exoplanets Mars is not a direct analogue of exoplanets like TRAPPIST-1 b and c, main subjects of this thesis, but the physical and climatic phenomena studied and calibrated on Mars can be transposed to rocky temperate exoplanets. Condensation of CO_2 in the poles, photochemistry between

[2]Some research suggests that Europa may have its own version of plate tectonics (Collins et al. 2022)

CO_2, CO and H_2O, heat redistribution during dust storms (thermal equilibrium regulated by dust opacity) and calmer periods (radiative heating of the surface) were simulated in climate models of Mars (e.g., Forget et al. 1999; Turbet et al. 2017), informed by the observations. The models I use in my work thus indirectly benefited from knowledge and modeling of solar system planets, especially Mars.

Icy moons Jupiter and Saturn, the two gas giants of the solar system, both possess hundreds of moons. Although the two planets are way too far from the sun for their satellites to have liquid water at their surface, observations suggest that sub-surface oceans exist on the Jupiter moons Europa (Sotin et al. 2009), Ganymede and Callisto (Spohn & Schubert 2003), and on the Saturn moon Enceladus (McKay et al. 2008). The JUICE mission (ESA), launched in 2023, will give more data on these oceans, their composition, and possible exchange with the surface through cryovolcanism.

Titan Titan may also possess a sub-surface liquid water ocean (Grasset et al. 2000). But more importantly, it is the only moon of the solar system with a substantial atmosphere. Its 1.5 bar atmosphere is composed mainly of nitrogen, and a few percent of methane. It is opaque at visible wavelengths because of the photochemical hazes composed of organic molecules. On this moon, methane is present in liquid form at the surface, and presents a cycle, like water on Earth (Raulin et al. 2012). However, methane is a very poor solvent compared to water. Short-lived (100 to 1000 years) liquid water at the surface is believed to exist after impacts of asteroids (Artemieva & Lunine 2003). Thus, several features of Titan justify its place in astrobiology and the sending of a probe (Dragonfly, NASA) dedicated to its study.

1.1.2.2 Exoplanets

Exoplanet science brings an immense sample of different planetary systems, widening the diversity of planets compared to our solar system. On the other hand, we only rely on remote observations and the data available for their study is very sparse.

Habitable zone Although we just saw that liquid water under surface could be a candidate for sheltering life, this kind of life, poorly coupled to the surface and with no atmosphere to probe, would not be accessible to observations in exoplanets. Likewise, a life form that would be totally unlike terrestrial life would probably be impossible to recognize. This is why we focus on hypothetical life forms that are detectable remotely, with only astronomical data. Thus, astrophysicists define a habitable planet as a planet that possesses liquid water at its surface (e.g., Kasting et al. 1993). For this, the planet must receive the right amount of energy from its star, and be neither too close to it (or the water will be vaporized in the atmosphere and/or escape), nor too far (or it will be in ice form). The region compatible with liquid water is called the habitable zone.

Biosignatures A biosignature is an evidence of the presence of life. For exoplanets, it must be remotely detectable through the limited possibilities of astronomical observations. On Earth, life is everywhere, and the biosphere has a global impact on Earth characteristics: the atmosphere contains 21% of O_2, produced by photosynthesis (gaseous biosignature), the vegetation covers a large part of emerged surface and is detectable from space through its spectral signature (surface biosignature), and the biosphere induces diurnal and seasonal composition changes (temporal biosignature) (Meadows et al. 2018). However, one measurement of O_2, for example, would not be a good biosignature. Indeed, O_2 can also be produced by abiotic sources (false positive, Selsis et al. 2002), and the first life forms on Earth did not produce O_2 in the atmosphere (false negative).
To avoid false positives, a robust biosignature must be a measurement that is not explainable by abiotic sources. On the other hand, researchers work on imagining various types of biosignatures in order to avoid false negatives. Most probably, before claiming a discovery of extraterrestrial life, the astrobiology community would have to gather several independent measurements that require a biosphere to be explained. To our knowledge, early stages of generalized life on Earth were not detectable by a global remote measurement, and an inhabited planet may be undetectable remotely.

1.1.3 Conclusion

Let us go back to the general questions addressed by astrobiology.
What is life ?: Although a very interesting metaphysical subject, astrobiology does not revolve around it. The definition of life will depend on the discipline: for a biologist who studies the transition from inert to living, life would probably be a membrane, with DNA or RNA and proteins. For astronomers who study exoplanets, a "habitable" planet is a planet with a liquid ocean, and life is something that resembles the one we know on Earth, with detectable metabolic processes and products.
What is the origin of life on Earth ? Biologists study the conditions on Early Earth that allowed for the emergence of a more and more complex chemistry, until the emergence of systems capable of self-replication and Darwinian evolution. We know it happened, as we are here. But we don't know if the combination of circumstances that enabled the development of Earth life is exceptional or if most planets like Earth would experience it.
Is there life beyond Earth ? We will never be able to answer "no" to this question. It is also possible that life beyond Earth exists, but that the closest inhabited planet is too far away from us to detect it. Thus, the question that we may be able to answer is: "Is life frequent enough that we will be able to detect some ?".

Among exoplanets, the most interesting ones for astrobiology are the rocky temperate ones, i.e. planets receiving an irradiation between the ones of Mercury and Mars[3]. With the James Webb Space Telescope, for the first time, their characterization is technically achievable.

1.2 Rocky planets in the era of JWST

In the past few years, the James Webb Space Telescope (JWST) allowed for considerable advances in the field of exoplanets characterization. However, some challenges remain, notably in the detection of small, rocky exoplanets. Here we provide an overview of the question.

1.2.1 Context

1.2.1.1 Before JWST

Although the existence of planets around other stars was expected from a long time, the first exoplanets were detected only in the 1990s (Mayor & Queloz 1995). Indeed, exoplanets do not produce their own light, are very small compared to their host star, and often too close to their stars to be resolved angularly anyway, making them difficult to detect, and even more to characterize.

Transit The most efficient detection technique to date is transit, i.e. the detection of a periodical dip in the light of a star corresponding to the passage of a planet obscuring part of the star to us (Charbonneau et al. 2000). Given that the radius of the star is known, the depth of the transit gives access to the radius of the planet, a first step towards exoplanets characterization. Moreover, transits are necessary for most atmospheric detection techniques (see sections 1.2.2 and 1.2.3), and therefore, we will focus on transiting planets in the rest of this thesis.

M dwarfs The transit method is strongly biased towards close-in planets. Indeed, the probability of an exoplanetary system to have the right inclination to transit is inversely proportional to the distance between the star and the planet. Moreover, only planets that are large enough compared to their host stars have a transit deep enough to be detected. Thus, hot Jupiters are the easiest type of planet to observe around sun-like stars. In order to detect and characterize smaller planets, we must then look around the smallest stars, i.e. M dwarfs (Nutzman & Charbonneau 2008; Barclay et al. 2018). These stars are also cooler, allowing access to temperate planets in transit. Finally, they are the most common spectral type in the galaxy, and thus in our close neighborhood (Triaud 2021), making them a good target for temperate rocky planets research. Almost all the discovered rocky temperate exoplanets orbit M dwarfs (`https://exoplanet.eu`).

[3]The exact meaning of "temperate" exoplanets can vary. This is the definition we chose for this thesis.

Atmospheres Only two years after the first transiting planet was discovered (Charbonneau et al. 2000), an atmosphere was detected around it (Charbonneau et al. 2002)[4] with the Hubble Space Telescope spectrograph STIS (Fig. 1.2): the transit depth was measured at different wavelength, allowing to detect a sodium absorption line indicating the presence of an atmosphere around the planet. The method of transit spectroscopy (section 1.2.2) is to date the main tool to detect and characterize exoplanetary atmospheres. In the same decade came the first measurements of thermal emission of exoplanets (section 1.2.3), through secondary eclipse, then orbital phase curve, with the Spitzer instrument IRAC (Fig. 1.2).

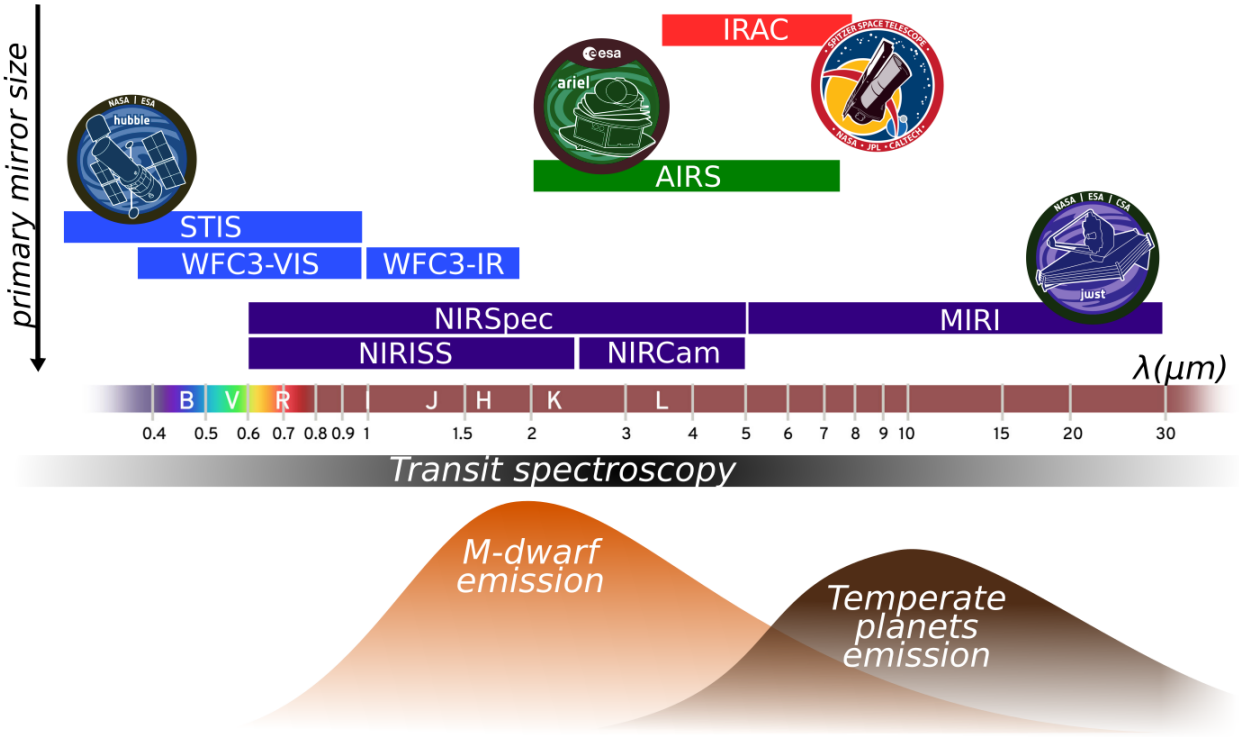

Figure 1.2: Wavelength coverage of different space telescope instruments and their interest for temperate rocky planets characterization.

Rocky exoplanets Before JWST, there have been a few tentative observations of rocky planets atmospheres. The ultra-hot super-Earth 55 Cancri e was observed in emission with the Spitzer space telescope, first by secondary eclipse depth measurements, then phase curve (Demory et al. 2012, 2016). The thermal phase curve of LHS 3844 b, a hot super-Earth (Kreidberg et al. 2019), showed no evidence of atmospheric redistribution. These emission observations were limited with the Spitzer telescope to hot exoplanets, temperate exoplanets producing not enough signal (Ducrot et al. 2020). Thus, transit spectroscopy was the preferred method at disposition for characterizing rocky temperate exoplanets. The TRAPPIST-1 system is the best target for this method. All planets of the system (see section 1.2.5) have been observed in transit with HST-WFC3 and Spitzer (De Wit et al. 2016; de Wit et al. 2018; Turbet et al. 2020a; Garcia et al. 2022). The observations ruled out thick, low molecular weight clear atmospheres for all planets (Ducrot et al. 2020; Gressier et al. 2022).
More compact secondary atmospheres (Note 1.2) could not be assessed with the sensitivity of HST, and emission observations were limited to the hottest targets. JWST was thus eagerly awaited to characterize the secondary atmospheres expected around temperate rocky exoplanets.

[4]It has been shown more recently that the signature most likely comes from the star and not the planet, because of the Rossiter-McLaughlin effect (Casasayas-Barris et al. 2021)

1.2.1.2 JWST

The James Webb Space Telescope was launched in December 2021 and started its first observations in 2022, just at the beginning of this PhD. It orbits the L2 Lagrange point. Its primary mirror is composed of 18 hexagonal segments of 1.3m, allowing for an unprecedented sensitivity. It features a 5-layer sunshield to allow for the instruments to be kept at very low temperature, and thus detect faint signals. Its instruments cover wavelengths between 0.6 and 28.5 microns, i.e. near-infrared (NIR) to mid-infrared (Fig. 1.2). JWST is a generalist telescope, but its main four science goals are to study the first objects to form in the early universe, galaxy formation and evolution, the birth of stars and planetary systems, and planetary systems and the origins of life. In total, roughly one third of JWST observational time is allocated to exoplanets and exoplanet formation. The observational time is divided in three categories: observations reserved for instrument team leads and members of the Science Working Group, i.e. Guaranteed Time Observers (GTO), General Observers (GO) programs, and Director's Discretionary Time observations (DDT), designed for urgent observations and/or observations that cannot be led by individual GO programs. GO programs are selected each cycle ($\sim$ 1 year) among proposals made by researchers of the community.

Exoplanets with JWST The large wavelength coverage of JWST is well adapted to the study of exoplanet atmospheres through transit spectroscopy and thermal emission. The capabilities of the telescope allow for more precision in the study of hot Jupiters, and give access to atmospheric characterization of smaller and colder planets (Espinoza & Perrin 2025). As in 2022, JWST capacities were expected to characterize atmospheres of rocky exoplanets, and the first cycle 1 and 2 GO proposals were aiming at this. However, while JWST precision is even better than expected (Gardner et al. 2023), all tentative observations so far resulted in non-detections (Lim et al. 2023; May et al. 2023; Lustig-Yaeger et al. 2023; Alderson et al. 2024; Kirk et al. 2024; Scarsdale et al. 2024; Rathcke et al. 2025a; Radica et al. 2025; Wachiraphan et al. 2024; Zhang et al. 2024; Xue et al. 2024; Weiner Mansfield et al. 2024; Luque et al. 2025), or at best tentative detections (Gressier et al. 2024 and Banerjee et al. 2024 for L 98-59 d, and Bello-Arufe et al. 2025 for L 98-59 b.). Rocky exoplanet atmospheres seem still out of reach, switching the scientific question from "What are rocky exoplanets atmospheres like ?" to "Are there atmospheres on rocky planets and why ?"

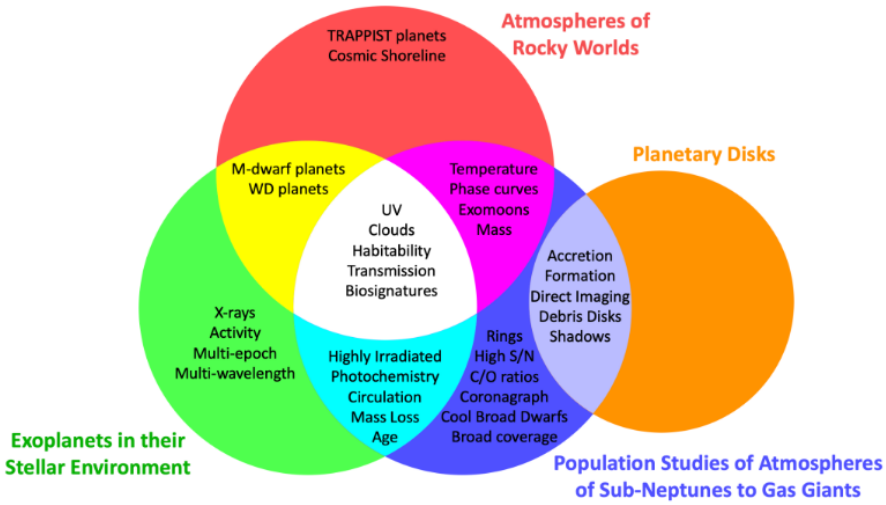

Figure 1.3: Figure from Redfield et al. (2024). Summary of the topics submitted by the exoplanet community

In 2024, the Working Group on Strategic Exoplanet Initiatives with HST and JWST provided a report (Redfield et al. 2024) summarizing the key science goals of the exoplanet community and including recommendations for the next HST and JWST observational strategies (Fig. 1.3). The Working Group (WG) identified three key science themes: understanding the prevalence and diversity of atmospheres on rocky-M dwarf worlds, population-level trends of exoplanet atmospheres from sub-Neptunes to gas giants, and exoplanets in the context of their stellar environments. The first theme, that is in interest particularly in

this manuscript, has been selected to be the object of a 500-hour DDT program, named the Rocky Worlds DDT program[5]. This program mainly consists in measuring secondary eclipses at 15 μm (see section 1.2.3) of various rocky exoplanets orbiting M-dwarfs with JWST, and in parallel characterize the stellar UV properties of these stars with HST. Targets are selected according to several priority criteria, notably their observability (depending on the size and temperature of the planet in comparison with those of the star, eclipse duration...), and their position with respect to the cosmic shoreline (described in section 1.2.4). The goal is to provide a large sample of emission observations of rocky exoplanets, and to give access to cooler planets, necessitating lengthy programs difficult to obtain with GO proposals. Four targets have been already selected for JWST observations with the DDT.

1.2.2 Transit spectra and stellar contamination

Principle The first method to detect and characterize exoplanetary atmospheres is transit spectroscopy. When a planet has an atmosphere, the starlight passing through it is absorbed at certain wavelengths corresponding to absorbing bands of molecules and atoms. When measuring the transit depth at different wavelengths, the reconstituted spectrum reveals the signature of the atmospheric components.
During a transit, the starlight that passes through the atmosphere probes only the terminator zone, i.e. the morning and evening sides that separate day- and night-side. The presence of aerosols like clouds or hazes can form an opaque layer, flattening the observed spectrum (e.g., Turbet et al. 2020a).
The depth of the spectral signatures is directly linked to the atmospheric scale height (see Note 1.1), and thus, the atmospheres easiest to characterize are hot and have a low mean molecular weight (i.e., hot Jupiters). For secondary atmospheres[6], the spectral features are smaller and thus more difficult to detect.

Note 1.1: Atmospheric scale height

The atmospheric scale height, $H = \frac{RT}{Mg}$ with R the ideal gas constant, T the temperature, g the gravity of the planet and M the molar mass of the gas, is computed from an idealized isothermal ideal gas atmosphere in equilibrium.

Stellar contamination Transit spectroscopy relies on measuring the difference between the incident light from the star, and the light transmitted through the atmosphere. The problem is that since the star can not be resolved spatially, it is assumed to be a homogenous, constant sphere. Observations of the sun and simulations show us it is not the case: all stars present time-dependent evolutions, and spatial inhomogeneities like hotter and cooler spots. For the coolest stars (i.e., M dwarfs), these cold spots can even include molecular features of species that can also be expected in exoplanets atmospheres, like H_2O.
During a transit, the planet passes in front of only a part of the star. If the chord described by the path of the planet is not perfectly representative of the whole surface of the star, it can induce false detections or hide molecular planet features (Rackham et al. 2018). Indeed, the total spectrum of the star is used as a proxy for the incident light through the planet potential atmosphere, but in reality the incident light is only the small annulus around the planet travelling the chord. This is the Transit Light Source Effect (Fig. 1.4). If the chord occults a stellar spot, it will be visible in the light curve and can be corrected. However, if, on the contrary, there are *unocculted* spots, they will result in features in the transit spectrum of the planet.

This effect has proven a major issue in the analysis of transit spectra of M-dwarf planets with JWST (Lim et al. 2023, Fig. 1.5). This is a strong limitation in the study of these planets. Some methods exist to mitigate it: through a modeling effort, with better models of M dwarfs starspots, and through an observational one, with starspots observations, and smart observational strategies like using a planet with no spectral features to probe the starspots (GO 6456, "Using stellar contamination proxy TRAPPIST-1 b to search for an atmosphere on TRAPPIST-1 e" Rathcke et al. 2025a). To bypass this issue, astronomers also turn to emission observations for which stellar contamination is less problematic.

[5] https://rockyworlds.stsci.edu/
[6] See Note 1.2

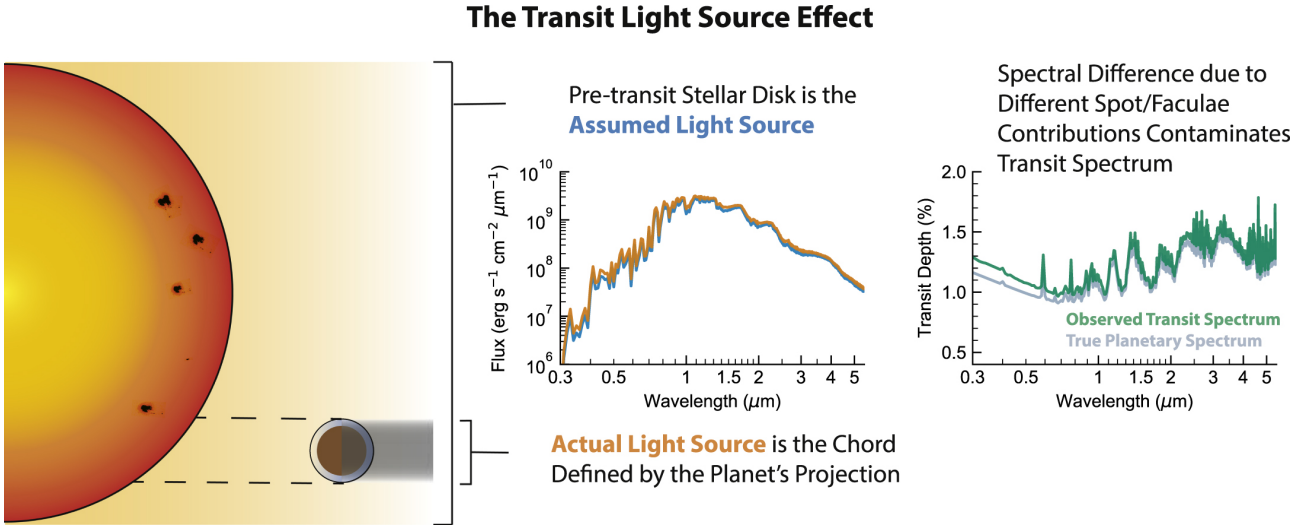

Figure 1.4: Figure from Rackham et al. (2018). The transit light source effect: the observed integrated spectrum of the star is a combination of different spectra, including hotter and colder spots, and this combination is modified when a planet hides a part of the stellar disk, resulting in contamination in the spectrum.

1.2.3 Observations in emission

Another method of exoplanet characterization is the study of its thermal emission (Fig. 1.5). It requires that the planet is hot enough to have an emission that can be detected by the instruments available.

Secondary eclipse When the planet passes behind its star, a small drop of luminosity can be observed in the thermal wavelengths. It corresponds to the dayside thermal emission that hides behind the star. The measurement of the eclipse depth can therefore give access to the brightness temperature of the dayside of the planet. This brightness temperature corresponds to the temperature of the surface only in the case of a bare rock or an optically thin atmosphere. In the case of a substantial atmosphere, the emission of the planet can come from layers of the atmosphere and potentially exhibit molecular features depending on the composition and structure of the atmosphere.

In the case of temperate rocky exoplanets, thermal dayside emission is accessible in photometry with the MIRI instrument of JWST (Fig. 1.2). Most secondary eclipse observations are made in the 15μm filter, which is a compromise between the sensitivity of the instrument and the maximization of the planet-to-star flux ratio, and correspond to a strong CO_2 band.
Apart from the TRAPPIST-1 system, detailed in section 1.2.5, several planets have been observed during secondary eclipse with JWST. LTT1445A b (Wachiraphan et al. 2024), GJ1132b (Xue et al. 2024), GJ486b (Weiner Mansfield et al. 2024), each observed with the MIRI low resolution spectrum (LRS), all show a thermal emission spectrum compatible with one of a dark bare rock. Thick atmospheres and bare rock with a high albedo are *a priori* disfavored for all these planets, although thinner atmospheres cannot be excluded. LHS 1478 b, observed in the MIRI 15 μm filter, presents an unexpectedly shallow eclipse (August et al. 2025), but this result is based on only one observation, the second observation being too contaminated by systematics. Several other planets have been and are being observed with this technique, notably at 15 μm with the GO 3730 (Hot Rocks Survey), and the Rocky Worlds DDT that will provide new data in the future.

Phase curve A more time-costly but more informative method is the observation of a phase curve: monitoring the light of the system during a full orbit of the planet (Fig. 1.6). The nightside flux of a planet can only be obtained for a transiting planet[7], by comparing the flux during the eclipse (star alone) to the

[7]Phase curves are nevertheless accessible to non-transiting planets, and thus have the advantage of offering a characterization technique for such exoplanets (Harrington et al. 2006; Cowan et al. 2007; Selsis et al. 2011).

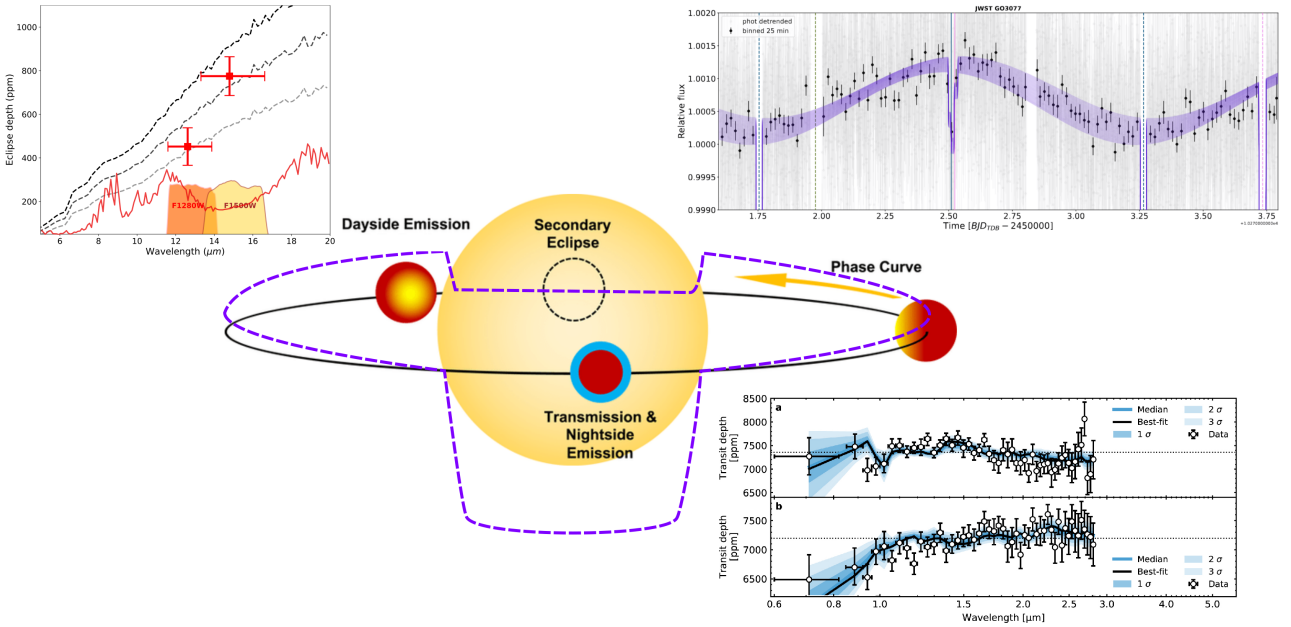

Figure 1.5: Different observational techniques with corresponding TRAPPIST-1 b results (Lim et al. 2023; Ducrot et al. 2024; Gillon et al. 2025).

minimum flux of the phase curve outside eclipses and transits (star plus nightside of the planet). Comparing the nightside and dayside emission gives information about the thermal redistribution on the planet: for a bare rock, there is no thermal redistribution and the nightside will give a flux ~ 0, while for a thick, redistributive atmosphere, the phase curve is expected to be flattened. A non-zero nightside flux indicating thermal redistribution, and an offset of the peak of emission indicating winds shifting the hottest point longitudinally, are indicative of an atmosphere.

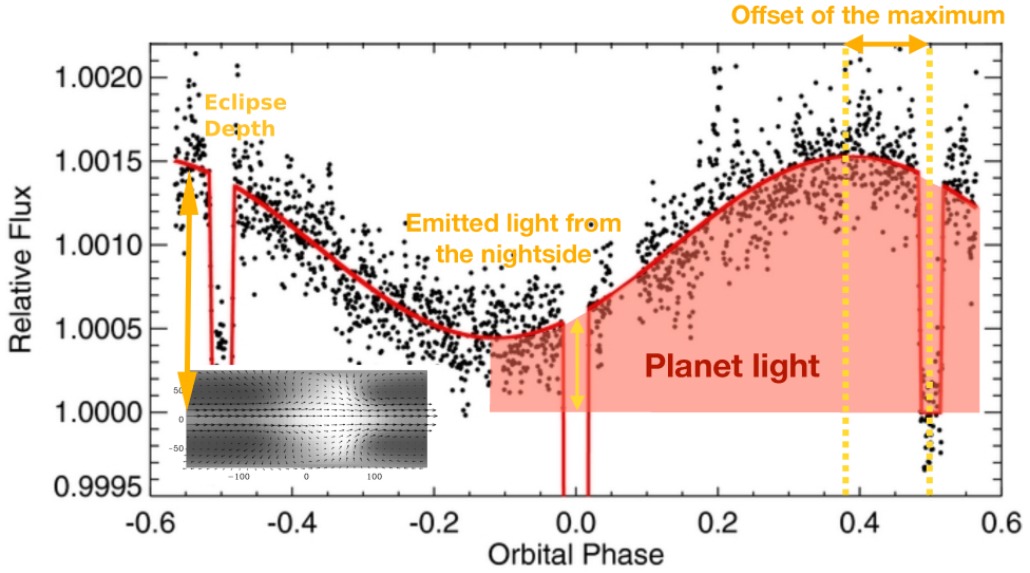

Figure 1.6: A phase curve of the hot Jupiter HD209458b observed by Spitzer at 4.5 μm, along with a GCM simulation of the planet. Eastwards winds (superrotation) shift the hottest point of the planet, thus creating an offset of the maximum of the phase curve. Figure adapted from Pluriel (2023).

Phase curve observations were initially only for hot exoplanets (e.g., Cowan et al. 2007; Demory et al. 2016), but JWST capabilities allowed astronomers to use this technique with more temperate planets, the coolest one observed being to date the TRAPPIST-1 system. Other rocky, hotter exoplanets have been

observed in spectral phase curve (Zieba et al. 2022; Zhang et al. 2024; Luque et al. 2025), with no hint of any heat redistribution indicating an atmosphere.

1.2.4 Cosmic shoreline

Our understanding of planetary formation and evolution, and thus resulting atmospheres, is strongly biased towards the solar system, and especially Earth. Through exoplanets and planetary disks observations together with formation and evolution models, researchers are trying to understand under which conditions rocky exoplanets can have an atmosphere. However, rocky planets studies are strongly limited by observations capacities, and most of the rocky planets accessible are very close to their very active M-dwarf star, which is not *a priori* the best situation for maintaining an atmosphere. Still, several models of planetary formation predicted that these planets could start with large quantities of volatiles (Krissansen-Totton et al. 2024), possibly counterbalancing atmospheric escape. The multiplying non-detections of rocky exoplanet atmospheres raise progressively the question: can rocky close-in exoplanets have an atmosphere at all ?

Note 1.2: Primary and secondary atmospheres

Planets can acquire an atmosphere during their formation in the protoplanetary disk. This kind of atmosphere is rich in hydrogen and thus extended (see Note 1.1). For small, rocky planets, this primary atmosphere is less massive and can be easily lost, but the planet can build a new volatile envelope through magma ocean, volcanic and impact degassing of materials[a]. This secondary outgassed atmosphere, depending on the redox state of the interior, will be composed of molecules of higher molecular weight (CO_2, H_2O, N_2, CH_4...) (Lichtenberg et al. 2023) and thus less extended.

[a]Rather than a strong distinction, primary and secondary atmosphere are probably overlapping in a smooth transition (Lichtenberg et al. 2023).

An empirical cosmic shoreline Zahnle & Catling (2017) showed that solar system bodies and extrasolar giant planets, when plotted in Escape Velocity vs Insolation, are divided in between those with an atmosphere and those without (Fig. 1.7). The division line corresponds to $I \propto v_{esc}^4$. They called it the cosmic shoreline: planets with a deep, thick atmospheres on one side of it, airless planets on the other, and planets like Earth are on the shoreline, i.e. where there is an atmosphere, but not too thick.
This empirical cosmic shoreline corresponds to the competition of two processes: the gravitation of the planets, allowing it to hold an atmosphere, and the atmospheric escape.

The $I \propto v_{esc}^4$ line is compatible with a thermal escape driven by the total insolation. The cosmic shoreline suggests that the process that determines the presence of an atmosphere around a planet in the solar system is atmospheric escape rather than initial volatile composition.

Extension to rocky exoplanets around M dwarfs Now that rocky exoplanet atmospheres are proving hard to detect, the extension of the cosmic shoreline for rocky exoplanets orbiting M-dwarfs has gained interest. First, it provides a priority metric for the Rocky Worlds DDT: indeed, in the quest for detection of atmosphere, we might as well aim for the ones more likely to have an atmosphere. Second, the high X-UV activity in the early life of M-dwarfs might make it harder for the rocky planets around them to maintain this atmosphere at the beginning - Pass et al. (2025) recently computed that the cumulative X-UV flux for M-dwarfs is even more important that previously suggested. The position of the cosmic shoreline is thus unknown for this kind of planet. Finally, only multiple observations will help better constrain a "unified cosmic shoreline" necessary to understand if the solar system is representative of planetary systems in general, and inform theories on how planets gain and maintain their atmosphere.

1.2.5 The TRAPPIST-1 system

The TRAPPIST-1 system was discovered by the project SPECULOOS (Search for habitable Planets EClipsing ULtra cOOL Stars), during its concept proof in 2015 with the TRAPPIST (Transiting Planets and Planetes-

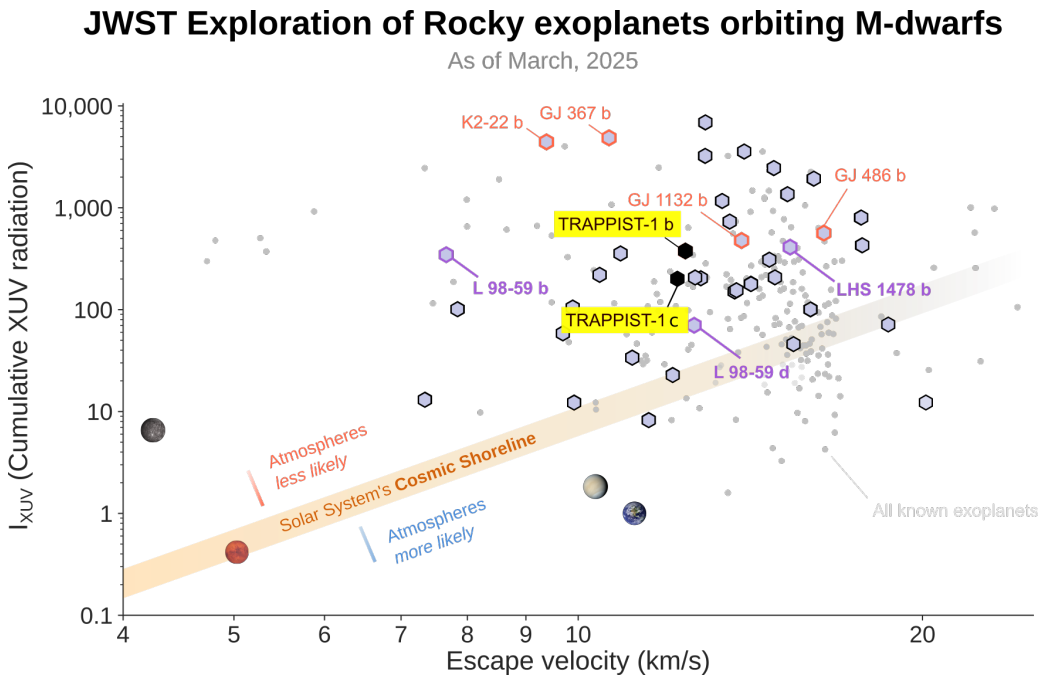

Figure 1.7: The cosmic shoreline for rocky exoplanets orbiting M-dwarfs observed by the JWST. Figure adapted from Espinoza & Perrin (2025). Grey points correspond to known rocky exoplanets orbiting M-dwarfs, hexagons represents objects observed by JWST. Planets for which observation showed that an atmosphere is unlikely are circled in red, and in purple are planets for which there could be a tentative detection of an atmosphere. TRAPPIST-1 b and c, the main subjects of this study, are highlighted in yellow.

imals Small Telescope) telescopes. The transit signatures turned out to be the ones of seven different planets (Gillon et al. 2016, 2017; Luger et al. 2017). Since then, this system is the star of rocky exoplanets science. A lot of different characteristics makes this system a unique opportunity for rocky exoplanets characterization.

A natural laboratory The system is composed of at least seven planets, each of earth-like mass and radius. The middle planets (e, f and g) could in theory hold liquid water on their surface (Turbet et al. 2020a). This is the only known such system. Besides, the TRAPPIST-1 system is situated nearby (∼39 light years), with very frequent transits and a very small star, which make them a very favorable target for observations. It has therefore been the source numerous publications every year since its discovery, and its planets are extremely well characterized.
The system is so compact (all planets are within 0.06 AU of the star) that the tides that the star exerts on the planets slowed down the rotation rate of the planets to a probable synchronous rotation (Revol et al. 2024), reduced their obliquity to zero and circularized their orbits (Turbet et al. 2020a). Besides, all planets are in a resonant chain. Their proximity make them exchange continuously angular momentum, leading to transit timing variations (TTVs) of a few minutes to an hour. The study of this TTVs is necessary to avoid missing transits during telescopes observations, but it also allows deriving precise planetary parameters (Agol et al. 2021, Table 1.1).

Before JWST, the system was observed with available telescopes (HST, Spitzer) in order to probe potential atmospheres (Gressier et al. 2022; Ducrot et al. 2020). However, the precision only allowed for excluding hydrogen-dominated atmospheres. Studies of the formation, atmospheric escape and atmosphere-interior interaction were lead to try to infer the probability of a higher molecular weight atmosphere (Bolmont et al. 2017a; Krissansen-Totton et al. 2018), but with so many unknowns, observations were needed to get to a definitive conclusion. In short, JWST observations of the TRAPPIST-1 system were expected to revolutionize rocky exoplanet research.

Planet:	b	c	d	e	f	g	h
$R\ [R_\oplus]$	$1.116^{+0.014}_{-0.012}$	$1.097^{+0.014}_{-0.012}$	$0.788^{+0.011}_{-0.010}$	$0.920^{+0.013}_{-0.012}$	$1.045^{+0.013}_{-0.012}$	$1.129^{+0.015}_{-0.013}$	$0.755^{+0.014}_{-0.014}$
$M\ [M_\oplus]$	1.374±0.069	1.308±0.056	0.388±0.012	0.692±0.022	1.039±0.031	1.321±0.038	0.326±0.020
$\rho\ [\rho_\oplus]$	$0.987^{+0.048}_{-0.050}$	$0.991^{+0.040}_{-0.043}$	$0.792^{+0.028}_{-0.030}$	$0.889^{+0.030}_{-0.033}$	$0.911^{+0.025}_{-0.029}$	$0.917^{+0.025}_{-0.029}$	$0.755^{+0.059}_{-0.055}$
$g\ [g_\oplus]$	1.102±0.052	1.086±0.043	0.624±0.019	0.817±0.024	0.951±0.024	1.035±0.026	0.570±0.038
$v_{esc}\ [v_{esc,\oplus}]$	1.109 ± 0.026	1.092 ± 0.022	0.701 ± 0.010	0.867 ± 0.012	0.997 ± 0.012	1.081 ± 0.013	0.656 ± 0.020
$S\ [S_\oplus]$	$4.153^{+0.161}_{-0.159}$	$2.214^{+0.086}_{-0.085}$	$1.115^{+0.043}_{-0.043}$	$0.646^{+0.025}_{-0.025}$	$0.373^{+0.015}_{-0.014}$	$0.252^{+0.010}_{-0.010}$	$0.144^{+0.006}_{-0.006}$
$a\ [10^{-2}\text{AU}]$	1.154±0.010	1.580±0.013	2.227±0.019	2.925±0.025	3.849±0.033	4.683±0.040	6.189±0.053
$R\ [10^8\ \text{cm}]$	$7.119^{+0.087}_{-0.077}$	$6.995^{+0.086}_{-0.077}$	$5.026^{+0.071}_{-0.066}$	$5.868^{+0.082}_{-0.075}$	$6.664^{+0.085}_{-0.077}$	$7.204^{+0.094}_{-0.085}$	$4.817^{+0.091}_{-0.088}$
$M\ [10^{27}\ \text{g}]$	8.211±0.412	7.814±0.335	2.316±0.074	4.132±0.130	6.205±0.184	7.890±0.226	1.945±0.122
$\rho\ [\ \text{g cm}^{-3}]$	$5.425^{+0.265}_{-0.272}$	$5.447^{+0.222}_{-0.235}$	$4.354^{+0.156}_{-0.163}$	$4.885^{+0.168}_{-0.182}$	$5.009^{+0.138}_{-0.158}$	$5.042^{+0.136}_{-0.158}$	$4.147^{+0.322}_{-0.302}$
$g\ [10\ \text{m s}^{-2}]$	1.080±0.051	1.065±0.042	0.611±0.019	0.801±0.024	0.932±0.024	1.015±0.025	0.558±0.037
$v_{esc}\ [\frac{\text{km}}{\text{s}}]$	12.400 ± 0.292	12.205 ± 0.241	7.839 ± 0.110	9.694 ± 0.133	11.145 ± 0.137	12.087 ± 0.142	7.335 ± 0.227
$S\ [10^6\ \frac{\text{erg}}{\text{cm}^2\text{s}}]$	$5.652^{+0.220}_{-0.216}$	$3.013^{+0.117}_{-0.115}$	$1.518^{+0.059}_{-0.058}$	$0.879^{+0.034}_{-0.034}$	$0.508^{+0.020}_{-0.019}$	$0.343^{+0.013}_{-0.013}$	$0.196^{+0.008}_{-0.008}$
$a\ [10^{11}\ \text{cm}]$	1.726±0.015	2.364±0.020	3.331±0.028	4.376±0.037	5.758±0.049	7.006±0.060	9.259±0.079
P [days]	1.510826	2.421937	4.049219	6.101013	9.207540	12.352446	18.772866

Table 1.1: TRAPPIST-1 planetary parameters from Agol et al. (2021)

Planet	b	c	d	e	f	g	h	Instrument(s)	Reference(s)
GTO 1177	5	–	–	–	–	–	–	MIRI F1500W	Greene et al. (2023)
GTO 1201	–	–	2	–	4	–	–	NIRISS/SOSS, NIRSpec/PRISM	Lim et al. 2025, Piaulet-Ghorayeb et al. 2025
GTO 1279	5	–	–	–	–	–	–	MIRI F1280W	Ducrot et al. (2024)
GTO 1331	–	–	–	4	–	–	–	NIRSpec/PRISM	Espinoza et al. 2025, Glidden et al. 2025
GO 1981	–	–	–	–	–	–	3	NIRSpec/PRISM	
GO 2304	–	4	–	–	–	–	–	MIRI F1500W	Zieba et al. (2023)
GO 2420	–	4	–	–	–	–	–	NIRSpec/PRISM	Rathcke et al. (2025a)
GO 2589	2	2	–	–	–	2	–	NIRISS/SOSS	Lim et al. (2023); Radica et al. (2025), Benneke et al. 2025
GO 3077	1.5	1	–	–	–	–	–	MIRI F1500W	Gillon et al. (2025)
GO 5191	4	4	–	–	–	–	–	MIRI F1280W	
GO 6456	15	–	–	15	–	–	–	NIRSpec/PRISM	

Table 1.2: Transit (blue), eclipse (red) and phase curve (green) observations planned on TRAPPIST-1 planets with the JWST, along with observational papers when available. Citations in black are currently under review.

JWST Observations of the TRAPPIST-1 planets That being so, TRAPPIST-1 planets have been the subject of numerous JWST proposals, summarized in Table 1.2. During cycle 1 and 2, all planets have been observed in transit spectroscopy. For now, only transits of TRAPPIST-1 b and c have been published. For TRAPPIST-1 b, the analysis of Lim et al. (2023) confirms the absence of a cloud-free hydrogen-rich atmosphere, but cannot conclude on a secondary atmosphere. The difference between the transit spectra between the two visits shows evidence for strong stellar contamination through the TLS effect (1.2.2). Radica et al. (2025) show similar results for TRAPPIST-1 c, and, by accounting for stellar contamination, find upper limits of ~ 1 bar for some secondary atmospheric compositions. Finally, Rathcke et al. (2025a) experimented stellar contamination correction through back-to-back transits of TRAPPIST-1 b and c during last observation of the GO 2420 program (a technique that is also meant to be used in GO 6456). They showed effective noise reduction, and insights on stellar inhomogeneities, but did not give new constraints on the planets. Besides, observations of GTO 1201 and GO 2589 were used to characterize TRAPPIST-1 stellar flares (Howard et al. 2023).

As for the emission observations, the two inner planets were the subject of five JWST programs in total. TRAPPIST-1 b has been observed at 15 μm (Greene et al. 2023), showing a high dayside flux, then at 12.8

μm, with a lower brightness temperature, still compatible with a bare rock scenario (Ducrot et al. 2024). TRAPPIST-1 c was also observed at 15μm (Zieba et al. 2023), excluding a thick CO_2 atmosphere but not thinner atmospheres. More recently, the GO 5191 observed four times both planets at 12.8 μm, one after the other. Finally, a combined emission phase curve of the system has also been observed (Gillon et al. 2025). TRAPPIST-1 c is the coldest planet observed in emission so far, and the phase curve, representing $\sim$ 60 hours of observations, was also a first for a planet this cold.

1.2.6 Conclusion

In short, rocky exoplanets, due to their size, and the expected size of their atmosphere, are the most difficult to characterize. Because of this, targets are chosen mostly on criteria of observability rather than probability of an atmosphere: even if M-dwarfs are probably harmful for atmospheres, they are for now the only stars around which it is possible to look for rocky exoplanets atmospheres. The global non-detection of such atmospheres shifted the goal of the field, from an optimistic "characterizing rocky exoplanet atmospheres" to an evaluation of the strength of atmospheric loss, in order to assess if rocky exoplanets are capable of maintaining an atmosphere at all. This question is considered a key priority in the community. The two main strategies to achieve it are stellar contamination correction on one side, and to multiply planetary emission observations on the other side (Rocky Worlds DDT program).

2. Methods

Contents

2.1 Observational data . . . 16
2.1.1 Observations with JWST/MIRI . . . 16
2.1.2 Data reduction and analysis . . . 18
2.2 Modeling atmospheres . . . 20
2.2.1 Hierarchy of atmospheric models . . . 20
2.2.2 1D atmospheric evolution model of `exo_k` . . . 22
2.2.2.1 Atmospheric Modeling . . . 22
2.2.2.2 Parametrization of horizontal heat redistribution . . . 23
2.2.3 3D simulations with the `Generic PCM` . . . 24
2.2.4 Opacity . . . 26
2.3 Computing observables . . . 26
2.3.1 1D: `exo_k` . . . 26
2.3.2 3D: `Pytmosph3R` . . . 27
2.3.3 Normalized flux and MIRI filters . . . 27
2.4 Comparing observations and models . . . 27
2.4.1 Computing statistical significance . . . 28
2.4.2 Phase curves . . . 28

My PhD was aimed at interpreting observational data of the TRAPPIST-1 inner planets with atmospheric models. Therefore, my work was at the interface between observation and modeling, and I found that there are many links between the two. In this chapter, I thus decided to propose an introduction to the different methods that intervene in the process of interpreting observational data : observations, data reduction and analysis (2.1), modeling of the atmosphere (2.2), computation of observables (2.3), and comparison between synthetic observables and data(2.4). Fig. 2.1 shows a summary of these methods, and how they interact together.

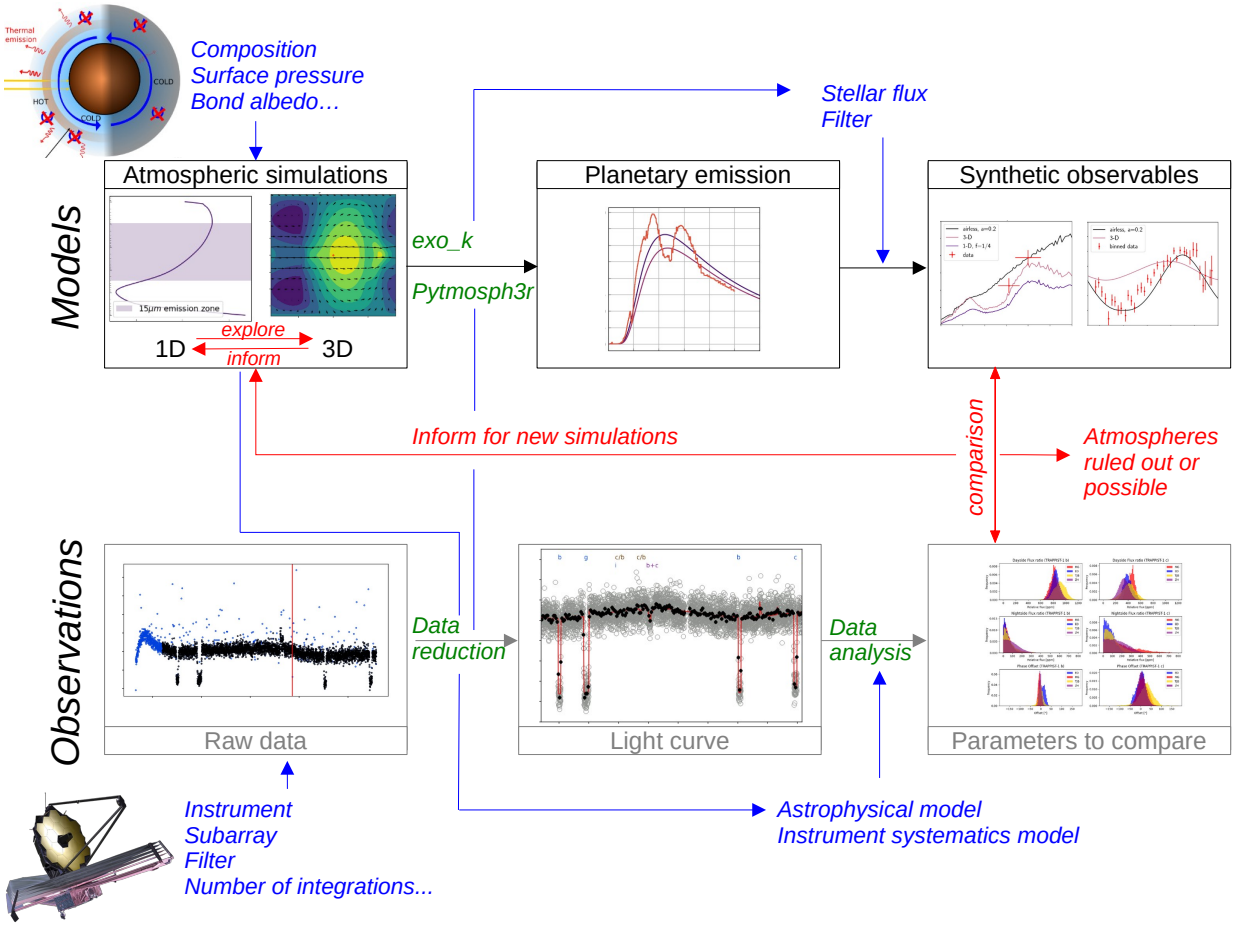

Figure 2.1: A scheme of the general methodology I used to interpret JWST observations with models. I did not perform myself the part concerning observational data.

2.1 Observational data

During my PhD, I did not conduct the observations and data reductions myself, but I worked a lot with observers. Here is an overview of the steps to observe and analyze TRAPPIST-1 planets in emission with JWST.

2.1.1 Observations with JWST/MIRI

Instrument All emission observations of the TRAPPIST-1 planets use the Mid-InfraRed Instrument of the JWST, MIRI. It can provide different observing modes (imaging, low-resolution spectroscopy, coronagraphy...). For targets like the TRAPPIST-1 planets, spectroscopy would require too many eclipses[1], so the imaging mode was used for all eclipse and phase curve observations.

Field of view Fig. 2.2a shows the different subarrays available for the MIRI image mode. First eclipse observations (GTO 1177, 1279, GO 2304) used the FULL array of MIRI (1024 × 1032 pixels), as it was the safe choice at the time (to ensure the star stayed in the field of view). Since first observations showed a good enough stability of the target, the phase curve used the BRIGHTSKY array (512 pixels × 512 pixels), and the latest program (GO 5191) used the sub-array 256. A smaller array is preferred as it allows for better sampling (see next paragraph) and decreases the data volume (convenient for a long observation

[1]For MIRI LRS slitless. New modes like MIRI LRS slit are being tested to get a better SNR and reduce the number of eclipses needed for spectroscopy (Pierre-Olivier Lagage and Achrène Dyrek private communication)

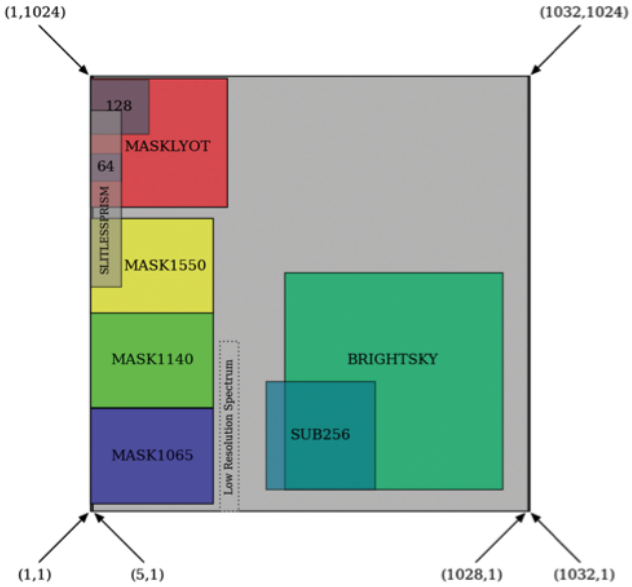

(a) Subarray locations for the MIRI imager. Image from Ressler et al. (2015).

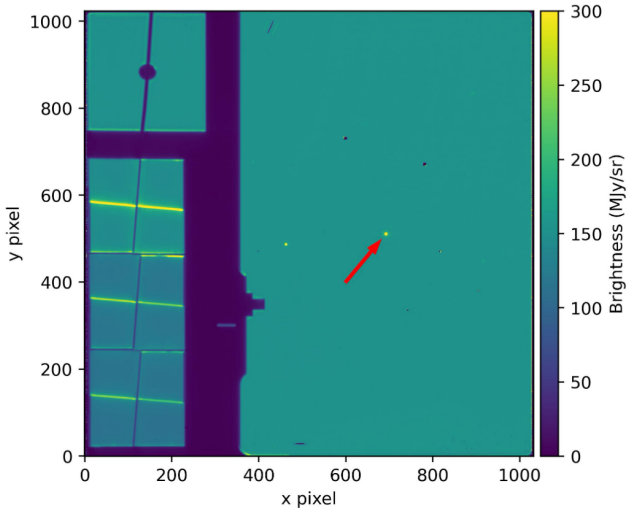

(b) Example of a MIRI integration for the observation of TRAPPIST-1 c at 15 μm from Zieba et al. (2023). The red arrow indicates TRAPPIST-1.

Figure 2.2: MIRI imager field of view.

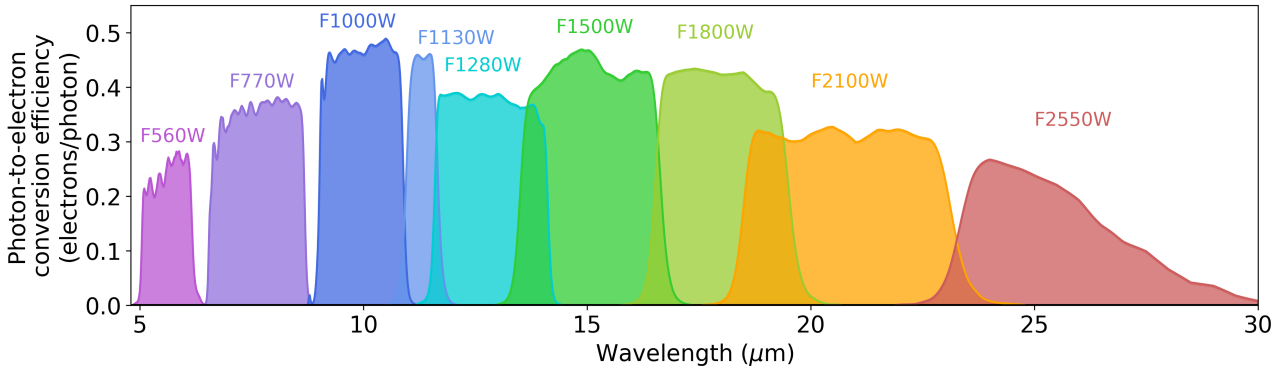

Figure 2.3: MIRI imager photometric filters. Figure credit: STScI MIRI Team

like the phase curve). Fig. 2.2b shows an example of an image of TRAPPIST-1, from the GO 2304 (see Table 1.2).

Filters The MIRI imager provides nine different photometric filters (Fig. 2.3). Photometric emission observations of rocky exoplanets typically use the F1500W (15 μm) filter, as: (i) it is in the wavelength range that maximizes the planet-to-star flux ratio (Fig. 1.2), (ii) this filter has a better SNR than F1800W and (iii) it covers an absorption band of CO_2. The phase curve was taken with this filter. Eclipses were observed for both planets at two different filters, F1500W and F1280W.

Readout pattern Contrary to UV and visible detectors (e.g., HST, ground-based telescopes), most IR detectors integrate flux using a non-destructive up-the-ramp sampling technique. For each pixel, the array is read out non-destructively (*frame*) during an *integration* (Fig. 2.4). Multiple non-destructive frames can be averaged in groups, but in the MIRI imaging mode, each group contains only one frame. Numbers of frame per group, groups per integration and integrations per exposure (i.e. a JWST observation) are set by the observer, according to different criteria (avoiding saturation, duration of a frame reading, data volume, sensitivity to cosmic rays...). An eclipse observation of TRAPPIST-1 b or c with the full MIRI array typically used ~300 integrations of ~15 groups. The phase curve had to be separated into two JWST exposures, due to the 48-hour limit for a JWST exposure. Exposures were made of 3473 and 1843 integrations, with 45

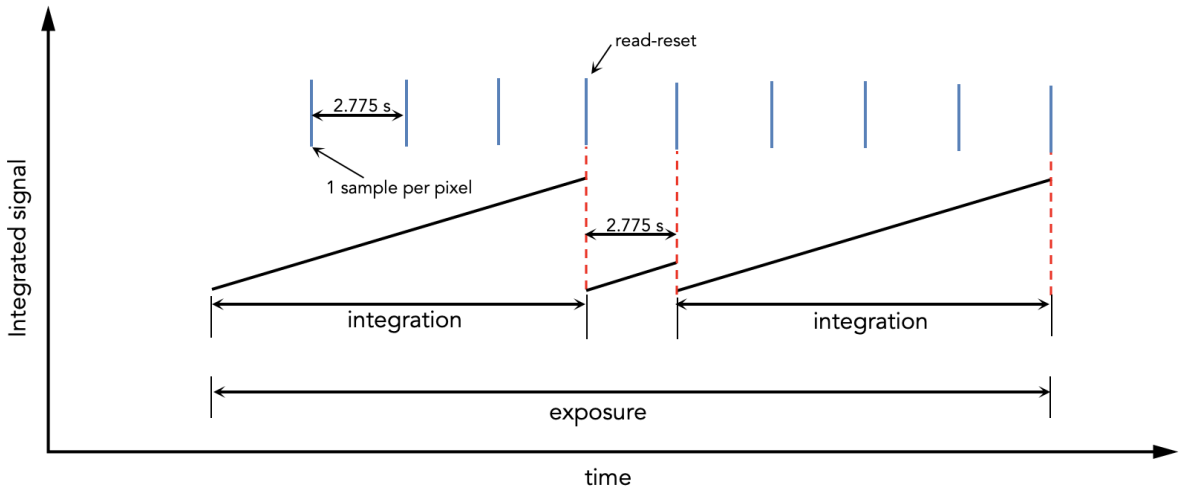

Figure 2.4: An illustration of the up-to-the-ramp readout technique with MIRI, for one pixel. From the JWST user documentation (https://jwst-docs.stsci.edu/jwst-mid-infrared-instrument/miri-instrumentation/miri-detector-overview/miri-detector-readout-overview/miri-detector-readout-fastr1).

groups per integration: the BRIGHTSKY subarray has a smaller group integration time (0.865s vs 2.775s), allowing for more groups per integration and thus better sampling, with a similar signal-to-noise ratio (∼840) and cadence (∼40s) than previous observations (Gillon et al. 2025).

Number of eclipses Finally, the number of eclipses were chosen according to the signal-to-noise ratio (SNR) expected. The precision can be computed by[2] :

$$\frac{\sqrt{1/N_{\rm in} + 1/N_{\rm out}}}{\rm SNR/integration} \tag{2.1}$$

where $N_{\rm in}$ and $N_{\rm out}$, the number of integrations during and outside eclipse for one visit, depend on the number of groups per integration and the time needed to read each group, as the duration of the observation (∼3-4h) is constrained by the eclipse itself. The SNR per integration is computed with the JWST Exposure Time Calculator. The noise decreases as $1/\sqrt{N}$, with N the number of eclipses. Observations of TRAPPIST-1 b with GTO 1177 and 1279 acquired 5 eclipses, while GO 2304 acquired 4 eclipses of TRAPPIST-1 b, and GO 5191 4 eclipses of each planet.

2.1.2 Data reduction and analysis

After data acquisition comes its calibration, reduction and analysis. It can be performed with the `Eureka!` data analysis pipeline (Bell et al. 2022). This pipeline is widely used, especially the data reduction steps, and it allowed me to use the well-written documentation[3] as a basis for this section, though other pipelines and home-made codes exist to perform data reduction and analysis from JWST observations. It is divided into several stages, that we will refer to in the following paragraphs.

Calibration *(Stages 1 and 2 of `Eureka!/jwst` pipeline)* As explained in the previous section, JWST detectors provide, for each integration, a ramp of non-destructive data. In order to convert this into flux, one must fit slopes to these ramps (stage 1) and calibrate them to astrophysical units (mJy) (stage 2). The pipeline `jwst` is dedicated to calibration for JWST data. Calibrated data can also be downloaded directly

[2] https://jwst-docs.stsci.edu/jwst-near-infrared-imager-and-slitless-spectrograph/niriss-example-science-programs/niriss-soss-time-series-observations-of-a-transiting-exoplanet/step-by-step-etc-guide-for-niriss-soss-time-series-observations-of-a-transiting-exoplanet#gsc.tab=0

[3] https://eurekadocs.readthedocs.io/en/latest/

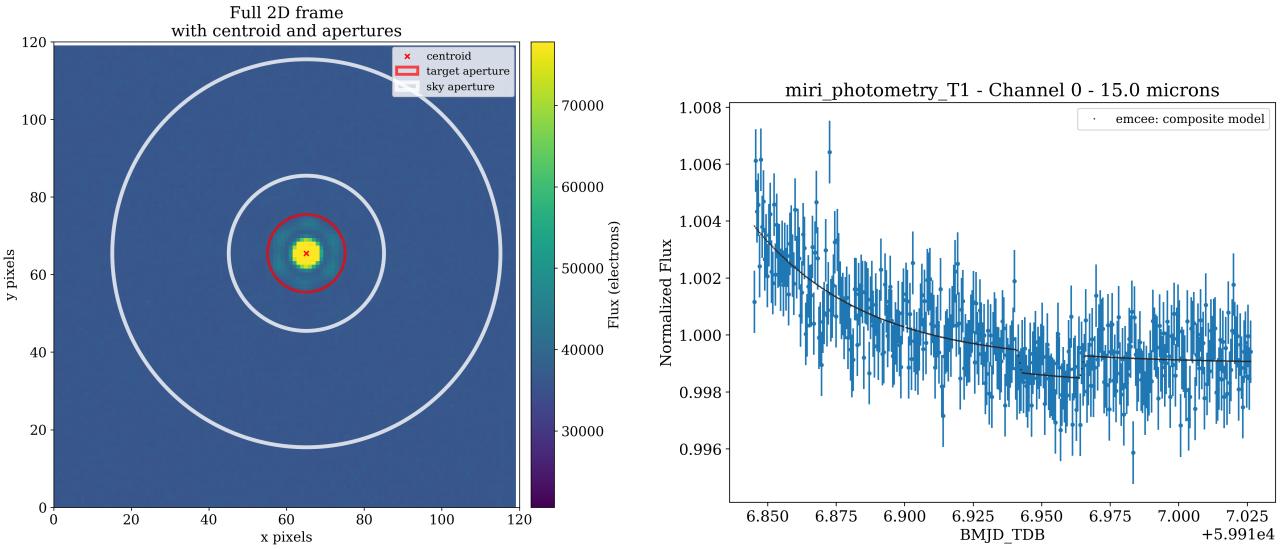

(a) Aperture photometry

(b) Fitted noise and astronomical model

Figure 2.5: Examples of data reduction and analysis steps for eclipse data from GO1177 (credit : Louis-Julien Cartigny)

from the JWST data, but most observers prefer to re-run the calibration, with the possibility to control the parameters (e.g., ramp-fitting weighting parameters, cosmic ray rejection threshold...).

Reduction *(Stages 3 and 4 of `Eureka!`)* After calibrating the data, one needs to extract the star signal from the background as efficiently as possible. For this, one performs aperture photometry (stage 3), which consists in selecting a disk containing the target point spread function, and an outer ring chosen to be representative of the background signal, and removing from the disk the background signal computed in the ring (Fig. 2.5a).
After this, stage 3 of `Eureka!` consists in generating a light curve from the data. In spectroscopic modes, it includes spectral binning, but in photometric mode it consists mostly in removing outliers by sigma-clipping.

Data analysis *(Stage 5 of `Eureka!`)* Finally, one can fit the extracted light curve to several parametric models :

Instrumental systematics model : The JWST observations come with time-dependent systematics. An exponential increase (or decrease) is often observed at the beginning of MIRI observations; this is known as a ramp (visible in Fig. 2.5b). It arises from instrumental systematics that depend on the history of the detector (Bell et al. 2023; Dyrek et al. 2024). These behaviors are difficult to predict, so we model them simply using exponential ramps. Additionally, other systematic models can be applied : a linear trend, a time variation in the position and width of the PSF, estimation of the white noise level.

Astrophysical model : The signal itself is fitted through astronomical light curve models. For transits and eclipses, the models are quite straightforward[4]. However, for phase curves, the shape of the signal directly depends on the presence or absence of atmosphere, making it more difficult for the data analysis (see section 2.4).
The different model parameters are then fitted together using Bayesian inference methods (Note 2.1). For the eclipse observation, eclipses were fitted both individually and altogether.

[4]The main unknown in transit light curves models is the limb-darkening coefficient of the star (Mandel & Agol 2002). This effect is not important in emission observations.

Note 2.1: Bayesian inference

Bayesian approach aims at finding model parameters that fit well the observations, but also that correspond to our prior knowledge about them. It is based on the Bayes theorem that can be written as:

$$p(\theta \mid y) = \frac{p(y \mid \theta)p(\theta)}{p(y)} \tag{2.2}$$

with y the observed data, θ the parameters of interest. We first assign a probability to a hypothesis - the *prior*, $p(\theta)$ -, and evaluate the agreement between the model and the data - the *likelihood*, $p(y \mid \theta)$ -, while $p(y)$ - the *evidence*-, is a normalizing constant. A bayesian analysis consists in updating the priors by the likelihood to produce *posterior distributions*, $p(\theta \mid y)$. For more details, see for example (Eadie et al. 2023).
The parameters of the model are estimated from the posterior distribution, obtained with parameter sampling algorithms (MCMC, nested sampling... see e.g. Al-Refaie et al. (2021)) that run the model a great number of times to fit the parameters.

Calibrating stellar flux The analysis described above uses a normalized flux, which is adapted to the analysis of the eclipse depth F_p/F_*. However, in order to get the absolute flux of the planet and infer its brightness temperature and Bond albedo, one must know precisely the stellar flux - it is thus important to have precise models and measurements of the stellar spectrum (Fauchez et al. 2025). Therefore, all emission papers perform a calibration of the stellar flux, measuring it during the eclipse. Note that the error bars for this measurement, for which several steps of data reduction and analysis do not apply, are much bigger than for the relative flux measurements of the eclipse depth and reach a few percents (see e.g. Gordon et al. (2024) for MIRI flux calibration). This will de discussed in more details in Chapter 5.

2.2 Modeling atmospheres

To interpret observational data, one must compare it to models. In this section, after presenting the range of commonly used models for atmospheres, I detail the two models that I used during my PhD, `exo_k` and the `Generic PCM` . Some notations I use in this section are provided in Table 2.1.

Notation	Description	Unit
F_p, F_*	Planetary/stellar flux integrated over their surface.	W or mJy
$\mathscr{F}_p$, $\mathscr{F}_*$	Planetary/stellar flux per unit of surface.	W/m^2
OLR	Outgoing Longwave Radiation (radiation of the planet),	W/m^2
ISR	Incoming Stellar Radiation (radiation from the star received by the planet)	W/m^2

Table 2.1: Notations

2.2.1 Hierarchy of atmospheric models

We cannot have access to spatially resolved observations of exoplanets, since all information come from the integrated light of the star-planet system. However, techniques like phase curve observations give indirect access to the 3D thermal structure of the planet. Moreover, one must remember that other observations are also 3D dependent : eclipse observations give access to the dayside of the planet, while transit spectroscopy probes the atmosphere at the terminator. Thus, 3D modeling is precious for interpreting observations. However, depending on the context, simpler, faster models can be useful. Here are a few types of models, listed from the simplest to the most complex:

"0-D" Energy Balance Models These models use averaged quantities to compute the emitted flux and temperature of the planet. The simplest model consists in computing the flux of the planet received from

the star, $F_{\text{rec}} = S_{\text{rec}}(1-A)ISR$, and equalizing it to the flux emitted by the planet, $F_p = S_{\text{emis.}}\varepsilon\mathscr{F}_p$. The reception surface of the planet is the disk of radius R_p, and if we suppose a planet with a uniform albedo and emitting temperature, the emission surface is the area of the planet. Thus, if we suppose an emissivity of 1 in the thermal wavelengths :

$$\pi R_p^2(1-A)ISR = 4\pi R_p^2 OLR \tag{2.3}$$

With $ISR = \mathscr{F}_*\left(\frac{R_*}{a}\right)^2 = \sigma T_*^4\left(\frac{R_*}{a}\right)^2$, one can then retrieve the equilibrium temperature :

$$T_{\text{eq}} = \left(\frac{F_p}{\sigma}\right)^{1/4} = (1-A)^{1/4}\sqrt{\frac{R_*}{2a}}T_* \tag{2.4}$$

This temperature corresponds to the case of full redistribution between the dayside and nightside of the planet.

1D vertical models with prescribed temperature profile These models are used for example in transit spectra retrievals (e.g., `TauREx` (Al-Refaie et al. 2021), `petitRADTRANS` (Mollière et al. 2019)): the temperature is fixed, and radiative transfer is computed for different atmospheric compositions in order to retrieve the best fit composition. These models are fast enough to perform bayesian retrieval (Note 2.1), but they are not self-consistent.

1D vertical Inverse Climate Models Inverse climate models suppose a temperature profile parameterized by surface temperature and pressure (usually, a dry adiabat in the deep atmosphere and an isotherm in the upper atmosphere - see Note 2.2), and compute radiative transfer at two wavelengths channels, corresponding to the star and planet emission. The outgoing long wave radiation (OLR) can then be compared to incoming stellar radiation (ISR) to assess the energetic balance. These models are also fast and allow for computation on a wide range of parameters, allowing to retrieve a thermal profile for a given ISR by equalizing the OLR to it. They are widely used, e.g. for habitable zone computations and mass-radius relationships. However, these models are not exactly at equilibrium, because although radiative balance is ensured at the top of atmosphere by $ISR = OLR$, it does not mean that each layer is at equilibrium.

Note 2.2: Adiabat

An adiabat is the temperature-pressure gradient of an atmosphere governed by vertical convection. When a temperature gradient is too strong, convection is triggered and the temperature is linked to the pressure by (in the dry case) : $\mathrm{d}T = \Gamma \mathrm{d}z$ with $\Gamma = -g/c_p$. Indeed, if a gas particle of mass m at altitude z is moved to $z + \mathrm{d}z$, its enthalpy varies by : $\mathrm{d}H = mc_p\mathrm{d}T = V\mathrm{d}P - T\mathrm{d}S = V\mathrm{d}P$ for an adiabatic exchange. At hydrostatic equilibrium, $\mathrm{d}P = -\frac{m}{V}g\mathrm{d}z$ so $\mathrm{d}T = \Gamma\mathrm{d}z$

1D vertical atmospheric evolution models Radiative-convective models (first developed by Manabe & Wetherald 1967) decompose a column of atmosphere in layers, evolve each layer after computing heating rates (see section 2.2.2), and take into account convection, and possibly condensation. These models are self-consistent, and they show the time evolution of the atmosphere, but they are more computationally expensive than the previous models (and some atmospheres take more time to converge than others), and, still, cannot take into account horizontal transport effects.

1D or 2D horizontal Energy Balance Models These fast, highly parameterized models (North 1975) compute a horizontally-dependent surface temperature through energetic horizontal balance. Since they simulate horizontal transport, they can describe equator-to-pole or dayside-to-nighside gradients, and thus are a good tool to simulate and interpret phase curves (Cowan & Agol 2011a).

"1.5-D" models Some efforts have been made to implement 3D redistribution into 1D atmospheric evolution models (Ih et al. 2023; Lincowski et al. 2023). They consist in parameterizing the 3D redistribution factor that is computed through a scaling law depending on the composition and pressure of the atmosphere (Koll 2022). However, this is only a proxy that cannot take into account more complex 3D effects. Indeed, this parametrization computes the redistribution factor in the deep atmosphere, but in the upper atmosphere the redistribution is less efficient, and according to the composition of the atmosphere, the emission does not necessarily come from the deepest layers. Thus, supposing a homogeneous redistribution factor for the whole column of atmosphere is a strong approximation.

3D Global Climate Models (GCMs) Finally, 3D climate models include 3D convective transport, and a variety of mechanisms at play (depending on the GCM, see section 2.2.3). These are the most complex models available, and allow for accurate climate simulations, but their convergence time are a strong limit to their use. Such models are widely used for the predictions (e.g., Showman & Guillot 2002; Rauscher et al. 2008; Selsis et al. 2011) and interpretations (e.g., Rauscher & Menou 2013; Teinturier et al. 2024) of phase curve observations, which are intrinsically three-dimensional.

Note on chemistry Most of these models work with a prescribed chemistry. The chosen composition of the atmosphere will impact the radiative transfer through molecular opacities. For some models, abundances at equilibrium can be computed from the temperatures and pressures of the model, with prescribed metallicity and C/O ratio. Some models present a photochemistry module that can take into account disequilibrium chemistry induced by high-energy radiation in the upper atmosphere, and thus modify the opacity. They slow down considerably the simulations. I will not expand on this as I exclusively used prescribed molecular chemistry during my PhD.

2.2.2 1D atmospheric evolution model of `exo_k`

2.2.2.1 Atmospheric Modeling

`exo_k` (Leconte 2021) possesses an atmospheric evolution model. From an initial temperature profile, and different parameters (surface albedo, incoming stellar radiation, atmospheric composition), it computes the temporal evolution of the atmosphere. In `exo_k` , the atmospheric column is decomposed into `Nlay` layers (Fig. 2.6). Levels correspond to the interfaces between layers; level `[0]` corresponds to the atmosphere top and level `[Nlay]` to the surface[5].

Radiative transfer The radiative transfer is computed with an algorithm (Toon et al. 1989) based on the two-stream approximation. This approximation consists in assuming (i) a plane-parallel geometry ($H \ll R_p$, with H the scale height of the hemisphere), allowing to describe the column of atmosphere with one coordinate, and (ii) that the radiation propagates in the direction of this coordinate, i.e. it can be described by upwards and downwards fluxes only. The net radiative flux $\Delta\hat{F}_{\rm net}$ is computed at each radiative layer, which possesses an opacity computed with `exo_k` . Then, the radiative heating rate is computed as $\hat{H}^{\rm rad} = \frac{\Delta\hat{F}_{\rm net}}{\hat{M}}$, with the mass per unit area $\hat{M} = \frac{\Delta\hat{P}_{\rm lev}}{g}$, and $\hat{X}$ representing vector quantities.

Other physical processes `exo_k` handles convection through a dry convective adjustment scheme, adjusting the temperature profile to an adiabat when it is unstable (Note 2.2). This results in a convective heating rate $\hat{H}^{\rm conv}$. It also handles moist processes : moist convection, condensation, and rainfall, for any species. I did not activate condensation in my `exo_k` simulations and thus will not give details about this.

Time integration Time evolution is computed from the conservation of energy : $c_p \partial_t \hat{T} = \hat{H}$ with $\hat{H}$ the total heating rate. With the reduced time defined as $t^* \equiv t/c_p$, the discretized time evolution is written like : $\hat{T}^{t^*+\Delta t^*} = \hat{T}^{t^*} + \Delta t^* \cdot \hat{H}(\hat{T}^{t^*})$

[5]This convention is different from the `Generic PCM` , where layers are counted from surface to top of atmosphere.

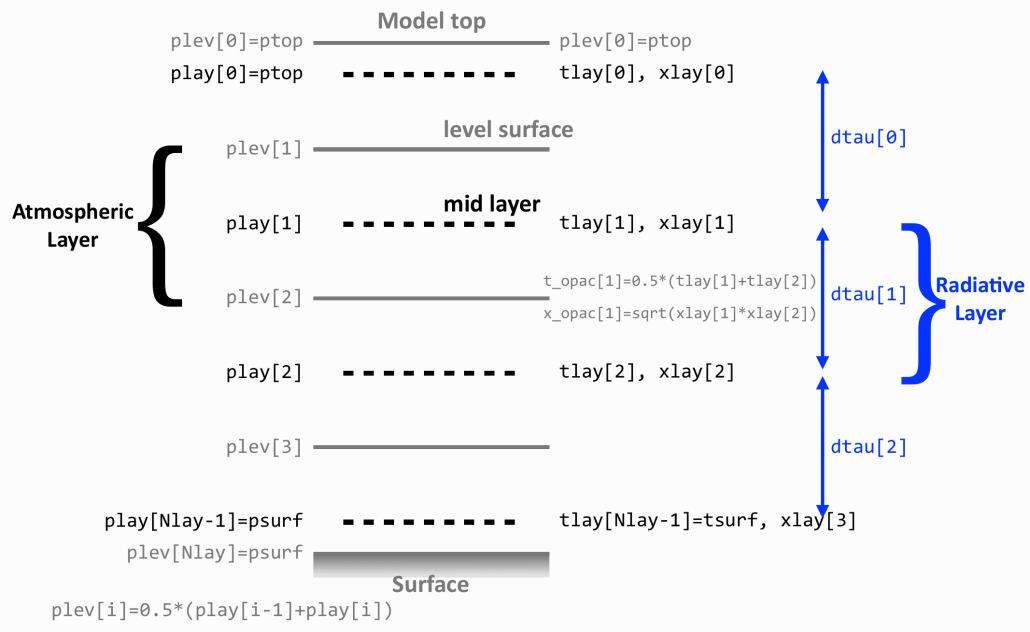

Figure 2.6: Schematic of atmospheric layers, levels and radiative layers in `exo_k` from the `exo_k` tutorial (`https://perso.astrophy.u-bordeaux.fr/~jleconte/exo_k-doc/exo_k_evol.html`)

Convergence acceleration `exo_k` comes with several acceleration algorithms, allowing to get faster to the equilibrium state, which usually is what the modeler is looking for. First, it computes a radiative timescale from the minimum of the inverse of the diagonal terms of the Jacobian matrix of the heating rates[6]. This smallest timescale is used as a time step to accelerate the code while ensuring enough time sampling. This Jacobian matrix can also be used to avoid computing heating rates each time. In addition, the code provides convergence acceleration, by computing independently radiative zones with their own time scales. This is particularly useful for optically thick atmospheres.

2.2.2.2 Parametrization of horizontal heat redistribution

`exo_k` can only compute one column of atmosphere. I used it with the goal to compute dayside emission of planets in order to interpret eclipse observations. I thus needed to provide a flux at top of atmosphere representative of the mean of the flux received in the dayside. We showed in section 2.2.1 that for a full redistribution case, $OLR = 1/4(1-A)ISR$. Thus, to compute a 1D atmospheric column representative of a planet with full redistribution, one must divide by 4 the value of the ISR at substellar point.
Another simple case is to model one homogeneous dayside temperature and a nightside temperature of zero. In this case, the surface of emission would be half of the surface of the sphere, and thus the factor would be $1/2$ instead of $1/4$.
Now let us compute the case of a zero-redistribution planet. The nightside receives zero flux from the star, and the temperature is thus $\sim$0. For the dayside, the substellar point is hotter, and is also the point that is directed towards star, which is also the direction of the observer during the eclipse. The resulting dayside emission of the planet towards the observer during the eclipse will thus be larger than the previous case.
If we decompose the dayside into rings of angle θ with the substellar point (Fig. 2.7), each ring will receive a flux from the star proportional to θ, thus emitting a flux proportional to θ ($OLR(\theta) = OLR_0 cos(\theta)$). We

[6]The Jacobian matrix shows how heating in a layer is related to a temperature change anywhere in the atmosphere, the main terms are the diagonal (negative) terms : when the temperature increases in a layer, it will emit more, and thus cool.

thus get :

$$\begin{aligned} F_p &= \int OLR(\theta) \mathrm{d}\vec{S}.\vec{u} \\ &= \int OLR_0 \cos\theta 2\pi R_p^2 \sin\theta \cos\theta \mathrm{d}\theta \\ &= 2\pi R_p^2 OLR_0 \int_0^{2\pi} \cos^2\theta \sin\theta \mathrm{d}\theta \\ &= 2\pi R_p^2 OLR_0 \int_1^0 \mu^2 \mathrm{d}\mu \\ &= 2/3\pi R_p^2 OLR_0 \end{aligned} \tag{2.5}$$

The factor for a zero redistribution case is thus 2/3.

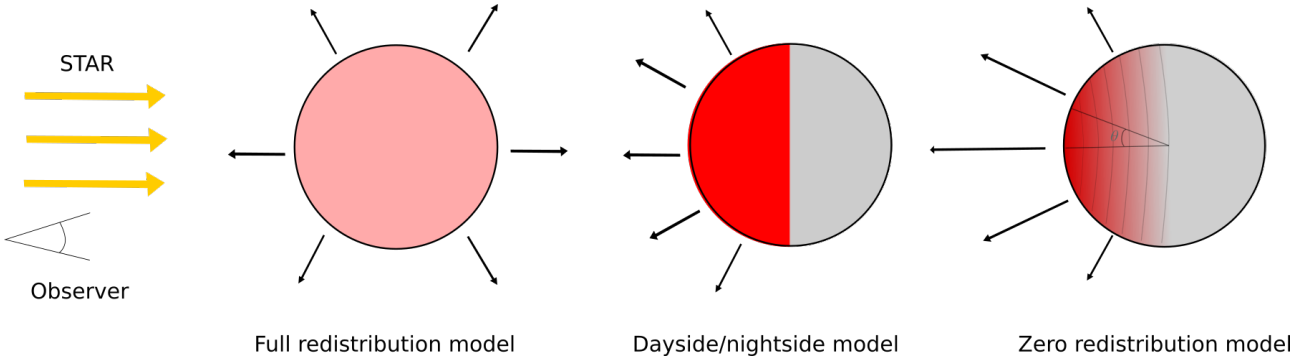

Figure 2.7: Different simple energy balance models corresponding to redistribution factors.

To account for horizontal heat redistribution, I therefore used a redistribution factor f spanning from 2/3, i.e. zero redistribution, to 1/4, full redistribution. This factor is used in several other papers of interpretation of eclipse data with 1D models (Ih et al. 2023; Lincowski et al. 2023). f is often computed from the parametrization of Koll (2022). I preferred to use a prescribed f, given that 1D modeling was in my case only a first step to 3D simulations, and that I found that this parametrization was not always accurate, depending on the type of atmosphere.

2.2.3 3D simulations with the `Generic PCM`

The `Generic PCM` is a 3D GCM developed mostly at LMD and Laboratoire d'Astrophysique de Bordeaux (LAB). It has been used on a large diversity of subjects on the solar system[7], and exoplanets : Gl581d (Wordsworth et al. 2011), GJ1214b (Charnay et al. 2015a,b), TRAPPIST-1 planets (Turbet et al. 2018), K2-18b (Charnay et al. 2021), WASP-43 b (Teinturier et al. 2024), and generic studies (Bolmont et al. 2016; Turbet et al. 2023).

Taking advantage of the fact that the horizontal and vertical physical processes and scales are very different, the GCM is structured into two main components : the "dynamics" part, dealing with horizontal fluxes, and the "physics" part, for vertical processes. The planet is divided into a horizontal grid, and for each grid point there is a vertical column for computation of radiative transfer (see Fig. 2.8).

Dynamical core The planet is horizontally discretized in a longitude-latitude grid[8], on which the primitive equations of meteorology are solved : horizontal motion equations (Navier-Stokes), thermodynamic first principle, and mass conservation (see for example Teinturier (2024) for more details).

[7] Some solar system objects have their specific PCM : Venus, Mars, Giant planets, Titan, Pluto.

[8] This dynamical core is common to the other solar system PCMs mentioned. A dynamical core with icosahedral discretization, `DYNAMICO`, is used for solar system gas giants

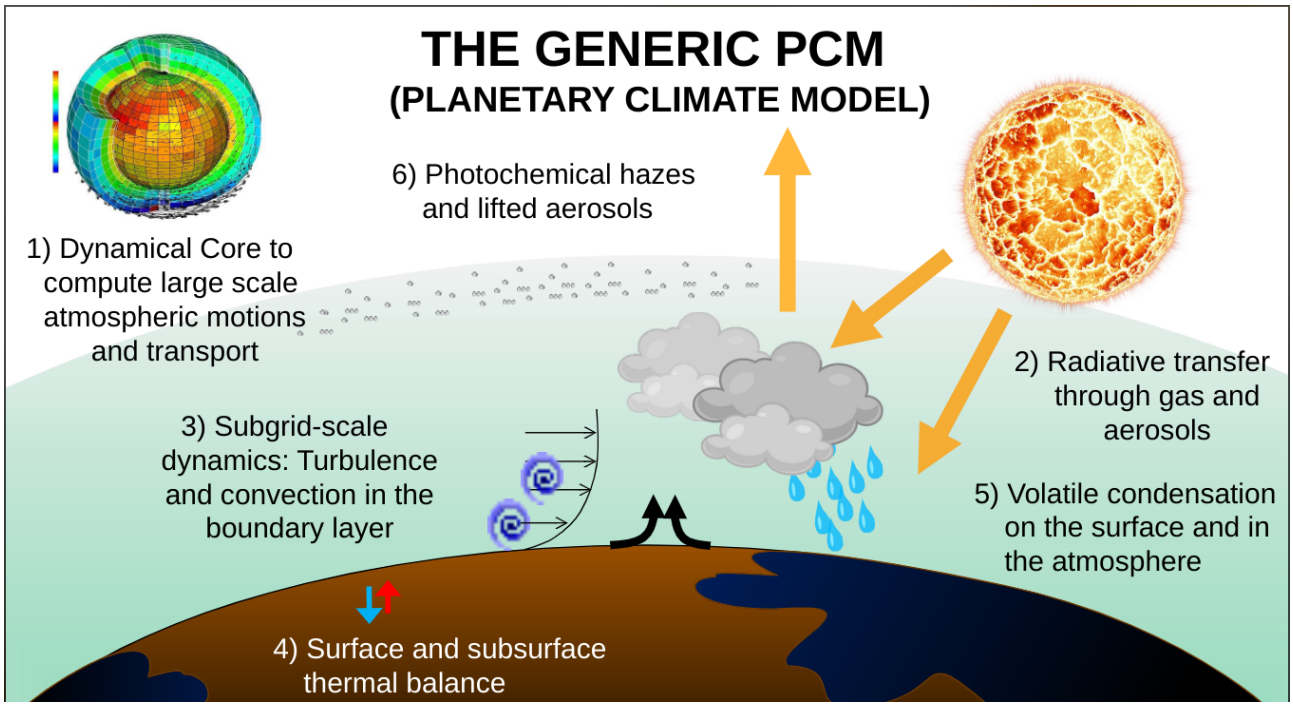

Figure 2.8: Overview of the `Generic PCM` . Credits: Martin Turbet

The computation of the dynamical core can be parallelized, with a maximum of $N_{lat}/2$ cores with N_{lat} the length of the latitude grid.

Radiative transfer Radiative transfer is performed using the two-stream approximation, similarly to `exo_k` . The column is decomposed into layers[9], and only upwards and downwards exchange between layers are computed. Heating rates are derived from the net radiative fluxes, allowing to evolve each layer.

Sub-grid scale parametrization One needs to parameterize the processes which are not resolved at our discretization scale - and which mix energy and momentum.
Convection: When the temperature gradient is too strong, the profile is unstable, the temperature is corrected to follow an adiabat[10], through a convective adjustment scheme.
Turbulence: Turbulence is a chaotic, small-scale movement of the gas. Its larger-scale effects are taken into account through a parametrization described in Wordsworth et al. (2013). Turbulence is particularly important near the surface.

Surface and subsurface The subsurface is modeled by several layers with a volumetric capacity and thermal inertia, which exchange heat through conduction.
In my case, I do not have any inputs of the surface of the TRAPPIST-1 planets, so the parameters are chosen by analogy to Mars, with no topography, and with a prescribed bond albedo.

Condensation The `Generic PCM` comes with a condensation scheme for CO_2, H_2O and generic species. I used the CO_2 condensation (Forget et al. 2013) in my work to study the potential collapse on thin, CO_2-rich atmospheres. The scheme forms CO_2 ice clouds or surface frost when a cell reaches 100% saturation. The cloud ice particle sediment at the surface, and the surface ice can re-sublimate.

Aerosols The model can handle aerosols (dust and hazes). Aerosols can have various origins, from photochemically-produced hazes in the upper atmosphere to dust lifted from the ground. In the `Generic`

[9] In my case, I have no topography, so I directly use pressure coordinates.
[10] Note 2.2

PCM , one can implement as many layers of aerosols as needed. For each aerosol layer, the user prescribes the type of aerosol from a set of files with optical properties, the lower and upper limits of the layer, as well as its total optical depth. The contribution of the aerosols in the radiative transfer is then computed from their extinction coefficient, single scattering albedo and asymmetry factor (Madeleine 2011). For specific cases -Early Earth, Mars (Montabone et al. 2015), Titan (Charnay 2014)-, the model was also designed to handle aerosol formation and evolution, through solving microphysics and photochemistry for hazes, and dust transport. This modeling, however, increases significantly the computational cost of the simulations and was not used in our work.

2.2.4 Opacity

Both the atmospheric model of exo_k and the Generic PCM need gas and atmospheric components' opacity data. Opacity of molecules is traditionally in cross-section vs wavelength or wave number. However, radiative transfer calculations are time-costly, and in order to run atmospheric models in a reasonable amount of time, one needs to have a low resolution. Since opacity lines vary a lot over wavelength, directly sampling the cross-sections leads to large errors. Instead, both models use the correlated-k approach (see Liou 1980, for a detailed explanation). The opacity data is decomposed into spectral bands. In each band, the reciprocal of the cumulative density function of the opacity within band is computed. Then this function, much smoother than the absorption spectrum, can be sampled into a limited number of points (Gauss points, g) and safely re-interpolated (Fig. 2.9). A way to illustrate the difference with the cross-section sampling approach is to say that in each band, the cross-section sampling assumes the absorption to be constant and the correlated-k allow the absorption to take a probabilistic value, weighted by the distribution function.

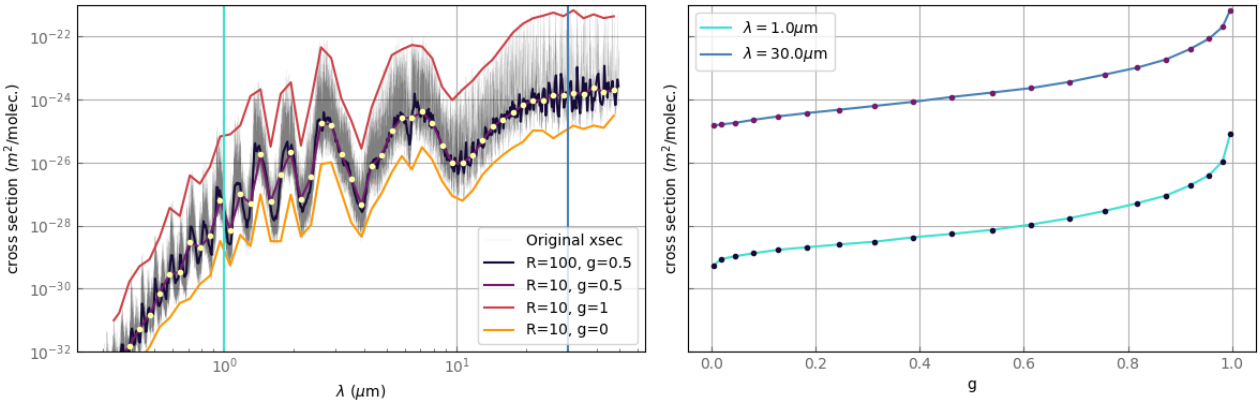

Figure 2.9: Illustration of the correlated k method. Left: correlated-k tables of H_2O with various resolution and Gauss points, along with the original cross-section data in gray. R=10 corresponds to the resolution I used for atmospheric models, R=100 to the resolution for computation of observables. Right: reciprocal density function for two wavelengths (shown as vertical lines on the left panel). Points illustrate the sampling.

exo_k is designed to handle various radiative opacities, easily compute correlated-k tables and even spectrally re-bin correlated-k tables (Leconte 2021). I used it to compute tables for various gas mixtures both for 1D model of exo_k and for the Generic PCM . I used a band resolution of $R \sim 10$ for modeling atmospheres, and upgraded it to $\sim$100 for computing emission observables (and 500 for transmission).

2.3 Computing observables

2.3.1 1D: exo_k

exo_k can simulate observables (in transit, emission and reflected light) from a given atmospheric composition and 1D temperature profile.

Secondary eclipse The secondary eclipse depth corresponds to the emission of the dayside of the planet. It is computed again using the two-stream approximation of Toon et al. (1989), used for the atmospheric evolution model. The radiative emission at the top of the atmosphere corresponds to the dayside flux of the planet.
The contribution of each layer, that I used to evaluate where the emission comes from, can be computed by the vertical contribution function:

$$C(P,\lambda) = B(T,\lambda)\frac{\mathrm{d}e^{\tau}}{\mathrm{d}\log P} \tag{2.6}$$

Transit The transit depth $\delta_\nu \equiv (R_p(\lambda)/R_*)^2$ corresponds to the ratio of the surface of the planet over the one of the star, plus one part that is the contribution of the atmosphere:

$$\delta_\nu = (\pi R_p^2 + \alpha_\nu)/(\pi R_*^2) \tag{2.7}$$

with:

$$\alpha_\nu = 2\pi \int_0^{z_{max}} (R_p + z)(1 - e^{-\tau_\nu(z)})\mathrm{d}z \tag{2.8}$$

In `exo_k` , the portion of absorbed light $(1-e^{-\tau})$ is computed at each radiative layer, as well as the area of the annulus covered by the layer $\pi\left((R_p+z+\mathrm{d}z)^2-(R_p+z)^2\right)$. The two quantities are multiplied and the result is summed over the atmosphere, to obtain the quantity α_ν.

2.3.2 3D: `Pytmosph3R`

`Pytmosph3R` (Falco et al. 2022) is designed to compute observables from 3D simulations. It takes as input a simulation file, with the temperature at each point, and performs radiative transfer computations over the grid. The atmospheric composition (gas, aerosols) can be read from the simulation file, or set by the user.

Emission For any phase of the planet, the emission can be obtained by computing the emission of each column of atmosphere of the simulation horizontal grid, then weighting it by the angle of with the observer. Half of the planet is hidden from the observer and thus does not contribute. `Pytmosph3R` can compute the emission over the wavelength grid and at different phases, corresponding to different angles with the observer. In all this manuscript, the transit (and nightside emission) corresponds to the phase fraction of 0 (and 1) while secondary eclipse/dayside emission corresponds to a phase fraction of 0.5.

Transmission Similarly, transmission spectroscopy for 3D is done by computing transmission at each point around the terminator in the simulation.

2.3.3 Normalized flux and MIRI filters

The emission observations are normalized fluxes F_p/F_*, over the MIRI filter, while `Pytmosph3R` provides a flux per unit of surface, depending on the wavelength. To compare with observations, we thus compute

$$F_p/F_* = \int_\lambda \frac{\mathscr{F}_p(\lambda)}{\mathscr{F}_*(\lambda)} \left(\frac{R_p}{R_*}\right)^2 W(\lambda)\mathrm{d}\lambda \tag{2.9}$$

with $W(\lambda)$ the response of the MIRI filter.
The stellar spectrum is normalized to correspond to a flux in the 15 μm MIRI filter of 2.528 mJy, corresponding to the absolute flux computation of Gillon et al. (2025).

2.4 Comparing observations and models

In this section, I present the comparison between observations and models as performed in Gillon et al. (2025) and Maurel et al. (2025). This comparison is not straightforward and has strong limits; I discuss it further in Chapter 7.

2.4.1 Computing statistical significance

In order to quantitatively compare the match between observational data and synthetic observables from atmospheric models, we use the following procedure.
We compute the χ^2 between model and observational data points:

$$\chi^2 = \sum_i \frac{(O_i - M_i)^2}{\sigma_i^2} \tag{2.10}$$

From the χ^2, we compute the upper-tail p-value

$$p = 1 - F_{\chi^2} \tag{2.11}$$

with F_{χ^2} the cumulative density function of the corresponding χ^2 random variable. The p-value corresponds to the probability of obtaining the observed data if the planet corresponds to the model.
To obtain a standard deviation in units of sigma, we compute the inverse of the cumulative density function of the normal law for the computed p-value:

$$Z = (1 - F_{\mathcal{N}})^{-1}(p/2) \tag{2.12}$$

For the eclipse observations, the data used are simply the eclipse depths.

2.4.2 Phase curves

For the phase curve, the observed data corresponds to a flux versus time. Like in the eclipse data, the flux was fitted with astrophysical and noise models to obtain a clean phase curve. However, the astrophysical model is complicated: (1) it must fit both planet b and c at the same time, while we would like to assess models for planets one at a time, and (2) it must make assumptions on the shape of the phase curve, which itself depends on the presence and composition of the atmosphere.
In our case, the shape of the phase curve was modeled by two different ways in the data analyzes : first, a sinus with 3 parameters (minimum flux, maximum flux, phase offset), and second with a quasi-Lambertian curve (Agol 2007):

$$\frac{F_p(t)}{F_*} = \frac{F_{p,D,max}}{F_*} \times \cos(\theta(t)/2)^\gamma \tag{2.13}$$

with γ as a free parameter. This second model corresponds to an airless case for $\gamma \sim 3$.
We decided to use the minimum flux, maximum flux, phase offset as points to compare in the χ^2 computation (Fig. 2.10), as we thought it was more robust. We discuss this in more details in the study of TRAPPIST-1 b in the next chapter (section 3.2.4).

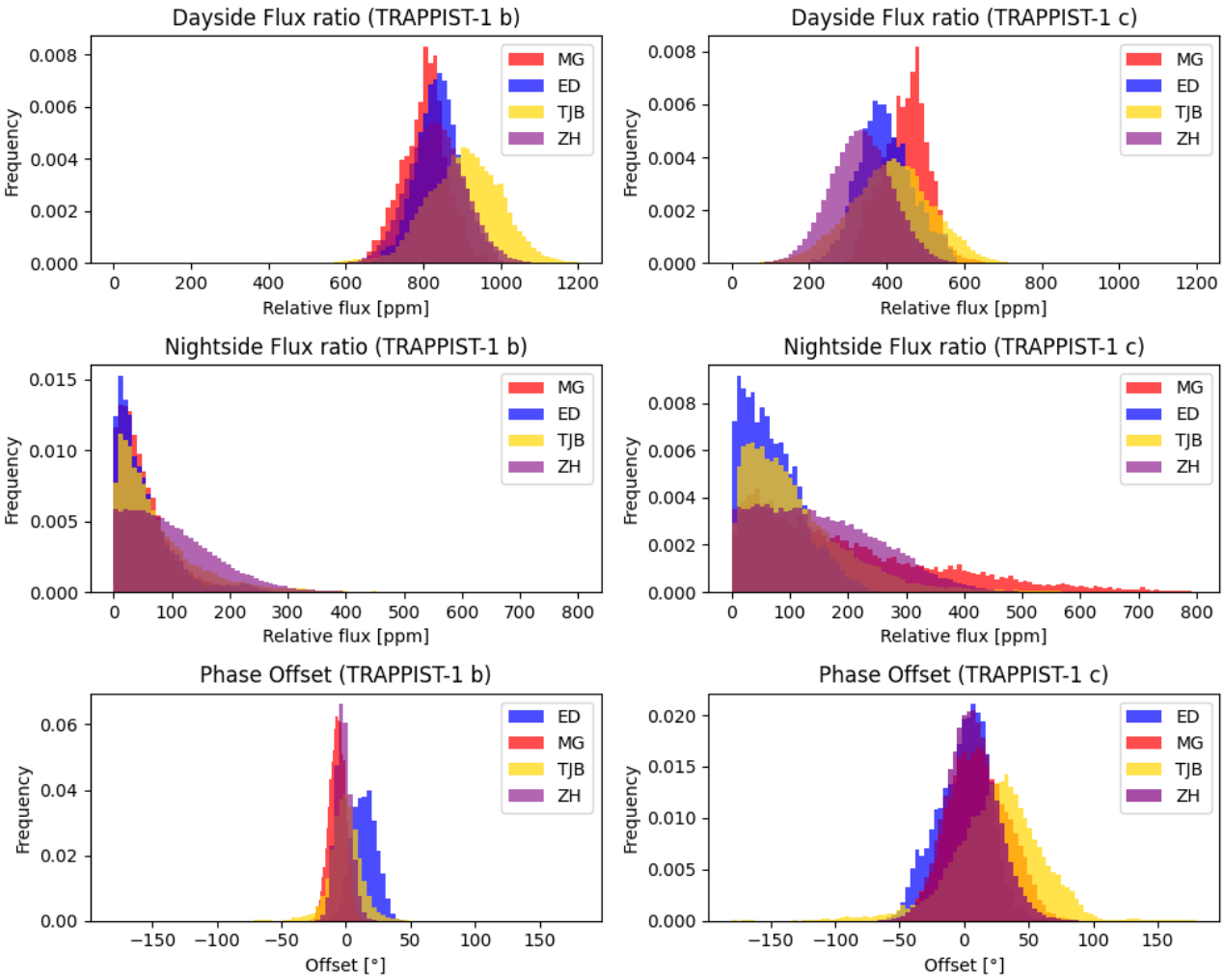

Figure 2.10: Posterior distribution functions from all analyzes of the phase curve of TRAPPIST-1 b and c in Gillon et al. (2025). These three parameters were used for comparison to the models. See Note 2.1 for an explanation of posterior distributions.

3. TRAPPIST-1 b

Contents

3.1 Introduction . . . 31
3.2 Methods . . . 33
3.2.1 3-D simulations with the Generic PCM . . . 33
3.2.1.1 Model parameters . . . 33
3.2.1.2 Model resolutions . . . 35
3.2.1.3 Radiative Transfer . . . 35
3.2.1.4 Convection and cloud formation . . . 35
3.2.1.5 Hazes and aerosols . . . 36
3.2.2 1-D radiative-convective simulations with `exo_k` . . . 36
3.2.3 Post-processing tools . . . 37
3.2.4 Comparison to data . . . 37
3.3 Results . . . 38
3.3.1 Residual, thin and thick, transparent atmospheres . . . 39
3.3.1.1 Principle . . . 39
3.3.1.2 A grid of N_2+CO_2 atmospheres . . . 40
3.3.1.3 Constraints from observations . . . 40
3.3.1.4 Eclipse depths . . . 40
3.3.1.5 Phase curve . . . 41
3.3.1.6 Constraints from atmospheric collapse . . . 41
3.3.1.7 Processes that can stop atmospheric collapse . . . 43
3.3.2 Thick, greenhouse-efficient atmosphere . . . 44
3.3.2.1 Principle . . . 44
3.3.2.2 Which gases have the right spectroscopic properties? . . . 44
3.3.2.3 Constraints from the secondary eclipse . . . 45
3.3.2.4 Constraints from the phase curve . . . 45
3.3.3 Atmospheres with a strong thermal inversion . . . 45
3.3.3.1 Principle . . . 45
3.3.3.2 Composition . . . 45
3.3.3.3 Constraints from the secondary eclipse . . . 48
3.3.3.4 Constraints from the phase curve . . . 48
3.4 Discussions . . . 51
3.4.1 Limitations in the model . . . 51
3.4.2 Limitations in the data analysis approach . . . 51
3.4.3 Comparison with previous studies . . . 52
3.4.4 Perspectives for the study of TRAPPIST-1 b . . . 52
3.5 Conclusion . . . 53
3.6 Appendix . . . 54

Preamble

I started my PhD in September 2022, soon after the successful launch of the JWST, and its promises to unveil temperate rocky exoplanets atmospheres. With its many observational and scientific opportunities, TRAPPIST-1 was observed a lot with the first occasions (GTO, and GO cycle 1). Unfortunately, all transmission observations were inconclusive due to the TLS effect (Lim et al. (2023), see section 1.2.2). However, TRAPPIST-1 b and c were also observed in emission. TRAPPIST-1 b, the warmest, had the advantage to be observed at two photometric filters. It was the TRAPPIST-1 planet for which the most observations were available, and by far the most observed rocky planet, and therefore a choice target to perform detailed modeling, informed by the observations. Moreover, an exceptional program of a full phase curve of TRAPPIST-1 was accepted for cycle 2, allowing me to be part of a large collaboration focused on the analysis and interpretation of this observation.

This chapter is the exact reproduction of a paper accepted for Astronomy and Astrophysics: Alice Maurel, Martin Turbet, Elsa Ducrot, Jérémy Leconte, Guillaume Chaverot, Gwenael Milcareck, Alexandre Revol, Benjamin Charnay, Thomas J. Fauchez, Michaël Gillon, Alexandre Mechineau, Emeline Bolmont, Ehouarn Millour, Franck Selsis, Jean-Philippe Beaulieu and Pierre Drossart, ***Constraints on the possible atmospheres on TRAPPIST-1 b: Insights from 3-D climate modeling****, accepted in A&A (06/09/2025).*
Since this paper is the companion to Gillon et al. (2025), the corresponding observational paper, which was accepted in Nature Astronomy, its publication was delayed to allow for a joint release of both articles. The manuscript of Gillon et al. (2025) is available in Appendix.

Abstract

Context. JWST observations of the secondary eclipse of TRAPPIST-1 b at 12.8 and 15 μm revealed a very bright dayside. These measurements are consistent with an absence of atmosphere. Previous 1-D atmospheric modeling also excludes – at first sight – CO_2-rich atmospheres. However, only a subset of the possible types of atmosphere has been explored and thus ruled out so far. Recently, a full thermal phase curve of the planet at 15 μm with JWST has also been observed, allowing for more information on the thermal structure of the planet.
Aims. We first seek atmospheres capable of producing a dayside emission compatible with secondary eclipse observations. We then aim to determine those, among them, compatible with the observed thermal phase curve.
Methods. We use a 1-D radiative-convective model and a 3-D global climate model (GCM) to simulate a wide range of atmospheric compositions and surface pressures. We then produce observables from these simulations and compare them to available emission observations.
Results. We find several families of atmospheres compatible at 2σ with the eclipse observations. Among them, some feature a flat phase curve and can be ruled out with the observation, and some produce a phase curve still compatible with the data (i.e., thin, N_2-CO_2 atmospheres, and CO_2 atmospheres rich in hazes). We also highlight different 3-D effects that could not be predicted from 1-D studies (redistribution efficiency, atmospheric collapse).
Conclusions. The available observations of TRAPPIST-1 b are consistent with an airless planet. This, and a thin CO_2-poor residual atmosphere are the most likely scenarios. However, our study shows that different atmospheric scenarios can result in a high eclipse depth at 15 μm. It may therefore be hazardous, in general, to conclude on the presence of an atmosphere from a single photometric point.

3.1 Introduction

Among the thousands of exoplanets discovered so far, only a few tens of them are temperate, with a size and/or a mass compatible with a rocky composition. Indeed, their small size makes them difficult to detect and even more difficult to characterize. Hu et al. (2024) report the potential detection of a secondary atmosphere on the hot planet 55 Cancri e; and a sulfur-rich atmosphere may have been detected

on L 98-59 d (Banerjee et al. 2024; Gressier et al. 2024), however, to date, no definitive detection of a secondary atmosphere has been made on a temperate, Earth-sized, rocky exoplanet. The James Webb Space Telescope (JWST) has the adequate sensitivity to probe the atmospheres of a few specific temperate rocky planets, mostly through transit spectroscopy and occultations (i.e. secondary eclipses). Those specific targets are exoplanets orbiting the coolest and smallest close-by stars, called red dwarf stars. Red dwarf stars are favorable targets (Triaud 2021; Nutzman & Charbonneau 2008; Sullivan et al. 2015; Barclay et al. 2018), because: (1) their small size makes it easier to detect and characterize small transiting planets, (2) their lower luminosities result in more frequent planetary transits and occultations for the same stellar irradiation, (3) they are the most common object in the Galaxy, and (4) temperate planets around them are more likely to be short-period rocky planets, allowing to accumulate many transits and occultations or to perform phase curve observations.

With its seven transiting temperate rocky planets around the coolest host star known to date, the TRAPPIST-1 system is the most studied system of this kind (Turbet et al. 2020a). Thanks to very precise measurements of radii (Ducrot et al. 2020) and masses (Agol et al. 2021), TRAPPIST-1 planets are so far the most well-known rocky planets outside our solar system. Since its discovery in 2016-2017 (Gillon et al. 2016, 2017), numerous studies assessed the possibility of atmospheres on these planets (Turbet et al. 2020a), and their detectability with the JWST (Lustig-Yaeger et al. 2019; Fauchez et al. 2019). The host star, with its high flux in the XUV and its long and hot pre-main sequence phase, is expected to result in significant atmospheric escape (Bolmont et al. 2017b; Bourrier et al. 2017). However, depending on the formation and evolution pathways of the planets, they could have retained a part of their primary atmosphere, or formed a secondary atmosphere (see Moore & Cowan (2020); Kite & Barnett (2020) for evolution of rocky planets and potential secondary atmospheres, Coleman et al. (2019); Turbet et al. (2020a) for the particular case of TRAPPIST-1).

Considering their transiting nature, combined with the infrared brightness (K = 10.3) and the Jupiter-like size of their host star ($\sim$ 12% the radius of Sun) they have been designated as the most promising candidates for the first detailed study of rocky, Earth-sized exoplanets with JWST (Gillon et al. 2020). Since the launch of the James Webb Space Telescope, all the TRAPPIST-1 planets have been observed in transit (JWST programs GTO 1201, GTO 1331, GO 1981, GO 2420, GO 2589, GO 6456). Unfortunately, the activity of the star can mimic the signatures from the planet's atmosphere in transit (Lim et al. 2023). Indeed, the host star's surface presents inhomogeneities that can cause artificial spectral features in the transit, due to unocculted spots on the star rather than an atmosphere on the planet (Rackham et al. 2018). A way out of the problem is to observe the planets in emission rather than in transmission spectroscopy. Indeed, in this case the surface inhomogeneities of the star have a much weaker impact, although not inexistent (Fauchez et al. 2025). The planets in the TRAPPIST-1 system which are hot enough to be observed with this method by the JWST are TRAPPIST-1 b and c. The two planets emissions have been observed through their secondary eclipses in the 15 μm MIRI filter for both planets (JWST programs GTO 1177, and GO 2304), and in the 12.8 μm filter for b (GTO 1279), upcoming for c (GO 5191).

The 15 μm eclipse observations of TRAPPIST-1 b have already ruled out –at first sight– a thick, CO_2 atmosphere (Greene et al. 2023), but they still left space for thinner atmospheres with different compositions (Ih et al. 2023). Taking into account the second photometric point, at 12.8 μm, (Ducrot et al. 2024) pointed out that secondary eclipses can also theoretically be compatible with a CO_2-dominated atmosphere rich in hazes. A way to break this degeneracy inherent to dayside emission is to observe phase curves in order to get the nightside thermal emission of the planet (Hammond et al. 2025).

Thereby, more recently, a phase curve of the system has been observed and carefully selected to be centered on the eclipses of TRAPPIST-1b and c (GO 3077). In this work, we present 1-D radiative-convective and 3-D numerical climate simulations of various types of atmosphere of TRAPPIST-1 b and compare them to all the available thermal emission observations (eclipses and phase curve). Although this work is an in-depth study of a single planet (the only moderately irradiated rocky planet for which we have such a large amount of observations), its approach and results are meant to be broadly applicable to other temperate, rocky exoplanets for which we have emission observations. This includes TRAPPIST-1c, but also LHS-1140 c, LHS-1478 b, GJ-3473 b, GJ-357 b, HD-260655 b, L-98-59 c, LTT-3780 b, TOI 1468 b and TOI-270 b (the nine planets of the Hot Rocks Survey, GO 3730), LP 791-18 d (GO 6457), Gl 486 b (GO 1743). Moreover,a

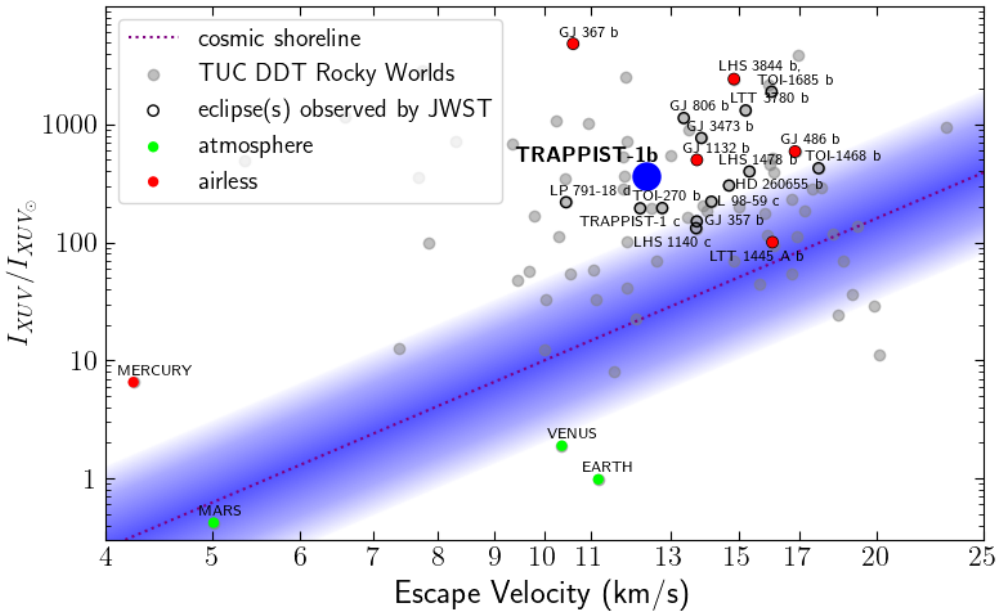

Figure 3.1: Exoplanets under consideration for the Rocky Worlds DDT. Planets above the cosmic shoreline are expected to have lost their atmosphere. The circled exoplanets have already been observed in emission during JWST's first 3 cycles. In red, the exoplanets for which the observations concluded there is no atmosphere. We also added the solar system terrestrial planets. The XUV irradiation is computed from Zahnle & Catling (2017).

500-hour Director's Discretionary Time program on JWST (Rocky Worlds DDT) will provide more mid-infrared observations of secondary eclipses of small, rocky exoplanets, in order to probe their ability to maintain an atmosphere(Fig. 3.1).

3.2 Methods

Starting from the secondary eclipse observations at 15 and 12.8 μm Greene et al. (2023); Ducrot et al. (2024), we attempted to identify all the possible families of atmosphere of TRAPPIST-1 b that could account for the high dayside emission flux measured in secondary eclipses. For this, we used a suite of numerical climate models, ranging from (1) 1-D radiative-convective simulations designed for a fast exploration of the parameter space to (2) 3-D global climate calculations to more reliably simulate the thermal structure and temperature contrasts across the planet, which play a major role in the planet's emission signal. These simulations are then post-processed with radiative transfer tools to generate synthetic eclipse spectra and thermal phase curves, for comparison to the observations.

In practice, we first carried out dozens of numerical climate simulations with the 1-D model `exo_k` (see section 3.2.2) for a wide range of atmospheric compositions, and computed secondary eclipse spectra (see section 3.2.3) for a large range of plausible atmospheric redistribution factors. For atmospheric compositions that yield good match with eclipse data, we used a 3-D climate model to produce much more realistic simulations (see section 3.2.1) with self-consistent heat redistribution, verified or not the good match with the eclipse data, and calculated thermal phase curves in the 15 μm MIRI filter. The list of all the 3-D simulations used in this work is given in Table 3.1.

The models and tools used in our study are detailed in the subsections below.

3.2.1 3-D simulations with the Generic PCM

For the 3-D atmospheric simulations of TRAPPIST-1 b, we used the `Generic Planetary Climate Model` (`Generic PCM`), a 3-dimensional numerical climate model which has now been extensively applied to a

Table 3.1: Summary of all the GCM simulations performed in this work. Surface pressure with * correspond to collapsing atmospheres. ** correspond to simulations with a circulation of the substellar point. We added the computed reduced χ^2 of the simulated atmospheres (see Section 3.2.4) and corresponding standard deviation in parentheses, computed as in Gillon et al. (2025).

Composition	Surface Pressure (bar)	χ^2 eclipse	χ^2 phase curve	χ^2 joint
Pure CO_2	1	23(6.5σ)	43(11σ)	35(12σ)
Pure CO_2	0.1*	17(5.6σ)	38(10σ)	30(11σ)
Pure CO_2	0.1**	17(5.6σ)	38(10σ)	30(11σ)
Pure CO_2	0.1**	17(5.6σ)	38(10σ)	30(11σ)
Pure CO_2	0.01*	10(4.1σ)	25(8.2σ)	19(9σ)
N_2 + 1% CO_2	1	25(6.7σ)	50(12σ)	40(13σ)
N_2 + 1% CO_2	0.1	15(5.2σ)	37(10σ)	29(11σ)
N_2 + 1% CO_2	0.01	3.7(2.2σ)	5.5(3.3σ)	4.8(3.7σ)
N_2 + 100 ppm CO_2	1	14(4.8σ)	37(10σ)	27(11σ)
N_2 + 100 ppm CO_2	0.1	3.3(2.1σ)	5.1(3.2σ)	4.4(3.5σ)
N_2 + 100 ppm CO_2	0.01*	3.6(2.2σ)	0.44(<1σ)	1.7(1.5σ)
N_2 + 1 ppm CO_2	1	2.4(1.7σ)	4.5(2.9σ)	3.7(3σ)
N_2 + 1 ppm CO_2	0.1	3.7(2.3σ)	0.17(<1σ)	1.6(1.4σ)
N_2 + 1 ppm CO_2	0.01	4(2.3σ)	0.62(<1σ)	2(1.7σ)
N_2+0.1ppm CO_2	1	2.8(1.9σ)	0.72(<1σ)	1.6(1.4σ)
N_2+0.01ppm CO_2	10	2.2(1.6σ)	17(6.5σ)	11(6.3σ)
N_2+20%CH_4+0.2%C_2H_4	10	1.8(1.4σ)	34(9.7σ)	21(9.5σ)
N_2+40%CH_4+0.4%CO_2	1	1.2(1σ)	20(7.2σ)	12(6.9σ)
CO_2+Hazes (Model 1)	1	0.35(<1σ)	0.44(<1σ)	0.4(<1σ)
CO_2+Hazes (Model 2)	1	1.8(1.4σ)	4.7(3σ)	3.5(2.9σ)
CO_2+Dust	1	1.7(1.3σ)	1.1(<1σ)	1.3(1.2σ)
CO_2+Tholins	1	15(5.1σ)	29(8.8σ)	23(10σ)
Airless, a=0.2	–	1.7(1.3σ)	1.5(1.3σ)	1.6(1.4σ)

Table 3.2: Summary of the parameters used for GCM simulations of TRAPPIST-1 b performed in this study.

Physical parameters	Values
Mass ($M_\oplus$)	1.374
Radius ($M_\oplus$)	1.116
Insolation ($S_\oplus$)	4.153
Rotation mode	synchronous/substellar circulation
Rotation rate (rad s^{-1})	4.8128×10^{-5}
Obliquity (°)	0
Orbital eccentricity	0
Bare ground albedo	0.1
Ground thermal inertia (J m^{-2} $s^{-1/2}$ K^{-1})	250
Surface Topography	flat
Surface roughness coefficient (m)	0.01
Internal Heat Flux (W m^{-2})	0
Stellar effective temperature (K)	2566
Stellar spectrum	2600 K BT-Settl with Fe/H = 0

large diversity of exoplanets Wordsworth et al. (2011); Charnay et al. (2015a); Bolmont et al. (2016); Turbet et al. (2018); Charnay et al. (2021); Turbet et al. (2023); Teinturier et al. (2024).

3.2.1.1 Model parameters

For the stellar, planetary and orbital parameters, we used the results of Agol et al. (2021). We assumed (unless otherwise stated) a circular, 0° obliquity, tidally-locked orbit. Table 3.2 summarizes all the parameters used to set up our simulations. Sensitivity tests for some of these parameters are detailed in section 3.3.

3.2.1.2 Model resolutions

For all our simulations, we used a standard horizontal resolution of 72 × 46 in longitude × latitude. For the vertical resolution, our standard simulations use 40 pressure layers, but for some simulations we had to change the number and distribution of pressure layers (suppressing layers for the simulation with atmospheric collapse ; adding and refining the upper layers grid for the simulation with a thermal inversion). Given that we simulated a broad range of atmospheric compositions in the `Generic PCM`, with various radiative and dynamical timescales involved, we adapted the time step (ranging from ∼0.5s to ∼60s) for all the simulations.

3.2.1.3 Radiative Transfer

Regarding the radiative transfer calculations, the model is based on the correlated-k approach Fu & Liou (1992). For the correlated-k tables, we use 31 spectral bands in the visible-near infrared (0.3 to 6.6 μm), corresponding to the stellar incoming radiation, and 40 in the thermal infrared (1 to 50 μm), corresponding to the planet emission wavelengths. This corresponds to a spectral resolution of R=10 for both regimes. We use 16 Gauss points for the cumulated distribution function (g) integration, 20 for the N_2-CO_2 atmospheres.

The correlated-k tables used are summarized in Table 3.3. The correlated-k tables of N_2+CH_4+C_2H_4 and N_2+CH_4+CO_2 has been calculated by combining single gas opacities from Exomol Hill et al. (2013); Mant et al. (2018); Hill et al. (2013); Chubb, Katy L. et al. (2021); Yurchenko et al. (2020) using `exo_k`. For N_2+CO_2 mixtures, original correlated-k tables have been calculated from line-by-line calculations of the high-resolution absorption spectra of CO_2 broaden by N_2 (Chaverot et al. in prep.). Absorptions have been computed following a Voigt profile with empirical corrections in the far wings (e.g., Tran et al. 2018) based on laboratory measurements Burch et al. (1969); Perrin & Hartmann (1989); Tran et al. (2011). For all atmospheric compositions, we also included the effect of Collision Induced Absorptions (CIAs) of

Table 3.3: Summary of the opacity cross-sections and continuum look-up tables used for the various molecules in the atmospheric simulations performed in this study.

Composition	References
k-correlated tables	
Pure CO_2	This work
N_2+CO_2	This work, excepting 0.1ppm of CO_2 from Exomol Chubb, Katy L. et al. (2021); Yurchenko et al. (2020)
N_2+CH_4+CO_2	Exomol Hill et al. (2013); Chubb, Katy L. et al. (2021); Yurchenko et al. (2020)
N_2+CH_4+C_2H_4	Exomol Hill et al. (2013); Mant et al. (2018)
CO_2+Hazes (simplified)	This work
CO_2+Hazes (Tholins)	This work + Khare et al. (1984); Drant et al. (2024)
CO_2+Dust	This work + Forget et al. (1999)
CO_2+H_2SO_4	This work + Lund Myhre et al. (2003)
CIA	
CO_2-CO_2	Gruszka & Borysow (1997); Tran et al. (2024)
N_2-N_2	Karman et al. (2019)
CH_4-CH_4	Karman et al. (2019)
CH_4-N_2	Karman et al. (2019)
CO_2-CH_4	Turbet et al. (2020c)

CO_2-CO_2 Gruszka & Borysow (1997); Tran et al. (2024) N_2-N_2 Karman et al. (2019), CH_4-CH_4 Karman et al. (2019), CO_2-CH_4 Turbet et al. (2020c) and CH_4-N_2 Karman et al. (2019).

3.2.1.4 Convection and cloud formation

The subgrid-scale dynamical processes (dry turbulent mixing and convection) are taken into account through a convective adjustment scheme which adjusts unstable temperature profile to the dry adiabat Forget et al. (1999).

For the study of the collapse of the CO_2 atmospheres, we activated the CO_2 condensation scheme Forget et al. (2013). This scheme is performed when a grid cell reaches 100% of saturation. CO_2 when condensing can form CO_2-ice clouds and/or surface frost. Cloud ice particles can sediment and accumulate at the surface, and the surface ice layer can itself re-sublimate in the atmosphere, depending on the thermodynamic conditions. The CO_2 ice albedo at the surface was set to 0.5 Forget et al. (2013), although this value has a limited impact given that CO_2 ice forms in the nightside, where there is no starlight to reflect. The CO_2 aerosols thus formed were radiatively active, and the number mixing ratio of cloud condensation nuclei fixed to 10^5 kg^{-1}, but tested the sensitivity by running simulations at 10^2 kg^{-1} and 10^8 kg^{-1}, and also by doing a test in which we turned off the radiative effect of CO_2 ice clouds.

3.2.1.5 Hazes and aerosols

For some simulations, we implemented and tested the effect of high-altitude aerosols. We first explored the effect of idealized hazes Ducrot et al. (2024). For this, we added a haze term to the correlated-k table of a pure CO_2 atmosphere, of the shape:

$$\sigma = f_{\text{haze}}\ \kappa\ (\lambda_0/\lambda)^2\ (M_{CO_2}/\mathcal{N}_a) \tag{3.1}$$

with $\kappa = 0.5\ cm^2/g$ and $\lambda_0 = 1\ \mu m$ Ducrot et al. (2024). The haze vertical mixing ratio profile was assumed to be constant. We varied different factors (haze mixing ratio profile, haze factor f_{haze}, see Equation 3.1) in 1-D (Appendix 3.6.3.1).

We also explored more realistic optical properties for different hazes and aerosols (Table 3.3). In this case the radiative transfer code computes the aerosols' contribution from their absorption coefficient,

single scattering albedo and asymmetry factor. These parameters depend on the radius distribution of the particles. For both `exo_k` and the `Generic PCM`, or all aerosols, we prescribe an upper and lower pressure layer, and the aerosols follow the atmospheric scale height between them. The parameters (upper and lower pressure layers, volume mixing ratio, and size distribution of aerosols) are detailed in the dedicated sections (section 3.3.3.2, Appendix 3.6.3.1).

3.2.2 1-D radiative-convective simulations with `exo_k`

We used the `exo_k` python library Leconte (2021) that includes a 1-D atmospheric evolution model (Selsis et al. 2023), in order to explore a wide range of possibilities in a limited amount of time. We performed $\sim$ 80 simulations in which we varied atmospheric composition (different proportions of N_2, CH_4, CO_2, C_2H_4, C_2H_6, NH_3, SO_2) and total atmospheric pressure (from 0.1 to 10 bar). We used the same stellar, planetary and orbital parameters as described above for the `Generic PCM` (Table 3.2). We also used the same correlated-k tables as in the `Generic PCM` (Table 3.3), also with a spectral resolution of 10, ranging between 0.3 and 50 μm). We only tested dry atmosphere cases.

We parameterized the 3-D redistribution for the incoming stellar flux with a multiplication factor f, that spans from 2/3 (no redistribution) to 1/4 (full redistribution):

$$ISR = f \times \sigma T_s^4 (R_s/a)^2$$

3.2.3 Post-processing tools

We computed the emission spectra of the modeled 1-D atmospheres with `exo_k`, and for the 3-D atmospheres we used `Pytmosph3R` Falco et al. (2022), a python library based on `exo_k` that computes observables (eclipse spectra, phase curves) directly from the `Generic PCM` 3-D outputs. When used in "emission" or "phase curve" mode, `Pytmosph3R` computes the emission for each column of the `Generic PCM` output, weighted by the angle of the observer. We used a stellar spectrum from the SPHINX model grid Iyer et al. (2023) interpolated to TRAPPIST-1's parameters. This spectrum, different from the one used in the GCM, was chosen for his closeness to the measured flux at 15 μm, allowing for a more accurate planet-to-star flux ratio - a criterion that is not sensitive in the GCM simulations, the stellar flux in the thermal infrared having a negligible effect on the GCM results.

We used correlated-k tables from the same opacity data (Table 3.3) at higher spectral resolution ($R \sim 100$) for the computation of the observables. To compare with the observations, we integrated the flux in the MIRI observed bands (F1280W and F1500W) with the available JWST MIRI filters documentation. We also computed the planet-to-star flux ratio by dividing the computed planet flux by the stellar flux. For this, we normalized the stellar spectrum with the 15 μm MIRI measurements of the stellar flux. At 12.8 μm, we find that the computed stellar flux is slightly lower than the measured flux (<2%).

3.2.4 Comparison to data

We compared our synthetic observables to the available JWST emission observations. First, to the eclipse depths of TRAPPIST-1 b at 15 μm Greene et al. (2023) and 12.8 μm Ducrot et al. (2024) (Fig. 3.3a); second, to the 15 μm thermal phase curve of b extracted from the observed combined phase curve of TRAPPIST-1 b and c Gillon et al. (2025). Gillon et al. (2025) performed four independent analyses, each one divided in several sub-analyses with different assumptions. We chose to compare our results to analysis #1-MG because the analysis of MG was highlighted in the paper and only the sub-analysis #1 allowed for an atmosphere on TRAPPIST-1 b. Note that contrary to Ducrot et al. (2024), our best-fit airless albedo is not 0.2, but $\sim$ 0.4 (see section 3.3.1.4). For the phase curve data, shown in Fig. 3.3b, we chose to compare three parameters extracted from the phase curve: the maximal flux, the minimal flux, and the peak offset to evaluate the match between our simulations and the observation. Indeed, the extracted phase curve of the planet b is quite dependent on the analysis pipeline – especially in this case where one must extract two signals (planet b and c) from one phase curve. Furthermore, any extracted phase curve is only one of the thousands of outputs of the MCMC analysis. On the other hand, the three variables extracted correspond to the posterior probability distribution functions of the analysis, and are thus much more robust. These

quantities are also physically interpretable (amplitude corresponds to heat redistribution, offset to shift of the hottest hemisphere). Note that due to the complexity of the GCM simulations, we cannot perform a bayesian retrieval like with a simpler, 1-D model. We simply tried to assess the match of our different simulations with the observations. For this, we computed the χ^2:

$$\chi^2 = \sum_i \frac{(O_i - M_i)^2}{\sigma_i^2} \tag{3.2}$$

with O_i the data points of the observations, σ_i their 1-σ uncertainty, and M_i the models results.

For the eclipse, the two data points correspond to the eclipse depths measured at 12.8 and 15 μm (Ducrot et al. (2024). For the phase curve, we extracted the dayside flux, nightside flux and peak offset from the analysis #1- MG of Gillon et al. (2025) and compared each of them.

Note that this χ^2 is a metric aiming at comparing the match of the different simulated atmospheres with the data, relatively to each other. Indeed, we cannot provide an absolute quantification of the mismatch that could be compared with other papers, because our approach is different from 1-D models, and we are not performing a proper fit, but rather evaluating a few realizations that we wanted to explore.

3.3 Results

We identified four distinct families of atmospheres that can produce a strong dayside emission matching the secondary eclipse MIRI observations Greene et al. (2023); Ducrot et al. (2024). These four families are summarized in the sketches of Fig. 3.2 and listed below:

- Thin, residual atmospheres: the thin atmosphere produces very little heat redistribution and greenhouse effect. In this case, the infrared brightness temperature is very close to the surface temperature, where most of the emission comes from. Here the planet behaves very closely to a bare rock planet.

- Non-condensible, thick, transparent atmospheres: the observer sees through the atmosphere directly the surface emission of the planet. In the absence of condensation and radiatively active species, the surface and the atmosphere only interact through sensible heat exchange, which is limited. Thus, the atmosphere can produce very efficient heat redistribution but does not interact sufficiently with the surface to deviate the surface temperature field from the bare-rock case. Such transparent atmospheres are difficult to probe remotely, except perhaps through Rayleigh scattering at visible wavelengths.

- Thick, greenhouse efficient atmospheres: the atmosphere is thick, and produces a very efficient greenhouse effect. The large scale dynamics of such thick atmospheres produces efficient horizontal mixing, resulting in very efficient heat redistribution. As a result, the day-to-night temperature contrast is very low. In such thick atmospheres, the temperature of the lower atmosphere can far exceed the brightness temperature measured by MIRI, due to the powerful greenhouse effect of the atmosphere. For such atmospheres to fit the eclipse data, the molecules present in the atmosphere must have absorption windows that let through the emission from the deeper, warmer layers of the atmosphere.

- Atmospheres with a strong thermal inversion: the atmosphere possesses species (for instance CH_4, or high-altitude hazes) that absorb efficiently at the wavelengths of the emission of the host star. A significant part of the stellar radiation is absorbed high in the atmosphere, producing strong shortwave heating, causing a thermal inversion. In this case, the CO_2 present in the atmosphere, with a strong absorption band at 15 μm, can now produce a strong signature in emission.

Fig. 3.3a shows the synthetic eclipse depths for four arbitrarily selected cases from the four families of atmospheric scenarios as a proof of concept. All of them can match the eclipse depth observations at the 2-σ confidence level.

The following subsections describe each of these atmospheric scenarios, show why they match the eclipse depth measurements, and how phase curves can be used to discriminate between them.

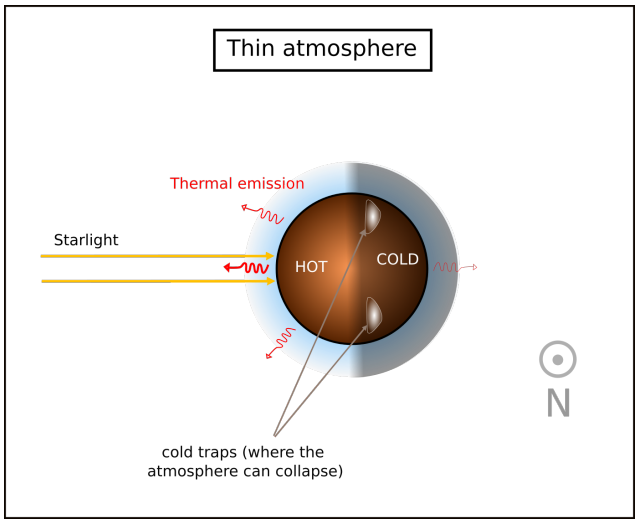

(a) Case 1a: Thin, residual atmospheres

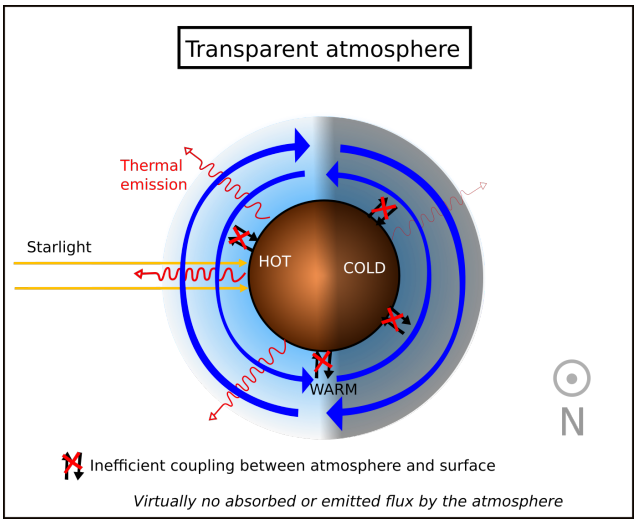

(b) Case 1b: Non-condensible, thick transparent atmos.

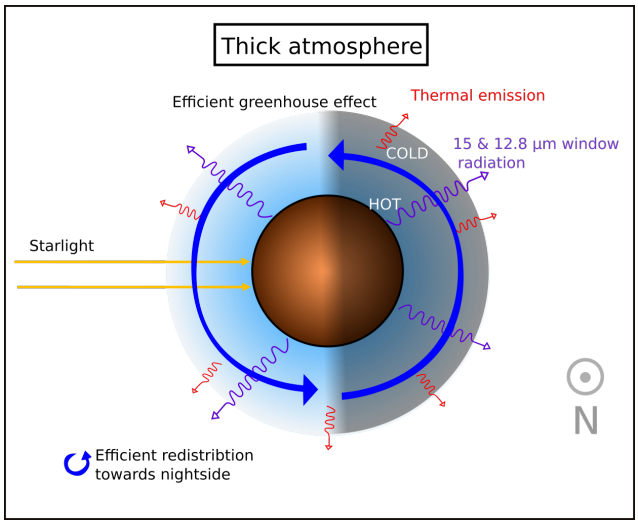

(c) Case 2: Thick, greenhouse efficient atmospheres

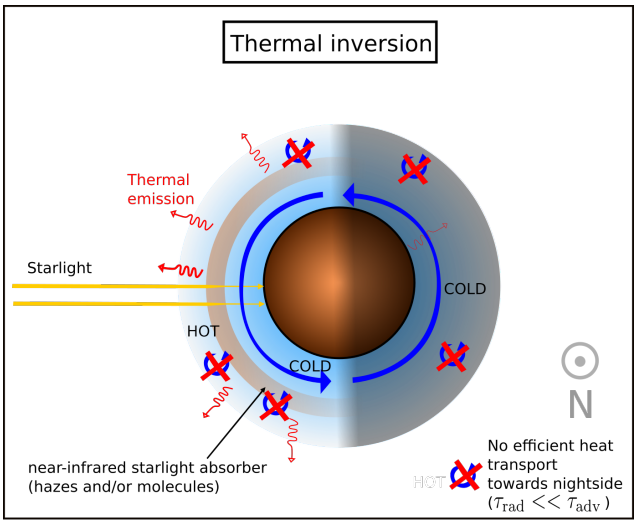

(d) Case 3: Atmospheres with a strong thermal inversion

Figure 3.2: Sketches of the different atmospheric scenarios studied in depth in this work, as seen from the North pole.

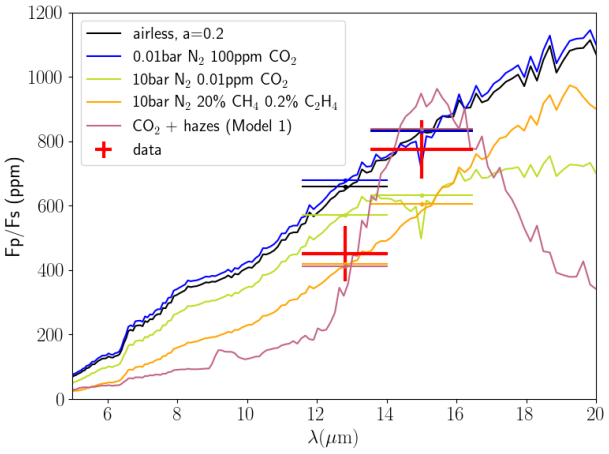

(a) Dayside emission versus wavelength for a bare rock, and for a representative of each family studied in the paper. The red data points and associated 1σ error bars are from Ducrot et al. (2024).

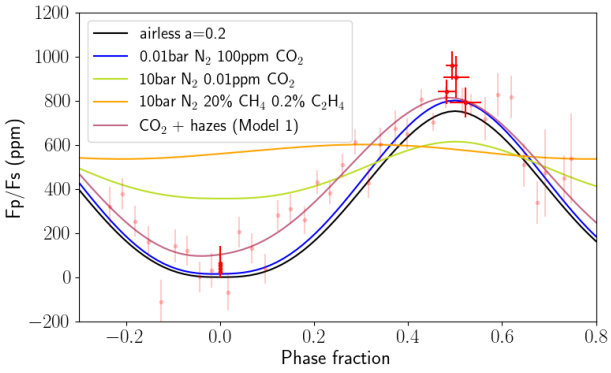

(b) Phase curves of the simulations from Fig. 3.3a and data from Gillon et al. (2025). The shallow points correspond to the binned results one of the MCMC outputs of analysis #1- MG of the paper. The non-transparent points to the maximum flux, minimum flux, and peak offset with 1-σ uncertainties resulting from different analyses of the paper.

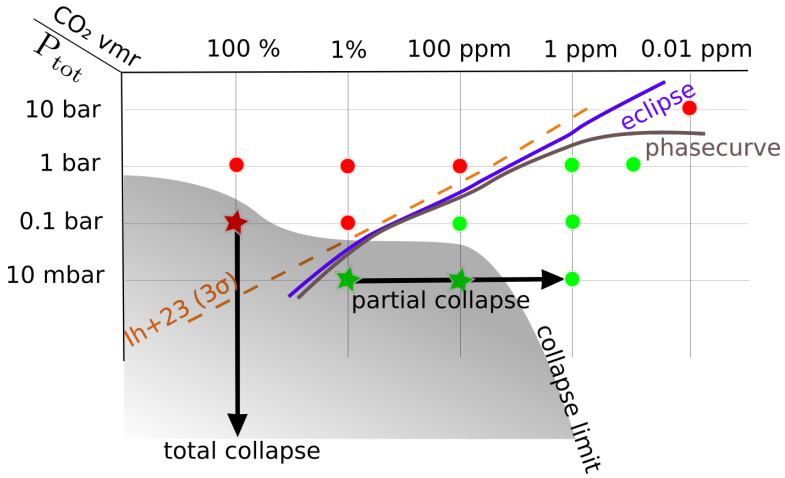

Figure 3.4: N_2-CO_2 grid of performed simulations. The points in red are not compatible with the observations, the green points match the data. The orange, purple and brown lines correspond respectively to the 3-σ limit of Ih et al. (2023), and limits from this work from eclipse and phase curve observation. The arrows indicate a collapse of the CO_2 present in the atmosphere. Dots correspond to stable atmosphere, stars to unstable ones. The grey area wraps the atmospheres unstable to collapse.

3.3.1 Residual, thin and thick, transparent atmospheres

3.3.1.1 Principle

The first two families of atmospheres that can match the measured eclipse depths are residual, thin atmospheres and thick, transparent atmospheres. To explore these scenarios quantitatively, we have decided to focus on CO_2-N_2-dominated atmospheres. We chose this composition for three distinct reasons: (1) first, they were initially proposed as good candidate molecules for a putative TRAPPIST-1 b's atmosphere Turbet et al. (2020a); Krissansen-Totton & Fortney (2022) ; (2) second, these are compositions that have been explored in detail in previous theoretical studies of TRAPPIST-1 b Ih et al. (2023); and (3) third, because CO_2 is the strongest absorber at 15 μm and a condensable species, which is the most conservative case for our reasoning and makes it a good representative of this category. The principle and mechanisms at stake that we describe here can be transposed to other compositions of residual and/or transparent atmospheres (see section 3.4).

To do this, we created a grid of 3-D GCM simulations of TRAPPIST-1 b for a wide range of CO_2 and N_2 partial pressures. Our results are described in the following subsections.

3.3.1.2 A grid of N_2+CO_2 atmospheres

We performed simulations varying total pressure (0.01 to 1 bar) and CO_2 volume mixing ratio (VMR) (1 ppm to 100%), using a grid inspired from Ih et al. (2023). For each 3-D simulation, we computed the eclipse depth spectrum, and the phase curve in the 15 μm (F1500W) MIRI filter. Compared to Ih et al. (2023), we added two extra points to specifically study the case of thick, "transparent" atmospheres with a low, constant CO_2 partial pressure of 10^{-7} bar, for a total pressure of 1 and 10 bar A specific study of these cases is presented in Appendix 3.6.1.1. Fig. 3.4 shows the grid of N_2+CO_2 atmosphere simulations we explored, and summarizes the various observational and theoretical constraints discussed in the following subsections.

3.3.1.3 Constraints from observations

Fig. 3.5 shows the observables resulting from the simulations of the grid. In order to compare them to the observations, we computed the reduced χ^2, provided in Table 3.1.

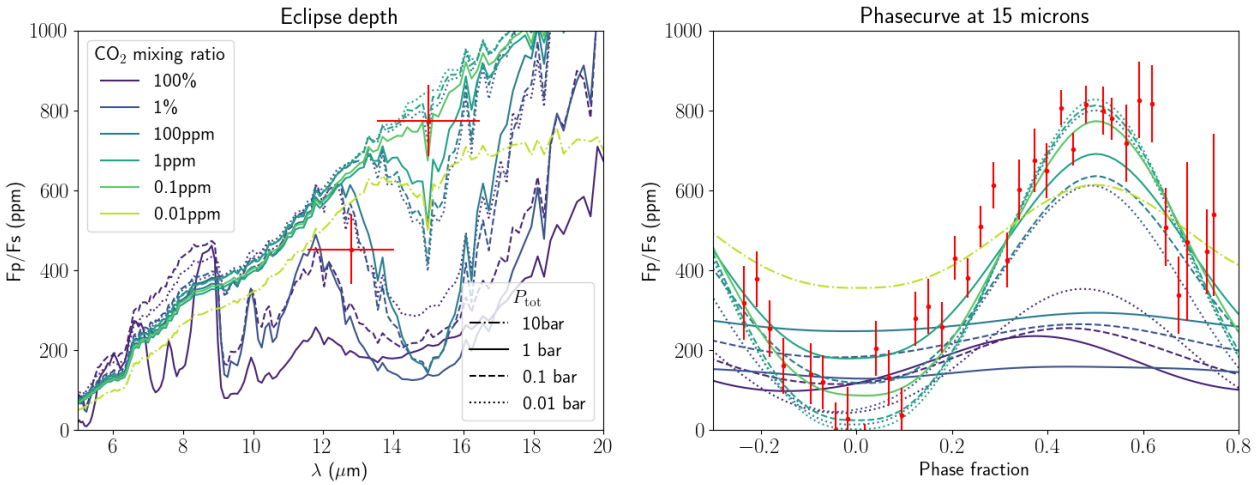

Figure 3.5: Synthetic eclipse spectra (left panel) and phase curves (right panel) for all the CO_2-N_2 atmospheres.

3.3.1.4 Eclipse depths

For the eclipse depths, the χ^2 is high for all the high-P_{CO_2}, and drops for the atmospheres that correspond to the 3-σ limit of Ih et al. (2023) (Fig. 3.4). It corresponds to all the cases that match the 15 μm data point within the 1-σ error bar in Fig. 3.5. We found that the eclipse depth is mostly dependent on the CO_2 partial pressure, and could not distinguish the different thicker "transparent" atmospheres with constant CO_2 partial pressure but variable total pressure.

In this study, the emission for an airless planet of albedo 0.2 is higher than in Ducrot et al. (2024). In their work, the albedo is assumed to be wavelength-independent, with the emissivity defined as ($\epsilon_\lambda = 1-A$). As a result, the surface temperature, governed by the equation $(1-A)ISR = \epsilon\sigma T^4$ (where ISR represents the incoming stellar radiation) becomes independent of the albedo, and the emission is directly proportional to the emissivity, (1-A). In contrast, with `exo_k`, we impose an albedo cutoff at $\lambda \geq 5\mu$m, which results in an emissivity $\epsilon_\lambda = 1-A_\lambda$ equal to 1 in thermal wavelengths. $\lambda = 5\mu$m was chosen to separate the zone of stellar emission and the zone of thermal planetary emission (Fig. 3.8). This leads to a surface temperature that depends on the albedo. Although the bolometric planet emission remains proportional to (1-A), thus maintaining the radiative balance, the emission at 15 μm is not. Finally, for the 3-D simulations, the albedo is assumed to be wavelength-independent, but the emissivity is set to 1, which gives similar results to `exo_k`, as the albedo at longer wavelengths does not significantly influence the radiative balance, due to the low stellar emission at these wavelengths, and conversely, the emissivity is important only in the thermal wavelengths.

In consequence the surface albedo of 0.1, corresponding to the assumption made in simulations presented in Ducrot et al. (2024), results in a high eclipse depth for the thinnest atmospheres. The complexity and time-consumption of the GCM simulations does not allow us to explore widely the effect of the surface albedo, but we tested it in 1-D for the different cases. (see Appendix 3.6.1.3). We found that a higher albedo lowers the continuum part (where we probe the surface), but not the CO_2 band when it is strong, because in this case we probe the emission directly from the atmosphere.

We thus consider that the match with the data would be better with a higher albedo, but it would not change our overall conclusions.

3.3.1.5 Phase curve

From the phase curve in the 15 μm band, as expected, the atmospheres that present a strong CO_2 feature in eclipse give a very low dayside flux. As we are probing in the atmosphere because of the CO_2 absorption, the redistribution is visible in these atmospheres through the non-zero nightside flux, and even a strong offset for the 1 bar 100% CO_2 case. These atmospheres are thus ruled out again, as expected.

The thinner atmospheres, with a higher dayside flux, low nightside flux and zero peak offset, can be considered an acceptable match, corresponding to the analysis in eclipse.

The only case where the phase curve brings a new constraint is for the thicker, more transparent atmosphere (see Appendix 3.6.1.1). In this case, even with a very low quantity of CO_2, the weak continuum absorption (CIA and continua) is enough for the atmosphere to absorb and re-emit in the nightside . The probed atmosphere is well enough mixed that the nightside flux is high, and thus, not compatible with the observations.

3.3.1.6 Constraints from atmospheric collapse

TRAPPIST-1 b is so close to its host star that it is very likely to be tidally-locked Turbet et al. (2020a). Therefore, in the absence of atmosphere, its dayside is expected to be very hot and its nightside very cold. An atmosphere can redistribute the heat from the dayside to the nightside, with an efficiency that depends on its thickness, composition and, in general, on the parameters that can impact large-scale dynamics Wordsworth et al. (2015); Koll (2022).

When reaching its condensation temperature, the gaseous CO_2 is expected to condense and form clouds, and/or frost on the ground. Therefore, if the nightside is cold enough, it will constitute a cold trap, collapsing the CO_2 of the atmosphere onto the surface Wordsworth et al. (2015); Turbet et al. (2018).

The `Generic PCM` simulations we performed include CO_2 condensation, allowing us to test this prediction. We thus used the model to explore for which cases (pressure, CO_2 mixing ratio) the collapse happens, and if the collapse is total, or if a secondary equilibrium is achieved Soto et al. (2015).

Details on a pure CO_2 simulation collapse We find that for a pure CO_2 case, the atmosphere collapses as soon as the initial pressure is 0.1 bar or below. This result is not impacted by the number mixing ratio of cloud condensation nuclei and radiative effect of CO_2 ice clouds. For this end member case, we performed the simulation of the collapse down to a few pascals (Fig. 3.6, solid black line), demonstrating that there is no secondary equilibrium possible. We computed the observables at different steps of the collapse, that are displayed in Appendix 3.6.1.2.

Simulations showed that the ice is mainly produced as a result of frost formation and not precipitation. Note that it implies that the collapse strongly depends on the temperature of the surface at the cold traps, which has been shown to be strongly dependent on the strength of turbulence on the nightside Auclair-Desrotour et al. (2022); Joshi et al. (2020).

Due to global dynamics, the cold traps are located close to the terminator, at mid-latitudes. As the atmosphere collapses, the greenhouse effect and redistribution become less efficient, the surface temperature drops, and the cold traps become more and more pronounced.

We tested the impact of the radiative effect of CO_2 ice aerosols parametrization: changing the ratio of the cloud condensation nuclei and turning off the radiative effect of the aerosols did not change our results.

Collapse for a N_2-CO_2 atmosphere For the N_2 atmospheres with 1% to 1 ppm of CO_2, partial pressure of CO_2 is lower so its condensation temperature decreases, and the N_2 participates in the redistribution of heat. Thus, the collapse is prevented for 0.1 bar atmospheres. For thinner atmosphere, when these processes are not sufficient to avoid collapse, CO_2 condenses, but not N_2. We called it a partial collapse (Fig. 3.4). In this case, the total pressure does not drop, but the CO_2 gas content drops. These atmospheres are thus collapsing towards an atmosphere with fewer CO_2 (for 0.1 bar total pressure, 1ppm is stable) eventually producing a transparent-type atmosphere, in better agreement with the JWST MIRI observations. Therefore, the case of a thin, N_2 atmosphere with a small amount of CO_2, which matches available data, can be considered as a resulting atmosphere of the CO_2-richer atmospheres, and not as implausible as it would look at first sight.

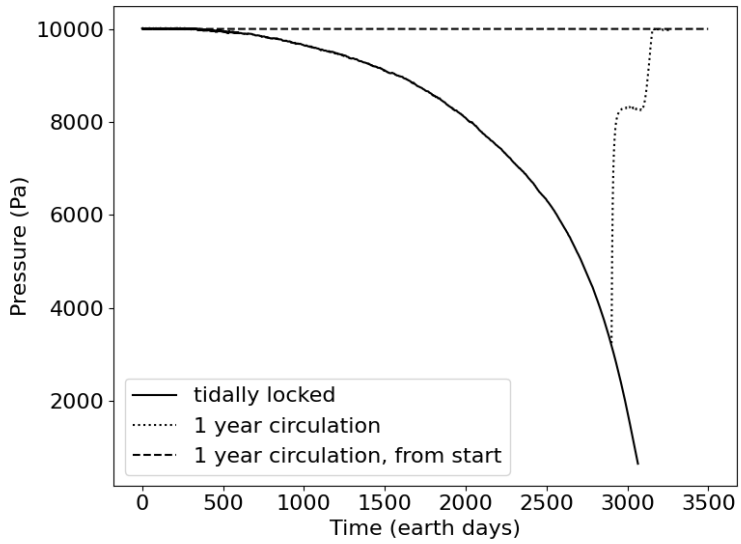

Figure 3.6: Total pressure of a pure CO_2 atmosphere against time, for the threshold case of a 0.1 bar atmosphere. In a tidally locked case, the atmospheres collapses totally in $\sim$ 10 earth years. If we set a circulation of the substellar point to 1 earth year, the 0.1 bar atmosphere becomes stable, and a partially collapsed atmosphere vaporizes all the CO_2 back to the atmosphere.

3.3.1.7 Processes that can stop atmospheric collapse

Non purely synchronous orbit Like a lot of exoplanets, TRAPPIST-1 b is close enough to its star to be expected to be in synchronous rotation due to tidal interaction with the star. But the TRAPPIST-1 system is so compact that planets gravitationally interact also with each other and this could result in a movement of the substellar point: libration, and a slow circulation of the substellar point. The circulation, if not too slow, can prevent collapse of the atmosphere by re-sublimating the ice caps when exposed to starlight. A 3:2 spin-orbit resonance could also prevent the collapse, but for TRAPPIST-1 b the tidal effects make it improbable Turbet et al. (2020a); Revol et al. (2024). We tested this hypothesis by simulating a 0.1 bar atmosphere of pure CO_2 (collapsing in the tidally locked case), with a substellar point circulation (i.e. synodic day) of 1 Earth year. A longer duration would have been interesting to investigate but too computationally expensive and time-consuming. First, we started like the tidally locked case, with a warm (500 K), isothermal, dry atmosphere, and in another case, we started from a partially collapsed atmosphere. In both tests, the reached equilibrium state was a dry, non-collapsed atmosphere. The timescale for the collapse of a 0.1 bar atmosphere of pure CO_2 being around 10 Earth years (Fig. 3.6), a circulation of the substellar point with a rotation period of 1 Earth year is enough to prevent collapse. We can expect that the characteristic time of the substellar drift must be not longer than the one of the collapse in order to prevent it. The complete rotation of the substellar point has already been suggested by several studies. Makarov et al. (2018) suggested possible spin-orbit resonances state in the spin evolution of the planets b, d, and e, before synchronization. Chaotic circulation of the substellar points has been explored by Vinson et al. (2019), Shakespeare & Steffen (2023), and Chen et al. (2023). They attribute the large librations rising from the chaotic motion in their simulations, coupled with a simplistic model of tides (e.g., Constant Time Lag model Hut (1981)). In addition, Revol et al. (2024) computed the synodic periods for each of the TRAPPIST-1 planets, finding a synodic day of about 70 Earth years for planet b.

In the end, for TRAPPIST-1 b, escaping atmospheric collapse thanks to the circulation of the substellar point is quite unlikely since simulations show that its circulation is not expected to be faster than one complete rotation of the substellar point per $\sim$ 70 Earth years Revol et al. (2024). However, the circulation of the substellar point is expected to be more important for the outer planets and should be taken into account for future GCM studies.

Table 3.4: Tidal heat flux constraints.

F_{int} ($W.m^{-2}$)	T_{eq} (K)	P_{cond} (bar)	h_{max} (m)	P_{base} (bar)
100	204	~ 1	–	–
10	115	$\sim$ 1.e-4	~ 1	~ 0.1
1	64	–	~ 10	~ 1
0.1	36	–	~ 100	~ 10

Tidal heat flux On TRAPPIST-1 b, the star-planet tidal interactions may induce an internal flux. The eccentricity from Agol et al. (2021) constrains this flux between 4×10^{-2} and 500 $W.m^{-2}$. An internal heat flux can impact CO_2 collapse in two ways: 1) if it is strong enough, it can prevent any condensation at the surface, and 2) it can limit the height of the ice caps because of the basal melting, thus limiting the amount of CO_2 that can be condensed at the surface.
First, we can compute the equilibrium temperature at the nightside induced by an internal heat flux:

$$\sigma T_{\mathrm{eq}}^4 = F_{\mathrm{int}}$$

If this temperature is superior to the condensation temperature of CO_2, CO_2 condensation can not occur, and thus no collapse. Thus, we can determine the minimum partial CO_2 pressure, corresponding to the pressure at which the condensation temperature is equal to the computed equilibrium temperature.
Second, the CO_2 ice cap can be limited by basal melting Turbet et al. (2017). The maximum volume of CO_2 ice is limited to an ice cap of the surface of the nightside and the maximum height fixed by basal melting. Thus, the maximum pressure of CO_2 that can condense corresponds to

$$P_{base} = \frac{1}{2} g \rho h_{max}$$

with g the gravity of the planet, and ρ the density of CO_2 ice.

We computed for different orders of magnitudes of the internal flux, the minimum pressure of CO_2 from 1), and the maximum condensed CO_2 from 2). Results are in Table 3.4.

From this table, we identified 3 regimes:
(a) For a flux of $\sim$ 100$W.m^{-2}$ and higher, the condensation pressure is higher than the boundary pressure at which the atmosphere starts collapsing $P_{collapse}$. Therefore, there is no collapse possible.
(b) For a flux of $\sim$ 1$W.m^{-2}$ and lower, the internal flux does not prevent condensation, and the maximum amount of CO_2 trapped correspond to a CO_2 pressure higher than $P_{collapse}$: thus, there is no constraint brought by the internal flux.
(c) For intermediate cases around 10$W.m^{-2}$, process (2) tells us that the amount of CO_2 condensed is limited to $\sim$ 0.1 bar, which is below $P_{collapse} \sim 0.3$ bar (for a pure CO_2 atmosphere). Thus, if there is an initial pressure between 0.1 bar and 0.3 bar, the atmosphere will not collapse completely, and there could be a remaining atmosphere, thinner than the initial limit $P_{collapse}$.

3.3.2 Thick, greenhouse-efficient atmosphere

3.3.2.1 Principle

This family of atmospheres represents high-redistribution, high-greenhouse effect cases. To produce an efficient greenhouse effect, the gases present in the atmosphere must have efficient absorption in the thermal infrared, where the planet emission is strong. This way, the atmosphere should prevent the thermal radiation to directly escape to space. In other words, it means that the atmosphere becomes optically thick very high in the atmosphere, producing a brightness temperature representative of the higher, likely colder atmospheric layers, and not of the hot surface and/or deep atmosphere. The more absorbent the atmosphere is, the higher atmospheric layers we will probe in secondary eclipses, and the colder the brightness temperature we will see.

In principle, this family of atmosphere should therefore be incompatible with the measured secondary eclipses at 12.8 and 15 μm. However, this family of atmosphere can theoretically generate a very high flux at the wavelengths measured by MIRI, if these wavelengths coincide with atmospheric absorption windows. This also requires that the atmosphere does not absorb too efficiently in the near infrared to let the stellar flux reach the deep atmosphere. Fig. 3.16 shows a proof-of-concept example where we set up an atmosphere for TRAPPIST-1 b with artificial opacities (high opacity set in the thermal infrared, but low opacities near 12.8 and 15 μm). This thought experiment, detailed in Appendix 3.6.2.1, is designed here simply to illustrate the mechanism at play.

3.3.2.2 Which gases have the right spectroscopic properties?

We looked for a composition that could produce such an effect. We do not focus on the plausibility of the composition, as there are still few constraints regarding planetary evolution. We allow ourselves the freedom to explore all compositions, with the sole criterion being compatibility with the data. Among a list of possible molecules (CH_4, CO, CO_2, C_2H_2, C_2H_4, C_2H_6, HCN, H_2O, H_2, H_2S, H_2O_2, NH_3, N_2, PH_3, SO_2) we selected the species that had a weaker absorption around 15 μm. C_2H_4 and C_2H_6, i.e. reduced gases and potential photochemistry products of CH_4, are the only molecules with such a feature (Fig. 3.17). Thus, to present this mechanism, an atmosphere must likely be reduced, and contain at least one of these gases. Other gases, transparent or with limited greenhouse effect, can be present in addition.

After an exploration in 1-D with `exo_k` with these two gases and N_2 and CH_4, we identified a composition that maximized the dayside emission: N_2 as the background gas, CH_4 (20%) and C_2H_4 (0.2%). This composition has been chosen for the 3-D `Generic PCM` simulations. We tried this composition with a total pressure of 10 bar.

Note that a larger quantity of CH_4 would make the atmosphere absorb too much in the near infrared, where TRAPPIST-1 emits a significant fraction of its flux, and act as an anti-greenhouse effect, preventing the stellar flux to go deep in the atmosphere (see section 3.3.3).

3.3.2.3 Constraints from the secondary eclipse

We show in Fig. 3.7 the results and observables of the simulation of N_2-CH_4-C_2H_4, with $P_{tot} = 10$ bar. Due to the strong greenhouse effect, the surface of the planet is quite hot: more than 600 K (compared to the equilibrium temperature of ~400 K). The thermal profiles of the dayside and nightside are superimposed in the deep atmosphere, because of the highly efficient redistribution. In the upper layers, the redistribution is less efficient, and the thermal profiles of dayside and nightside diverge. The layers from which the main part of the 15 μm band pass emission comes from (shown in shadowed area) are between 1 bar and 0.01 bar, because even with the opacity "window", the atmosphere becomes optically thick due to the opacity scaling with atmospheric pressure, and one cannot probe all the way down to the surface.

Thus, the eclipse depth is around 600 ppm for 15 μm, corresponding to a brightness temperature of only ~425 K, and 450ppm / ~415 K for 12.8 μm.

3.3.2.4 Constraints from the phase curve

Still in Fig. 3.7, the wind and temperature map at the emission layers shows strong eastwards winds, moving heat towards the nightside of the planet. These winds have also the effect of moving the hottest point eastwards the substellar point.

The modelled phase curve reproduces these features: it is globally flat, because of heat redistribution, and the maximum of the phase curve is shifted slightly ahead of the time of the eclipse, because of the shift of the hottest point.

In conclusion, such an atmosphere is compatible with the eclipse depth measurements, but is ruled out by the phase curve.

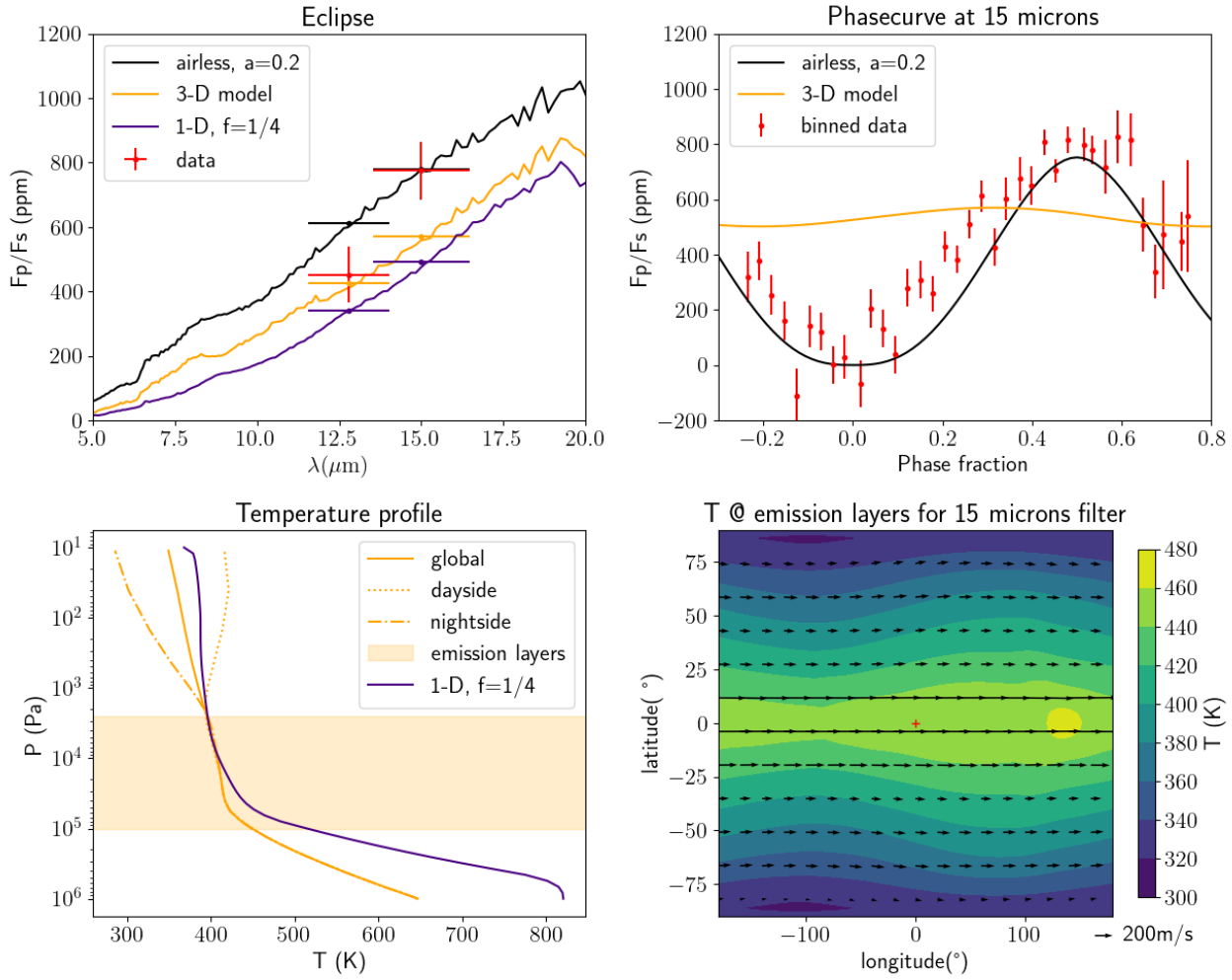

Figure 3.7: Thick atmosphere case (10 bar, N_2 atmosphere with 20% of CH_4 and 0.2% of C_2H_4). Upper panels: the synthetic observables and observed data - eclipse depth versus wavelength (left) and phase curve (right). Lower panels: the temperature profile (left) and map (right). The temperature map corresponds to a sum of the atmospheric layers, weighted by their contribution to the emission at 15 μm. We added the similarly weighted wind vectors as black arrows. The shadowed area in the right panel corresponds to the layers contributing to 95% of the emission. The difference between the 1-D and 3-D temperature profiles is discussed in Appendix 3.6.2.3.

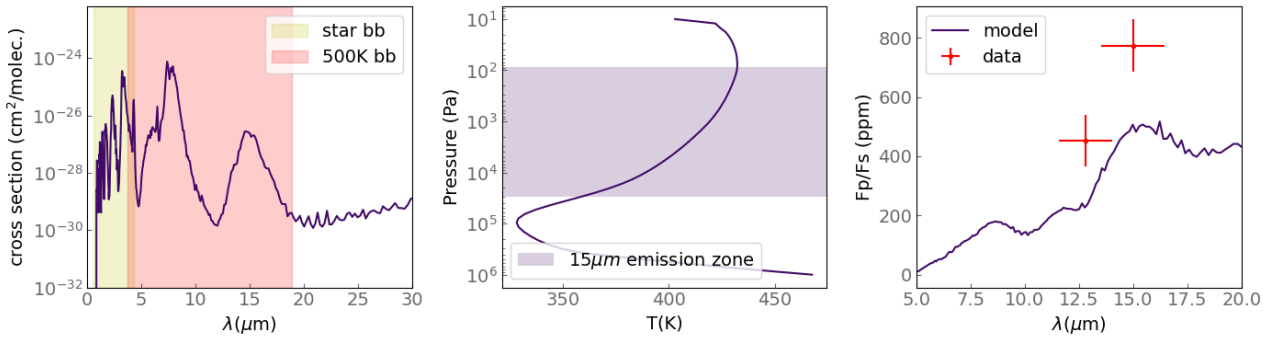

Figure 3.8: 1-D case of thermal inversion (10 bar, N_2+40% CH_4+0.4%CO_2). Left: the opacity of the atmosphere with the zone of emission of the star and the planet. Middle: the temperature profile and the layers of emission of the atmosphere at 15 μm. Right: the eclipse depth. The methane absorbs partly in the star-emission region, creating the thermal inversion in the temperature profile. The CO_2 absorbs in the 15 μm band, thus the emission layers at 15 μm are high enough in the atmosphere, where the temperature is high. Thus, the eclipse depth is higher.

3.3.3 Atmospheres with a strong thermal inversion

3.3.3.1 Principle

In first approximation, Earth's atmosphere is transparent in the visible, and opaque in the IR, allowing most of the light from the Sun to go through all the atmosphere, warming the surface, which re-emits this energy in the infrared, and the atmosphere itself absorbs this light. This process tends to make the atmosphere warmer close to the surface, and colder as we go up in the atmosphere. On Earth, the ozone layer absorbs in the UV, heating the atmosphere directly from the top. It creates a so-called thermal inversion: the atmosphere goes hotter as we go up, in what is called the stratosphere.

In the case of TRAPPIST-1 b, the star is colder than the sun, and its spectrum is thus shifted towards infrared wavelengths. A significant part of the emission of the star is in the near infrared. Thus, a strong thermal inversion can happen quite easily, if the atmosphere contains some kind of absorber in the stellar emission range. Aerosols, but also molecules like CH_4, can absorb in the near infrared. In this section, we explore thermal inversion created by different kinds of components.

If there is a thermal inversion, a molecule with an absorption band at the observed wavelength will result in observations probing higher in the atmosphere, as usual, but this time, it means that one will probe higher temperatures. The absorption band of the molecule is thus expected to be observed as an emission band (Fig. 3.8).

3.3.3.2 Composition

Thermal inversion with gas We tested an atmosphere with a high amount of CH_4, to create the inversion, and some CO_2, to be seen in emission. We supposed a redistribution factor of 1/4 (total redistribution) for the 1-D simulations. The results of the best case in 1-D are shown in Fig. 3.8. The chosen composition is N_2 as background gas, 40% of CH_4, and 0.4% of CO_2. The 3-D study of this atmosphere is shown in Fig. 3.9. The eclipse depth in 3-D is much higher than in 1-D, because the redistribution in the probed region is not total, contrary to the assumption made in 1-D.

Note that such an amount of CH_4 is expected to produce hazes in the upper layers, and that these hazes are expected to contribute to the thermal inversion.

Thermal inversion with simplified hazes Our simplified model for hazes, from Ducrot et al. (2024), is described in 3.2.1.5. We found that, using the value of $f_{\text{haze}} = 7.0 \times 10^{-4}$ (Equation 3.1) as in Ducrot et al. (2024), we probe a very high-altitude region of the atmosphere, where the heat redistribution is inefficient. Indeed, despite the strong winds, at such low pressure the radiative timescale ($\tau_{\text{rad}} = \frac{C_p P}{g\sigma T^3}$

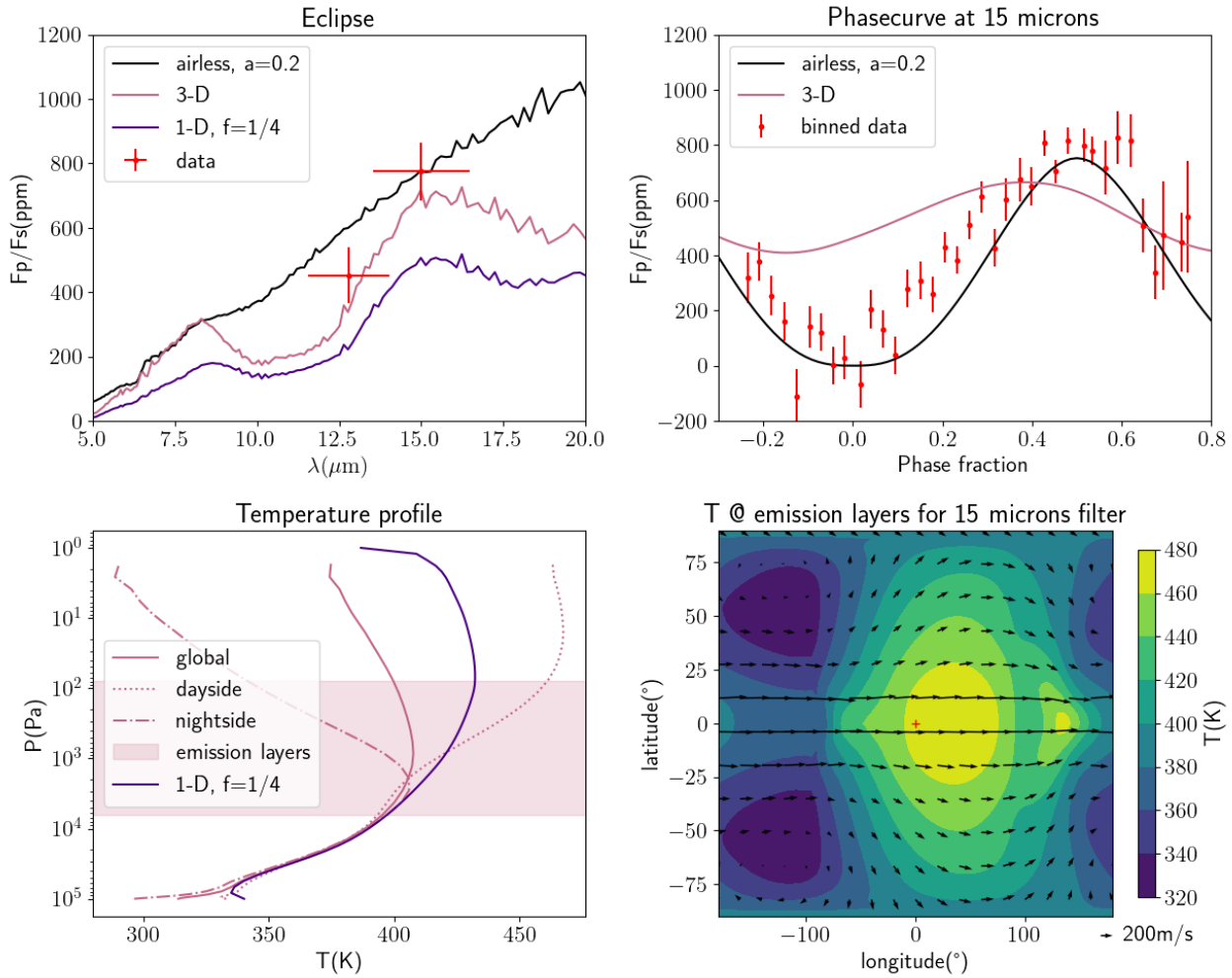

Figure 3.9: Thermal inversion: 1 bar, N_2+40% CH_4+0.4%CO_2. The panels are the same as Fig. 3.7.

$\sim 10^2$s at P=10 Pa, with C_p the heat capacity of the atmospheric gas, g the gravity of the planet and σ the Stefan-Boltzmann constant) is very short compared to the advection timescale ($\tau_{\rm adv} = \frac{R_p}{v} \sim 10^4$s, with R_p the radius of the planet and v the wind horizontal speed). Therefore, the dayside at this height is much hotter than the 1-D prediction that assumed a full redistribution. In order to match the data we thus tried two different options: 1. Add a simplified single-scattering albedo of 0.5 by lowering the incoming stellar flux of a factor 2 (Model 1 , corresponding to *Haze high* in Gillon et al. (2025)) and 2. Lower the haze factor $f_{\rm haze}$ to $f_{\rm haze} = 3.0 \times 10^{-5}$, while adding a small simplified single-scattering albedo of 0.2 (Model 2, corresponding to *Haze low* in Gillon et al. (2025)). These cases are shown in Fig. 3.10.

Thermal inversion with more realistic aerosols We also tested for aerosols for which we had more realistic optical properties: Titan-like tholins, H_2SO_4, and martian dust. A 1-D study of the impact of the different parameters can be found in Appendix 3.6.3.1. For all aerosols tested, the single-scattering albedo was high in the near infrared, preventing a strong heating of the high atmosphere. Thus, a strong quantity of aerosols was needed to get a strong flux at 12.8 and 15 μm. The most efficient aerosols for the thermal inversion are the largest, and only the dust particles allowed for a strong flux at 15 μm compatible with the eclipse depth. For all the cases tested, the aerosols are very high and in large quantities, making the high atmosphere opaque at all wavelengths. At these low pressures, the CO_2 does not have a strong radiative effect, and is not seen in emission. Instead, the emission from the atmosphere corresponds to a blackbody at the temperature of the high atmosphere. We selected two cases to test in 3-D: first, a layer of dust (with an effective radius of 100 μm) between pressures 1000 and 1 Pa, with a constant volume mixing ratio (VMR) of 3.5×10^{-18}, and second, a layer of tholins (effective radius 1 μm, between 10 and 1 Pa, VMR=1.×10−13). Note that for the dust case, the opacity is so important that there is not enough flux to go through the atmosphere, resulting in an isotherm rather than a thermal inversion (see Appendix 3.6.3.1).

3.3.3.3 Constraints from the secondary eclipse

For the inversion with gas and with simplified hazes, one can see that contrary to all other simulations, the CO_2 band is not seen in absorption, but in emission. This is consistent with the eclipse observations, since the 15 μm brightness temperature (478 ± 27 K) is higher than the 12.8 one (424 ± 28 K). For the inversion with realistic aerosols, the CO_2 is not visible as the atmosphere becomes optically thick too high.

For the simplified hazes case, the haze factor and single-scattering albedo were fit to obtain a satisfying match with the observations (Fig. 3.10). This case, although fine-tuned, gives the best agreement to the data (Table 3.1).

For both cases from aerosol optical properties (dust and tholins), the aerosol layer in the high atmosphere is so opaque that it mimics a surface, and the emission spectrum is similar to a bare rock (Fig. 3.11).

3.3.3.4 Constraints from the phase curve

For all cases, we probe high enough in the atmosphere to have a non-flat phase curve: despite the efficient mixing in the deeper atmosphere, the upper atmosphere presents a hotter dayside because the heat redistribution is less efficient there. For the CH_4 case (Fig. 3.9) and the simplified haze Model 2 (Fig. 3.10), though, the probed pressures includes part of the well-mixed atmosphere, resulting in a low amplitude, high minimum temperature in the phase curve, but also a strong offset, because of the eastwards shift of the hottest point due to the super-rotation.

For the simplified haze Model 1 (Fig. 3.10) and more realistic aerosols, the probed region is so high, that all the redistribution is inefficient there, and the phase curve presents a quasi-zero nightside flux, a very high dayside flux, and no peak offset, thus matching the observations if the upper atmosphere is hot enough. Thus, to be compatible with the observations, the thermal inversion must be strong, and one needs a strong enough absorption at 15 μm to probe very high in the atmosphere. The hazes compatible are therefore abundant very high in the atmosphere and very dense. For the realistic aerosol optical properties (Fig. 3.11), the probed temperature is slightly too low to match the data. Indeed, the realistic aerosols have a high single-scattering albedo, reflecting part of the stellar flux in space, so the upper layers temperature is lower than in the simplified cases, and the emission is weaker.

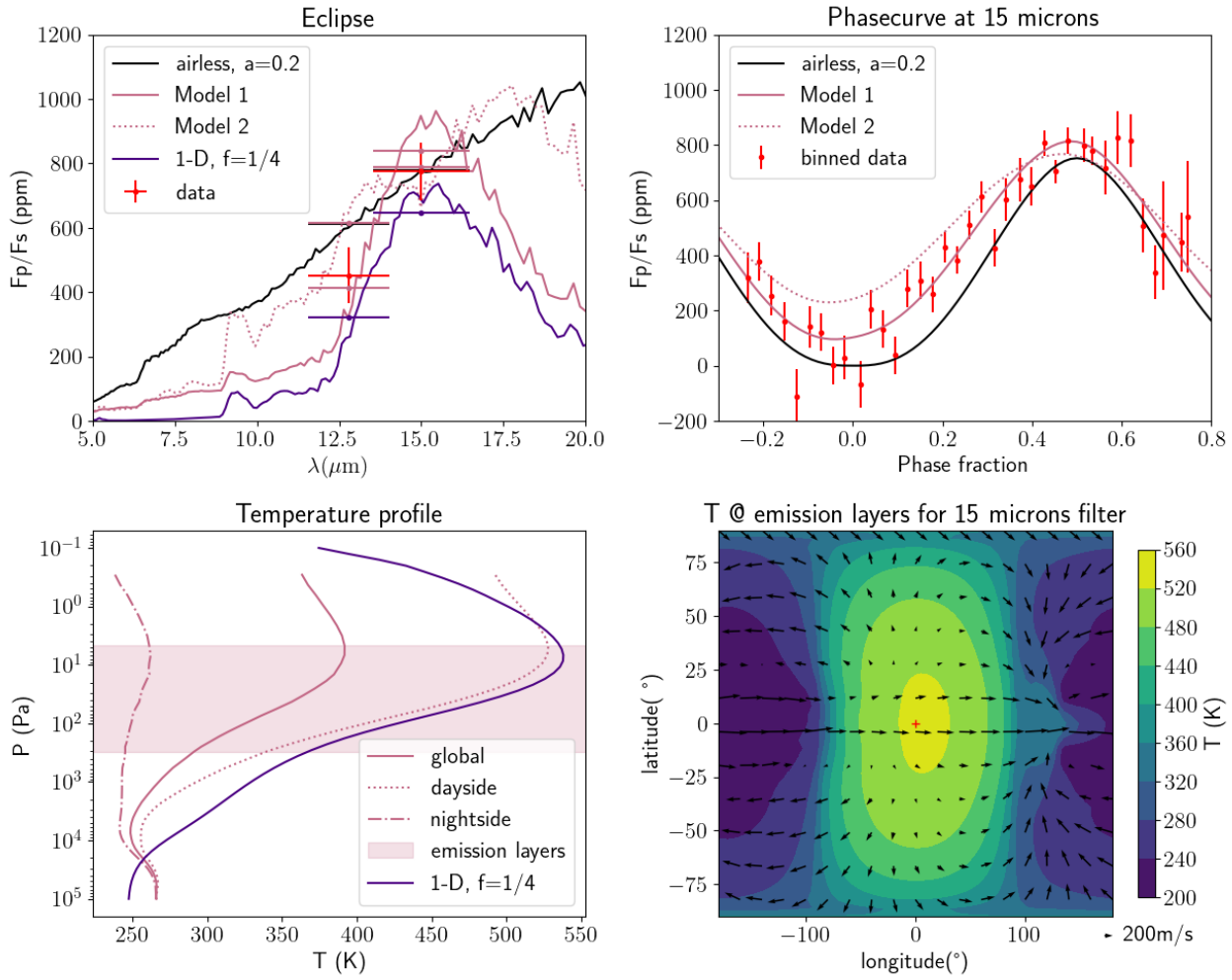

Figure 3.10: Thermal inversion: CO_2+ simplified hazes. The panels are the same as Fig. 3.7. Model 1 and Model 2 for the hazes are described in the text. The temperatures and winds of the lower panels correspond to the Model 1 case, which is the model closest to the data.

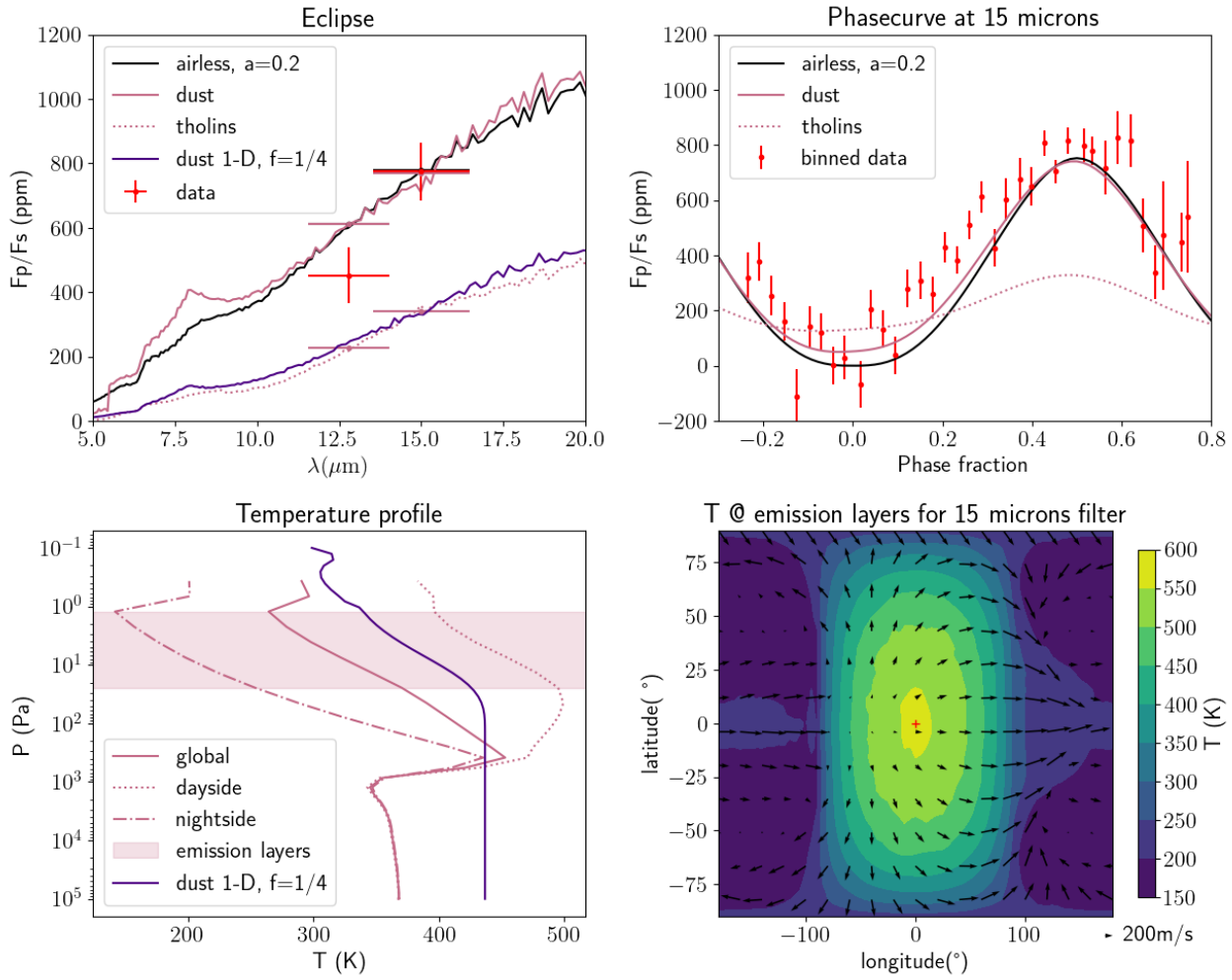

Figure 3.11: Thermal inversion: CO_2+ aerosols with realistic optical properties. The panels are the same as Fig. 3.7. Parameters for dust and tholins are described in the text. The temperatures and winds of the lower panels correspond to the dust case, which is the model closest to the data. The difference between the 1-D and 3-D thermal profiles is discussed in Appendix 3.6.3.2.

In summary, the emission signature is influenced by the type, abundance, and location of the absorbing species within the atmosphere. Three cases stand out: (1) When the stellar absorber is weak, such as CH_4, the emission originates from deeper atmospheric layers, with CO_2 detected in emission but resulting in a phase curve with low amplitude. (2) For more efficient absorbers, such as those in the simplified haze Model 1, the emission comes primarily from the upper atmosphere, leading to a phase curve with high amplitude mimicking the bare rock signal. (3) Finally, if the stellar absorber is highly efficient and abundant, it can render the entire atmosphere optically thick. Under these conditions, CO_2 will no longer be observed in emission, and the resulting emission signature will resemble that of an airless rock.

3.4 Discussions

3.4.1 Limitations in the model

The GCM allows for more realistic simulations, but they are too complex and expensive to pretend to explore the whole parameter space of exoplanet atmospheres. Among the parameters that we arbitrarily fixed and the hypotheses made, we note some that could have an impact on our results.

- The internal heat flux of the planet, set to zero in our simulations, could prevent the atmospheric collapse for thin atmospheres, as already discussed in section 3.3.1.6
- The surface albedo changes the flux at 15 and 12.8 μm, in particular for optically thin atmospheres. We discuss its impact on the eclipse depth in Appendix 3.6.1.3.
- The hazes we added in our simulations are highly idealized: we prescribed the vertical position and quantity of the hazes in the atmosphere. A more in-depth study of the formation of hazes would be necessary to assess whether the assumptions we made about haze properties are possible.
- Moreover, a CO_2-CH_4-rich atmosphere is not expected to be thermochemically stable Krissansen-Totton et al. (2018); Watanabe & Ozaki (2024). However, for this study we only tried to identify gas mixtures matching the data, without any prior on the expected composition. We recall that this is the first time as many observations are obtained on this category of planet (relatively temperate, Earth-size exoplanet around M-star), and leave the question of plausibility for future work.
- Apart from the N_2-CO_2 case, we did not study the formation and impact of clouds on our simulated atmospheres. At the pressure and temperature range studied, H_2O is the only condensable species. Condensation of water around TRAPPIST-1 planets have been studied already in Turbet et al. (2023).

3.4.2 Limitations in the data analysis approach

For a transit spectrum or a secondary eclipse, one fits the time-dependent data with a well-known light curve shape, and extracts the transit/eclipse depth from it. The extraction of the phase curve is not as straightforward. Indeed, the shape of the phase curve depends on the properties of the planet and its hypothetical atmosphere. Thus, one must make physical assumptions regarding the planet to parameterize the shape of the phase curve, so the data reduction is not as well decoupled from the physical interpretation as in the case of transits and eclipses.

Moreover, in our case, the observed phase curve from Gillon et al. (2025) contains the contribution of TRAPPIST-1 b and c. Thus , it is delicate to extract the contribution of TRAPPIST-1 b alone in our study. The most relevant approach would be to perform a joint fit of the two planets, but this is out of the scope of this study.

3.4.3 Comparison with previous studies

Lim et al, 2023 We computed synthetic transit spectra for the atmospheres that match all the data in emission, in order to check that these are compatible with the information available from transmission (see Appendix 3.6.4). Our signal is typically below 100 ppm which is undetectable from the data of Lim

et al. (2023). Thus, these scenarios can be neither ruled out nor verified from transmission spectroscopy information.
However, it is important to keep this in mind for future observations of TRAPPIST-1 system de Wit et al. (2024), in particular observation strategies using TRAPPIST-1 b considered airless as a probe to correct for stellar contamination (JWST GO 6456).

Ih et al, 2023 First, we compared our eclipse spectra from Fig. 3.5 with the ones from Ih et al. (2023) at same pressure and composition and obtained good agreement for atmospheres with little CO_2. For the atmospheres that are optically thick, e.g. pure CO_2 atmospheres, the flux in the CO_2 band is lower in our simulations, probably because of differences between our temperature profiles (the higher atmosphere is colder in our simulations).

Though we studied in depth the condensation of CO_2, we did not perform simulations for the other compositions in Ih et al. (2023). N_2, CO, O_2 and CH_4 should not condense under TRAPPIST-1 b conditions. SO_2 and H_2O, though, are more condensable than CO_2 (Fray & Schmitt (2009),Turbet et al. (2018)), and Ih et al. (2023) found that a 1 bar O_2 atmosphere with 100ppm H_2O and a 0.1 bar O_2 atmosphere with 100ppm SO_2 would fit the observations. Considering the surface temperature in our 100ppm CO_2 simulations at these pressures, we found that the minimum surface temperature are below the condensation point of SO_2 and H_2O, and therefore most of the SO_2 and/or H_2O is expected to collapse for a tidally-locked case.

Ducrot et al, 2024 In Ducrot et al. (2024), the authors introduced the hypothesis of a thick, hazy atmosphere that allowed seeing CO_2 in emission. They expected an efficient redistribution for such a thick atmosphere. We found that with such an atmosphere, the redistribution is indeed efficient in the deep atmosphere, but in the higher, less dense atmosphere, which is actually the part that is probed at 15 μm, the heat redistribution becomes less efficient because of the very short radiative timescale at low pressure, allowing for a much brighter dayside, and a high amplitude phase curve (Fig. 3.10), an effect which was not represented by the 1-D study.

3.4.4 Perspectives for the study of TRAPPIST-1 b

We highlighted different atmospheres that could produce observables compatible with our data available. Are there additional emission observations of TRAPPIST-1 b that could distinguish between the remaining cases ? The thin, residual atmospheres are by construction very similar to a bare rock, and cannot be distinguished by observation. For the atmospheres with thermal inversion, we saw that, depending on the aerosols, there can be a CO_2 emission band, or no spectral features in emission. Only the case of a thermal inversion with CO_2 in emission could be investigated by more observations.

A phase curve at 12.8 μm could in principle help distinguish between some thermal inversion scenarios (with a lighter amplitude at 12.8 μm than 15 μm) and the airless case. However, the hazy atmosphere is still not transparent at these wavelengths, thus not resulting in a totally flat phase curve, and simulations of observations show that the signal-to-noise ratio would be too weak to distinguish the different scenarios (Fig. 3.12a).

Secondary eclipse observations far from the CO_2 band, where some hazy models are expected to give much less flux than airless models, could be interesting. We used the JWST Exposure Time Calculator (ETC) to compute the expected precision on the occultation depth of TRAPPIST-1 b at 10 and 18 μm. Using the following formula we can compute the precision on the occultation depth:

$$\text{precision} = \frac{\sqrt{(1/N_{in} + 1/N_{out})}}{SNR_{point}} \tag{3.3}$$

Where N_{in} is the number of points during the occultation and N_{out} is the number of points outside the occultation, during a single visit.

For MIRI filter F1800W with SUB256 (to maximize the number of groups per integration) we obtain an SNR per point equal to 600 and an exposure time equal to 89.56s for 299 groups per integration. We

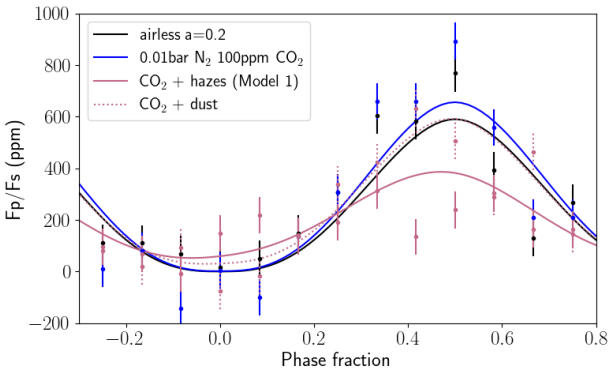

(a) Phase curves in the 12.8 μm MIRI filter for an airless body and the remaining atmospheric families, along with corresponding simulated observational points.

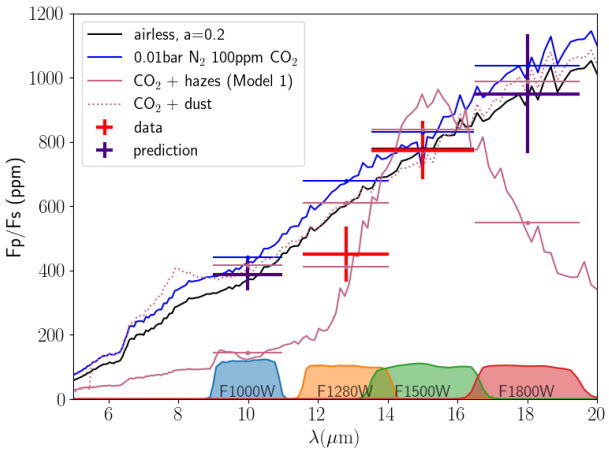

(b) Dayside emission for an airless body and the remaining atmospheric families. The red points are from Ducrot et al. (2024). The purple points are predicted observation points for 5 visits for an airless body of albedo 0.2.

compute a precision of 371 ppm for 1 visit. For F1000W we compute a precision of 97ppm in one visit (SNR of 868.49 and exposure time of 13.18s). Fig. 3.12b shows the predicted observations for 5 visits. We compute that we would need at least 8 visits to distinguish between a bare-rock scenario and the hazy, CO_2 emission case with an observation at 18 μm, but only two visits at 10 μm. This is to distinguish between two extreme cases, however, a hazy atmosphere emission can stand between these two cases, and even mimic an airless scenario (see section 3.3.3.3).

3.5 Conclusion

Starting from the secondary eclipse observations, we performed a study of atmospheres on TRAPPIST-1 b that would produce a high brightness temperature at 12.8 and 15 μm. After exploring the parameter space in 1-D, we found several families of atmospheres that do so, and selected representatives of each family to study in 3-D. The 3-D study brought several results that could not be predicted in 1-D:

- Thin, condensable atmospheres: we identified the process of atmospheric collapse, through cold traps condensation, that allowed us to rule out some atmospheres that are thus not stable. Crossing this information with the observations allowed us to narrow the window of possible thin, N_2-CO_2 atmospheres (Fig. 3.4). This result can be extended to other compositions (section 3.4.3).

- Thick, transparent atmospheres: we found that even a very small opacity, such as N_2-N_2 collisionnally induced absorption, is enough to make the atmosphere radiatively active and emit a flux in the nightside, making such an atmosphere incompatible with the phase curve data (Appendix 3.6.1.1).

- Thick, greenhouse-efficient atmospheres: we highlighted a type of thick, highly redistributive atmosphere that gives a similar dayside emission than a bare rock, but that could be ruled out with the phase curve observation (Fig. 3.7). Atmospheres with these characteristics are reduced atmospheres (containing CH_4 and C_2H_4 or C_2H_6), in order to provide an atmospheric window for radiation to escape from deeper layers to give the high flux observed by JWST photometry.

- Atmosphere with thermal inversion: for this kind of atmosphere already proposed in Ducrot et al. (2024), we found that the 1-D hypothesis of a full redistribution is not accurate, since the flux is coming from high in the atmosphere where the heat redistribution becomes inefficient. Furthermore, this effect – if the hazes have the right altitude and properties – can result in a phase curve with a very strong day-night amplitude and no offset, compatible with the observations (Fig. 3.10). Only atmospheres with a thermal inversion and hazes or aerosols can match the phase curve data.

In summary, we showed that an airless planet and a thin, residual atmosphere are not the only scenarios compatible with the secondary eclipse observations: we proposed three families of thick atmospheres (transparent atmospheres with almost no condensing/absorbing species, reduced atmospheres with an opacity window at 15 μm, and atmospheres with a thermal inversion) that also match the eclipse data. The phase curve observation showing a very cold nightside and no peak offset was needed to rule out some cases (thick, reduced atmospheres thick, transparent atmospheres and atmospheres with a thermal inversion but no hazes). Taking into account all the emission observations available, we showed that TRAPPIST-1 b is either a bare rock, or possesses a very thin atmosphere poor in absorbing and/or condensing gases, or could possess an atmosphere with a thermal inversion and hazes, although this last case seems unlikely and fine-tuned.

Though this study was dedicated to TRAPPIST-1 b, as this planet had an unprecedented amount of observed data in emission (eclipse depth at two different wavelengths, and phase curve), the methodology of this study is applicable to other rocky targets to be observed with JWST. Moreover, our results (atmospheric collapse, question of heat redistribution...) can qualitatively apply to other close-in rocky exoplanets observed in emission. In particular, we call attention to the degeneracy of a high eclipse depth at 15 μm, making it hazardous to conclude that a planet is airless just from this photometric point.

3.6 Appendix

3.6.1 CO_2-N_2

3.6.1.1 Thick transparent atmosphere

We studied the influence of P_{tot} for a constant partial pressure of CO_2 in order to test the thick-transparent atmosphere case. Fig. 3.13 shows the observables for different tests of atmospheres from the "transparent" family, and the temperature distribution for the 10 bar, N_2+0.1ppm CO_2 atmosphere. One can see that the surface is well decoupled from the atmosphere, since the temperature profile of the atmosphere is almost the same in the nightside and dayside, although the surface presents strong differences between day and night (lower left panel).

For a fully transparent atmosphere, the heat redistribution should not be detectable in the phase curve as the emission comes from the surface. Yet, atmospheres composed of real gases can not be completely transparent, and even a small opacity allows for the atmosphere to absorb and re-emit part of the radiation from the surface, where the heat is redistributed and the nightside warmer. Thus, one can see that the 10 bar atmosphere phase curve has a weaker amplitude, with a nightside flux of almost 400 ppm. Part of the absorption is caused by collisionnaly induced absorption of N_2, and part of it by the remaining CO_2 present in the atmosphere. When we remove these contributions ("transparent" case in the figure), the phase curve is similar to a thin atmosphere.

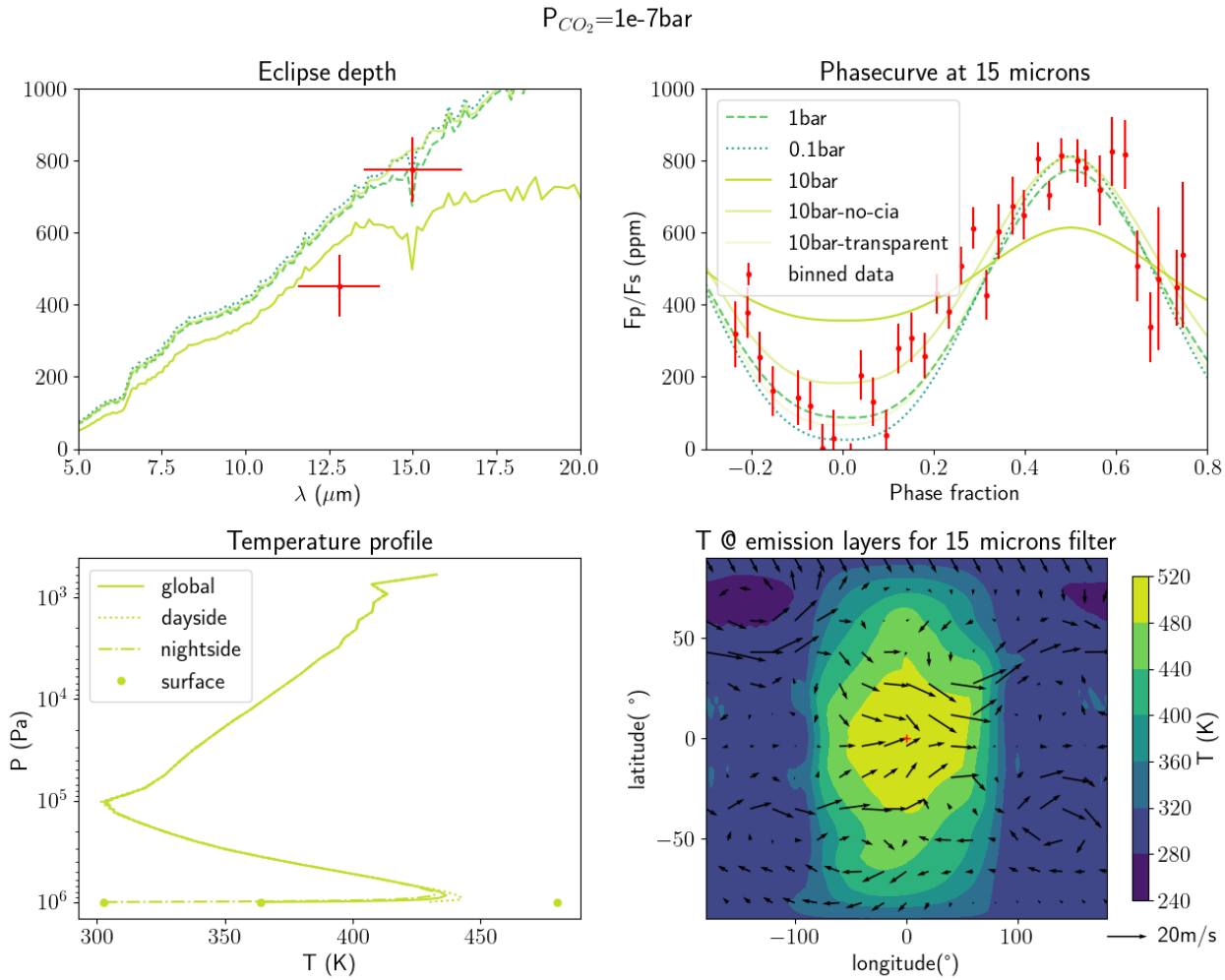

Figure 3.13: Upper panels: observables of the "transparent" atmospheres. The CO_2 partial pressure is 1.e-7 bar, except for the "transparent" case where the observables have been calculated for P_{CO_2}=1.e-15 bar. For the "no CIA" case, the collisionnally induced absorptions have not been included in the opacity computation. Lower panels: temperature profile and map for the 10 bar case. The atmosphere is very well mixed, but there is no efficient coupling with the surface, and the surface has a hot dayside and cold nightside.

3.6.1.2 Pure CO_2

We show in Fig. 3.14 the observables and temperature for the case of a collapsing, pure CO_2 atmosphere, with the boundary of the CO_2 ice cap.

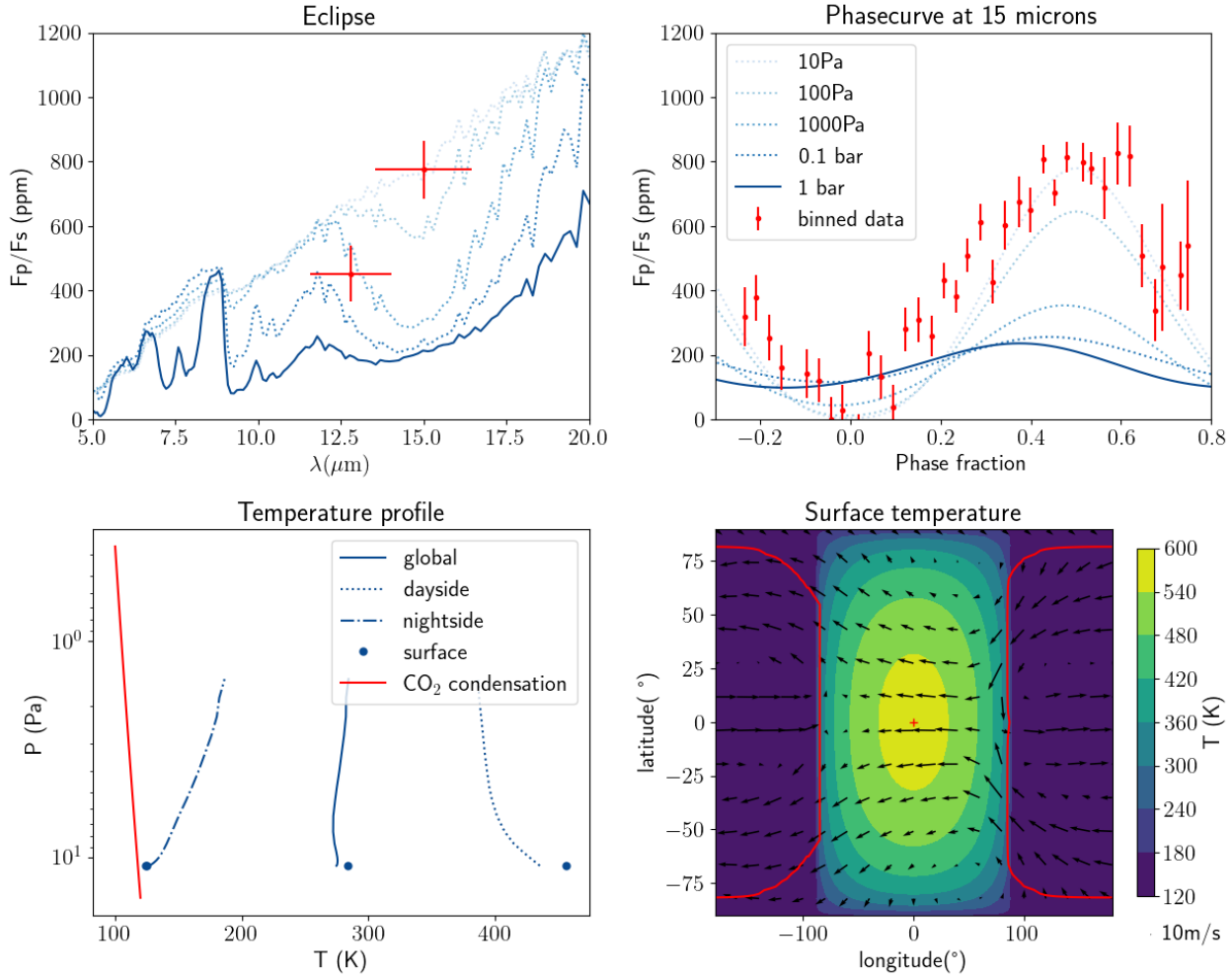

Figure 3.14: Pure CO_2 case. Upper part: observables (right: phase curve at 15 μm, left: eclipse depth). The dotted lines represent non-stable atmosphere: these are snapshots of the atmosphere during its collapse. Lower part: physical quantities. Temperature profiles and temperature map for the 10 Pa case (compatible with the observations, but not stable). In the lower right panel, the red contour shows the CO_2 ice caps. The red dot is the substellar point. In the lower left panel, the red line correspond to the CO_2 condensation curve.

3.6.1.3 Effect of surface albedo

We studied the effect of the surface albedo for several atmospheres from the CO_2-N_2 grid in Fig. 3.15. If the CO_2 absorption band is strong (a,c), the atmosphere is optically thick at 15 μm and the surface albedo does not matter at this wavelength. For cases with little CO_2 proportion (b,d), there is no saturation effect and the albedo lowers the whole spectrum equally. We can then suppose that for low CO_2 proportion, increasing the albedo can decrease the eclipse depth for 12.8 and 15 μm, although for high CO_2 proportion, increasing the albedo would decrease the eclipse depth at 12.8 μm, but not at 15 μm.

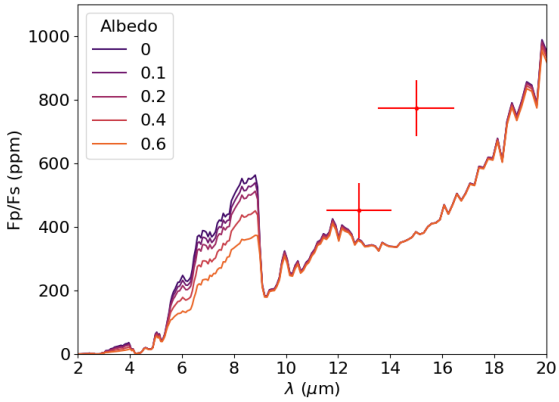

(a) Pure CO_2, 1 bar

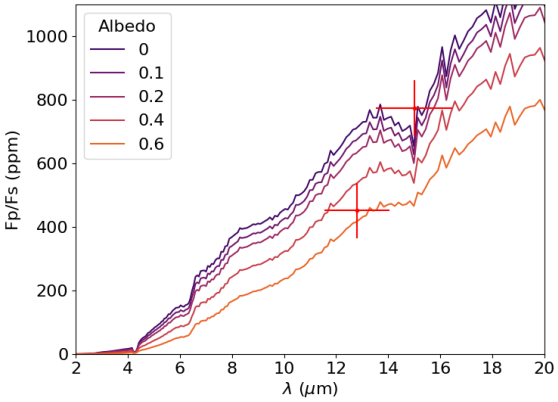

(b) 1 ppm CO_2, 1 bar

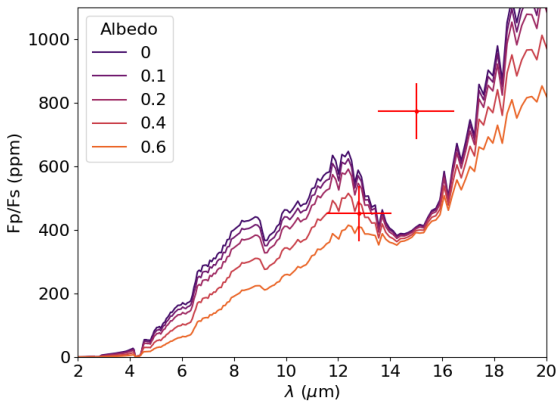

(c) Pure CO_2, 0.01 bar

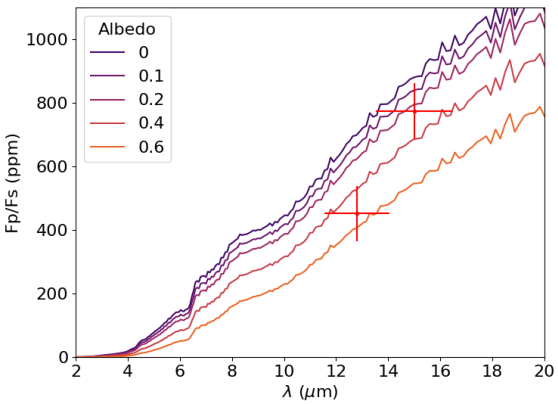

(d) 1 ppm CO_2, 0.01 bar

Figure 3.15: Effect of the surface albedo for different cases of N_2-CO_2 atmospheres (results of 1-D simulations).

3.6.2 Thick atmosphere with an opacity window

3.6.2.1 Proof-of-concept

Fig. 3.16 shows a 1-D proof-of concept of the family of the thick atmospheres. We designed an unrealistic opacity of the atmosphere meeting our requirements: a high opacity in the range of thermal emission of the planet, a window around the probed wavelengths, and a weaker opacity at the range of emission of the star, to let the stellar flux reach the surface of the planet. We ran the 1-D radiative transfer code `exo_k` and tuned the values of the opacity to reach the eclipse observation points. Thanks to the absorption window, the main part of the emission at 12.8 and 15 μm comes from deep in the atmosphere, where the temperature corresponds to the measured brightness temperature of the observations.

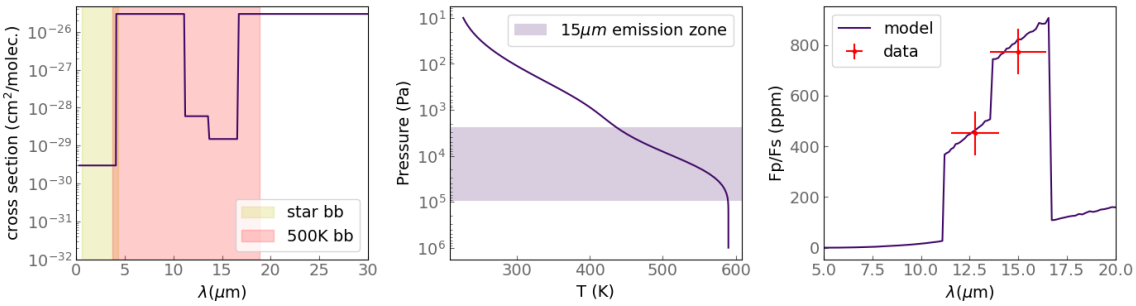

Figure 3.16: 1-D study of thick atmosphere with greenhouse effect with an opacity window at the observed wavelengths. Left: the idealized opacity vs wavelength. The yellow window corresponds to the zone of emission of the star, the red one to the planet. Middle: the temperature profile, the window corresponds to the layers of 95% of the emission. Right: the corresponding eclipse depth.

3.6.2.2 Opacities

We show in Fig. 3.17 the opacities of different molecules. We look for molecules that absorb in most of the planet emission range, but less in the MIRI filters at 12.8 and 15 μm. C_2H_4 and C_2H_6 present these features.

3.6.2.3 3-D effect

We provide the thermal profiles in 1-D and 3-D of different simulations in Fig. 3.18 in order to illustrate the 3-D effect resulting in a mean thermal profile colder than 1-D computations. In 1-D, the deep atmosphere is convective, and the thermal profiles follows an adiabat. In addition to the usual `exo_k` simulations, we performed two 1-D `PCM` simulation, one starting from the `exo_k` thermal profile (*hot start*) and the other from the 3-D mean profile (*cold start*), in order to make sure the difference between the 3-D `Generic PCM` simulations and the 1-D simulations comes from 3-D effects. The thermal profile of the 1-D `PCM` converges indeed towards a profile close to the `exo_k` profile.
In 3-D, the deep atmosphere is well mixed horizontally, but the poles are colder than the equator region. This leads to subsidence at the poles, forcing an adiabat that is colder than in the 1-D case. This changes the circulation regime, counter-intuitively making the surface temperature colder at the equator than at the poles, and preventing convection at the equator region.

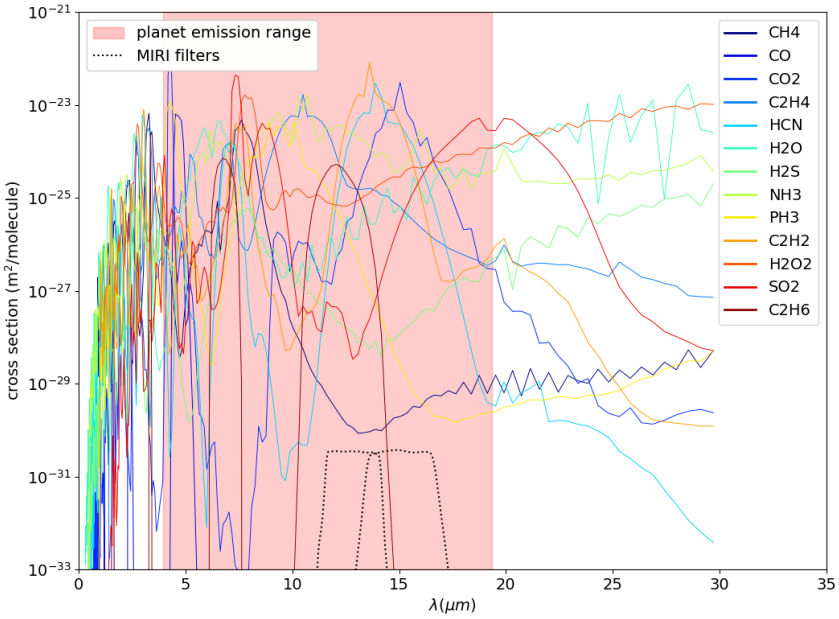

Figure 3.17: Opacities of molecules. In dotted lines, the MIRI filters where the molecules must not absorb too much in order to produce the right effect. In red, the planet blackbody emission range.

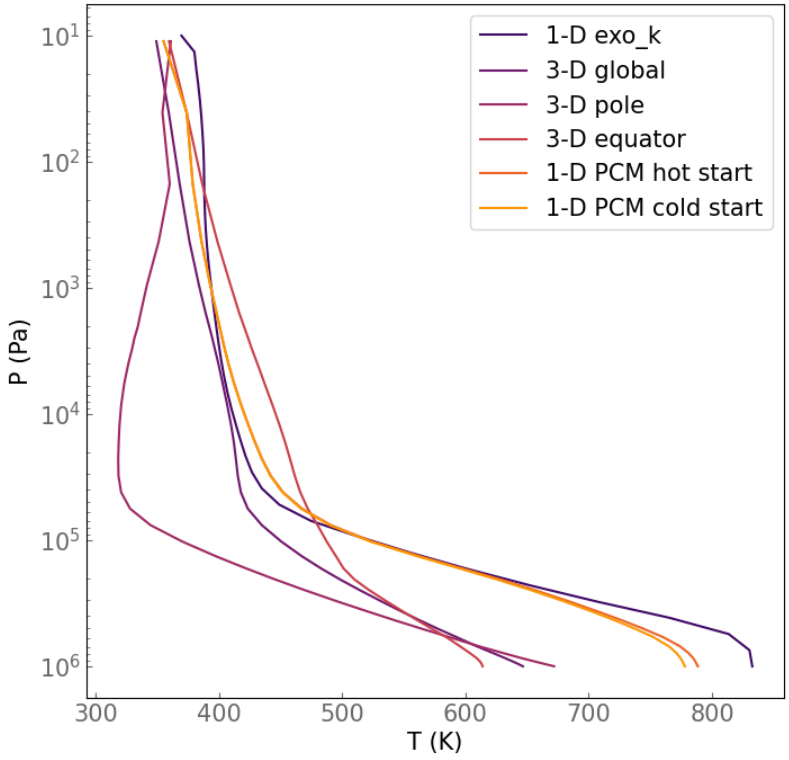

Figure 3.18: Thermal profiles for different simulations of a 10-bar, N_2 atmosphere with 20% CH_4 and 0.2% C_2H4.

3.6.3 1-D study of hazes

3.6.3.1 Parameter study

We conducted a study in 1-D with `exo_k`. First, we varied different parameters of the simplified model presented in 3.2.1.5. Then, we compared the model with different aerosol optical properties (extinction coefficient, single scattering albedo, and asymmetry factor) from laboratory measurements, and finally we varied some parameters for two selected aerosol types. The parameters of each 1-D simulations are summarized in Table 3.5.

Table 3.5: Parameters for the aerosol parameter study.

Study	Aerosol type	P_{bot} (Pa)	P_{top} (Pa)	f_{haze}	VMR	SSA	r_{eff} (m)
a	Simplified	1×10^{2}	$1. \times 10^{0}$	$7. \times 10^{-4}$	–	0	–
	Simplified	1×10^{3}	$1. \times 10^{1}$	$7. \times 10^{-4}$	–	0	–
	Simplified	1×10^{4}	$1. \times 10^{0}$	$7. \times 10^{-4}$	–	0	–
	Simplified	1×10^{4}	$1. \times 10^{1}$	$7. \times 10^{-4}$	–	0	–
	Simplified	1×10^{5}	$1. \times 10^{0}$	$7. \times 10^{-4}$	–	0	–
b	Simplified	1×10^{5}	$1. \times 10^{0}$	$1. \times 10^{-5}$	–	0	–
	Simplified	1×10^{5}	$1. \times 10^{0}$	$1. \times 10^{-4}$	–	0	–
	Simplified	1×10^{5}	$1. \times 10^{0}$	$1. \times 10^{-2}$	–	0	–
	Simplified	1×10^{5}	$1. \times 10^{0}$	$7. \times 10^{-4}$	–	0	–
c	Tholins (Khare)	1×10^{3}	1×10^{0}	–	1×10^{-13}	free	1×10^{-6}
	Tholins (Drant)	1×10^{3}	1×10^{0}	–	1×10^{-13}	free	1×10^{-6}
	H_2SO_4	1×10^{3}	1×10^{0}	–	1×10^{-13}	free	1×10^{-6}
	Dust	1×10^{3}	1×10^{0}	–	1×10^{-18}	free	1×10^{-4}
	Simplified	1×10^{5}	$1. \times 10^{0}$	$7. \times 10^{-4}$	–	0	–
d	Tholins (Khare)	1×10^{3}	1×10^{0}	–	1×10^{-13}	0.5	1×10^{-6}
	Tholins (Drant)	1×10^{3}	1×10^{0}	–	1×10^{-13}	0.5	1×10^{-6}
	H_2SO_4	1×10^{3}	1×10^{0}	–	1×10^{-13}	0.5	1×10^{-6}
	Dust	1×10^{3}	1×10^{0}	–	1×10^{-18}	0.5	1×10^{-4}
	Simplified	1×10^{5}	$1. \times 10^{0}$	$7. \times 10^{-4}$	–	0	–
e	Tholins (Khare)	1×10^{3}	1×10^{0}	–	1×10^{-13}	free	1×10^{-8}
	Tholins (Khare)	1×10^{3}	1×10^{0}	–	1×10^{-13}	free	1×10^{-7}
	Tholins (Khare)	1×10^{3}	1×10^{0}	–	1×10^{-13}	free	1×10^{-6}
	Dust	1×10^{3}	1×10^{0}	–	1×10^{-18}	free	1×10^{-8}
	Dust	1×10^{3}	1×10^{0}	–	1×10^{-18}	free	1×10^{-6}
	Dust	1×10^{3}	1×10^{0}	–	1×10^{-18}	free	1×10^{-4}
f	Tholins (Khare)	1×10^{3}	1×10^{0}	–	1×10^{-18}	free	1×10^{-6}
	Tholins (Khare)	1×10^{3}	1×10^{0}	–	1×10^{-15}	free	1×10^{-6}
	Tholins (Khare)	1×10^{3}	1×10^{0}	–	1×10^{-12}	free	1×10^{-6}
	Dust	1×10^{3}	1×10^{0}	–	1×10^{-21}	free	1×10^{-4}
	Dust	1×10^{3}	1×10^{0}	–	1×10^{-18}	free	1×10^{-4}
	Dust	1×10^{3}	1×10^{0}	–	1×10^{-15}	free	1×10^{-4}

1. Impact of the vertical distribution profile of the hazes (Fig. 3.19a): we find that the most important is that the hazes are present at the top of the atmosphere. If the upper layer of the atmosphere is hazeless, the CO_2 present in this layer is seen in absorption. The presence or absence of hazes in the deeper atmosphere is not important.

2. Impact of the factor f_{haze} (Fig. 3.19b): This factor corresponds to the quantity of hazes present in the atmosphere. We find, like Ducrot et al. (2024), that 7.e-4 is optimal, as a lower quantity of hazes results in a thermal inversion deeper in the atmosphere, and the CO_2 band probes in the upper atmosphere. Thus, we confirm that the case we present is fine-tuned.

3. Comparison with real aerosol optical properties (Fig. 3.19c): For all the different aerosols that we could test, we do not get a CO_2 emission band. Martian dust results in a thermal inversion allowing for a high eclipse depth.

4. Impact of the single-scattering albedo (Fig. 3.19d): With a single scattering albedo fixed to 0.5, independent of the wavelength, we can reproduce some features of our simplified model.

5. Impact of the size of the aerosols (Fig. 3.19e): We find that, for two different types of aerosols (tholins and dust), the largest aerosols give inversions upper in the atmosphere, and thus highest eclipse depth.

6. Impact of the volume mixing ratio (Fig. 3.19f): We varied the volume mixing ratio (VMR) for the same two types of aerosols. For the dust case, the highest VMR leads to the highest eclipse depth, although there is a saturation at $\sim 1 \times 10^{-15}$. For tholins, for VMR $\sim 1 \times 10^{-12}$ there is an inversion, but it is not strong enough to give a high eclipse depth.

With these results, we identify that the realistic single scattering albedo of the aerosols, that is very high in the shortest wavelengths (Fig. 3.20), is responsible for the absence of CO_2 seen in emission by reflecting a very large part of the stellar emission, prohibiting a strong heating of the upper atmosphere.

In all our cases, either there is no strong thermal inversion in the upper layers and CO_2 is seen in absorption, or the hazes seem to be optically thick at all wavelength, resulting in an isotherm in the deep atmosphere instead of a thermal inversion, and a thermal emission that reproduces a blackbody radiation with the temperature of the upper atmosphere.

In conclusion, only dust type aerosols are able to reproduce a strong eclipse depth, and no aerosol reproduces the CO_2 emission band that is seen with the simplistic haze model.

3.6.3.2 Convergence issues

Some of these simulations contain a high amount of aerosols, and only a very small part of the radiation goes through the atmosphere. Therefore, the deep atmosphere is getting almost no flux, and its convergence is extremely long. Indeed, the time step of the simulations is necessarily short, because of the small radiative timescale at the high atmosphere, whereas in the deep atmosphere the evolution timescale is way longer than the time step. `exo_k` comes with several acceleration routines, making it possible to converge this type of atmosphere. However, the `Generic PCM` does not, and our 3-D simulation of the dust scenario is not converged in the deep atmosphere. This does not impact our conclusion on observables as the thermal emission comes from the upper parts of the atmosphere, that are converged. Fig. 3.21 shows that the 1-D `exo_k` profile is similar, when not converged, to the 3-D profile.

3.6.4 Transit spectra

We computed transit spectra for representatives of the families that match the eclipse depths and phase curve: N_2-CO_2 atmospheres (here, 1 bar with 1ppm of CO_2), and atmospheres with thermal inversion (here, the hazes from the simplified hazes Model 1). The hazes distinguish from the bare rock and N_2-CO_2 case by a slope in the shortest wavelengths. However, this feature is of the order of dozens of ppm which is for now too dim to be observed. Nevertheless, these features could be of importance for future observations of the system, especially when TRAPPIST-1 b is used as a probe to correct for stellar contamination.

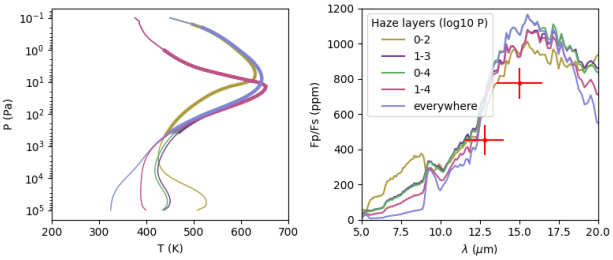

(a) Vertical profile of hazes. The haze VMR is constant between two layers of pressure, and set to 0 outside this band.

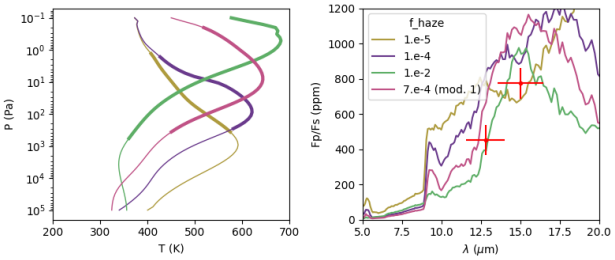

(b) Haze factor f_{haze}. For this case, the haze vertical profile is a constant.

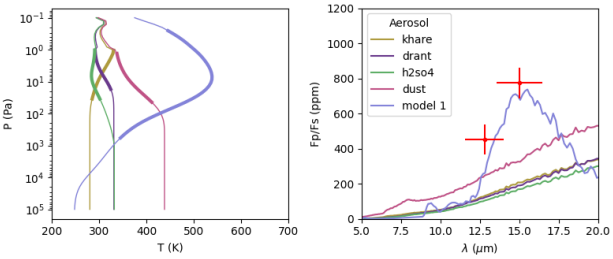

(c) Aerosol optical properties. For all cases, the aerosol VMR is constant between P=1000 and 1 Pa.

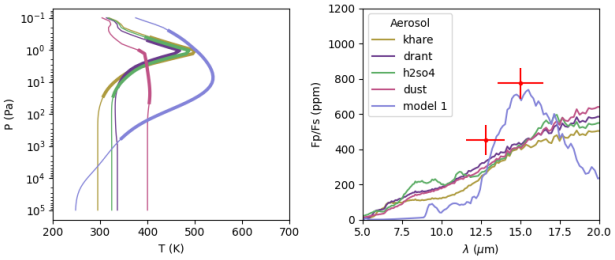

(d) Aerosol optical properties, with single-scattering albedo fixed to 0.5. The parameters are the same as panel (c), but with a single scattering albedo set to 0.5, independent of wavelength.

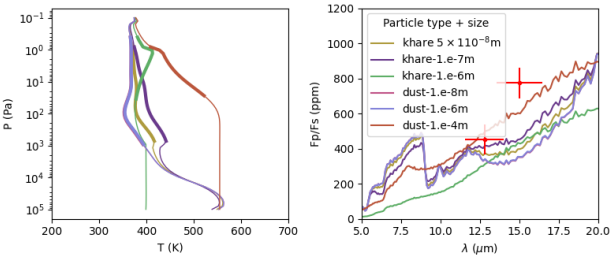

(e) Particle size. Comparison of different radii of particle for two aerosol types: dust, and tholins.

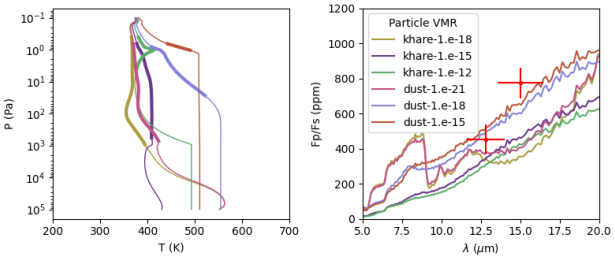

(f) Particle volume mixing ratio. Comparison of different mixing ratios for dust and tholins.

Figure 3.19: Temperature profile and eclipse depth for different parameterizations of aerosols. Each panel illustrates the influence of a parameter.

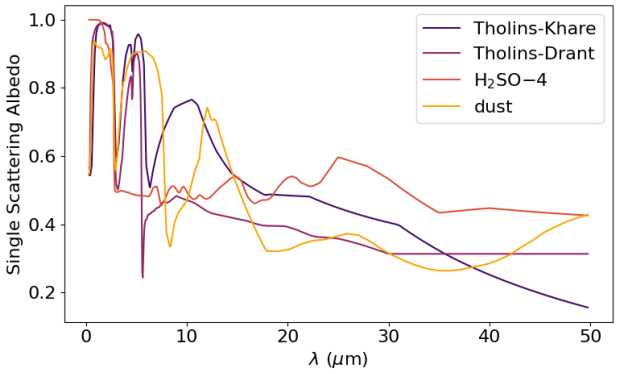

Figure 3.20: Single scattering albedo vs wavelength for different aerosol types. The radii of aerosols are 10×10^{-6} for tholins and H_2SO_4 and 10×10^{-4} for dust.

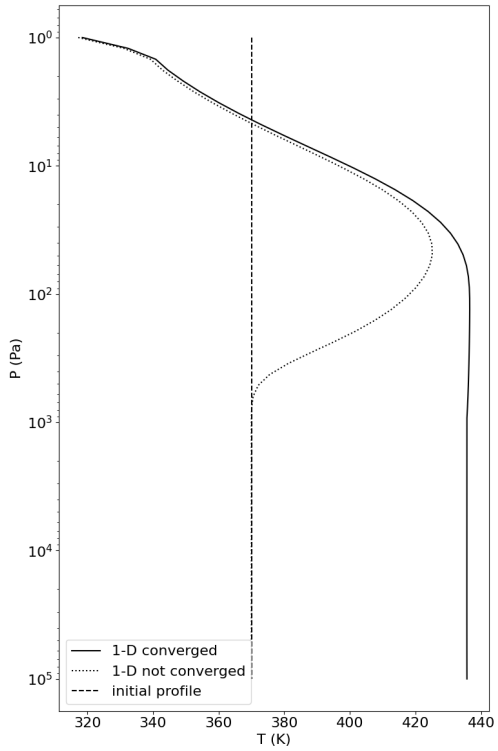

Figure 3.21: Thermal 1-D profile for the dust case, converged versus not converged. Initial profile is a 370 K isotherm.

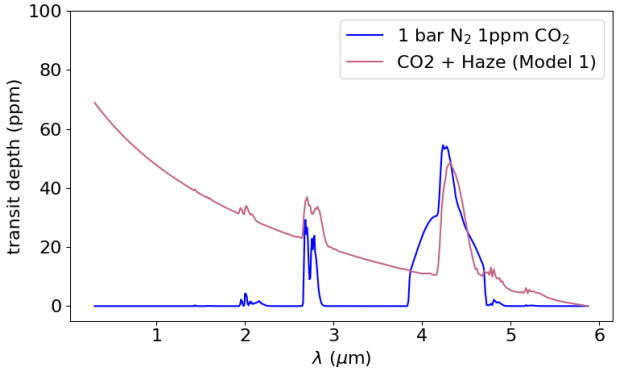

Figure 3.22: Transit spectra computed for scenarios that match all the available emission observations. The transit spectrum has been offset to have a minimum value of 0.

4. TRAPPIST-1 c

Contents

4.1 Introduction . . . 65
4.2 Methods . . . 66
4.2.1 Strategy . . . 66
4.2.2 Models and tools . . . 67
4.2.2.1 1D simulations with `exo_k` . . . 67
4.2.2.2 Generic PCM 3D simulations . . . 67
4.2.2.3 Post-processing . . . 67
4.2.2.4 "3D" bare rock simulations . . . 67
4.2.2.5 Comparison to data . . . 67
4.3 Results . . . 68
4.3.1 Bare rocks . . . 68
4.3.2 Atmospheres . . . 68
4.3.2.1 N_2-CO_2 atmospheres . . . 68
4.3.2.2 N_2-SO_2 atmospheres . . . 69
4.3.2.3 Reduced atmosphere with thermal inversion . . . 70
4.3.2.4 Addition of "neutral" trace gases . . . 71
4.3.2.5 Excluded atmospheres . . . 71
4.4 Discussions . . . 72
4.4.1 Limits of this work . . . 72
4.4.2 Comparison to previous studies . . . 72
4.4.3 Perspectives for TRAPPIST-1 c . . . 72
4.4.4 Comparison with TRAPPIST-1 b . . . 73
4.5 Conclusion . . . 73
4.6 Appendix . . . 74
4.6.1 Parameters for the simulations . . . 74
4.6.2 Bare rock albedos . . . 74
4.6.3 3D results . . . 75
4.6.4 Atmosphere with inversion . . . 81
4.6.5 Excluded atmospheres . . . 81

Preamble

TRAPPIST-1 c, like b, is warm enough to be observed in emission with only a few eclipses. It was the object of a Cycle 1 program (GO 2304, Zieba et al. 2023), that revealed an eclipse depth slightly smaller than one could expect from a low albedo bare rock. The phase curve observation (Gillon et al. 2025) was less informative than for the b planet, since the contribution of TRAPPIST-1 c was smaller. On the other hand, a partial eclipse of the planet was detected during the observation of TRAPPIST-1 b at 12.8 micron, suggesting a very high dayside emission at this wavelength. This motivated a JWST program to observe four eclipses of TRAPPIST-1 b and c at 12.8 micron (GO 5191), on which I am a co-investigator. The data reduction, analysis and interpretation are still ongoing with the collaboration. They are performed by six teams in parallel, resulting in six different pipelines and thus six different results. All results are consistent with each other at this stage, but additional verifications are performed, notably concerning the absolute flux of the star, the variability of the eclipses, and crossings between the pipelines. Out of these six pipelines, only two performed a global fit, computing the eclipse depth at 12.8 and 15 μm in the same analysis. I compared my simulations to the results of these two pipelines, and for the following work I chose to use the analysis that was the most consistent with previous results.

The following chapter is a paper in preparation for A&A. It is based on soon-to-be published observations (Gillon et al. 2025), but also on recent observations from GO 5191. The data analysis is almost definitive at this stage and any change in the results should be minor.

Abstract

TRAPPIST-1 c was first observed in secondary eclipse at 15 μm. Then, a phase curve of the system, featuring the contribution of the b and c planet, was observed, excluding full redistribution for TRAPPIST-1 c but leaving room for a low nightside flux. Finally, the planet was observed at another filter, 12.8 μm. This last observation showed a very high eclipse depth, slightly above the one expected from a zero albedo bare rock. We aimed to interpret this rich observational data by determining which bare rock albedos and atmospheres can be ruled out by the observations, and which are still compatible. We simulated observables for TRAPPIST-1 c for simplified bare rocks of various albedos, and atmospheres with 1D and 3D models, and we compared these observables to the data available. Despite the high eclipse depth at 12.8 μm, the bare rock scenario is not ruled out. We find three main compositions of atmosphere that produce an eclipse depth with the accurate features: atmospheres with CO_2, atmospheres with SO_2 and atmospheres of CH_4 and C_2H_6 with a thermal inversion. Atmospheres must be $\sim$0.1 bar and below to produce low enough nightside flux. Addition of a gaz with no strong spectral features at 12.8 or 15 μm is possible. Atmospheres of pure CH_4, H_2O or a transparent gaz like N_2, O_2 or CO are excluded. In summary, the available observations exclude thick atmospheres but leave room for some thinner atmospheres. The feature at 12.8 μm is intriguing, but the precision of the data does not allow to definitely exclude the possibility of a bare rock.

4.1 Introduction

Rocky temperate exoplanets, while very exciting planets for exobiology, are a challenge to observe and characterize due to their small size, and the compactness of their potential high-molecular-weight secondary atmospheres. So far, there is no conclusive detection of an atmosphere on any such planet.

The TRAPPIST-1 system (Gillon et al. 2016, 2017) represents an exceptional opportunity for rocky exoplanets characterization: seven rocky planets transiting a very cool M-dwarf, all temperate and several in the habitable zone. Thanks to the frequent transits of the planets and the compactness of the system, the orbital and planetary parameters are very well constrained (Ducrot et al. 2020; Agol et al. 2021). The system has been therefore the subject of numerous studies, notably assessing the probability of the presence of atmospheres (Turbet et al. 2020b) and predicting their detectability with JWST (Lustig-Yaeger et al. 2019; Fauchez et al. 2019). Like all M-dwarf systems, the high XUV flux and long pre-main sequence phase of the

host star are expected to trigger efficient atmospheric escape (Bolmont et al. 2017b; Bourrier et al. 2017), but the possibility of a remaining partial primary atmosphere or a later-formed secondary atmosphere depends on unknown volatile inventories and evolution pathway of the planet. Moreover, Krissansen-Totton et al. (2024) showed that less irradiated planets are more likely to form substantial secondary atmospheres, and thus that a lack of atmosphere on the warmest planets would not indicate that the outer ones are airless. Soon after the start of JWST observations, all TRAPPIST-1 planets have been observed in transit spectroscopy (GTO 1201, GTO 1331, GO 1981, GO 2420, GO 2589, GO 6456), with the hope of characterizing the most promising system among rocky, temperate exoplanets. Unfortunately, the inhomogeneities at the surface of the star prevent atmospheric detection, because of unocculted spots mimicking planetary atmospheric features (Rackham et al. 2018; Lim et al. 2023; Radica et al. 2025; Rathcke et al. 2025b). To limit this stellar contamination, one can observe in emission through the secondary eclipse, allowing to probe the brightness temperature of the dayside of the planet. In the TRAPPIST-1 system, TRAPPIST-1 b and c are warm enough to produce a mid-infrared signal detectable with only a few eclipse observations. Four JWST programs have investigated this technique, in the 15 μm and 12.8 μm filters for both planets (GTO 1177, GO 2304, GTO 1279 and GO 5191, Greene et al. 2023; Zieba et al. 2023; Ducrot et al. 2024). Last but not least, a phase curve of the system, centered on a double eclipse, have been observed at 15 μm (Gillon et al. 2025, GO 3077), allowing to probe the horizontal redistribution of heat on these planets. Concerning TRAPPIST-1 b, the comparison of atmospheric models with the eclipse at 15 μm (Ih et al. 2023), then 12.8 μm (Ducrot et al. 2024) and finally the phase curve (Maurel et al. 2025) favored an airless scenario, while noticing the possibility of finely tuned high altitude hazes mimicking an airless planet. As for TRAPPIST-1 c, the 15 μm observation resulted in an eclipse deep enough to rule out a thick, CO_2 atmosphere, but also too shallow for a null albedo bare rock (Zieba et al. 2023). The remaining scenarios were CO_2-poor/thin atmospheres, bare rocks with a moderate albedo, and steam atmospheres (Turbet et al. 2023; Lincowski et al. 2023). The extracted phase curve for TRAPPIST-1 c (Gillon et al. 2025) is less constraining than for the b planet, as its contribution is less important. A flat phase curve indicating fully efficient heat redistribution is excluded but the nightside flux ($F_{\mathrm{c,Night,max}} = 62^{+60}_{-43}$ ppm) leaves room for low to moderate heat redistribution. Finally, the 12.8 μm observation is surprisingly higher than the 15 μm observation, contrary to the prediction for a bare rock

In this work, we propose an interpretation of the emission observations of TRAPPIST-1 c (eclipses and phase curve) with a combined approach of numerous 1-D radiative-convective simulations and a few 3-D numerical climate simulations.

4.2 Methods

4.2.1 Strategy

We adopt an observationally-driven approach. We start from the observational constraints available in emission with the MIRI instrument on JWST: two eclipse depth measurements, at 12.8 and 15 μm, and one phase curve extracted from the 15 μm combined phase curve of TRAPPIST-1 b and c. From these observations, we first assess the possibility of a bare rock hypothesis, at different albedos. This also allows us to choose which ground albedo to use in our atmospheric simulations. We then identify families of atmospheres that can match the observational features: a deep eclipse at 12.8 microns, a shallower eclipse at 15 microns, and a phase curve that presents no strong sign of heat redistribution. For each family of atmospheres, we explore in 1D a wide range of surface pressures and compositions. Then, from each 1D exploration, we identify an atmospheric scenario that is expected to match the data, and run a GCM simulation with the same parameters to evaluate the 3D distribution of temperature, notably (i) reliably simulate the observables that would produce such an atmosphere - especially the phase curves, that cannot be accurately predicted from a 1D model - and (ii) test for atmospheric collapse. Because of their high computational cost, we only ran a few 3D simulations, and focused on atmospheres that were good candidates to match the observations.

4.2.2 Models and tools

4.2.2.1 1D simulations with `exo_k`

For the fast, 1D simulations, we used the forward 1D radiative-convective model from the python library `exo_k` (Leconte 2021). We take the parameters from Agol et al. (2021), assuming a circular orbit. The radiative transfer calculations are based on correlated-k tables (Fu & Liou 1992), computed with `exo_k` from single gas opacities from `Exomol` (see Appendix 4.6.1, Table 4.5). We compute tables between 0.3 and 50 microns, with a resolution R=10.
We supposed no 3D redistribution in our 1D simulations, i.e. $ISR = \frac{2}{3}\sigma T_s^4(\frac{R_s}{a})^2$, with ISR the incoming stellar radiation, a the semi-major axis, R_s and T_s the stellar radius and effective temperature and σ the Stefan-Boltzmann constant.

4.2.2.2 Generic PCM 3D simulations

We use the `Generic Planetary Climate Model (Generic PCM)` (Wordsworth et al. 2011; Charnay et al. 2015a; Bolmont et al. 2016; Turbet 2018; Charnay et al. 2021; Turbet et al. 2023; Teinturier et al. 2024; Maurel et al. 2025) for the 3D simulations of TRAPPIST-1 c.
We use the same stellar, planetary and orbital parameters as for the 1D simulation, with no obliquity and a tidally locked planet. We adopt a resolution of 72 (longitude) × 46 (latitude) × 40 (pressure layers), with 4600 dynamical steps per day (∼45s). All simulation parameters are in Appendix, Table 4.4. We also use correlated-k tables from the same single gas opacities, with a resolution of R=10 for both the channel dedicated to the stellar incoming radiation (0.3 to 6.6 μm) and the one dedicated to planet emission wavelengths (1 to 50 μm). References for the gas opacities are summarized in Appendix, Table 4.5.
For more details, see Maurel et al. (2025).

4.2.2.3 Post-processing

To compute observables from our simulations, we used the radiative transfer model from `exo_k` and its 3D extension `Pytmosph3R` (Falco et al. 2022), which can compute transmission, emission and phase curves spectra from `Generic PCM` outputs.
We used the SPHINX model grid (Iyer et al. 2023) for the stellar spectrum, and we integrated the planetary flux in the MIRI observed bands and divided it by the observed stellar flux in order to get the planet-to-star flux ratios (more details in Maurel et al. (2025)).

4.2.2.4 "3D" bare rock simulations

For the bare rocks simulations, we computed the temperature at each surface grid point from the incoming stellar radiation ($\sigma T^4 = (1-A)ISR$). We then computed the planetary emission with `pytmosph3R`, with an extremely thin and transparent atmosphere.
Note that with our derivation, it is the bolometric planetary emission that is proportional to (1-A), contrary to e.g. Ducrot et al. (2024) where the emission at 12.8 and 15 μm is directly proportional, resulting in diverging results for bare rocks. A more detailed description of our assumptions and the ones of Ducrot et al. (2024) is given in Appendix (4.6.2).

4.2.2.5 Comparison to data

To evaluate the match between the observational data and modeled atmospheres, we follow the procedure from Gillon et al. (2025) and Maurel et al. (2025).
We compute the χ^2, then the standard deviation in units of sigma $Z = (1-F_{\mathcal{N}})^{-1}(p/2)$, with the p-value $p = 1-F_{\chi^2}$, F_X the cumulative density function of a random variable, and $\mathcal{N}$ the normal law.
The variables used in the computation of these χ^2 are the eclipse depths at the two observed wavelengths for the eclipse data, and the dayside flux, nightside flux and peak offset for the phase curve data, as the precise shape of the phase curve depends on the analysis pipeline and can not be used for comparison as

it is (Gillon et al. 2025; Maurel et al. 2025). For the phase curve, we chose to use the analysis #3-MG of Gillon et al. (2025), which corresponds to a bare rock, blackbody assumption for TRAPPIST-1 b (consistent with the conclusions of Gillon et al. (2025) and Maurel et al. (2025)), and free parameters for TRAPPIST-1 c.

4.3 Results

4.3.1 Bare rocks

We first tested bare rocks with different albedos (Fig. 4.1) in order to assess how they can match the data, and to select the best surface albedo to put in our atmospheric simulations.
The best fit albedo for the 15 μm point is around A=0.4, indicating a high albedo surface, while the 12.8 μm point is even higher than a blackbody with 0 albedo. However, an intermediate albedo surface like 0.2 or 0.3 matches the eclipse best with a standard deviation of 2.4σ, indicating that the data cannot rule out the bare rock case at 3σ.
Since a null albedo bare rock results in an eclipse depth at 12.8 μm lower than the observed value, and an atmosphere with moderately absorbing gas is expected to lower the emission at 15 μm, we chose to model atmospheres with a surface albedo of 0, anticipating that this would be the best fit for atmospheric models.

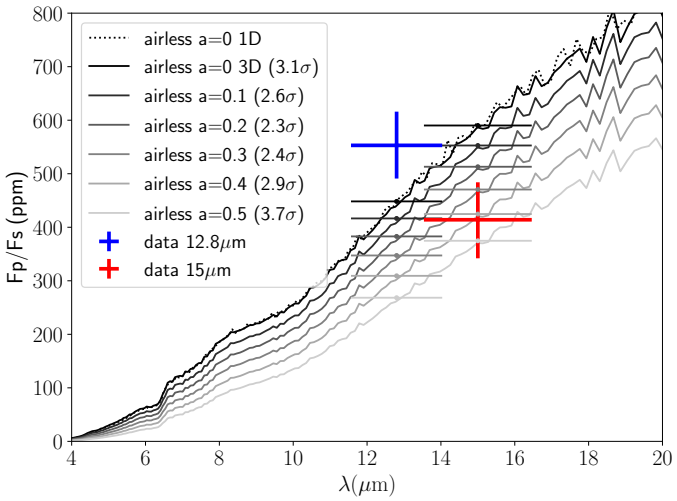

Figure 4.1: Bare rock emission simulations for different albedos. When not stated, the simulation is in "3D" (section 4.2.2.4).

	eclipse	phase curve	joint
A=0	4.6	3.2	3.8
A=0.1	4.4	2.2	3
A=0.2	4.8	1.3	2.7
A=0.3	5.8	0.81	2.8
A=0.4	7.7	0.65	3.5
A=0.5	11	0.96	4.9

Table 4.1: Reduced chi-squared for the bare rocks.

4.3.2 Atmospheres

We look for atmospheres that would produce the observed eclipse feature, i.e. an eclipse deeper at 12.8 μm than at 15 μm. This feature is the opposite of the TRAPPIST-1 b case (Ducrot et al. 2024), and we will thus look for atmospheric scenarios different from Maurel et al. (2025). The shallower eclipse depth at 15 μm can be explained by at least three scenarios: (i) a classical atmosphere (with no thermal inversion) with an absorption band around 15 μm, (ii) a greenhouse-efficient atmosphere with an absorption window at 12.8 μm, and (iii) an atmosphere with a thermal inversion and an absorption band at 12.8 μm. For each scenario we found a composition corresponding, respectively CO_2, SO_2 and CH_4 with C_2H_6 (all with N_2 as a background gas). Fig. 4.2 shows the observables from our 3D simulations of one or several members of each scenario.

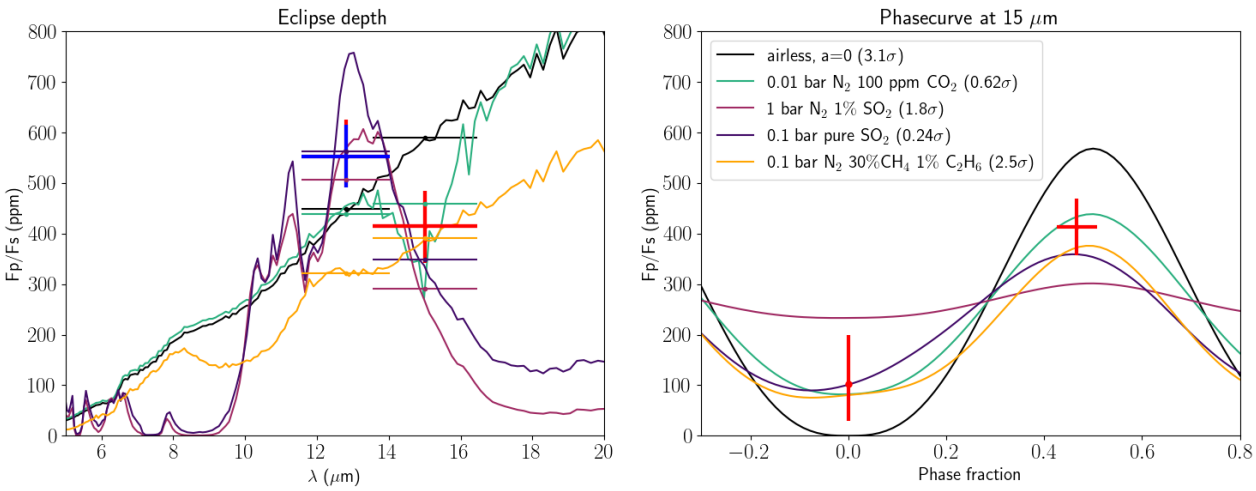

Figure 4.2: Computed observables for different 3D models. Left: dayside emission versus wavelength. The red data points are temporary results. Right: phase curve in the 15 μm MIRI filter. Data points are from analysis #3- MG of Gillon et al. (2025). Corresponding chi-squared are displayed in appendix, Table 4.7. The σ corresponds to the comparison with all available data (two eclipses, and phase curve)

4.3.2.1 N_2-CO_2 atmospheres

We varied total pressure between 1 bar and 0.01 bar and CO_2 volume mixing ratio between 100% and 1 ppm. The corresponding eclispe spectra are displayed in Fig. 4.3.

As expected, the presence of CO_2 lowers the eclipse depth at 15 μm, compared to the zero albedo bare rock. Except for large quantities of CO_2[1], the greenhouse effect of the atmospheres is not sufficient to increase the continuum part of the spectrum by more than a few percents compared to the airless case. For small amounts of CO_2, the 12.8 μm eclipse depth is not affected and the match with observation is thus better than a bare rock, while for larger amounts, the CO_2 absorption band spans on a larger part of the spectrum and the match with observation decreases. The corresponding chi-squared can be found in Table 4.2.

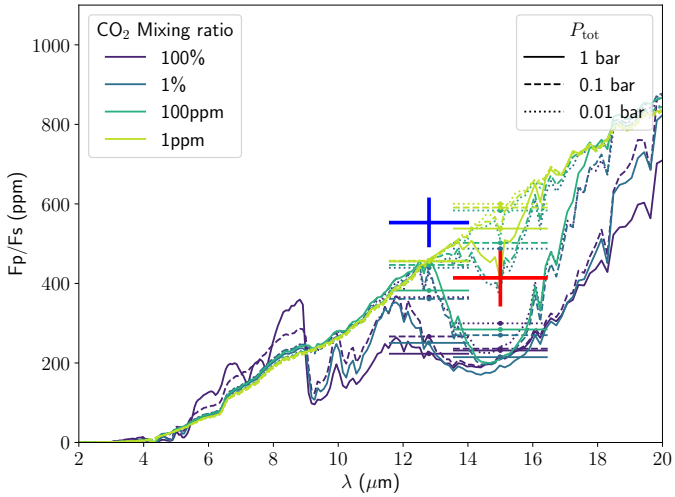

	100%	1%	100ppm	1ppm
1 bar	37	34	12	5.6
0.1 bar	29	15	4.5	8.8
0.01 bar	12	4.5	8.3	9.5

Table 4.2: Reduced chi-squared for the 1D N2-CO2 grid.

Figure 4.3: Eclipse spectra for the different N_2-CO_2 atmospheres of the 1D grid.

The best matches are 1 bar-1 ppm, 0.1 bar-100 ppm and 0.01 bar-1%. We chose to test in 3D the 0.1

[1]In these cases, the increase of flux around 8.5 μm corresponds to a deep window of absorption of the CO_2

bar-100 ppm case, as we expected the 0.01 bar case to collapse and the 1 bar case to provide a phase curve too flat for the data.
The 3D simulation produces observables compatible with the observations (Fig. 4.2). The temperature map and vertical profile are displayed in Appendix 4.6.3.

4.3.2.2 N_2-SO_2 atmospheres

We computed N_2-SO_2 atmospheres with the same surface pressure and composition grid as for CO_2. SO_2 absorbs more than CO_2, and rather than an absorption band at 15 μm, it presents a window around 12.8 μm. Therefore, the eclipse depths look very different: we observe a large increase of flux around 12.8 μm (above the airless expected emission) corresponding to the temperature near the surface, experiencing a strong greenhouse effect, while the rest of the emission spectrum is below a null albedo bare rock emission level (Fig. 4.4).

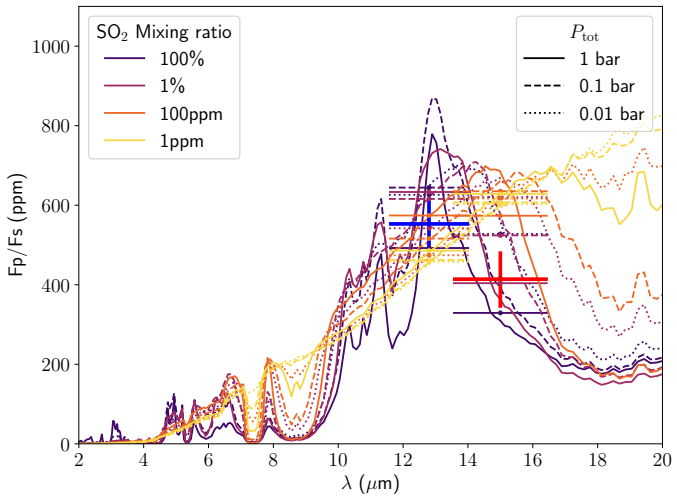

Figure 4.4: Eclipse spectra for the different N_2-SO_2 atmospheres of the 1D grid.

	100%	1%	100ppm	1ppm
1 bar	2.8	1.3	5.3	11
0.1 bar	1.6	3.2	10	9.7
0.01 bar	3.7	8.7	10	9.6

Table 4.3: Reduced chi-squared for the 1D N2-SO2 grid.

The computed chi squared (Table 4.3) show a better agreement for the atmospheres with the most SO_2. We simulated the 1 bar, 100% and 1% SO_2 cases, but they both led to a flat phase curve (Fig. 4.2), and we simulated the 0.1 bar, pure SO_2 atmosphere, that gives a quite good agreement with the observations, but part of its nightside surface temperature is below the condensation temperature of SO_2 (see Appendix 4.6.3), suggesting that this atmosphere would collapse (Maurel et al. 2025).

4.3.2.3 Reduced atmosphere with thermal inversion

The third family of atmosphere corresponds to atmospheres with a thermal inversion. The thermal inversion is created by an absorbing species in the wavelength emission range of the star. In the case of TRAPPIST-1, which is very cool and emits a significant part of its light in the near-infrared, the presence of a large quantity of CH_4 can create an inversion. The atmosphere absorbing part of the stellar light, it gets warmer in higher layers. In this case, probing higher in the atmosphere means probing a hotter part of the atmosphere, and therefore the species that absorb in the observed wavelength are seen in emission (Fig. 4.5). This case was studied in details in Maurel et al. (2025). Here, a thermal inversion with species with a strong absorption band around 12.8 μm could explain the high eclipse depth at this wavelength. C_2H_6 does possess such a feature (Fig. 4.5). We thus tested an atmosphere with CH_4 and C_2H_6. In 1D, the best result was for a 1 bar atmosphere of N_2 with 30% of CH_4 and 0.1% of C_2H_6 (Fig. 4.5). However, since, in this case, the 15 μm observations probe deep in the atmosphere, where redistribution is efficient, we decided to test an atmosphere of 0.1 bar as we expected thicker atmosphere to be inconsistent with the phase curve observation.

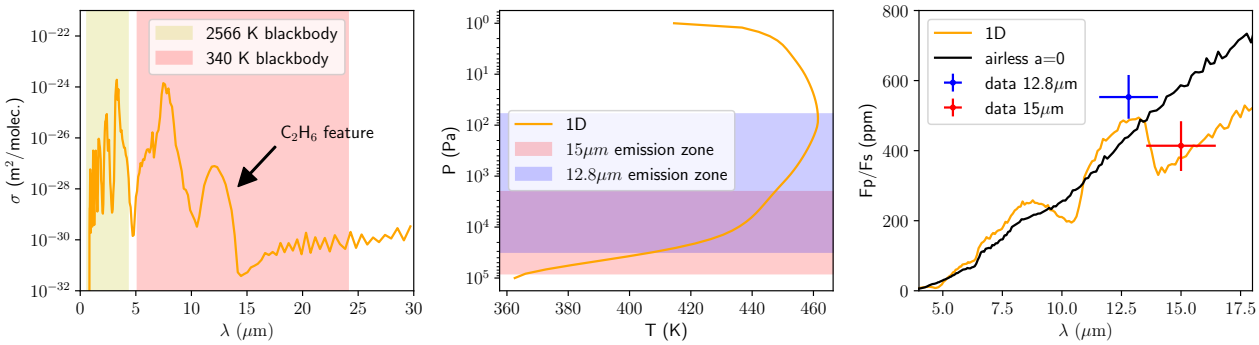

Figure 4.5: 1D simulation of an atmosphere with thermal inversion (0.1 bar, 30% CH_4, 0.1%C_2H_6). Left: Opacity of the atmosphere, with the region of stellar emission and planetary emission. Center: thermal profile, with the layers of emission of the atmosphere at 15 μm and 12.8 μm. Right: eclipse depth.

We thus modeled in 3D a 0.1 bar atmosphere of N_2 with 30% of CH_4 and 0.1% of C_2H_6, which was a good fit to the data in 1D . Results are in Fig. 4.10. This composition of atmosphere produces indeed an inversion, and a phase curve compatible with the data, but the emission spectrum does feature a strong difference between 12.8 and 15 μm. This is mainly due to the low surface pressure, that does not allow to probe deep in the colder parts of the atmosphere, contrary to the 1D 1 bar case (Fig. 4.5). A comparison between the 0.1 and 1 bar case in 1D is provided in Appendix 4.6.4.

4.3.2.4 Addition of "neutral" trace gases

Since we do not expect atmospheres to be composed of only one or two gases of our convenience, we explored in 1D the impact of additional gases in our results. Fig. 4.6 shows the impact on adding H_2O to a 0.1 bar atmosphere of various mixing ratios of CO_2. We chose the quantities of H_2O to match Lincowski et al. (2023). Results in the observables are different from them because we use a fixed redistribution factor.

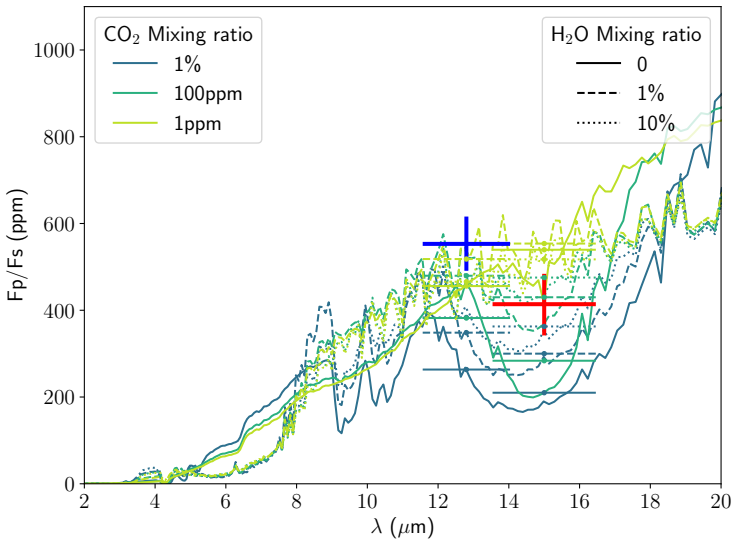

Figure 4.6: Impact of the addition of H_2O on the eclipse depth for different N_2-CO_2 atmosphere, from 1D simulations.

Since H_2O does not have specific absorption bands around 12.8-15 μm, its impact is to globally increase the eclipse depths due to greenhouse effect. However, it is also expected to decrease the dayside emission by its warming in the nightside, an effect that is not taken into account in our 1D simulations.

Besides, modifying the Bond albedo would allow for adjusting the overall level of the eclipse depth, and thus we consider that trace gases that do not have specific absorption features at 12.8-15 μm do not alter significantly our results.

4.3.2.5 Excluded atmospheres

Finally, we investigated in 1D other compositions of atmospheres that could be expected from evolution models (Krissansen-Totton & Fortney 2022), to see if they can be excluded from the comparison with the observations. We tested 0.1bar atmospheres made of pure species: CH_4, H_2O, CO and NH_3. The simulations are detailed in Appendix 4.6.5. In summary, a pure atmosphere of CH_4 is already ruled out from its eclipse signature, while for the other molecules tested, the eclipse depth is quite similar to a bare rock, thus neither ruled out, nor favored over a bare rock. However, for steam atmospheres and transparent atmospheres, the emission comes from close to the surface, where the heat redistribution is efficient, and these atmospheres are *a priori* expected to give a flat phase curve, incompatible with the observed one.

4.4 Discussions

4.4.1 Limits of this work

Exploration of the parameters The atmospheric models we use (1D and 3D) take some incompressible time to converge. Hence, we could not explore an infinite range of possibilities. While we chose carefully the ground albedo from a preliminary study of bare rock studies, we did not explore directly its impact in the atmosphere. A partial study of the impact of the ground albedo in 1D is performed in Maurel et al. (2025). Besides, like in Maurel et al. (2025), we fixed the internal heat flux to 0, but a sufficient heat flux could prevent atmospheric collapse of SO_2.
Finally, we explored a limited range of atmospheres. We studied each molecule (CO_2, SO_2, etc.) separately, since combining them would multiply the number of simulations to perform. However, we studied the addition of a trace gaz in section 4.3.2.4. We note that given the precision of the data, a subtle fit with numerous gaz species in very small quantities seems inappropriate.

Separate treatment of TRAPPIST-1 b and c This detailed study of TRAPPIST-1 c follows the one of TRAPPIST-1 b (Maurel et al. 2025). Yet, the phase curve includes the contribution of both planets, and these compositions were separated in the data analysis, potentially inducing new sources of error. A joint study could avoid this caveat.

Model intercomparison Finally, we only used one 3D GCM and one tool for the production of observables. A comparison with other models could benefit this study and will be performed in future work, notably within the CUISINES collaboration (Sohl et al. 2024).

4.4.2 Comparison to previous studies

This work extends the one of Lincowski et al. (2023), with new observables (phase curve at 15 μm and eclipses at 12.8 μm), different modeling tools, and more types of atmospheres. Lincowski et al. (2023) already ruled out Venus-like atmospheres with the 15 μm photometric point. They also explored steam and N_2-CO_2 atmospheres, globally compatibles with the 15 μm eclipse depth. In this work, we show that some N_2-CO_2 atmospheres are compatible with the data, but we rule out steam atmospheres of a few bars, as it produces a phase curve too flat.

4.4.3 Perspectives for TRAPPIST-1 c

The four eclipses of TRAPPIST-1 c at 12.8 μm confirmed a higher dayside flux at 12.8 μm than 15 μm, which is a hint for the presence of an atmosphere. We highlighted several types of atmospheres that would explain such an observation, but unfortunately the precision is currently not sufficient to exclude a bare

rock at 3σ. More observations of eclipses at 12.8 and 15 μm could help definitely rule out this case. Assuming that the value of the points remains unchanged, additional observations of only 2 eclipses at each band[2] at 12.8 and 15 μm would reduce the error bars enough to rule out the airless scenario at 3σ.

4.4.4 Comparison with TRAPPIST-1 b

Eclipse observations of TRAPPIST-1 b show the inverse feature of TRAPPIST-1 c, i.e. an eclipse depth at 12.8 μm lower than the one expected from a blackbody corresponding to the 15 μm measurement. If we compute the flux ratio between 15 and 12.8 μm:

$$X = \frac{(F_p/F_*)_{15}}{(F_p/F_*)_{12.8}} \tag{4.1}$$

we get $X_b = 1.71 \pm 0.17$ and $X_c = 0.74 \pm 0.15$: the two quantities differ by more that 5σ. This discrepancy could be investigated further to compare the two planets together and interpret how informative this difference can be. Besides, the new eclipses of TRAPPIST-1 c were observed jointly with TRAPPIST-1 b eclipses during the GO 5191, allowing to compare directly the two measurements.

4.5 Conclusion

We conducted a series of 1D and 3D simulations to interpret the multiple observational data available : two photometric points at 12.8 and 15 μm, and a phase curve at 15 μm. The most striking feature of the observational data is a high eclipse depth at 12.8 μm compared to the one at 15 μm. We first compared bare rocks simulations with various albedos. We then studied three types of atmosphere that produce a higher eclipse depth at 12.8 μm: atmospheres with CO_2, atmospheres with SO_2 that induce a strong greenhouse effect, and atmospheres with a thermal inversion and a molecule seen in emission. For CO_2 atmospheres, we showed that a 0.1 bar N_2 atmosphere with 100ppm CO_2 produces observables very close to the observations. For SO_2, the atmospheres we simulated in 3D either produced a nightside flux too high for the observations, or ended up with a surface temperature low enough for SO_2 to condense. However, we find it likely that a sweet spot can be found to have a stable, SO_2-rich atmosphere compatible with the data. The atmosphere with a thermal inversion did not produce a strong feature at 12.8 μm. We also tested in 1D that the impact of the addition of a gas with no feature at 12.8 or 15 μm did not alter our results significantly. Finally, we explored other compositions of atmosphere, and excluded a pure atmosphere of 0.1 bar and more of CH_4 because of its spectral features, and of CO and H_2O because of the heat redistribution it would trigger.
In summary, we highlighted several types of atmospheres very compatible with the data, and excluded other types. But we also showed that an airless scenario cannot be excluded with the current precision of the data, suggesting that further observations at the same wavelengths could help bring a more definitive conclusion on the characterization of this planet. Such observations are further motivated by the fact that the current data available suggest a difference with TRAPPIST-1 b: precise observational data would thus allow to compare the two planets together.

[2]This number is strongly depending on the data analysis, and may be subject to change. It goes up to 10 eclipses with the other analysis available.

4.6 Appendix

4.6.1 Parameters for the simulations

Here we give the different parameters used in the simulations. Table 4.4 provides a summary of the parameters used for GCM simulations of TRAPPIST-1 c performed in this study. Table 4.5 gathers the opacity cross-sections and continuum look-up tables used for the various molecules in the atmospheric simulations (1D and 3D).

Table 4.4: GCM parameters

Physical parameters	Values
Mass ($M_\oplus$)	1.308
Radius ($R_\oplus$)	1.097
Insolation ($S_\oplus$)	2.214
Rotation mode	synchronous
Rotation rate (rad s^{-1})	3.00260×10^{-5}
Obliquity (°)	0
Orbital eccentricity	0
Bare ground albedo	0
Ground thermal inertia (J m^{-2} $s^{-1/2}$ K^{-1})	250
Surface Topography	flat
Surface roughness coefficient (m)	0.01
Internal Heat Flux (W m^{-2})	0
Stellar effective temperature (K)	2566
Stellar spectrum	2600 K BT-Settl with Fe/H = 0

Table 4.5: Opacity data

Composition	References
k-correlated tables	
N_2	*Transparent gas*
CO_2	Exomol (Chubb, Katy L. et al. 2021; Yurchenko et al. 2020)
SO_2	Exomol (Underwood et al. 2016)
CH_4	Exomol (Hill et al. 2013)
C_2H_6	Lupu et al. (2022)
CIA	
CO_2-CO_2	Gruszka & Borysow (1997); Tran et al. (2024)
N_2-N_2	Karman et al. (2019)
CH_4-CH_4	Karman et al. (2019)
CH_4-N_2	Karman et al. (2019)

4.6.2 Bare rock albedos

In general, the spectral albedo of a body, $A(\lambda)$, is linked to its spectral emissivity $\epsilon(\lambda)$ by

$$A(\lambda) + \varepsilon(\lambda) = 1 \tag{4.2}$$

On another hand, when computing emission from a bare rock (in 1D or a grid point in 3D), we use

$$\int_\lambda F_{\text{planet}} = \int_\lambda F_{*,\text{received}} \tag{4.3}$$

with $F_{\text{planet}} = \varepsilon(\lambda)\sigma T^4$ and $F_{*,\text{recieved}} = (1-A(\lambda))ISR$.

However, most models use bolometric albedo and emissivity. Directly combining equations 4.2 and 4.3, as in Ducrot et al. (2024), then results in:

$$(1-A)\sigma T^4 = (1-A)ISR \tag{4.4}$$

The derived temperature becomes thus independent of the albedo, and the emission of the planet is proportional to the emissivity (1-A), at every wavelength.
A way to be more realistic is to use the fact that the albedo is important for the reception of the energy of the star, so at the star's wavelengths, while the emissivity is important for the planetary emission wavelengths, in the mid-infrared. Both the Generic PCM and exo_k use this:

- In the Generic PCM, the emissivity is set to 1 ; equation 4.2 is not respected.
- in exo_k, there is an albedo cutoff, fixing it to zero at large wavelengths.

A more precise model is of course necessary to account for the wavelength-dependency of the emissivity, by using reflectance data of rocks, and converting them to an albedo and computing the emissivity with equation 4.2.

Table 4.6 summarizes the hypotheses made by different codes and papers, that explain the differences in the inferred Bond albedo for bare rocks.

Table 4.6: Comparison of the hypotheses for albedo and emissivity

	Albedo		Emissivity	
Model	IR	VIS	IR	VIS
Ducrot+24	A	A	1-A	1-A
`exo_k`	0	A	1	1-A
`Generic PCM`	A	A	1	1
Surface models	A(λ)	A(λ)	1-A(λ)	1-A(λ)

4.6.3 3D results

This section gathers the 3D results of the different GCM simulations performed. Table 4.7 shows the corresponding chi-squared. For each simulation, we provide a figure with the opacity corresponding to the atmospheric composition, the synthetic observables along with the observed data, as well as the temperature profile and map of the atmosphere.

	eclipse	phase curve	joint
airless, A=0	2.1	3.2	2.8
airless, A=0.3	3	0.81	1.7
0.01 bar N_2 100 ppm CO_2	1	0.094	0.46
1 bar N_2 1% SO_2	0.068	1.9	1.2
0.1 bar pure SO_2	0.2	0.39	0.31
0.1 bar N_2 30%CH_4 1% C_2H_6	3.4	0.19	1.5
10 bar H_2O 1 bar N_2	2.1	3.1	2.7

Table 4.7: Reduced chi-squared for every 3D atmospheric simulation performed, and for two cases of bare rocks.

N_2-CO_2 atmosphere (Fig. 4.7) CO_2 features an absorption band around 15 μm (top panel). For a N_2 atmosphere of 0.1 bar with 100 ppm of CO_2, the redistribution and greenhouse effect are limited: the atmosphere emits mostly from the surface and close to the surface (bottom left panel), and the temperature

map is close to one of a bare rock[3]. As a result, the emission of the planet is very close to the one of a bare rock, except in the 15 μm band where it is slightly lower due to the CO_2 absorption band. The simulated observables are thus very close to the observations.

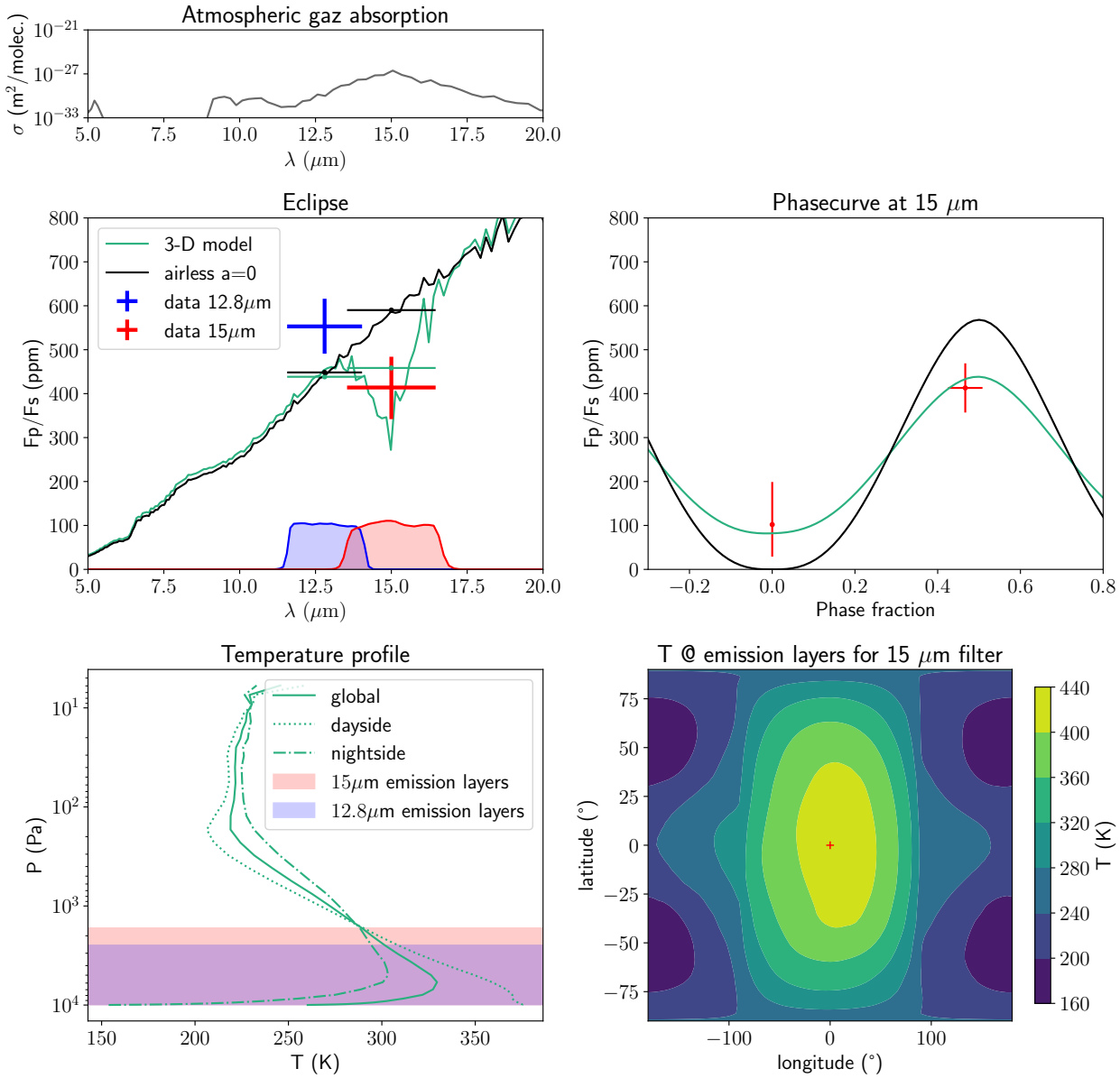

Figure 4.7: Simulation of a 0.1 bar N_2 atmosphere with 100ppm CO_2. Top left panel: opacity of the atmospheric gaz mix. Two upper panels: synthetic observables with observed data - eclipse depth (left) and phase curve at 15 μm (right). Two lower panels: temperature profile, along with layers of emission (left) and temperature map weighted by these layers (right).

Atmospheres with SO_2 (Fig. 4.8 and 4.9) Contrary to CO_2, SO_2 features an absorption window around 12.5 μm rather than an absorption band at 15 μm. In consequence, atmospheres with a significant amount of SO_2 produce an efficient greenhouse effect, and the emission at 12.8 μm is stronger that one of a blackbody - which correspons to the observations. In the case of a 1 bar atmosphere with 1% of SO_2, however, the horizontal heat redistribution is extremely efficient, and the temperature is the similar in the

[3]On the nightside, the surface emits very efficiently its heat towards space. Due to limited vertical mixing in the atmosphere on the nightside, this results in a strong temperature inversion. This effect has already been observed (Wordsworth 2015) in radiatively transparent atmospheres.

dayside and nightside. Thus, the corresponding phase curve is very flat, not comptatible with the data. For the pure SO_2, 0.1 bar case, the phase curve is compatible with the data. However, part of the surface in the nightside is colder than the SO_2 condensation temperature: such an atmosphere would collapse.

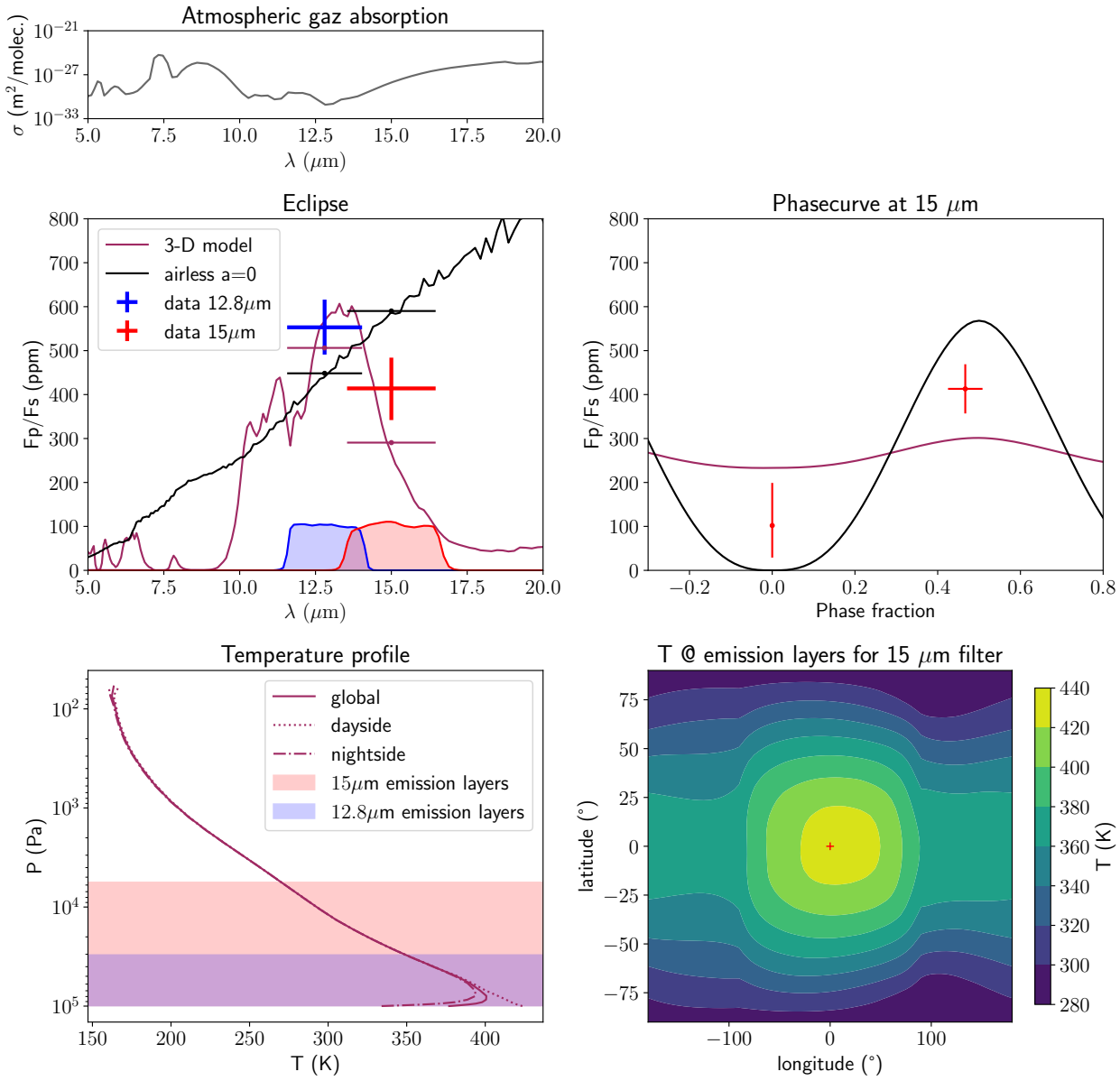

Figure 4.8: Simulation of a 1 bar N_2 atmosphere with 1% SO_2. Panels are the same as Fig. 4.7

Atmosphere with a thermal inversion (Fig. 4.10) For the thermal inversion case, we chose an atmosphere with CH_4 and C_2H_6. CH_4 features strong absorptions in the near infrared, and up to 10μm (top panel), triggering the inversion. C_2H_6 has a strong but delimited absorption band around 12.5 μm, allowing to probe a higher part of the atmosphere in the 12.8 μm filter. In consequence, the atmosphere is colder at the surface (lower left panel). The emission layers at 12.8 μm are indeed higher than the 15 μm layers, but the difference does not create a strong feature in the eclipse spectrum.

Steam atmosphere (Fig. 4.11) Finally, we analyze the steam atmosphere of Turbet et al. (2023). The atmosphere is 11 bar thick, with a very efficient horizontal heat redistribution, and features a flat phase curve. The layers of emission are between 0.1 bar and 0.01 bar; the deeper layers do not play a radiative

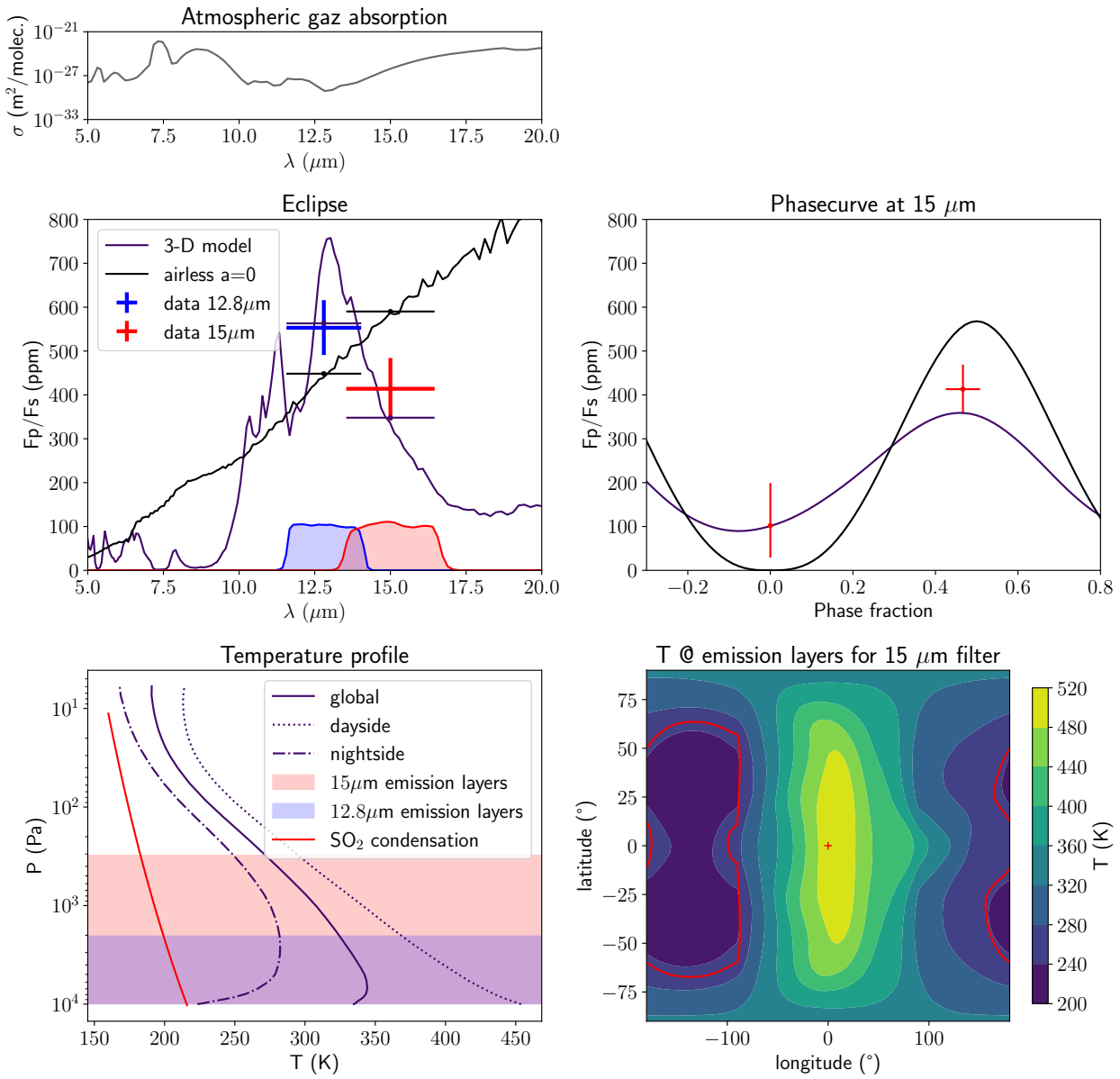

Figure 4.9: Simulation of a 0.1 bar pure SO_2 atmosphere. Panels are the same as Fig. 4.7. The red contours in the temperature map enclose the zone where the surface temperature is colder than the SO_2 condensation temperature.

role, and the thermal day and night profiles are similar up to 0.01 bar. We can thus expect that thinner atmospheres up to ∼0.5 bar would also produce a flat phase curve, and thus exclude these atmospheres.

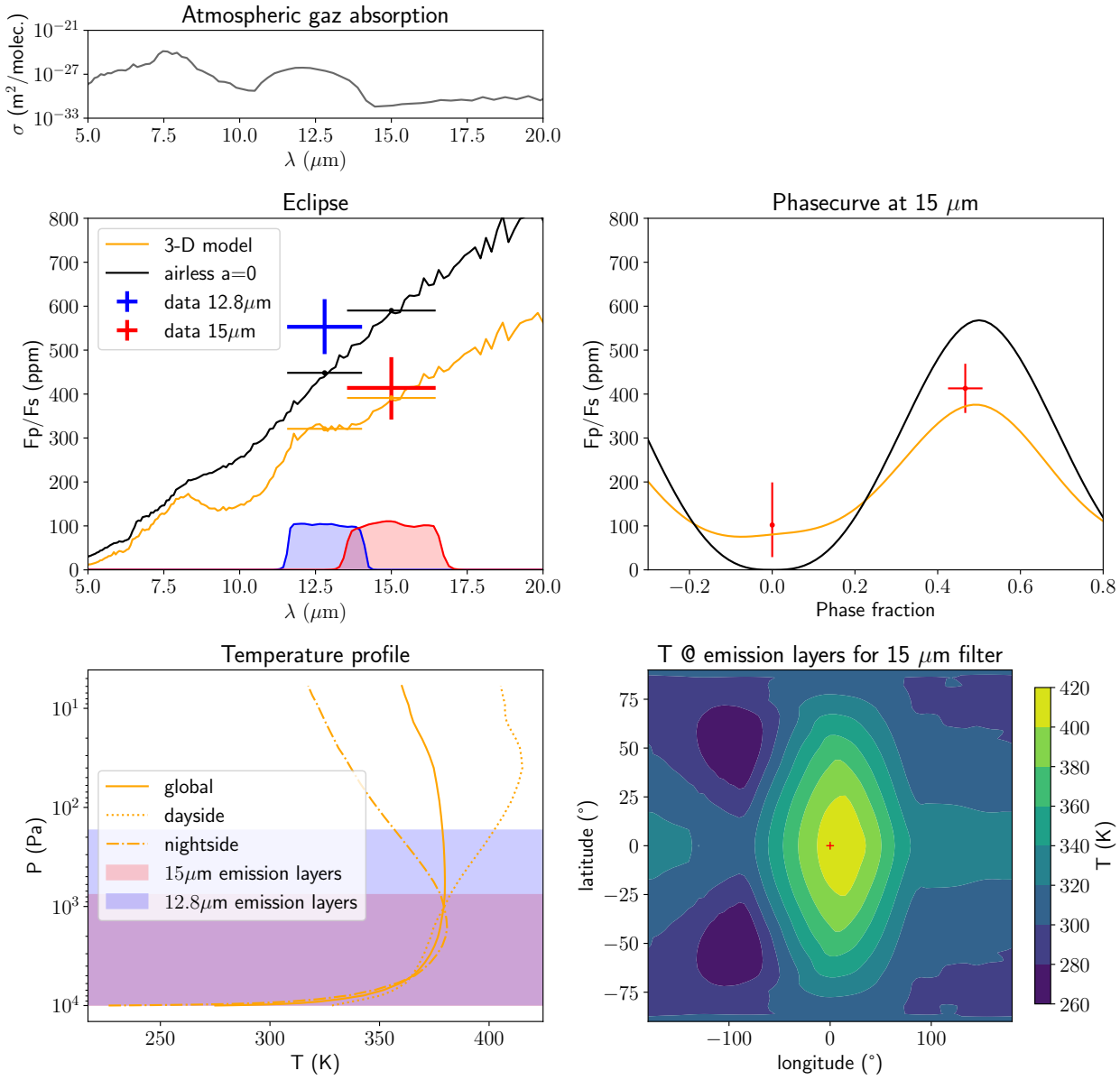

Figure 4.10: Simulation of a 0.1 bar N_2 atmosphere with 30% CH_4 and 0.1% C_2H_6. Panels are the same as Fig. 4.7

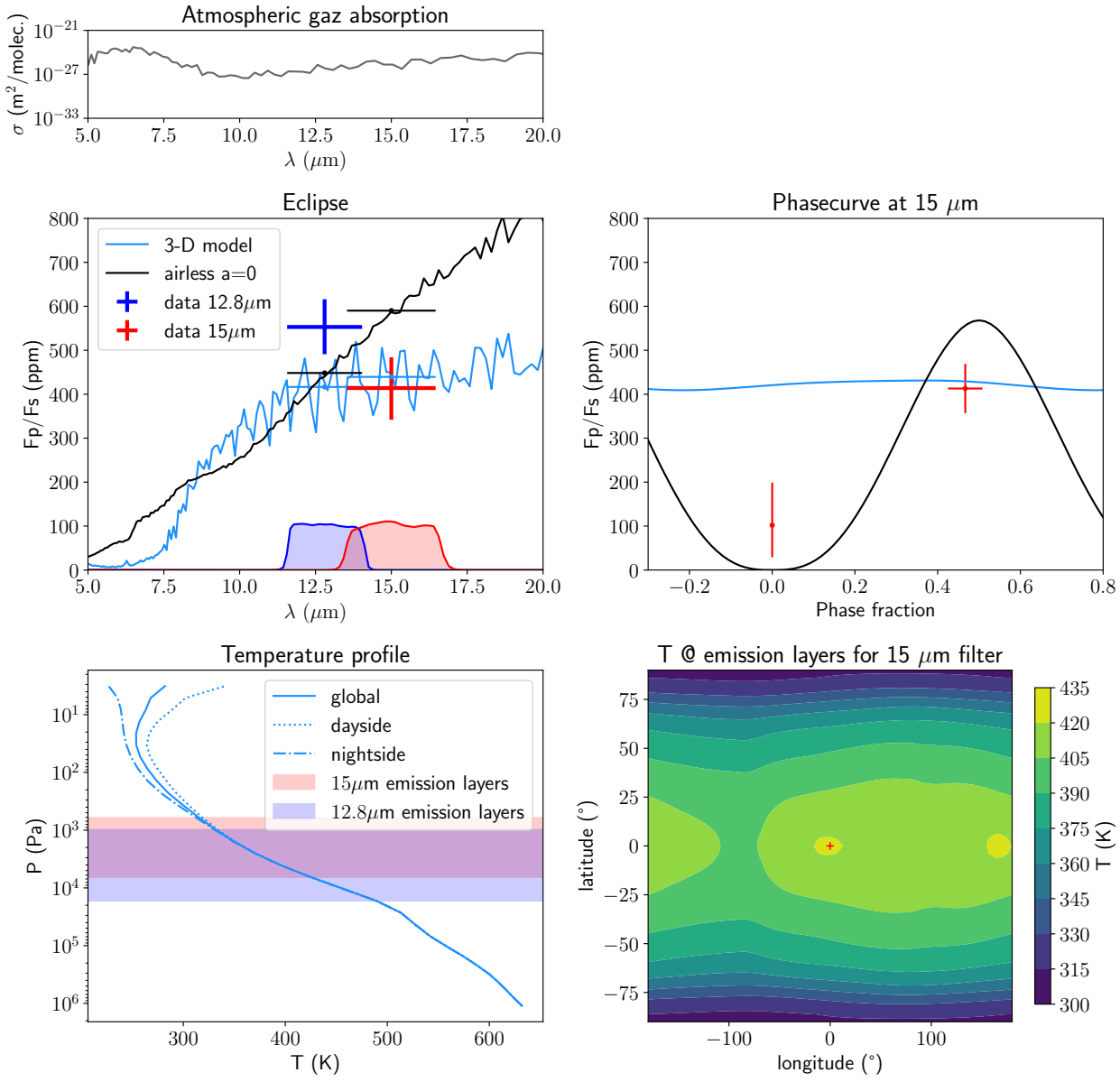

Figure 4.11: Simulation of an atmosphere of 10 bar of H_2O and 1 bar of N_2. Panels are the same as Fig. 4.7

4.6.4 Atmosphere with inversion

Fig. 4.12 shows the difference between a 1 bar and 0.1 bar simulation for the thermal inversion case. In the 1 bar case, the emission layers go deep in the atmosphere, allowing for probing different layers between 12.8 and 15 μm, and thus creating a strong feature in the eclipse spectrum. With a 0.1 bar atmosphere, the feature is fainter, because the atmosphere stops at 0.1 bar and at temperatures higher than 400 K.

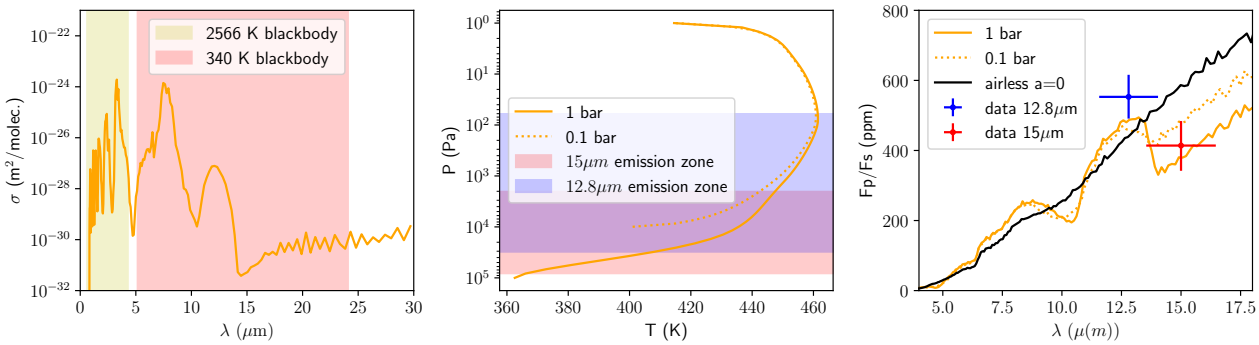

Figure 4.12: Comparison of 1D simulations of an atmosphere with thermal inversion (30% CH_4, 0.1%C_2H_6). Left: Opacity of the atmosphere, with the region of stellar emission and planetary emission. Center: thermal profile, with the layers of emission of the atmosphere at 15 μm and 12.8 μm (for the 1 bar case). Right: eclipse depth.

4.6.5 Excluded atmospheres

We provide here the details about the excluded atmospheres mentioned in section 4.3.

For CH_4 (Fig. 4.13), the molecule absorbs stellar light, triggering atmospheric inversion. 12.8 and 15 μm correspond to a range of low absorption, so the probed region is close to the surface, where temperature is lower. Thus, the corresponding eclipse depth at 12.8 μm is too low to match the data.

NH_3 (Fig. 4.14) is very absorbing in the mean infrared region, triggering a high greenhouse effect. The surface reaches therefore very high temperatures, but the atmosphere emits at upper layers, that are at a temperature close to the bare rock computed one. Thus, its emission is indistinguishable from one of a bare rock.

CO (Fig. 4.15), like N_2 and O_2, is almost completely transparent, and its emission does not differ from a bare rock in 1D.

Finally, we tested a steam atmosphere, in 1D and 3D. The 1D case (Fig. 4.16) shows an observable close to a bare rock. However, in 3D (Fig. 4.11), we can see that a 10 bar atmosphere produces a flat phase curve at 15 μm, because the atmosphere is very well redistributed. Moreover, since the emission layers at 15 μm are between 0.1 and 0.01bar (Fig. 4.11), we can extend the result and say that atmospheres of 0.1 bar and more are probably ruled out by the phase curve data (see section 4.6.3).

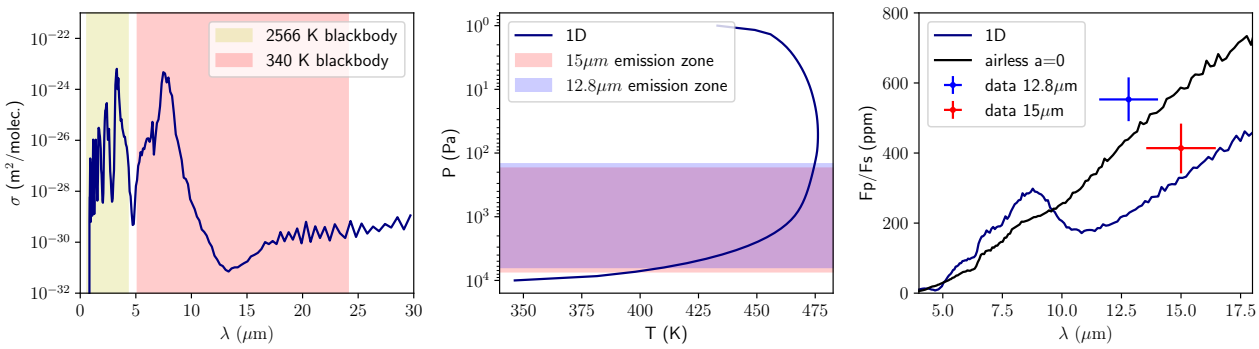

Figure 4.13: Pure CH_4 atmosphere. Labels are the same as Fig. 4.12.

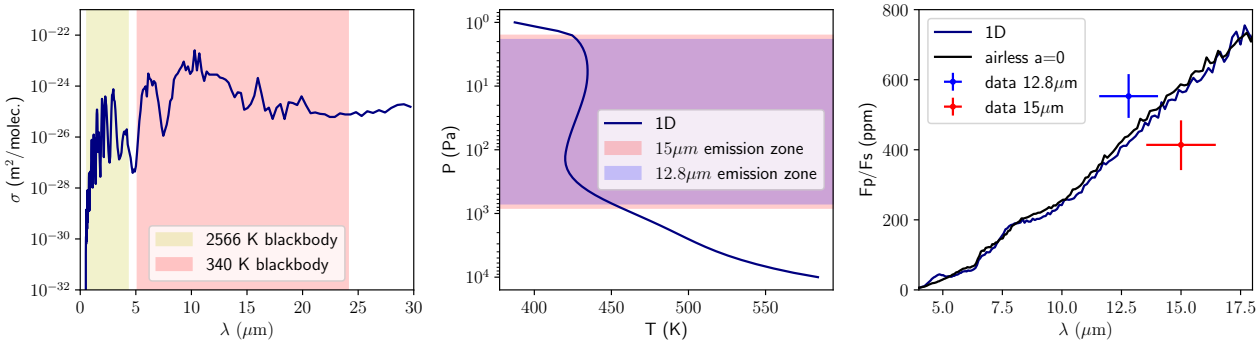

Figure 4.14: Pure NH_3 atmosphere

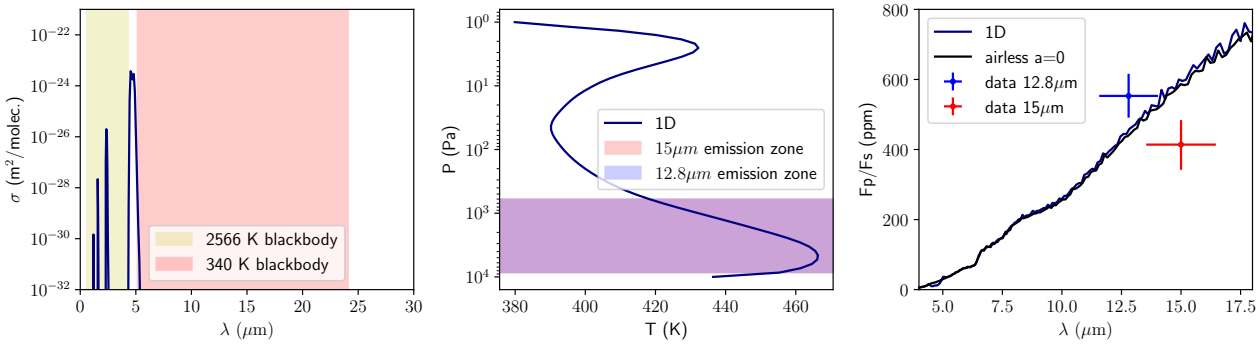

Figure 4.15: Pure CO atmosphere

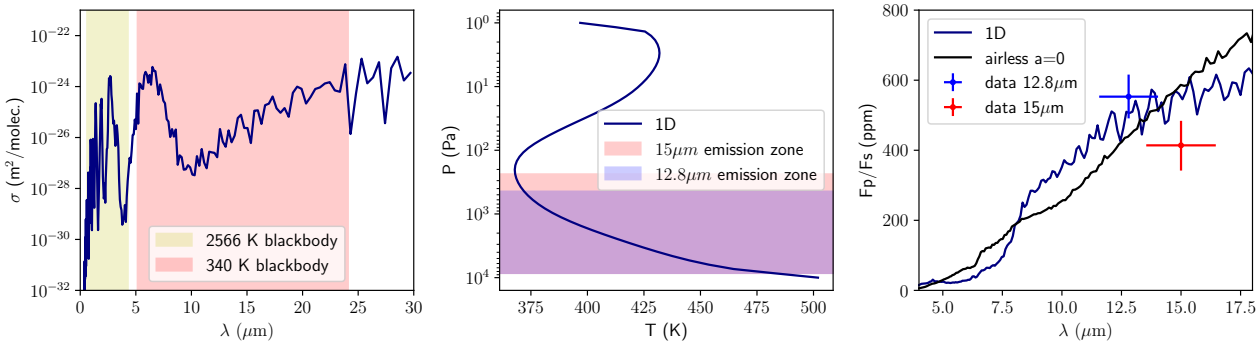

Figure 4.16: Pure H_2O atmosphere

5. TRAPPIST-1 external planets

Contents

5.1 Emission observation of TRAPPIST-1 e . . . 84
5.2 Emission of external planets from available emission data . . . 85
5.2.1 General Idea . . . 85
5.2.2 Methods . . . 86
5.2.2.1 Modeling . . . 86
5.2.2.2 Observational data . . . 86
5.2.3 Results . . . 86
5.2.4 Perspectives . . . 87

Preamble

TRAPPIST-1 b and c are the only planets of the system that have been observed in emission, since their thermal emission dominates the ones of the outer planets (Table 5.1). However, they are also the most likely to have lost their atmosphere through atmospheric escape, and they receive enough insolation to reach the runaway greenhouse limit, meaning that all the water is expected to be in the atmosphere, excluding them from the habitable zone. The external planets are more likely to have an atmosphere (Krissansen-Totton et al. 2024), and TRAPPIST-1 e, f and g could maintain liquid water at their surface with only a moderate amount of CO_2 to heat their atmosphere (Turbet et al. 2018).

Planet	b	c	d	e	f	g	h	d+e+f+g+h
T_{eq} (K)	398	340	283	250	218	197	172	
T_{day} (K)	508	434	362	319	278	252	219	
F_p/F_* @15 μm (ppm)	913	612	195	183	150	122	31	681
F_p/F_* @12.8 μm (ppm)	725	465	139	124	95	73	17	448

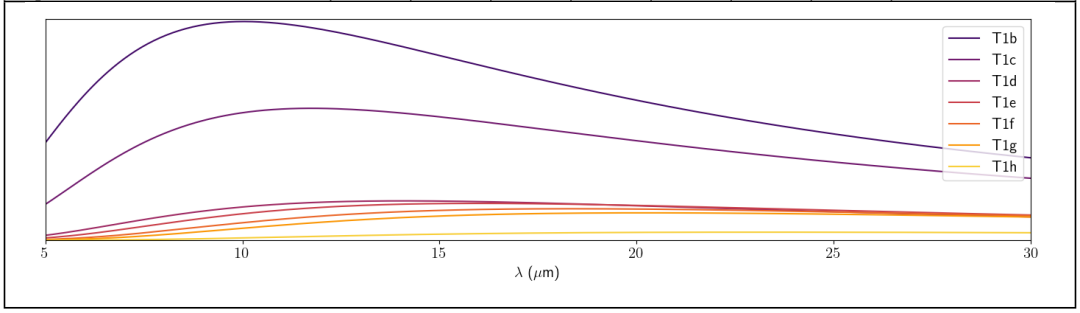

Table 5.1: Comparison of the expected flux for the different planets of the system. T_{day} correspond to the global temperature of the dayside (see Chapter 2, eq. 2.5) for a zero-albedo case, and F_p/F_* correspond to the eclipse depth at different filters. Below we show the relative thermal emissions of the different planets in the system.

Here we present two initiatives to investigate the TRAPPIST-1 outer planets in emission. The first, intuitive idea to access the thermal emission of the external planets is to dedicate enough observational time to try to detect it with multiple secondary eclipse observations. This was the subject of a proposal, presented in section 5.1. Another possibility is to try to detect the combined emission of the outer planets using available eclipse and phase curve data. This work is described in section 5.2.

5.1 Emission observation of TRAPPIST-1 e

This is a summary of a JWST proposal for Cycle 4 in which I was a co-Investigator. The proposal was not accepted, but ranked first quintile.

TRAPPIST-1 e is the best candidate for habitability in its system, as it is in an irradiation zone where a wide range of different atmospheric scenarios can hold surface liquid water. It is also expected to retain an atmosphere under a wide range of volatile initial inventory and degassing/atmospheric loss scenarios. Krissansen-Totton et al. (2024) showed that the cooler temperate exoplanets (habitable zone and beyond) should have a substantial secondary atmosphere, due to the expected rapid crystallisation of their primary magma ocean, that traps part of their initial volatile content under the surface of the planet. It leaves large contents of volatiles protected from the high irradiation of the Pre Main Sequence of the red dwarfs, then available to create a secondary atmosphere through degassing, later in the evolution of the planet. This suggests that the cosmic shoreline could be shifted for the Habitable Zone planets and beyond (Fig. 5.1).

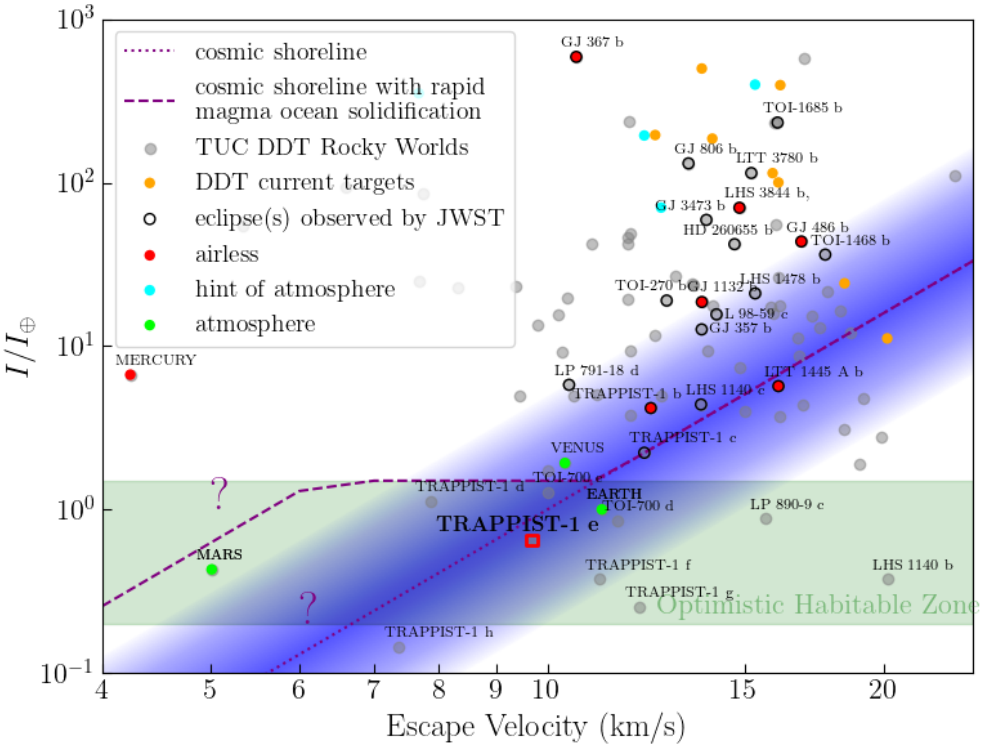

Figure 5.1: Position of Targets Under Consideration (TUC) of the Rocky Worlds DDT relative to the cosmic shoreline (Zahnle & Catling 2017), with the results of published observations. The figure illustrates that HZ planets, which should have a much shorter magma ocean phase, are more resilient to atmospheric erosion (Krissansen-Totton et al. 2024).

Among the rocky exoplanets transiting M-dwarfs, only a dozen are in the Habitable Zone. With the issue of the stellar contamination in transit, and their weak emission, they are at the limit of current observational capabilities. TRAPPIST-1 e is one of them, and it is also the most favorable for observations: TRAPPIST-1 is the smallest star known to host exoplanets and one of the coolest, allowing for a high signal-to-noise ratio

(Fig. 5.2a). The system is also exceptionally well constrained (Chapter 1, 1.2.5) allowing for precise and well-informed observations and timings.
For an airless case, the eclipse depth is expected to be 183 ppm. On the contrary, a CO_2-rich atmosphere, which is expected from atmospheric scenarios, would result in an undetectable eclipse of a few ppm. As the precision reached with one eclipse is 124 ppm, 16 eclipses would reach a precision of 31 ppm. Thus, a detection of the eclipse with 16 observations would rule out the atmospheric cases, while a non-detection would indicate an atmosphere around TRAPPIST-1 e (Fig. 5.2b).

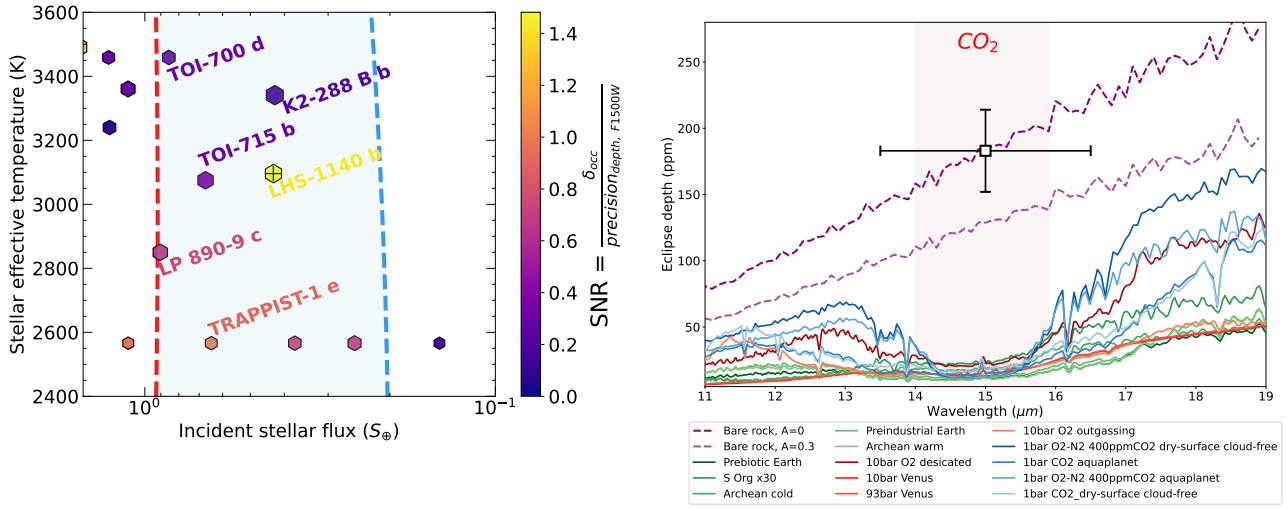

(a) (b)

Figure 5.2: *Right:* Stellar temperature vs irradiation received by all known rocky transiting HZ planets amenable for atmospheric characterization with JWST. The color bar shows the signal-to-noise ratio (SNR) for secondary eclipse observations with MIRI F1500W. Figure from Elsa Ducrot. *Left:* TRAPPIST-1e emission spectrum. Comparison of the measurement derived from 16 eclipses with MIRI F1500W for a null-albedo bare rock scenario (black marker) with plausible atmospheric models for TRAPPIST-1e. All cases with an atmosphere have a quasi-null emission at 15 μm, because they all contain enough CO_2 to absorb all the flux.

5.2 Emission of external planets from available emission data

This is a summary of the work of Louis-Julien Cartigny during his M1 internship that I supervised with Elsa Ducrot from January to June 2025. I was responsible for the modeling part, at the beginning of the internship, while Elsa Ducrot oversaw the observational aspects.

5.2.1 General Idea

So far, only TRAPPIST-1 b and c have been observed in emission, since they are the only ones warm enough to offer an acceptable precision in only $\sim$ 5 eclipses. For example, the next planet of the system, TRAPPIST-1 d, with its irradiation close to Earth's, (Table 1.1), is around twice less irradiated than TRAPPIST-1 c, so we can expect a thermal emission around twice less important. To reach the same level of precision than the TRAPPIST-1 c eclipse observations, one would need around four times more observations, i.e. 16 eclipses. For the observed phase curve of the system, the fainter emission and longer periods of the planets d and beyond make their contribution harder to detect (Table 5.1).
On the other hand, we have a very large amount of emission observations of TRAPPIST-1 b and c: in total, for TRAPPIST-1 b, five visits at 15 μm and nine eclipses at 12.8 μm, and for TRAPPIST-1 c, four visits at 15 μm and at 12.8 μm, plus one sixty-hour long observation of the phase curve of the system. This offers discontinuous but numerous observations of the system at different times.

Although the outer planets are not individually detectable in emission in existing observations, their combined emission may be: it could reach 681 ppm at 15 μm and 448 ppm at 12.8 μm in the zero-albedo bare rock case (Table 5.1). We explored the possibility of analyzing these numerous available emission observations to detect the combined signal from the outer planets and distinguish between two opposite scenarios: five airless planets (no thermal redistribution) or five planets with thick atmospheres (full redistribution).

5.2.2 Methods

Our general strategy was to model a general phase curve of the system with the contribution of every planet, then to place every observation on this phase curve to assess if there are some observations where the contributions of the planets sum up and could be detectable.

5.2.2.1 Modeling

For this project, we use very simple "atmospheric" models[1], since we do not need a fine modeling of the situation but rather an estimation of the timing and amplitude of the contributions of the planets.

Thick atmospheres For the scenario where all outer planets have thick atmospheres, we consider each planet produces a flat phase curve, with a flux corresponding to a blackbody at the equilibrium temperature for a zero-albedo planet $T_{\rm eq} = (1/4)^{1/4}\sqrt{\frac{R_*}{a}}T_*$ (see equation 2.4).

Airless planets We use $T_{\rm day} = (2/3)^{1/4}\sqrt{\frac{R_*}{a}}T_*$ (equation 2.5) for the dayside contribution, i.e. the maximum of the phase curve of each planet. The minimum of the phase curve is zero. The phase curve variations are modeled as a sinusoidal curve.

TTV implementation Gravitational interactions between planets induce transit (and eclipse) timing variations. These TTV are well modeled (Agol et al. 2021) and are taken into account at each observation by correcting the transit closest to the observation with the corresponding predicted TTV from the model from Agol et al. (2021).

5.2.2.2 Observational data

Usually, for emission observations, the flux is normalized during the analysis step, and the quantity of interest is the flux variation (secondary eclipse or full phase curve), in ppm. If we had one visit, we could use relative flux to detect the flux of the outer planets, but in our case the visits are not continuous and the normalization changes. We thus decided to first use the calibrated "stellar" flux, which corresponds to the absolute flux measurement during the eclipse, i.e. without the contribution of the planet in eclipse, to see if we can detect variability in this flux that could be correlated with the dayside flux of the outer planets. We started with only one point per visit, noting that the visits are only ∼5h long when the periods of planets d to h go from 6 to 18 days.

5.2.3 Results

Amplitude of contributions Contributions of the different planets in the case of all bare rocks is displayed in Fig. 5.3. As expected, planets b and c dominate the flux, but the contribution of the outer planets, especially d and e, when in phase, can add up to a flux comparable to TRAPPIST-1 c, typically reachable with JWST - but it would require a lot of time to observe the flux changing.

[1] L.-J Cartigny nevertheless developed a complete, accurate code for modeling light curves of planetary systems. https://github.com/LJ-Cartigny/Exoplanets_Phase_Curves

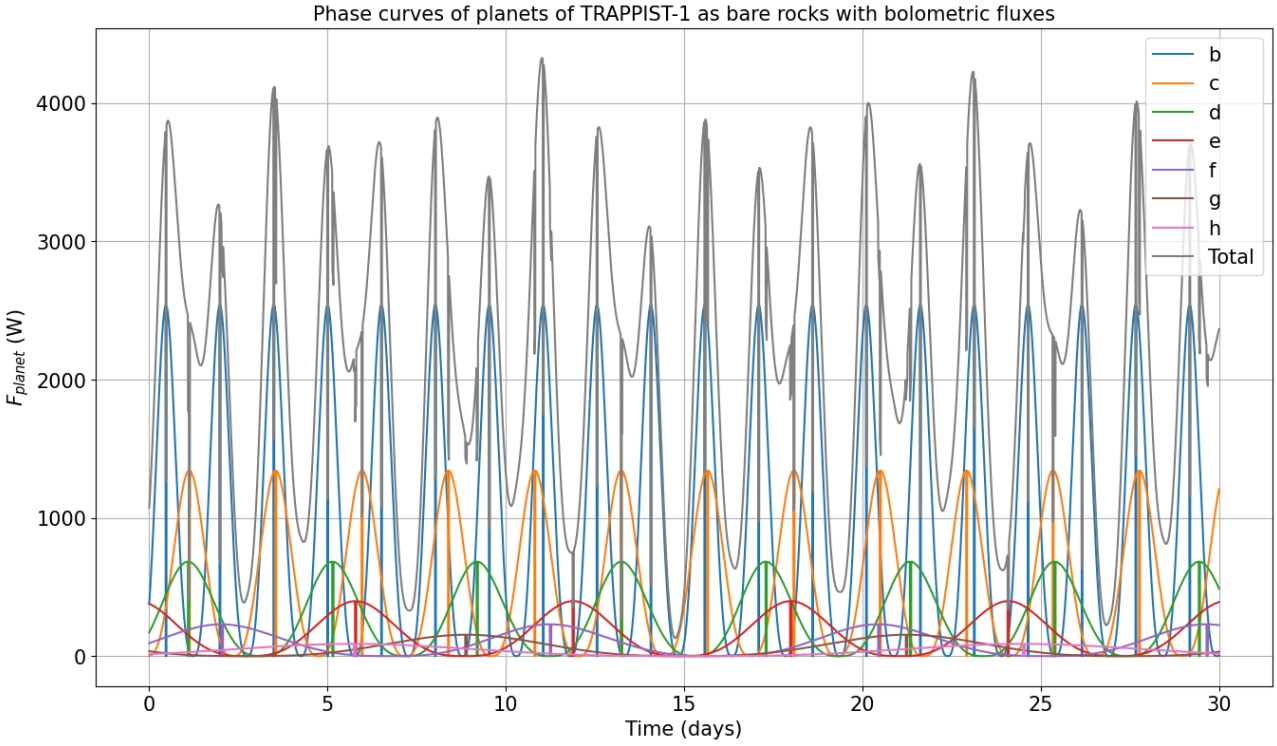

Figure 5.3: Bolometric flux emitted by each planet, and the resulting phase curve. Eclipses are displayed but not transits.

Timing of observations Fig. 5.4 shows the phase curve of the outer planets only (for better clarity), along with all JWST visits. The observations occur at different moments of contributions of the outer planets, allowing *a priori* to detect a difference between the atmospheric scenario, and the bare rock one. Especially, visits 2 and 5 of GO 1177 happen in very different configurations, displaying the largest difference (∼500 ppm) in the bare rock case (for the same wavelength filter).

Error bars Finally, we compared the synthetic phase curve to the observed flux at each visit. Results are displayed Fig. 5.5. One can see that the error bars are way too large compared to the predicted phase curve features. This comes from the fact that the observational data used, the absolute flux, is much less constrained than the usual relative flux of eclipse/phase curve observations.

5.2.4 Perspectives

Using only the measured in-eclipse stellar flux for each visit, one cannot conclude on the presence or absence of atmospheres on the external planets due to the large error bars on the absolute flux measurements. We thought of several follow-ups to this work in order to get around the issue of the error bars.

Global reduction We plan to perform a global reduction of all the available observational data, treating the different visits as one long observation with interruptions, similarly to what is done for ground observations with interruptions during the day. This would come down to work with relative fluxes over the whole period, allowing for more precision. However, we do not know how consistent the JWST observations are from one visit to another, and it may not give coherent results.

Absolute flux The question of the measurement of absolute flux with the MIRI imager is major. Despite the fact that in eclipse measurements, the quantity of interest is the eclipse depth, absolute flux is also of importance for the estimation of the flux emitted by the planet. Calibration of the "stellar" flux is thus a question that is currently discussed in the TRAPPIST-1 collaboration. Gordon et al. (2024) performed a

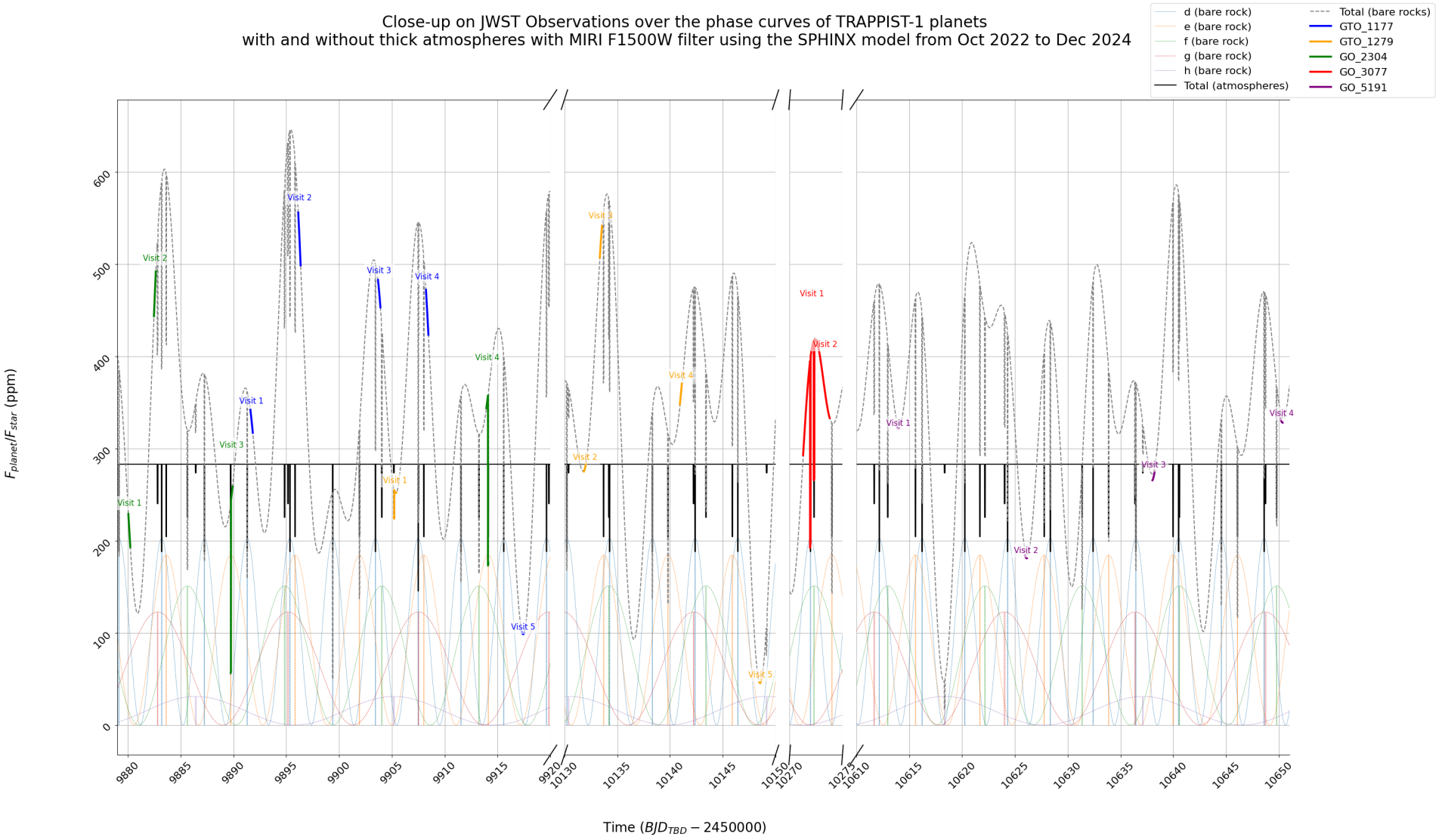

Figure 5.4: Simulation of the phase curves of the outer planets of TRAPPIST-1 in absolute fluxes using the SPHINX model for the F1500W MIRI filter. Transits are not displayed for better readability. The JWST observations are displayed in color over the total curve for the bare rock case. The flux of each outer planet as a bare rock is displayed to show its phase over time.

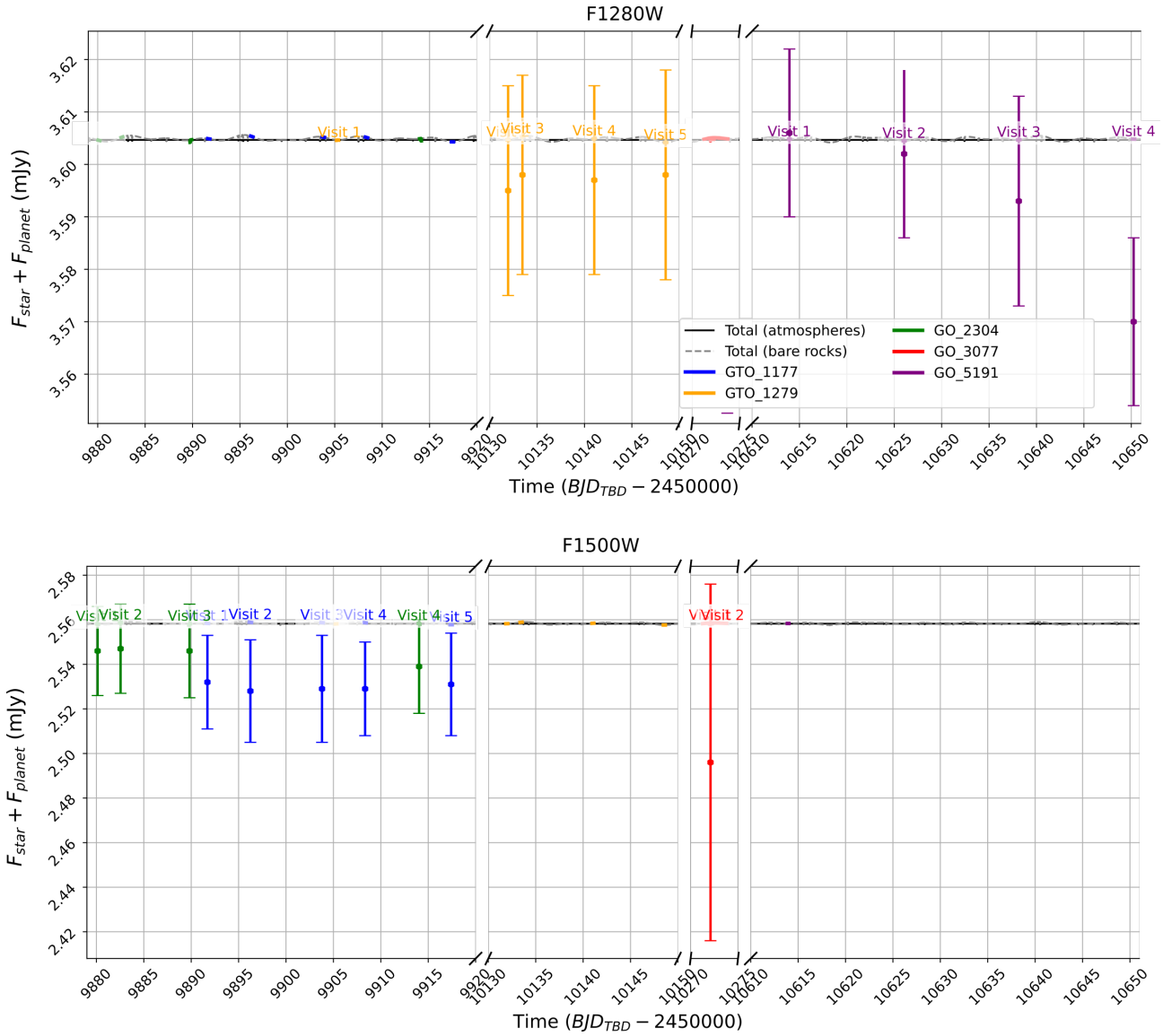

Figure 5.5: Modeled phase curve of the system, along with absolute flux observations from every visit of JWST. Upper panel: 12.8 μm measurements, lower panel: 15 μm. Visit 1 of GTO 1279 is not displayed as the observational strategy from this visit was different from the others and less precise (Ducrot et al. 2024).

thorough study of the absolute flux calibration with MIRI, propose new aperture photometry corrections, and compute a 1% uncertainty for absolute flux measurements. However, Fig. 5.5 shows that measured points of one program are very close to each other, and do not follow the random distribution one may expect from the size of the error bars. It would thus be interesting to work on the modeling of this incertitude, and see if part of it is a systematics error that can be removed when comparing different visits of a program, for example.

New observations Finally, the code developed by L.-J Cartigny, `Exoplanets_Phase_Curves` allows us to identify timings where the slope of the general phase curve is maximum, which would be the best times to observe new data and try to detect an eventual slope.

6. Conclusions

Contents

Planets of the TRAPPIST-1 system 91
What can we learn from emission observations of rocky planets ? 92

During this PhD, I had the opportunity to compare atmospheric models of rocky temperate exoplanets to observational data: it was the first time that the thermal flux of a rocky temperate planet, and even one about as irradiated as Venus (TRAPPIST-1c), was detected (Kreidberg & Stevenson 2025). To this end, I developed a pipeline that mobilizes different existing tools to:

- Model a wide range of atmospheres in 1D and their corresponding observables
- Identify families of atmospheres compatible with the data
- Test some representatives of these atmospheres in 3D
- Evaluate their compatibility with the observational data

This methodology was applied to TRAPPIST-1 b and c, the main topics of my PhD and targets for which we have the most observational data at the moment. This thorough study of two planets allowed me in particular to get insight about the presence of an atmosphere on TRAPPIST-1 b and c, but also to experiment about how informative different types of observations in emission can be. This last question is particularly relevant, as transmission spectroscopy is limited by the TLS effect and thus emission observations are becoming the norm for rocky exoplanets (notably with the Rocky Worlds DDT).

Planets of the TRAPPIST-1 system

TRAPPIST-1 b After the first observation in emission of TRAPPIST-1 b by Greene et al. (2023), showing a deep eclipse at 15 μm, a large part of the community concluded directly that the planet was a bare rock. However, these conclusions were based on a very narrow range of types of atmospheres considered. Thus, and encouraged by the (at the time) upcoming observations of the eclipses at 12.8 μm and the phase curve at 15 μm, we decided to investigate further and model different types of atmospheres expected to produce the measured eclipse depth (Chapter 3). We showed by highlighting four such types of atmosphere (thin residual atmospheres, thick, transparent atmospheres, thick greenhouse-efficient atmospheres and atmospheres with a thermal inversion, Fig. 3.2) that the 15 μm eclipse alone could not be sufficient to rule out an atmosphere, which was later confirmed in an analysis by Hammond et al. (2025). For thin, residual atmospheres, we showed that some atmospheres would collapse due to the presence of cold spots (Fig. 3.4). Finally, the phase curve observation revealed a phase curve with no offset and a very low to no nightside flux, strong clues towards a bare rock case. We highlighted that for phase curves with a

thermal inversion, the part of the atmosphere that is observed corresponds to upper layers, and that since the high atmosphere is less well redistributed, it produces a thermal phase curve showing no sign of heat redistribution, mimicking a bare rock. However, this particular type of atmosphere requires a very dense aerosol layer at high altitude with particular optical properties to produce a strong enough inversion. Such a situation is thus considered too finely tuned and very unlikely compared to the bare rock case. Thus, we consider that TRAPPIST-1 b can be safely considered a bare rock at this point.

TRAPPIST-1 c The second planet is cooler, and less constrained by emission observations since we have observed fewer eclipses. The phase curve discards full heat redistribution, and thus the standard thick atmospheres (i.e., atmospheres with efficient heat redistribution and no thermal inversion) of >0.1 bar, but cannot exclude thinner atmospheres. The two photometric points of the eclipse observations show a higher eclipse depth at 12.8 μm than 15 μm, which cannot be produced by a bare rock, but the precision of the observation does not allow to confidentially reject the bare rock case yet (Chapter 4). Atmospheres with SO_2 or CO_2 - as well as atmospheres with a thermal inversion and C_2H_6 - could reproduce this feature. Other compositions of atmospheres (pure CH_4, H_2O, NH_3, N_2, O_2, CO) do no better than an airless scenario. In short, several types of atmosphere could still explain the data better than a bare rock, but we do not have the adequate precision to claim a detection of an atmosphere.

Outer planets We performed a tentative re-analysis of the emission data to characterize the outer planets by trying to detect a change of their combined emission during different observational windows (Chapter 5). We did not get conclusive results yet, due to the difficulty of reducing the uncertainty on absolute flux data compared to relative flux, but showed that with long enough observations a variabiality of 400ppm could be observed, which is detectable by JWST MIRI F1500W.

What can we learn from emission observations of rocky planets ?

Thanks to the in-depth study of the TRAPPIST-1 system emission observations and potential atmospheres, I acquired some expertise on what we can conclude about the presence or absence of an atmosphere on a rocky planet from emission observations. I was thus able to confirm and extend the work of Hammond et al. (2025), which discusses which emission observations can constitute reliable detections of atmospheres. Table 6.1 summarizes, for each type of observation, which type of bare rock and atmosphere, if any, can produce a corresponding observable. For the phase curve, the observable highlighted is the nightside flux (Hammond et al. 2025), although there is also the peak offset that could be used. In my simulations, though, the presence of a peak offset implied the presence of a nightside flux, and vice versa, so I will not discuss specifically the peak offset here.

Standard bare rocks and atmospheres We usually assume temperate airless planets to produce a high dayside flux, due to a very low to no heat redistribution, and a low albedo (Mansfield et al. 2019). Airless planets phase curves are thus expected to have no nightside flux or peak offset. For atmospheres, it is often assumed that an atmosphere would result in a low dayside flux, due to molecular absorption and heat redistribution towards nightside. Similarly, such a standard atmosphere creates a phase curve with a non-zero nightside flux.

Non-standard bare rocks In theory, a non-zero nightside flux for a bare rock could come from internal heat flux. Radioactive heating is not expected to produce a detectable nightside flux (Hammond et al. 2025), and internal heat transport is also expected to be too weak (Meier et al. 2021). However, tidal heating, which depends on orbital parameters (rotation rate, obliquity, eccentricity) but also internal structure of the planet, could amount to a nightside temperature that could be detected in an observed phase curve (see Gillon et al. (2025) in Appendix A, also Bolmont et al. in prep).
At the opposite side, Hammond et al. (2025) showed that some rocks could result in a high Bond albedo, allowing in theory for bare rocks to produce a low eclipse depth. However, this can be considered unlikely,

as bodies in the Solar system all have a low Bond albedo[1]. Finally, examples in Hammond et al. (2025) tend to suggest that most bare rocks emissions at two wavelengths (12.8 and 15 μm) do not deviate far from a blackbody - contrary to CO_2-containing atmosphere - so we consider that an airless body is very unlikely to produce a feature detectable with these two photometric bands.

Non-standard atmospheres During this PhD, I found some families of substantial atmospheres that can produce a large eclipse depth: transparent atmospheres, thick, greenhouse-efficient atmospheres and atmospheres with a thermal inversion (Chapter 3, Fig. 3.2). Thus, a deep eclipse in one broadband filter cannot be sufficient to conclude on the absence of an atmosphere . Similarly, among these families, the atmospheres with thermal inversion produce a zero nightside flux and no peak offset, mimicking the behavior of an airless planet. In consequence, there is in theory none of the observations proposed that could conclusively rule out the possibility of an atmosphere. However, the plausibility of the remaining atmospheres can be taken into account, like for TRAPPIST-1 b in the precedent section, to make conclusions.

Finally, in any case comes the question of significance[2]. For example, in the case of TRAPPIST-1 c in Chapter 4, the flux is indeed higher at 12.8 μm than at 15 μm, but the precision of the data is not high enough to conclusively rule out the bare rock hypothesis. More generally, we note that the segmentation between atmosphere and bare rock is somehow arbitrary, since there is a continuity between a thick atmosphere and a bare rock. In this sense, ruling out atmospheres can only mean putting an upper limit to the total pressure of the atmosphere. Such a limit depends on the composition of the atmosphere.

(a) Eclipse at 15 μm

	Dayside flux/Eclipse depth	
	High	Low
ATMOS.	**see chap. 3**	standard thick atmos.
BARE ROCK	low albedo	high albedo

(b) Eclipse at 2 photometric points

	Deviation to a blackbody	
	None	Deviation
ATMOS.	thin, low CO_2...	**see chap. 4**
BARE ROCK	standard bare rock	rock emiss. feature

(c) Phase curve

	Nightside flux	
	0	>0
ATMOS.	**see chap. 3**	standard thick atmos.
BARE ROCK	standard bare rock	internal flux

(d) Transit spectroscopy

	Transit spectrum	
	Featureless	Features
ATMOS.	TLS effect, aerosols	any atmosphere
BARE ROCK	standard bare rock	TLS effect

Table 6.1: Different methods to detect an atmosphere. Cells in red indicate cases very unlikely, cells in orange cases moderately unlikely.

In short, the high degeneracy of bare rock and atmospheric cases, coupled with the limited precision of the observations that are testing the limits of the capacities of JWST, make it difficult to make definitive conclusions on the presence or absence of an atmosphere.

[1]Except for icy bodies, which are not a possibility for dayside of temperate exoplanets.

[2]A question that is present everywhere in the field of exoplanet characterization, even for giant planets. See for example Welbanks et al. (2025)

7. Perspectives

Contents

7.1 TRAPPIST-1 system . . . 94
7.2 Future observations . . . 95
7.2.1 TRAPPIST-1 . . . 95
7.2.2 Other temperate rocky exoplanets . . . 95
7.3 Population level studies for rocky exoplanets . . . 96
7.4 Comparison between models and observations . . . 97
7.4.1 Examples in the literature . . . 97
7.4.2 Limits of the statistical methods . . . 99
7.4.3 Tentative practices and conclusion . . . 99
7.5 Improvements of the methodology . . . 100

In the light of my conclusions, I present here some perspectives relative to my work and research field. This thesis is a detailed study of mainly two planets, TRAPPIST-1 b and c, but it can be used similarly for other rocky exoplanets. Besides, results from each individual planet can be extended (with caution) to others - see, as an example, how I relied on TRAPPIST-1 b results for the TRAPPIST-1 c case (Chapter 4). Thus, perspectives of this work extend both in the direction of a further study of this particular system, and also towards the general topic of rocky exoplanets emission observations. After mentioning possible extensions of my work on planets of the TRAPPIST-1 system (7.1), I discuss general perspectives on observation strategy, for the TRAPPIST-1 system and beyond (7.2), and the possibility of population-level studies (7.3). Then, I address the methodological but crucial subject of comparison between models and observations (7.4), and finally I propose some other future improvements in the methodology I adopted for this work (7.5).

7.1 TRAPPIST-1 system

My work to interpret emission data of the TRAPPIST-1 planets has a lot of possible improvements and extensions, that I discuss in the dedicated sections in Chapter 3, 4 and 5. Here I present some perspectives for the further study of the planets of the TRAPPIST-1 system, based on already available observations, that I found worth highlighting.

New eclipses of TRAPPIST-1 b at 12.8 μm GO 5191 was dedicated to investigate the intriguing emission of TRAPPIST-1 c at 12.8 μm, but each of the four observations was scheduled to encompass one eclipse of TRAPPIST-1 c, and also one of TRAPPIST-1 b. This will help bring better constraints on the eclipse depth of TRAPPIST-1 b. We could use the new value of eclipse depth to update our results for TRAPPIST-1 b.

Comparison of TRAPPIST-1 b and c The eclipse photometry is quite different between the two planets: for TRAPPIST-1 b, the flux at 15 μm is higher than the flux at 12.8 μm, and vice versa for TRAPPIST-1 c. One way to quantify this is to compute the ratio between the 15 and 12 μm flux (Chapter 4, equation 4.1). This quantity differs by more than 5σ for the two planets (see section 4.4.4). This difference suggests that the two planets do not have the same composition, and it could be interesting to investigate this further.

7.2 Future observations

To explore prospects of future observations to detect atmospheres in general, I rely on Table 6.1 from the Conclusions, that shows that in emission, nightside flux derived from phase curve observations or chromatic secondary eclipses can be more reliably informative on the presence of an atmosphere than eclipse observations at 15 μm. Hammond et al. (2025) comes to the same conclusion[1], and remarks that observing eclipses at two filters can be approximately as costly as observing a phase curve, depending on the parameters of the planetary system.

7.2.1 TRAPPIST-1

Concerning the TRAPPIST-1 system, for which we have already a lot of data in emission - and in transmission -, comes the question of which further observations could be useful to eliminate degeneracy and obtain more definitive conclusions.

Planet b Further observations of TRAPPIST-1 b to definitively rule out the hazy atmosphere with inversion seems for now not appropriate. To justify such observations, one would first need to further model such atmospheres, to (i) make sure they are possible (haze formation by photometry or dust transport), and (ii) determine if such aerosols could be actually distinguished from a bare rock, and select such observables (more details in the discussion of Chapter 3). However, this question should be kept in mind as TRAPPIST-1 b is meant to be used as an airless probe during back-to-back transits (GO 6456, see Introduction, section 1.2.2).

Planet c For TRAPPIST-1 c, the current precision of the data does not allow for definitive conclusions. The eclipse "feature", i.e. lower eclipse depth at 15 μm than 12.8 μm, is particularly intriguing, and more eclipse observations at these wavelengths could maybe help exclude the blackbody case if it turns out to be representative. Only a few eclipses at both filters could maybe exclude the airless scenario at 3σ (see Chapter 4, section 4.4.3).

Outer planets We propose (Chapter 5.1) an observation of 16 eclipses of TRAPPIST-1 e to detect, or rule out, an atmosphere around the planet. For now, we do not have other relevant emission observation of the outer planets to propose; these planets' emission is indeed very faint and, requesting observational time for the combined emission of outer planets seems premature before performing the additional analyses mentioned in the perspectives of Chapter 5.

Star and transits Finally, while emission is a convenient way to bypass the transit light source effect, it has its limits (see Table 6.1). Correcting the TLS effect necessitates effort to characterize the star's inhomogeneities. Besides, the interpretation of eclipse depth depends strongly on the measured stellar flux. In summary, we need to know well the star in order to characterize its planets. This is why de Wit et al. (2024) advocates for observing a full stellar rotation of TRAPPIST-1 in order to better characterize the star, and hopefully correct for stellar contamination.

[1] Our work on the TRAPPIST-1 system nevertheless adds some insight, notably for the case of a zero nightside flux created by an atmosphere with inversion.

7.2.2 Other temperate rocky exoplanets

The Working Group on Strategic Exoplanet Initiatives with HST and JWST (Redfield et al. 2024) identified understanding the prevalence and diversity of atmospheres on rocky-M dwarf worlds as a key science theme, and preconized a 500-hour DDT program to do a survey of such planets in thermal emission. This program is currently being implemented, and dozens of Targets Under Consideration have been identified. Four planets have been selected for DDT observations, that probe both sides of the cosmic shoreline: LTT 1445 A b ($T_{\rm eq} \sim 430$ K) and c (514 K), LHS 1140 b (220 K) and GJ 3929 b (584 K).
Our work with the TRAPPIST-1 planets showed that one photometric point of eclipse observations was not enough to conclude on the presence/absence of an atmosphere, and thus questions the strategy of a large 15 μm eclipse survey for detecting atmospheres. Our conclusions and Hammond et al. (2025) show that a phase curve with a non-negligible nightside flux or two (or more) photometric points disagreeing with a bare rock curve could be considered a more definitive proof of atmosphere. Hammond et al. (2025) proposed three strategies for the 500-hour DDT: (i) 15 μm observations of eclipses for ∼20 exoplanets (highly degenerate), (ii) 15 μm and 12.8 μm observations for ∼10 exoplanets, or (iii) 15 μm phase curves for ∼10 exoplanets. To their conclusions, we add that from our experience the double eclipse needs a high divergence from the bare rock or a high precision to definitely rule out a bare rock explanation. One could combine strategies, by first selecting promising targets from 15 μm shallow eclipse depth, and then spending more time on these targets with either a phase curve or more eclipses at different wavelengths. However, as shows this work on the TRAPPIST-1 system, some targets ruled out by their high dayside emission can also in theory have substantial atmospheres, and, more generally, it is tricky to conclude with such sparse data.

In short, conclusively detecting or ruling out an atmosphere on an individual planet is difficult. The first targets of the Rocky Worlds DDT, LTT 1445 A c and GJ 3929 b, will be observed for respectively 11 and 15 eclipses, which will allow for a precision better than the usual GO targets. However, this does not solve the degeneracy mentioned above. Individual studies of exoplanets with more observational data, like in this work, help better constrain this degeneracy. Meanwhile, another approach made possible by the DDT is to renounce individual detections and look for a trend in all the observed planets.

7.3 Population level studies for rocky exoplanets

To date, a dozen of rocky exoplanets orbiting M-dwarfs have been observed in secondary eclipse, and with the Rocky Worlds DDT program and other JWST proposals, this number is expected to grow. These observations can be synthesized to look for trends, as it has already been done for other types of exoplanets (e.g., hot jupiters or hot super-Earths, Cowan & Agol 2011b; Demory 2014). For now, Coy et al. (2025) investigated a possible link between the instellation of the planet and its eclipse depth (relatively to the one of a zero-albedo bare rock). For now, they found a tentative trend in the brightness temperature for nine planets (Fig. 7.1).

To do this, they homogeneously re-derived the brightness temperature ratio, defined as:

$$\mathscr{R} \equiv \frac{T_d}{T_{d_0}} \tag{7.1}$$

with T_d the measured brightness temperature and T_{d_0} the brightness temperature of the dayside for a zero-albedo bare rock case. From this, one can also derive an effective albedo, i.e. the Bond albedo necessary to reproduce the observed brightness temperature: $A_i = 1 - \mathscr{R}^4$. They evaluated two models, a standard linear regression and a log-linear regression, and compared them to a flat line no-trend model. In order to assess the significance of the trend, they used several statistical tests (t-tests, chi-squared statistsic, Akaike information criterion, and Bayesian information criterion). Though the log-linear model is favored over the null hypothesis, the statistical evidence is not strong enough to validate the trend.

If confirmed, this trend could be explained by the presence of thin atmospheres on colder planets, with warmer planets being bare rocks, but also by space-weathering in warmer planets for all bare rocks planets. An important difficulty in this kind of study is to compare data that have been acquired by various methods

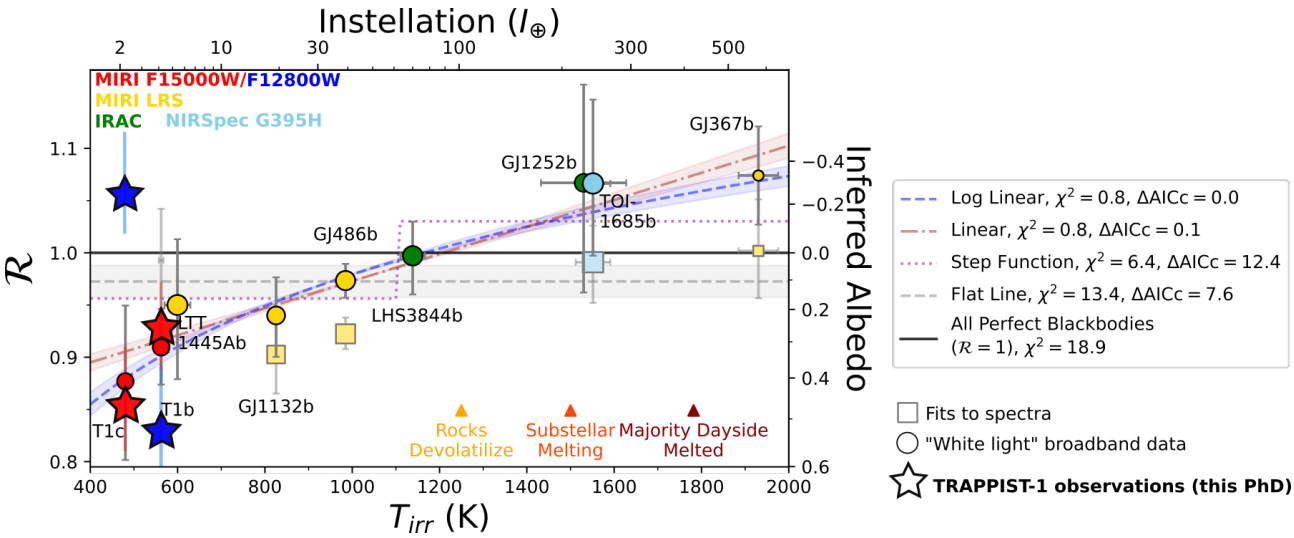

Figure 7.1: Tentative trend in the brightness temperature of rocky exoplanets adapted from Coy et al. (2025). We added our own computations of $\mathcal{R}$ separately for 12.8 and 15 μm.

(instrument, observational strategy...). Notably, the work of Coy et al. (2025) derives a brightness temperature from MIRI 15 μm photometric points or LRS observations. Since it derives only one brightness temperature, it cannot take into account multiple observational point that may differ, like for TRAPPIST-1 b and c. As an illustration, we added our own computed $\mathcal{R}$ for each MIRI filter in Fig. 7.1.

Hence, statistical studies of rocky temperate exoplanets from the growing number of observations available is a promising method, especially fit to exploit the upcoming data from the Rocky Worlds DDT, promising a various sample of observed exoplanet from both sides of the cosmic shoreline. However, it carries its own challenges and limits, and, by their nature, such studies do not fully capitalize on every specific observations of individual planets.

7.4 Comparison between models and observations

During my PhD, I was confronted to the question of comparing my atmospheric models to the observational data. It turned out to be a complicated subject. For the interpretation of the eclipse and, mainly, the phase curve, I was confronted to several issues:

Forward model assessment My models correspond to forward modeling; contrary to a lot of what is done in exoplanet atmospheres, I do not fit the parameters of the model with a bayesian retrieval code, since my models are too computationally demanding for such a treatment. Thus comes the question on how to quantitatively assess the compatibility of a model with the data.

Extraction of the phase curve To extract the phase curve from the data, observers must fit the observational points to an "astrophysical" model (see section 2.1). Contrary to the transit and eclipse light curve, modeling the shape of the phase curve implies to make assumptions on the temperature distribution on the planet, and the data analysis and modeling are not as nicely decoupled[2].

In order to address these issues, I propose to review a few examples of other phase curve observations and their comparison with GCMs, then discuss the statistical tools for model assessment versus data, and finally to propose tentative rigorous practices. This is more of an ongoing reflection than an accomplished work.

[2]In the case of the contribution of several planets like for TRAPPIST-1, this issue is even worse

7.4.1 Examples in the literature

Here I discuss the analytical treatment of three phase-curve observations and their eventual comparison with GCMs.

WASP-103 b This ultra-hot Jupiter was observed in phase curve with HST/WFC3 and Spitzer. Kreidberg et al. (2018) presents the results of the observations, including a comparison to GCM simulations. With its equilibrium temperature of 2500 K, and period of 22 hours, this planet is one of the dozens of systems observed in phase curve before the JWST. Its strong thermal emission results in a better data quality than the phase curve of TRAPPIST-1 b and c.
Concerning the model used for the phase curve extraction, (Kreidberg et al. 2018) developed `SPIDERMAN` (Louden & Kreidberg 2018), a model for generating phase curves from arbitrary brightness temperature maps. They performed different parametric analyses: a uniform dayside/nightside temperature map, a spherical harmonics map (with four free parameters), and a physically motivated model from Zhang & Showman (2017) with nightside temperature, day-to-night temperature change, and ratio between advective and convective timescale. In addition, they also used a simple sinusoidal phase curve. The fitted temperature maps and corresponding phase curves are shown in Fig. 7.2.

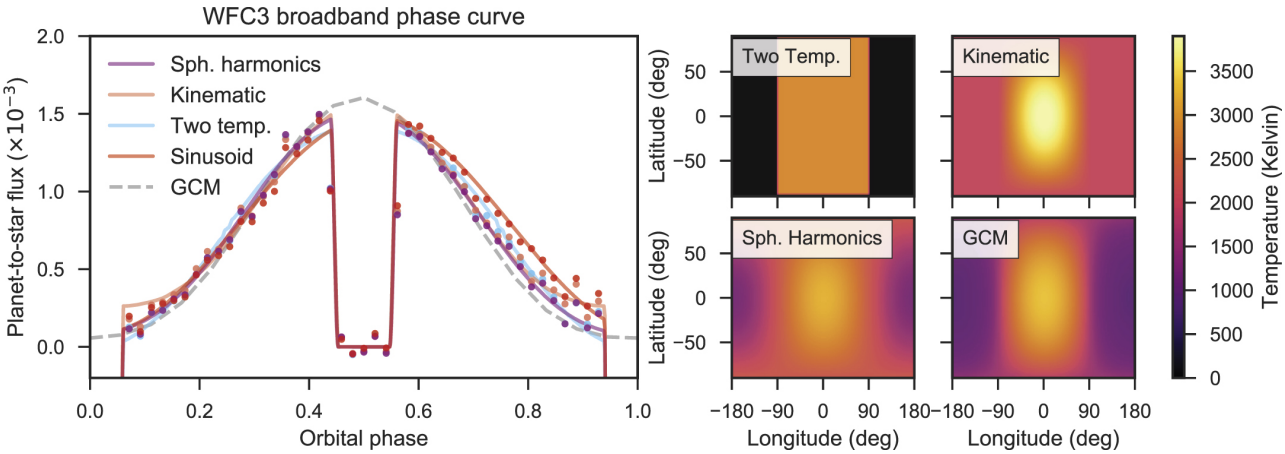

Figure 7.2: Left: fits to the broadband WFC3 phase curve compared to a GCM. The colored lines correspond to different temperature maps fit to the data, and the dashed gray line is from the GCM. Right: temperature maps from the best-fit models and the GCM at a pressure of 0.1 bar. Figure from Kreidberg et al. (2018)

GCM simulations were run and used to interpret the data, but no quantitative comparison between them is proposed in the paper. Chi-squared and standard deviation were computed only for fits of 1D models to the phase-resolved emission spectra.

LHS 3844 b This planet is the second rocky exoplanet observed in phase curve, after the ultra-hot 55 Cancri e. Its ∼800 K equilibrium temperature made it possible to detect the thermal phase curve with Spitzer (Kreidberg et al. 2019). Two kinds of models were used for the phase curve extraction: a sinusoidal temperature map (with four coefficients), and a sinusoidal model directly for the phase curve (with minimum, maximum flux and peak offset as free parameters), the two models giving similar results.
In this paper, they use a simple model with parameterization of heat redistribution inspired by Koll (2022). GCM simulations were mostly used to validate the scaling of the parametric model, and only the parametric model was quantitatively compared with the data through standard deviation, but the derivation is not described.

WASP-43 b A phase curve of this planet was observed with JWST/MIRI/LRS (ERS-1366) (Bell et al. 2024). This spectrally resolved observation is extremely precise compared to the one of TRAPPIST-1 (Fig. 7.3). It allowed for very rich data analysis and interpretation.
The data analysis was performed with the `eureka!` pipeline, using a spherical harmonics model for the

shape of the phase curve. A study was performed to determine the number of spherical harmonics needed to fit the data best. The second order model was significantly preferred over lower orders, while higher orders did not improve the fit significantly. This observation was thoroughly compared to GCM results

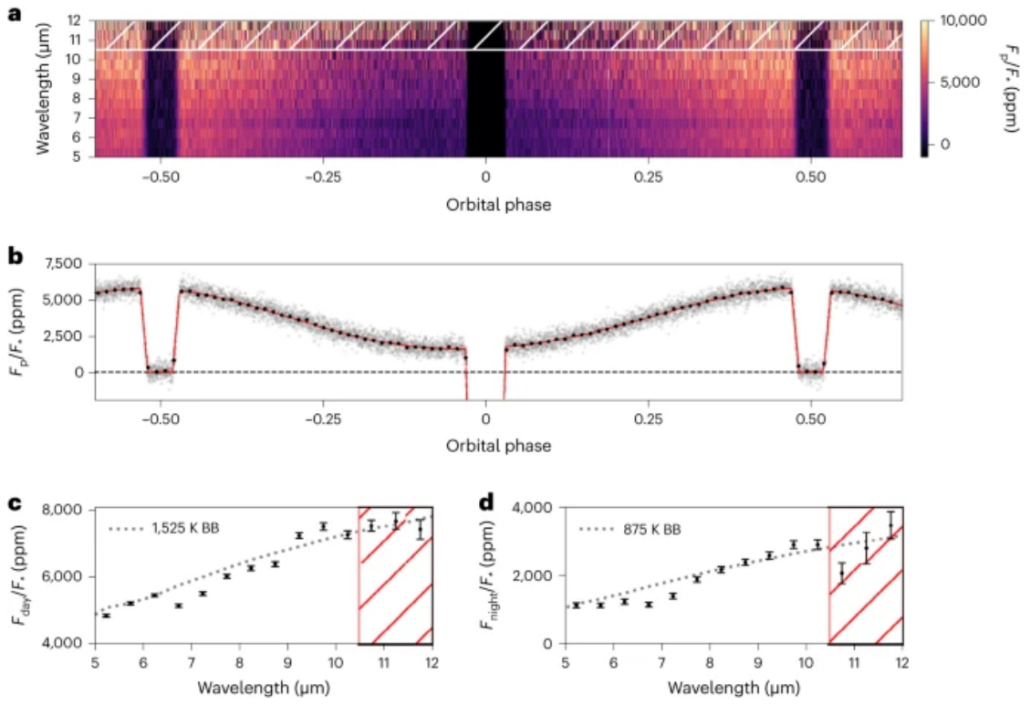

Figure 7.3: Spectroscopic light curve, while light phase curve and emission spectra from WASP-43 b (ERS-1366). Figure from Bell et al. (2024).

(see also Teinturier et al. (2024)), but no quantitative assessment of the match between the phase curve observation and the GCM observables was performed.

In summary, observers use different models for extracting the phase curve from raw observation. For precise data (WASP-43 b with JWST), a second order spherical harmonics decomposition is enough. For less precise data, the dayside flux, nightside flux and peak offset are commonly used as main results of the phase curve. The method of Louden & Kreidberg (2018) seems interesting as it is based on a more physical quantity, the spatial distribution of the brightness temperature.
Concerning the match between GCM and observations, none of the papers derive quantitative assessment of it.

7.4.2 Limits of the statistical methods

I here question the relevance of the statistical tools used in the "goodness-of-fit" assessment of most of this PhD.

Reduced chi-squared/degrees of freedom In the process of assessing the match between observational data and models, we need to compute the chi-squared, and evaluate its number of degrees of freedom. This allows to derive the reduced chi-squared, but also to compute the standard deviation from it. However, we are not using linear models, and assessing their number of degrees of freedom is not straightforward, and the use of this concept is overall questionable (Andrae et al. 2010). While the chi-squared test is adapted to compare similar models *from one another*[3], using the reduced chi-squared, or the number of degrees of

[3]A word of caution, also from Andrae et al. (2010): the random noise of the data implies that the value of the chi-squared is also subject to noise, and thus there is an incertitude on the value of the chi-squared itself, which can impact the results but is rarely taken into account.

freedom to find an *absolute* goodness-of-fit or statistical significance seems not adapted. Moreover, deriving p-values and standard deviations from reduced chi-squared theoretically requires numerous data points to compare with the observations.

7.4.3 Tentative practices and conclusion

Forward model assessment Andrae et al. (2010) suggests using the residuals for model comparison, by comparing normalized residuals to a Gaussian centered on 0 and with σ=1. This comparison must be in turn quantified, Andrae et al. (2010) propose for example the Kolmogorov-Smirnov test. This, or other statistical tests adapted to the situation, could allow for a more rigorous model assessment.
More generally, however, it is remarkable that for every example in the literature, there is no quantitative assessment performed: with the limitations of GCM modeling, constraining to perform only a few simulations for each planet, is a rigorous quantitative assessment necessary ? Is such an assessment even possible ? These questions seem very important and should probably be addressed by GCM modelers together with observers.

Phase curve extraction For phase curves like the one of TRAPPIST-1, it seems like the quality of the data is not enough to extract much more from the phase curve than the dayside, nightside flux and peak offset. However, it is important to be able to decouple the data analysis from atmospheric modeling, and propose an astrophysical model in the data analysis fitting that does not make strong assumptions on the shape of the phase curve. In this sense, the model of Louden & Kreidberg (2018) coupled with adapted temperature maps from spherical harmonics (Cowan & Agol 2008) could be relevant. It could be also interesting to try and compare non-fitted data directly to models.

Joint analysis for the phase curve of TRAPPIST-1 b and c Finally, our study of TRAPPIST-1 b and c presented the specificity of a double phase curve: the observed curve includes contributions of both planets that need to be disentangled. This complicates even more the question of comparison between model and observations. In this work, we chose to treat each planet separately: first, we studied TRAPPIST-1 b, concluded its phase curve was the one of a bare rock, and then we analysed the contribution of TRAPPIST-1 c, considering TRAPPIST-1 b could be considered a bare rock. It required to disentangle the signals of the two planets during the data analysis step. We could instead model the emission both planets at the same time and compare it to the data.

7.5 Improvements of the methodology

The methodology developed during this PhD for interpreting observational data with atmospheric models could be improved. Beside the question of the model assessment and extraction of the phase curve, discussed in the previous section, here are some ideas to improve the pipeline.

Surface models Since we focused on atmospheric models, we did not explore at all the question of surfaces. For now, models used for data interpretation are either atmospheric models with a very simplistic surface, or surfaces with no atmosphere (e.g., Gillon et al. (2025)). It could be interesting to implement better models of surfaces than fixed, wavelength-independent Bond albedos, especially for thin atmospheres for which a large part of the emission comes from the surface.

Bayesian retrieval for 1D exploration For now, we explored the parameter space in 1D only "by hand", and following intuitions on families of atmospheres that could produce a given observational feature. This is limited in several ways: first, we can miss an entire family of atmosphere. Second, we cannot fully optimize the parameters (composition, surface pressure, surface albedo). A more comprehensive exploration of the parameter space could be performed with Markov Chain Monte Carlo (MCMC) methods. However, even in 1D, the model we use is complex. Its convergence time depends strongly on the atmosphere that is modeled. Hence, implementing such a method would require some work and the use of a cluster. We note

that such a comprehensive exploration of the parameters would still be limited by the inherent limitations of 1D studies with horizontal heat redistribution parameterization, notably: optimizing the parameters of an atmosphere in 1D to fit the data does not mean the same atmosphere in 3D is also optimized.

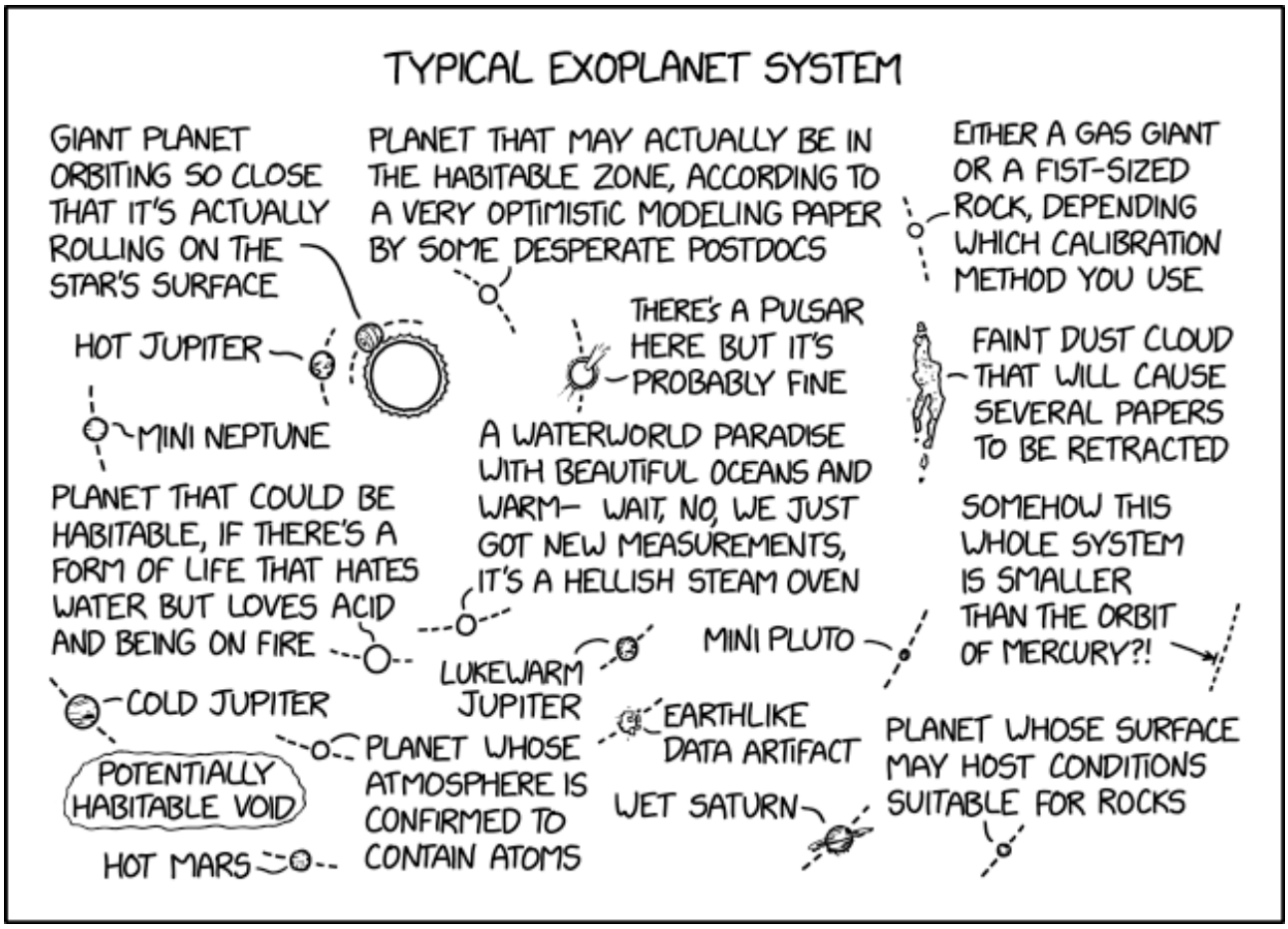

Figure 7.4: A rather pessimistic view of exoplanetary science. From https://xkcd.com/3103/

Bibliography

Agol, E., Rounding up the wanderers: optimizing coronagraphic searches for extrasolar planets. 2007, *MNRAS*, 374, 1271

Agol, E., Dorn, C., Grimm, S. L., et al., Refining the Transit-timing and Photometric Analysis of TRAPPIST-1: Masses, Radii, Densities, Dynamics, and Ephemerides. 2021, *Plan. Sci. J.*, 2, 1

Al-Refaie, A. F., Changeat, Q., Waldmann, I. P., & Tinetti, G., TauREx 3: A Fast, Dynamic, and Extendable Framework for Retrievals. 2021, *ApJ*, 917, 37

Alderson, L., Batalha, N. E., Wakeford, H. R., et al., JWST COMPASS: NIRSpec/G395H Transmission Observations of the Super-Earth TOI-836b. 2024, *AJ*, 167, 216

Andrae, R., Schulze-Hartung, T., & Melchior, P., Dos and don'ts of reduced chi-squared. 2010

Artemieva, N. & Lunine, J., Cratering on Titan: impact melt, ejecta, and the fate of surface organics. 2003, *Icarus*, 164, 471

Auclair-Desrotour, P., Deitrick, R., & Heng, K., Meta-modelling the climate of dry tide-locked rocky planets. 2022, *A&A*, 663, A79

August, P. C., Buchhave, L. A., Diamond-Lowe, H., et al., Hot Rocks Survey I: A possible shallow eclipse for LHS 1478 b. 2025, *A&A*, 695, A171

Banerjee, A., Barstow, J. K., Gressier, A., et al., Atmospheric Retrievals Suggest the Presence of a Secondary Atmosphere and Possible Sulfur Species on L98-59 d from JWST NIRspec G395H Transmission Spectroscopy. 2024, *ApJ*, 975, L11

Barclay, T., Pepper, J., & Quintana, E. V., A Revised Exoplanet Yield from the Transiting Exoplanet Survey Satellite (TESS). 2018, *ApJS*, 239, 2

Bell, T. J., Ahrer, E.-M., Brande, J., et al., Eureka!: An End-to-End Pipeline for JWST Time-Series Observations. 2022, *Journal of Open Source Software*, 7, 4503

Bell, T. J., Crouzet, N., Cubillos, P. E., et al., Nightside clouds and disequilibrium chemistry on the hot Jupiter WASP-43b. 2024, *Nat. Astro.*, 8, 879

Bell, T. J., Kreidberg, L., Kendrew, S., et al., A First Look at the JWST MIRI/LRS Phase Curve of WASP-43b. 2023, *arXiv e-prints*, arXiv:2301.06350

Bello-Arufe, A., Damiano, M., Bennett, K. A., et al., Evidence for a Volcanic Atmosphere on the Sub-Earth L 98-59 b. 2025, *ApJ*, 980, L26

Bolmont, E., Libert, A.-S., Leconte, J., & Selsis, F., Habitability of planets on eccentric orbits: Limits of the mean flux approximation. 2016, *A&A*, 591, A106

Bolmont, E., Selsis, F., Owen, J. E., et al., Water loss from terrestrial planets orbiting ultracool dwarfs: implications for the planets of TRAPPIST-1. 2017a, *MNRAS*, 464, 3728

Bolmont, E., Selsis, F., Owen, J. E., et al., Water loss from terrestrial planets orbiting ultracool dwarfs: implications for the planets of TRAPPIST-1. 2017b, *MNRAS*, 464, 3728

Bourrier, V., Ehrenreich, D., Wheatley, P. J., et al., Reconnaissance of the TRAPPIST-1 exoplanet system in the Lyman-α line. 2017, *A&A*, 599, L3

Bryson, S., Kunimoto, M., Kopparapu, R. K., et al., The Occurrence of Rocky Habitable-zone Planets around Solar-like Stars from Kepler Data. 2021, *AJ*, 161, 36

Burch, D. E., Gryvnak, D. A., Patty, R. R., & Bartky, C. E., Absorption of Infrared Radiant Energy by CO_2 and H_2O IV Shapes of Collision-Broadened CO_2 Lines*. 1969, *Journal of the Optical Society of America (1917-1983)*, 59, 267

Casasayas-Barris, N., Palle, E., Stangret, M., et al., The atmosphere of HD 209458b seen with ESPRESSO. No detectable planetary absorptions at high resolution. 2021, *A&A*, 647, A26

Charbonneau, D., Brown, T. M., Latham, D. W., & Mayor, M., Detection of Planetary Transits Across a Sun-like Star. 2000, *ApJ*, 529, L45

Charbonneau, D., Brown, T. M., Noyes, R. W., & Gilliland, R. L., Detection of an Extrasolar Planet Atmosphere. 2002, *ApJ*, 568, 377

Charnay, B. 2014, Tropospheric dynamics and climatic evolution of Titan and the early Earth, Theses, Universite Pierre et Marie Curie - Paris VI

Charnay, B., Blain, D., Bézard, B., et al., Formation and dynamics of water clouds on temperate sub-Neptunes: the example of K2-18b. 2021, *A&A*, 646, A171

Charnay, B., Meadows, V., & Leconte, J., 3D Modeling of GJ1214b's Atmosphere: Vertical Mixing Driven by an Anti-Hadley Circulation. 2015a, *ApJ*, 813, 15

Charnay, B., Meadows, V., Misra, A., Leconte, J., & Arney, G., 3D Modeling of GJ1214b Atmosphere: Formation of Inhomogeneous High Clouds and Observational Implications. 2015b, *ApJ*, 813, L1

Chen, H., Li, G., Paradise, A., & Kopparapu, R. K., Sporadic Spin-orbit Variations in Compact Multiplanet Systems and Their Influence on Exoplanet Climate. 2023, *ApJ*, 946, L32

Chubb, Katy L., Rocchetto, Marco, Yurchenko, Sergei N., et al., The ExoMolOP database: Cross sections and k-tables for molecules of interest in high-temperature exoplanet atmospheres. 2021, *A&A*, 646, A21

Cockell, C. 2020, Astrobiology: Understanding Life in the Universe (Wiley-Blackwell)

Coleman, G. A. L., Leleu, A., Alibert, Y., & Benz, W., Pebbles versus planetesimals: the case of Trappist-1. 2019, *A&A*, 631, A7

Collins, G. C., Patterson, G. W., Detelich, C. E., et al., Episodic Plate Tectonics on Europa: Evidence for Widespread Patches of Mobile-Lid Behavior in the Antijovian Hemisphere. 2022, *J. Geophys. Res. (Plan.)*, 127, e2022JE007492

Cottin, H., Kotler, J. M., Bartik, K., et al., Astrobiology and the Possibility of Life on Earth and Elsewhere.... 2017, *Space Sci. Rev.*, 209, 1

Cowan, N. B. & Agol, E., Inverting Phase Functions to Map Exoplanets. 2008, *ApJ*, 678, L129

Cowan, N. B. & Agol, E., A Model for Thermal Phase Variations of Circular and Eccentric Exoplanets. 2011a, *ApJ*, 726, 82

Cowan, N. B. & Agol, E., The Statistics of Albedo and Heat Recirculation on Hot Exoplanets. 2011b, *ApJ*, 729, 54

Cowan, N. B., Agol, E., & Charbonneau, D., Hot nights on extrasolar planets: mid-infrared phase variations of hot Jupiters. 2007, *MNRAS*, 379, 641

Coy, B. P., Ih, J., Kite, E. S., et al., Population-level Hypothesis Testing with Rocky Planet Emission Data: A Tentative Trend in the Brightness Temperatures of M-Earths. 2025, *ApJ*, 987, 22

de Wit, J., Doyon, R., Rackham, B. V., et al., A roadmap for the atmospheric characterization of terrestrial exoplanets with JWST. 2024, *Nat. Astro.*, 8, 810–818

De Wit, J., Wakeford, H. R., Gillon, M., et al., A combined transmission spectrum of the Earth-sized exoplanets TRAPPIST-1 b and c. 2016, *Nature*, 537, 69

de Wit, J., Wakeford, H. R., Lewis, N. K., et al., Atmospheric reconnaissance of the habitable-zone Earth-sized planets orbiting TRAPPIST-1. 2018, *Nat. Astro.*, 2, 214

Demory, B.-O., The Albedos of Kepler's Close-in Super-Earths. 2014, *ApJ*, 789, L20

Demory, B.-O., Gillon, M., de Wit, J., et al., A map of the large day-night temperature gradient of a super-Earth exoplanet. 2016, *Nature*, 532, 207

Demory, B.-O., Gillon, M., Seager, S., et al., Detection of Thermal Emission from a Super-Earth. 2012, *ApJ*, 751, L28

Drant, T., Garcia-Caurel, E., Perrin, Z., et al., Optical constants of exoplanet haze analogs from 0.3 to 30 µm: Comparative sensitivity between spectrophotometry and ellipsometry. 2024, *A&A*, 682, A6

Ducrot, E., Gillon, M., Delrez, L., et al., TRAPPIST-1: Global results of the Spitzer Exploration Science Program Red Worlds. 2020, *A&A*, 640, A112

Ducrot, E., Lagage, P.-O., Min, M., et al., Combined analysis of the 12.8 and 15μm JWST/MIRI eclipse observations of TRAPPIST-1 b. 2024, *Nat. Astro.*, 9, 358–369

Dyrek, A., Ducrot, E., Lagage, P. O., et al., Transiting exoplanets with the Mid-InfraRed Instrument on board JWST: From simulations to observations. 2024, *A&A*, 683, A212

Eadie, G. M., Speagle, J. S., Cisewski-Kehe, J., et al., Practical Guidance for Bayesian Inference in Astronomy. 2023, *arXiv e-prints*, arXiv:2302.04703

Espinoza, N. & Perrin, M. D., Highlights from Exoplanet Observations by the James Webb Space Telescope. 2025, *arXiv e-prints*, arXiv:2505.20520

Falco, A., Zingales, T., Pluriel, W., & Leconte, J., Toward a multidimensional analysis of transmission spectroscopy. I. Computation of transmission spectra using a 1D, 2D, or 3D atmosphere structure. 2022, *A&A*, 658, A41

Fassett, C. I. & Head, J. W., The timing of martian valley network activity: Constraints from buffered crater counting. 2008, *Icarus*, 195, 61

Fauchez, T. J., Rackham, B. V., Ducrot, E., Stevenson, K. B., & de Wit, J., Stellar Models Also Limit Exoplanet Atmosphere Studies in Emission. 2025, *arXiv e-prints*, arXiv:2502.19585

Fauchez, T. J., Turbet, M., Villanueva, G. L., et al., Impact of Clouds and Hazes on the Simulated JWST Transmission Spectra of Habitable Zone Planets in the TRAPPIST-1 System. 2019, *ApJ*, 887, 194

Forget, F., Hourdin, F., Fournier, R., et al., Improved general circulation models of the Martian atmosphere from the surface to above 80 km. 1999, *J. Geophys. Res.*, 104, 24155

Forget, F., Wordsworth, R., Millour, E., et al., 3D modelling of the early martian climate under a denser CO_2 atmosphere: Temperatures and CO_2 ice clouds. 2013, *Icarus*, 222, 81

Fray, N. & Schmitt, B., Sublimation of ices of astrophysical interest: A bibliographic review. 2009, *Planet. Space Sci.*, 57, 2053

Fu, Q. & Liou, K. N., On the correlated k-distribution method for radiative transfer in nonhomogeneous atmospheres. 1992, *Journal of Atmospheric Sciences*, 49, 2139

Garcia, L. J., Moran, S. E., Rackham, B. V., et al., HST/WFC3 transmission spectroscopy of the cold rocky planet TRAPPIST-1h. 2022, *A&A*, 665, A19

Gardner, J. P., Mather, J. C., Abbott, R., et al., The James Webb Space Telescope Mission. 2023, *PASP*, 135, 068001

Gillon, M., Ducrot, E., Bell, T. J., et al., First JWST thermal phase curves of temperate terrestrial exoplanets reveal no thick atmosphere around TRAPPIST-1 b and c. 2025, Nature, arXiv:2509.02128

Gillon, M., Jehin, E., Lederer, S. M., et al., Temperate Earth-sized planets transiting a nearby ultracool dwarf star. 2016, *Nature*, 533, 221

Gillon, M., Meadows, V., Agol, E., et al. 2020, in Bulletin of the American Astronomical Society, Vol. 52, 0208

Gillon, M., Triaud, A. H. M. J., Demory, B.-O., et al., Seven temperate terrestrial planets around the nearby ultracool dwarf star TRAPPIST-1. 2017, *Nature*, 542, 456

Gordon, K. D., Sloan, G. C., Garcia Marin, M., et al., The James Webb Space Telescope Absolute Flux Calibration. II. Mid-infrared Instrument Imaging and Coronagraphy. 2024, *AJ*, 169, 6

Grasset, O., Sotin, C., & Deschamps, F., On the internal structure and dynamics of Titan. 2000, *Planet. Space Sci.*, 48, 617

Greene, T. P., Bell, T. J., Ducrot, E., et al., Thermal emission from the Earth-sized exoplanet TRAPPIST-1 b using JWST. 2023, *Nat*, 618, 39

Gressier, A., Espinoza, N., Allen, N. H., et al., Hints of a Sulfur-rich Atmosphere around the 1.6 $R_\oplus$ Super-Earth L98-59 d from JWST NIRspec G395H Transmission Spectroscopy. 2024, *ApJ*, 975, L10

Gressier, A., Mori, M., Changeat, Q., et al., Near-infrared transmission spectrum of TRAPPIST-1 h using Hubble WFC3 G141 observations. 2022, *A&A*, 658, A133

Gruszka, M. & Borysow, A., Roto-Translational Collision-Induced Absorption of CO_2 for the Atmosphere of Venus at Frequencies from 0 to 250 cm^{-1}, at Temperatures from 200 to 800 K. 1997, *Icarus*, 129, 172

Hammond, M., Guimond, C. M., Lichtenberg, T., et al., Reliable Detections of Atmospheres on Rocky Exoplanets with Photometric JWST Phase Curves. 2025, *ApJ*, 978, L40

Harrington, J., Hansen, B. M., Luszcz, S. H., et al., The Phase-Dependent Infrared Brightness of the Extrasolar Planet υ Andromedae b. 2006, *Science*, 314, 623

Hill, C., Yurchenko, S. N., & Tennyson, J., Temperature-dependent molecular absorption cross sections for exoplanets and other atmospheres. 2013, *Icarus*, 226, 1673

Horowitz, N. H. 1986, To Utopia and back. The search for life in the solar system

Howard, W. S., Kowalski, A. F., Flagg, L., et al., Characterizing the Near-infrared Spectra of Flares from TRAPPIST-1 during JWST Transit Spectroscopy Observations. 2023, *ApJ*, 959, 64

Hu, R., Bello-Arufe, A., Zhang, M., et al., A secondary atmosphere on the rocky exoplanet 55 Cancri e. 2024, *Nature*, 630, 609

Hut, P., Tidal evolution in close binary systems. 1981, A&A, 99, 126

Ih, J., Kempton, E. M. R., Whittaker, E. A., & Lessard, M., Constraining the Thickness of TRAPPIST-1 b's Atmosphere from Its JWST Secondary Eclipse Observation at 15 μm. 2023, *ApJ*, 952, L4

Iyer, A. R., Line, M. R., Muirhead, P. S., Fortney, J. J., & Gharib-Nezhad, E., The SPHINX M-dwarf Spectral Grid. I. Benchmarking New Model Atmospheres to Derive Fundamental M-dwarf Properties. 2023, *ApJ*, 944, 41

Joshi, M. M., Elvidge, A. D., Wordsworth, R., & Sergeev, D., Earth's Polar Night Boundary Layer as an Analog for Dark Side Inversions on Synchronously Rotating Terrestrial Exoplanets. 2020, *ApJ*, 892, L33

Karman, T., Gordon, I. E., van der Avoird, A., et al., Update of the HITRAN collision-induced absorption section. 2019, *Icarus*, 328, 160

Kasting, J., Peter Ward and Donald Brownlee's "Rare Earth". 2001, *Perspectives in Biology and Medicine*, 44, 117

Kasting, J. F., Whitmire, D. P., & Reynolds, R. T., Habitable Zones around Main Sequence Stars. 1993, *Icarus*, 101, 108

Khare, B. N., Sagan, C., Arakawa, E. T., et al., Optical constants of organic tholins produced in a simulated Titanian atmosphere - From soft X-ray to microwave frequencies. 1984, *Icarus*, 60, 127

Kirk, J., Stevenson, K. B., Fu, G., et al., JWST/NIRCam Transmission Spectroscopy of the Nearby Sub-Earth GJ 341b. 2024, *AJ*, 167, 90

Kite, E. S. & Barnett, M. N., Exoplanet secondary atmosphere loss and revival. 2020, *PNAS*, 117, 18264

Koll, D. D. B., A Scaling for Atmospheric Heat Redistribution on Tidally Locked Rocky Planets. 2022, *ApJ*, 924, 134

Kopparapu, R. K., Ramirez, R., Kasting, J. F., et al., Habitable Zones around Main-sequence Stars: New Estimates. 2013, *ApJ*, 765, 131

Kreidberg, L., Koll, D. D. B., Morley, C., et al., Absence of a thick atmosphere on the terrestrial exoplanet LHS 3844b. 2019, *Nature*, 573, 87

Kreidberg, L., Line, M. R., Parmentier, V., et al., Global Climate and Atmospheric Composition of the Ultra-hot Jupiter WASP-103b from HST and Spitzer Phase Curve Observations. 2018, *AJ*, 156, 17

Kreidberg, L. & Stevenson, K. B., A first look at rocky exoplanets with JWST. 2025, *arXiv e-prints*, arXiv:2507.00933

Krijt, S., Kama, M., McClure, M., et al. 2023, in Astronomical Society of the Pacific Conference Series, Vol. 534, Protostars and Planets VII, ed. S. Inutsuka, Y. Aikawa, T. Muto, K. Tomida, & M. Tamura, 1031

Krissansen-Totton, J. & Fortney, J. J., Predictions for Observable Atmospheres of Trappist-1 Planets from a Fully Coupled Atmosphere-Interior Evolution Model. 2022, *ApJ*, 933, 115

Krissansen-Totton, J., Garland, R., Irwin, P., & Catling, D. C., Detectability of Biosignatures in Anoxic Atmospheres with the James Webb Space Telescope: A TRAPPIST-1e Case Study. 2018, *AJ*, 156, 114

Krissansen-Totton, J., Olson, S., & Catling, D. C., Disequilibrium biosignatures over Earth history and implications for detecting exoplanet life. 2018, *Science Advances*, 4, eaao5747

Krissansen-Totton, J., Wogan, N., Thompson, M., & Fortney, J. J., The erosion of large primary atmospheres typically leaves behind substantial secondary atmospheres on temperate rocky planets. 2024, *Nat. Comm.*, 15, 8374

Leconte, J., Spectral binning of precomputed correlated-k coefficients. 2021, *A&A*, 645, A20

Lichtenberg, T., Schaefer, L. K., Nakajima, M., & Fischer, R. A. 2023, in Astronomical Society of the Pacific Conference Series, Vol. 534, Protostars and Planets VII, ed. S. Inutsuka, Y. Aikawa, T. Muto, K. Tomida, & M. Tamura, 907

Lim, O., Benneke, B., Doyon, R., et al., Atmospheric Reconnaissance of TRAPPIST-1 b with JWST/NIRISS: Evidence for Strong Stellar Contamination in the Transmission Spectra. 2023, *ApJ*, 955, L22

Lincowski, A. P., Meadows, V. S., Zieba, S., et al., Potential Atmospheric Compositions of TRAPPIST-1 c Constrained by JWST/MIRI Observations at 15 μm. 2023, *ApJ*, 955, L7

Liou, K. 1980, An Introduction to Atmospheric Radiation, An Introduction to Atmospheric Radiation (Elsevier Science)

Louden, T. & Kreidberg, L., SPIDERMAN: an open-source code to model phase curves and secondary eclipses. 2018, *MNRAS*, 477, 2613–2627

Luger, R., Sestovic, M., Kruse, E., et al., A seven-planet resonant chain in TRAPPIST-1. 2017, *Nat. Astro.*, 1, 0129

Lund Myhre, C. E., Christensen, D. H., Nicolaisen, F. M., & Nielsen, C. J., Spectroscopic Study of Aqueous H2SO4 at Different Temperatures and Compositions: Variations in Dissociation and Optical Properties. 2003, *The Journal of Physical Chemistry A*, 107, 1979

Lupu, R., Freedman, R., Gharib-Nezhad, E., & Molliere, P. 2022, High resolution opacities for H2/He atmospheres, Data set, Zenodo, https://doi.org/10.5281/zenodo.6600976

Luque, R., Coy, B. P., Xue, Q., et al., A Dark, Bare Rock for TOI-1685 b from a JWST NIRSpec G395H Phase Curve. 2025, *AJ*, 170, 49

Lustig-Yaeger, J., Fu, G., May, E. M., et al., A JWST transmission spectrum of the nearby Earth-sized exoplanet LHS 475 b. 2023, *Nat. Astro.*, 7, 1317

Lustig-Yaeger, J., Meadows, V. S., & Lincowski, A. P., The Detectability and Characterization of the TRAPPIST-1 Exoplanet Atmospheres with JWST. 2019, *AJ*, 158, 27

Madeleine, J.-B. 2011, Dust and clouds on Mars: Remote sensing, modeling of climate feedbacks and paleoclimate applications, Theses, Université Pierre et Marie Curie - Paris VI

Makarov, V. V., Berghea, C. T., & Efroimsky, M., Spin-orbital Tidal Dynamics and Tidal Heating in the TRAPPIST-1 Multiplanet System. 2018, *ApJ*, 857, 142

Manabe, S. & Wetherald, R. T., Thermal Equilibrium of the Atmosphere with a Given Distribution of Relative Humidity. 1967, *Journal of the Atmospheric Sciences*, 24, 241

Mandel, K. & Agol, E., Analytic Light Curves for Planetary Transit Searches. 2002, *ApJ*, 580, L171

Mansfield, M., Kite, E. S., Hu, R., et al., Identifying Atmospheres on Rocky Exoplanets through Inferred High Albedo. 2019, *ApJ*, 886, 141

Mant, B. P., Yachmenev, A., Tennyson, J., & Yurchenko, S. N., ExoMol molecular line lists – XXVII. Spectra of C2H4. 2018, *MNRAS*, 478, 3220

Maurel, A., Turbet, M., Ducrot, E., et al., Constraints on the possible atmospheres on TRAPPIST-1 b: insights from 3D climate modeling. 2025, A&A, arXiv:2509.02120

May, E. M., MacDonald, R. J., Bennett, K. A., et al., Double Trouble: Two Transits of the Super-Earth GJ 1132 b Observed with JWST NIRSpec G395H. 2023, *ApJ*, 959, L9

Mayor, M. & Queloz, D., A Jupiter-mass companion to a solar-type star. 1995, *Nature*, 378, 355

McEwen, A. S., Ojha, L., Dundas, C. M., et al., Seasonal Flows on Warm Martian Slopes. 2011, *Science*, 333, 740

McKay, C. P., Porco Carolyn C., Altheide, T., Davis, W. L., & Kral, T. A., The Possible Origin and Persistence of Life on Enceladus and Detection of Biomarkers in the Plume. 2008, *Astrobiology*, 8, 909

Meadows, V. S., Reinhard, C. T., Arney, G. N., et al., Exoplanet Biosignatures: Understanding Oxygen as a Biosignature in the Context of Its Environment. 2018, *Astrobiology*, 18, 630

Meier, T. G., Bower, D. J., Lichtenberg, T., Tackley, P. J., & Demory, B.-O., Hemispheric Tectonics on Super-Earth LHS 3844b. 2021, *ApJ*, 908, L48

Merino, N., Aronson, H. S., Bojanova, D. P., et al., Living at the Extremes: Extremophiles and the Limits of Life in a Planetary Context. 2019, *Frontiers in Microbiology*, Volume 10 - 2019

Miller, S. L., A Production of Amino Acids Under Possible Primitive Earth Conditions. 1953, *Science*, 117, 528

Mollière, P., Wardenier, J. P., van Boekel, R., et al., petitRADTRANS: A Python radiative transfer package for exoplanet characterization and retrieval. 2019, *A&A*, 627, A67

Montabone, L., Forget, F., Millour, E., et al., Eight-year climatology of dust optical depth on Mars. 2015, *Icarus*, 251, 65

Moore, K. & Cowan, N. B., Keeping M-Earths habitable in the face of atmospheric loss by sequestering water in the mantle. 2020, *MNRAS*, 496, 3786

North, G. R., Theory of Energy-Balance Climate Models. 1975, *Journal of the Atmospheric Sciences*, 32, 2033

Nutzman, P. & Charbonneau, D., Design Considerations for a Ground-Based Transit Search for Habitable Planets Orbiting M Dwarfs. 2008, *PASP*, 120, 317

Pass, E. K., Charbonneau, D., & Vanderburg, A., The Receding Cosmic Shoreline of Mid-to-late M Dwarfs: Measurements of Active Lifetimes Worsen Challenges for Atmosphere Retention by Rocky Exoplanets. 2025, *ApJ*, 986, L3

Peretó, J., Out of fuzzy chemistry: from prebiotic chemistry to metabolic networks. 2012, *Chem. Soc. Rev.*, 41, 5394

Perrin, M. Y. & Hartmann, J. M., Temperature-dependent measurements and modeling of absorption by CO2-N2 mixtures in the far line-wings of the 4.3 μm CO2 band. 1989, *Journal of Quantitative Spectroscopy and Radiative Transfer*, 42, 311

Pluriel, W., Hot Exoplanetary Atmospheres in 3D. 2023, *Remote Sensing*, 15

Poulet, F., Bibring, J.-P., Mustard, J. F., et al., Phyllosilicates on Mars and implications for early martian climate. 2005, *Nature*, 438, 623

Rackham, B. V., Apai, D., & Giampapa, M. S., The Transit Light Source Effect: False Spectral Features and Incorrect Densities for M-dwarf Transiting Planets. 2018, *ApJ*, 853, 122

Radica, M., Piaulet-Ghorayeb, C., Taylor, J., et al., Promise and Peril: Stellar Contamination and Strict Limits on the Atmosphere Composition of TRAPPIST-1 c from JWST NIRISS Transmission Spectra. 2025, *ApJ*, 979, L5

Rathcke, A. D., Buchhave, L. A., Wit, J. d., et al., Stellar Contamination Correction Using Back-to-back Transits of TRAPPIST-1 b and c. 2025a, *ApJ*, 979, L19

Rathcke, A. D., Buchhave, L. A., Wit, J. d., et al., Stellar Contamination Correction Using Back-to-back Transits of TRAPPIST-1 b and c. 2025b, *ApJ*, 979, L19

Raulin, F., Brassé, C., Poch, O., & Coll, P., Prebiotic-like chemistry on Titan. 2012, *Chem. Soc. Rev.*, 41, 5380

Rauscher, E. & Menou, K., Three-dimensional Atmospheric Circulation Models of HD 189733b and HD 209458b with Consistent Magnetic Drag and Ohmic Dissipation. 2013, *ApJ*, 764, 103

Rauscher, E., Menou, K., Cho, J. Y., Seager, S., & Hansen, B. M. S., On Signatures of Atmospheric Features in Thermal Phase Curves of Hot Jupiters. 2008, *ApJ*, 681, 1646

Redfield, S., Batalha, N., Benneke, B., et al., Report of the Working Group on Strategic Exoplanet Initiatives with HST and JWST. 2024, *arXiv e-prints*, arXiv:2404.02932

Ressler, M. E., Sukhatme, K. G., Franklin, B. R., et al., The Mid-Infrared Instrument for the James Webb Space Telescope, VIII: The MIRI Focal Plane System. 2015, *PASP*, 127, 675

Revol, A., Bolmont, É., Sastre, M., et al., Drifts of the substellar points of the TRAPPIST-1 planets. 2024, *A&A*, 691, L3

Scarsdale, N., Wogan, N., Wakeford, H. R., et al., JWST COMPASS: The 3–5 μm Transmission Spectrum of the Super-Earth L 98-59 c. 2024, *AJ*, 168, 276

Selsis, F., Despois, D., & Parisot, J.-P., Signature of life on exoplanets: Can Darwin produce false positive detections? 2002, *A&A*, 388, 985

Selsis, F., Leconte, J., Turbet, M., Chaverot, G., & Bolmont, E., A cool runaway greenhouse without surface magma ocean. 2023, *Nature*, 620, 287–291

Selsis, F., Wordsworth, R. D., & Forget, F., Thermal phase curves of nontransiting terrestrial exoplanets: I. Characterizing atmospheres. 2011, *A&A*, 532, A1

Selsis, F., Wordsworth, R. D., & Forget, F., Thermal phase curves of nontransiting terrestrial exoplanets. I. Characterizing atmospheres. 2011, *A&A*, 532, A1

Shakespeare, C. J. & Steffen, J. H., Day and night: habitability of tidally locked planets with sporadic rotation. 2023, *MNRAS*, 524, 5708

Showman, A. P. & Guillot, T., Atmospheric circulation and tides of "51 Pegasus b-like" planets. 2002, *A&A*, 385, 166

Sohl, L. E., Fauchez, T. J., Domagal-Goldman, S., et al., The CUISINES Framework for Conducting Exoplanet Model Intercomparison Projects, Version 1.0. 2024, *Plan. Sci. J.*, 5, 175

Sotin, C., Tobie, G., Wahr, J., & Mckinnon, W., Tides and Tidal Heating on Europa. 2009, Europa

Soto, A., Mischna, M., Schneider, T., Lee, C., & Richardson, M., Martian atmospheric collapse: Idealized GCM studies. 2015, *Icarus*, 250, 553

Spohn, T. & Schubert, G., Oceans in the icy Galilean satellites of Jupiter? 2003, *Icarus*, 161, 456

Sullivan, P. W., Winn, J. N., Berta-Thompson, Z. K., et al., The Transiting Exoplanet Survey Satellite: Simulations of Planet Detections and Astrophysical False Positives. 2015, *ApJ*, 809, 77

Teinturier, L. 2024, Caractérisation et modélisation 3D de l'atmosphère d'exoplanètes et de naines brunes, par courbe de phases, Ph.D. thesis, 2024UNIP7010

Teinturier, L., Charnay, B., Spiga, A., et al., The radiative and dynamical impact of clouds in the atmosphere of the hot Jupiter WASP-43 b. 2024, *A&A*, 683, A231

Toon, O. B., McKay, C. P., Ackerman, T. P., & Santhanam, K., Rapid calculation of radiative heating rates and photodissociation rates in inhomogeneous multiple scattering atmospheres. 1989, *J. Geophys. Res.*, 94, 16287

Tran, H., Boulet, C., Stefani, S., Snels, M., & Piccioni, G., Measurements and modelling of high pressure pure CO2 spectra from 750 to 8500cm-1. I—central and wing regions of the allowed vibrational bands. 2011, *Journal of Quantitative Spectroscopy and Radiative Transfer*, 112, 925

Tran, H., Hartmann, J. M., Rambinison, E., & Turbet, M., Collision-induced absorptions by pure CO₂ in the infrared: New measurements in the 1150–4500 cm⁻¹ spectral range and empirical modeling for applications. 2024, *Icarus*, 422, 116265

Tran, H., Turbet, M., Chelin, P., & Landsheere, X., Measurements and modeling of absorption by CO2 + H2O mixtures in the spectral region beyond the CO2 ν3-band head. 2018, *Icarus*, 306, 116

Triaud, A. H. M. J. 2021, in ExoFrontiers; Big Questions in Exoplanetary Science, ed. N. Madhusudhan (IOP Publishing), 6–1

Turbet, M. 2018, Habitability of planets using numerical climate models. Application to extrasolar planets and early Mars., Theses, Sorbonne Université / Université Pierre et Marie Curie - Paris VI

Turbet, M., Bolmont, E., Bourrier, V., et al., A Review of Possible Planetary Atmospheres in the TRAPPIST-1 System. 2020a, *Space Science Reviews*, 216, 100

Turbet, M., Bolmont, E., Chaverot, G., et al., Day-night cloud asymmetry prevents early oceans on Venus but not on Earth. 2021, *Nature*, 598, 276

Turbet, M., Bolmont, E., Ehrenreich, D., et al., Revised mass-radius relationships for water-rich rocky planets more irradiated than the runaway greenhouse limit. 2020b, *A&A*, 638, A41

Turbet, M., Bolmont, E., Leconte, J., et al., Modeling climate diversity, tidal dynamics and the fate of volatiles on TRAPPIST-1 planets. 2018, *A&A*, 612, A86

Turbet, M., Boulet, C., & Karman, T., Measurements and semi-empirical calculations of CO_2 + CH_4 and CO_2 + H_2 collision-induced absorption across a wide range of wavelengths and temperatures. Application for the prediction of early Mars surface temperature. 2020c, *Icarus*, 346, 113762

Turbet, M., Fauchez, T. J., Leconte, J., et al., Water condensation zones around main sequence stars. 2023, *A&A*, 679, A126

Turbet, M., Forget, F., Leconte, J., Charnay, B., & Tobie, G., CO_2 condensation is a serious limit to the deglaciation of Earth-like planets. 2017, *EPSL*, 476, 11

Underwood, D. S., Tennyson, J., Yurchenko, S. N., et al., ExoMol molecular line lists – XIV. The rotation–vibration spectrum of hot SO2. 2016, *MNRAS*, 459, 3890

Vinson, A. M., Tamayo, D., & Hansen, B. M. S., The chaotic nature of TRAPPIST-1 planetary spin states. 2019, *MNRAS*, 488, 5739

Wachiraphan, P., Berta-Thompson, Z. K., Diamond-Lowe, H., et al. 2024, The Thermal Emission Spectrum of the Nearby Rocky Exoplanet LTT 1445A b from JWST MIRI/LRS, https://arxiv.org/abs/2410.10987

Ward, P. & Brownlee, D. 2000, Rare earth : why complex life is uncommon in the universe

Wassmann, M., Moeller, R., Rabbow, E., et al., Survival of Spores of the UV-Resistant Bacillus subtilis Strain MW01 After Exposure to Low-Earth Orbit and Simulated Martian Conditions: Data from the Space Experiment ADAPT on EXPOSE-E. 2012, *Astrobiology*, 12, 498

Watanabe, Y. & Ozaki, K., Relative Abundances of CO2, CO, and CH4 in Atmospheres of Earth-like Lifeless Planets. 2024, *ApJ*, 961, 1

Weiner Mansfield, M., Xue, Q., Zhang, M., et al., No Thick Atmosphere on the Terrestrial Exoplanet Gl 486b. 2024, *ApJ*, 975, L22

Welbanks, L., Nixon, M. C., McGill, P., et al., The Challenges of Detecting Gases in Exoplanet Atmospheres. 2025, *arXiv e-prints*, arXiv:2504.21788

Wordsworth, R., Atmospheric Heat Redistribution and Collapse on Tidally Locked Rocky Planets. 2015, *ApJ*, 806, 180

Wordsworth, R., Forget, F., Millour, E., et al., Global modelling of the early martian climate under a denser CO_2 atmosphere: Water cycle and ice evolution. 2013, *Icarus*, 222, 1

Wordsworth, R. D., Forget, F., Selsis, F., et al., Gliese 581d is the First Discovered Terrestrial-mass Exoplanet in the Habitable Zone. 2011, *ApJ*, 733, L48

Wordsworth, R. D., Kerber, L., Pierrehumbert, R. T., Forget, F., & Head, J. W., Comparison of "warm and wet" and "cold and icy" scenarios for early Mars in a 3-D climate model. 2015, *J. Geophys. Res. (Plan.)*, 120, 1201

Xue, Q., Bean, J. L., Zhang, M., et al., JWST Thermal Emission of the Terrestrial Exoplanet GJ 1132b. 2024, *ApJ*, 973, L8

Yurchenko, S. N., Mellor, T. M., Freedman, R. S., & Tennyson, J., ExoMol line lists – XXXIX. Ro-vibrational molecular line list for CO2. 2020, *MNRAS*, 496, 5282

Zahnle, K. J. & Catling, D. C., The Cosmic Shoreline: The Evidence that Escape Determines which Planets Have Atmospheres, and what this May Mean for Proxima Centauri B. 2017, *ApJ*, 843, 122

Zhang, M., Hu, R., Inglis, J., et al., GJ 367b Is a Dark, Hot, Airless Sub-Earth. 2024, *ApJ*, 961, L44

Zhang, X. & Showman, A. P., Effects of Bulk Composition on the Atmospheric Dynamics on Close-in Exoplanets. 2017, *ApJ*, 836, 73

Zieba, S., Kreidberg, L., Ducrot, E., et al., No thick carbon dioxide atmosphere on the rocky exoplanet TRAPPIST-1 c. 2023, *Nature*, 620, 746

Zieba, S., Zilinskas, M., Kreidberg, L., et al., K2 and Spitzer phase curves of the rocky ultra-short-period planet K2-141 b hint at a tenuous rock vapor atmosphere. 2022, *A&A*, 664, A79

A. Gillon & Ducrot et al. 2025

The following appendix is the manuscript of Gillon et al. (2025), accepted in Nature Astronomy. It is the observational paper companion to Maurel et al. (2025), presented in Chapter 3.

First JWST thermal phase curves of temperate terrestrial exoplanets reveal no thick atmosphere around TRAPPIST-1 b and c

Michaël Gillon [1,†*], Elsa Ducrot [1,2,3,†*], Taylor J. Bell [4,5,6], Ziyu Huang [7], Andrew Lincowski [8,9], Xintong Lyu [10], Alice Maurel[11,12], Alexandre Revol [13,14], Eric Agol [8], Emeline Bolmont [13,14], Chuanfei Dong [7], Thomas J. Fauchez [15,16,17], Daniel D.B. Koll [12], Jérémy Leconte [18], Victoria S. Meadows [8], Franck Selsis [18], Martin Turbet [12,18], Benjamin Charnay [2], Laetitia Delrez [1], Brice-Olivier Demory [18,20], Aaron Householder [21,22], Sebastian Zieba [23], David Berardo [21], Achrène Dyrek [3], Billy Edwards [24], Julien de Wit [21], Thomas P. Greene [5], Renyu Hu [25,26], Nicolas Iro [27], Laura Kreidberg [23], Pierre-Olivier Lagage[3], Jacob Lustig-Yaeger [28], Aishwarya Iyer [15]

[1]Astrobiology Research Unit, Université de Liège, Allée du 6 août 19, Liège, 4000, Belgium.
[2]LIRA, Observatoire de Paris, CNRS, Université Paris Diderot, Université Pierre et Marie Curie, 5 place Jules Janssen, 92190 Meudon, France.
[3]AIM, CEA, CNRS, Université Paris-Saclay, Université de Paris, F-91191 Gif-sur-Yvette, France.
[4]Bay Area Environmental Research Institute, NASA Ames Research Center, M.S. 245-6, Moffett Field, 94035 CA.
[5]Space Science and Astrobiology Division, NASA Ames Research Center, M.S. 245-6, Moffett Field, 94035 CA.
[6]AURA for the European Space Agency (ESA), Space Telescope Science Institute, 3700 San Martin Drive, Baltimore, MD 21218, USA.
[7]Department of Astronomy, Boston University, Boston, MA 02215, USA.

[8]Department of Astronomy and NASA Nexus for Exoplanet System Science, Virtual Planetary Laboratory Team, University of Washington, Seattle, WA, USA.
[9]Eastern Wyoming College, Torrington, WY, USA.
[10]Department of Atmospheric and Oceanic Sciences, Peking University, Beijing, China.
[11]Sorbonne Universités, UPMC Université Paris 6 et CNRS, UMR 7095, Institut d'Astrophysique de Paris, 98 bis bd Arago, 75014 Paris, France.
[12]Laboratoire de Météorologie Dynamique/IPSL, CNRS, Sorbonne Université, Ecole Normale Supérieure, Université PSL, Ecole Polytechnique, Institut Polytechnique de Paris, 75005 Paris, France.
[13]Département d'astronomie de l'Université de Genève, Chemin Pegasi, 51, 1290 Sauverny, Switzerland.
[14]Centre sur la Vie dans l'Univers, Université de Genève, Switzerland.
[15]NASA Goddard Space Flight Center, 8800 Greenbelt Road, Greenbelt, MD 20771, USA.
[16]Sellers Exoplanet Environment Collaboration (SEEC), NASA Goddard Space Flight Center, USA.
[17]Integrated Space Science and Technology Institute, Department of Physics, American University, Washington DC, USA.
[18]Laboratoire d'astrophysique de Bordeaux, Univ. Bordeaux, CNRS, B18N, allée Geoffroy Saint-Hilaire, 33615 Pessac, France.
[19]Center for Space and Habitability, University of Bern, Gesellschaftsstrasse 6, 3012 Bern, Switzerland..
[20]Space Research and Planetary Sciences, Physics Institute, University of Bern, Gesellschaftsstrasse 6, 3012 Bern, Switzerland..
[21]Department of Earth, Atmospheric and Planetary Sciences, Massachusetts Institute of Technology, Cambridge, MA 02139, USA.
[22]Kavli Institute for Astrophysics and Space Research, Massachusetts Institute of Technology, Cambridge, MA 02139, USA.
[23]Center for Astrophysics, Harvard & Smithsonian, 60 Garden Street, Cambridge, MA 02138, USA.
[24]SRON, Netherlands Institute for Space Research, Niels Bohrweg 4, NL-2333 CA, Leiden, The Netherlands.
[25]Jet Propulsion Laboratory, California Institute of Technology, Pasadena, CA 91109, USA.
[26]Division of Geological and Planetary Sciences, California Institute of Technology, CA 91125, USA.
[27]Institut für Planetenforschung, Deutsches Zentrum für Luft- und Raumfahrt (DLR), D-12489 Berlin, Germany.

[28]Johns Hopkins Applied Physics Laboratory, Laurel, Maryland 20723, USA.

*Corresponding author(s). E-mail(s): michael.gillon@uliege.be; elsa.ducrot@obspm.fr;
† These authors contributed equally to this work.

Abstract

We report JWST/MIRI 15 $\boldsymbol{\mu}$m phase curves of TRAPPIST-1 b and c, revealing thermal emissions consistent with their irradiation levels, assuming no efficient heat redistribution. We find that TRAPPIST-1 b shows a high dayside brightness temperature (490 $\pm$ 17 K), no significantly detectable nightside emission ($\boldsymbol{F_{\mathrm{b,Night,max}} = 39^{+55}_{-27}}$ ppm), and no phase offset—features consistent with a low-albedo, airless ultramafic rocky surface. TRAPPIST-1 c exhibits a lower dayside brightness temperature (369 $\pm$ 23 K), and a nightside flux statistically indistinguishable from that of TRAPPIST-1 b ($\boldsymbol{F_{\mathrm{c,Night,max}} = 62^{+60}_{-43}}$ ppm). Atmosphere models with surface pressures $\geq$1 bar and efficient greenhouse effects are strongly disfavored for both planets. TRAPPIST-1 b is unlikely to possess any substantial atmosphere, while TRAPPIST-1 c may retain a tenuous, greenhouse-poor $\boldsymbol{O_2}$-dominated atmosphere or be similarly airless with a more reflective surface. These results suggest divergent evolutionary pathways or atmospheric loss processes, despite similar compositions. These measurements tightly constrain atmosphere retention in the inner TRAPPIST-1 system.

Keywords: Exoplanets, Ultracool Dwarfs

1 Main

Small rocky planets are known to be common in temperate orbits around low-mass M-dwarfs [1]. An outstanding question concerns the survivability of their planets' atmospheres over billions of years. The TRAPPIST-1 system represents a unique laboratory to empirically address this question with JWST [2, 3]. Notably, the two inner planets have irradiations large enough (~4.15 and 2.2 $S_\oplus$) to enable the photometric measurement of their thermal emission with the JWST MIRI instrument. A large thermal emission was measured for the dayside of planet b at 15 μm (program GTO 1177) [4], suggestive of poor atmospheric heat redistribution, and consistent with the emission of a null-albedo bare-rock scenario or with some low-density atmosphere scenarios [5]. More recently, a similar measurement was performed with MIRI at 12.8 μm (program GTO 1279) [6]. The combined analysis of the 12.8 and 15 μm data showed that they could be well fitted by either an airless planet model with a relatively fresh surface (and albedo $\simeq$ 0.1), or by a thick, pure-CO_2 atmosphere with photochemical hazes resulting in CO_2 being seen in emission [6]. For planet c's dayside, a relatively

high thermal emission was measured with MIRI at 15 μm (program GO 2304) that disfavored both a dense CO_2-rich atmosphere or a null albedo bare rock scenario, and left room for some alternative atmospheric (CO_2-poor, low density) and airless (low to moderate albedo surface) scenarios [7], as well as for steam atmospheres [8, 9]. As predicted by ref. [10], these initial observations highlight the challenge of definitively detecting—or ruling out—exoplanet atmospheres based solely on their photometric dayside emission. In this context, ref. [10] demonstrated that phase curves are essential to detect or rule out the presence of atmospheres through nightside thermal emission.

Thanks to their resonant orbits and fortuitous orientation, planets b and c regularly have their thermal curves 'in phase', meaning that their occultations happen at the same time. Their individual phase curves add up then in a constructive way, resulting in a combined phase curve whose amplitude could be boosted up to >1000 ppm in the case of poor heat distribution for both planets. To constrain further the presence/absence of atmospheres around the planets, such a combined phase curve of the two planets was observed at 15 μm with MIRI from Nov 22 to Nov 25, 2023 (Program GO 3077), covering a full phase curve of b and a partial (90%) phase curve of c. These observations were obtained in imaging mode using the BRIGHTSKY (512 × 512 pixels) detector of MIRI and filter F1500W. In total, 5336 integrations were gathered, with a cadence of 39s, resulting in 59 hours of continuous observations. The goal of these observations was to further constrain the presence/absence of an atmosphere around the planets by assessing the efficiency of heat redistribution to their night sides.

Four independent analyses of all existing MIRI data on TRAPPIST-1 at 15μm (secondary eclipses + phase curve) were conducted (see Methods), all yielding consistent results. Among them, the analysis by co-author MG was chosen due to its achieving the smallest standard deviation in the light curve residuals. A brief overview of this 'fiducial' analysis is provided in the main text, with comprehensive details of all four analyses available in the Methods section. The images of program 3077, 1177 and 2304 were calibrated using `Eureka!` [11] and the JWST pipeline (see Methods for details). The photometric extraction was then done on the calibrated images with `IRAF/DAOPHOT` [12] and an aperture radius of 4 pixels. The resulting light curves were normalized and outliers were discarded using a 4-σ clipping algorithm with a 20-min moving median on the fluxes and external parameters. The top panel of Supplementary Fig. 1 shows the resulting raw light curve of program 3077. Its first ∼4 hours contains a large structure that we attribute to an instrumental effect due to the stabilization of the detector. The light curve also shows a double flare-like structure. We discarded the data points corresponding to these two structures.

We performed three global Markov Chain Monte Carlo (MCMC) analyses of the 10 light curves of programs 1177, 2304, and 3077 (Supplementary Table 1) with the code `Trafit` [13, 14]. The selected model included the phase curves of planets b and c, two transits of b, one transit of c, one transit of g, the double occultation of b and c, some planet-planet occultations of c by b, four low-amplitude flares (Fig. 1 and Supplementary Fig. 2), and the low-amplitude transit of a putative planet candidate i with an orbital period larger than h (see Fig. 1 and Extended Data Fig. 3). It also included a model for instrumental systematic effects. A quadratic limb-darkening law [15] was assumed for the star; see Methods for details.

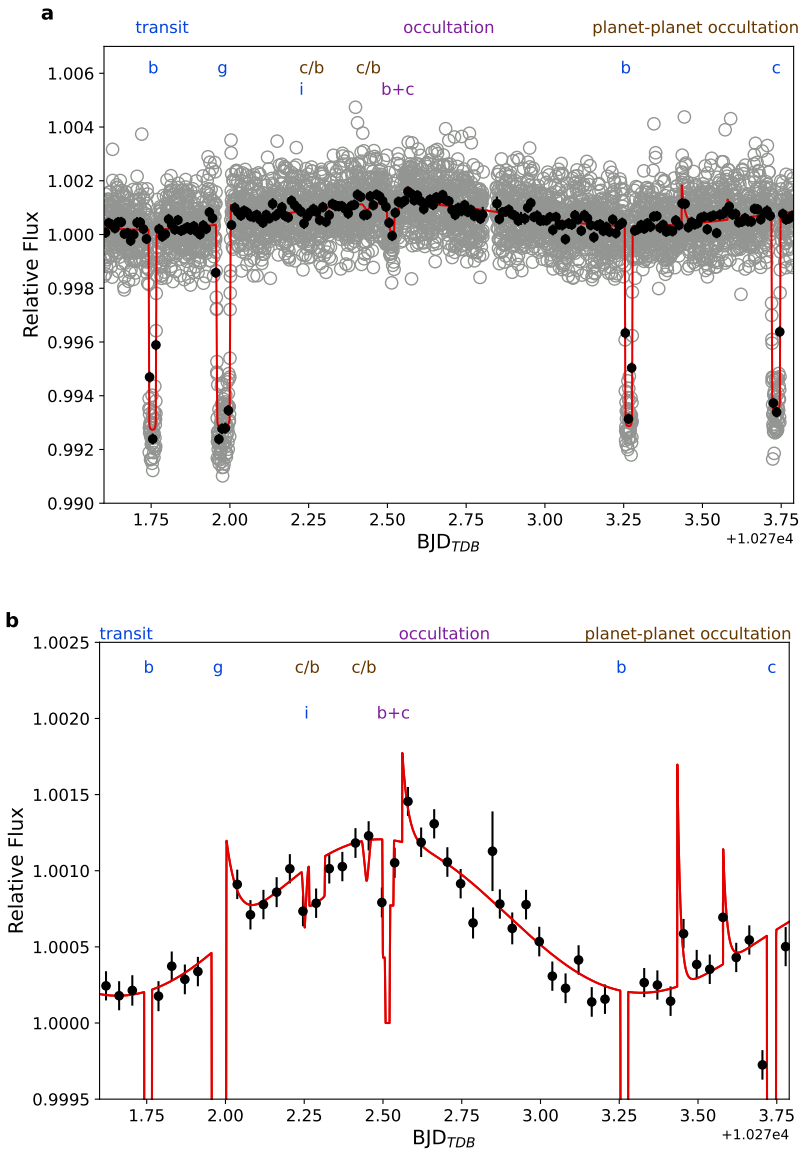

Fig. 1 | Detrended Program 3077 light curve. a. Detrended 3077 program light curve obtained in analysis #1, with the best-fit planet model deduced from the same analysis superimposed. The initial 4 hours of observations are cut as well as the double flares occurring around 2.8 days (see Methods). Transits, occultations, and planet-planet occultations are shown. Points binned per 0.01d (14.4 min) are shown as black dots, with error bars equal to the standard deviation of the points within the bin. **b**. Zoom on the phase curve. In addition to transits of b (1.75, 3.25 days), transits of c (3.75 days), transits of g (1.90 days), transits of putative i (2.26 days), occultations of b and c (2.30 and 2.53 days), and planet-planet occultations of b by c (2.25 and 2.46 days), mini-flares are modeled (2, 2.6, 3.45 and 3.6 days). Only points binned per 60 min are shown for clarity.

Our nominal analysis #1 adopted the phase curve model of ref. [16] assuming that the planets are tidally locked and may have some significant heat distribution, as expected in the presence of an atmosphere. Our second analysis # 2 assumed that both planets were airless and adopted the quasi-Lambertian phase-curve model from ref. [17]. Our third analysis assumed an airless planet phase curve model for b only. The three MCMC analyses assumed informative prior probability distribution functions (PDFs) for some parameters of the system (Extended Data Table 1). The convergence of the MCMC chains was checked using the Gelman and Rubin statistical test [18].

Table 1 shows the median and 1-σ errors of the posterior PDFs of the parameters derived in the three MCMC analyses. The posterior PDFs for the day- and night-side fluxes ($F_{b,day}$, $F_{c,day}$, $F_{b,night}$, $F_{c,night}$) as inferred from analysis #1 are shown in the Methods section for each planet, and for their sum, on Extended Data Fig. 2. Fig. 2 shows the range of best fit models for the global analysis #1 of all existing 15μm observations of TRAPPIST-1 (GTO 1177, GO 2304 and GO 3077) when drawing from the posterior distribution of $F_{b,day}$, $F_{c,day}$, $F_{b,night}$, $F_{c,night}$, and the phase curve offsets δ_b, and δ_c.

The nominal analysis (#1) fully discards a full heat redistribution for both planets. It leads, for planet b, to a night-side flux and a phase curve offset consistent with zero, as expected for a bare rock scenario. The results for c are more ambiguous. They are consistent with an airless scenario, but also leave room for significant heat redistribution (see below). Indeed, the night side flux and the phase curve peak offset are both consistent with zero but also (at 3-σ) with values as large as 232 ppm (vs 392^{+63}_{-75} ppm measured for its occultation depth) and +76 deg, respectively (see Methods). The posterior PDF of the sum of their night-side fluxes is consistent with zero at the 2-σ confidence level (see Methods, Extended Data Fig. 2). The quasi-Lambertian model assumed for both planets in the analysis #2 fits the data as well as the atmosphere model assumed in the analysis #1, further supporting an inefficient heat redistribution for both planets. Analysis #3 does not bring further constraints on the presence/absence of an atmosphere around c.

We compute a Bayes factor of 12.8 in favor of the detection of the occultations of planet c by planet b, which is too low to conclude to a decisive detection (Bayes factor >100 [38]). The transit of the planet candidate i is detected at ∼4 sigma in analysis #1 (transit depth = 305^{+70}_{-80} ppm), but at less than 3 sigma in the two other analyses, which is also too low for a robust detection. If real, this planet would have a radius ∼0.2 $R_\oplus$, similar to Neptune's moon Triton, which would make it the smallest exoplanet known so far. Given the transit duration >2hr, its orbital period should be larger than 20d, but it is very poorly constrained by the data (our inferred posterior PDF closely resembles the assumed prior PDF). Another hypothesis to explain this deviation in the data could be the existence of non-white-noise statistical fluctuation.

To explore the possibility of atmospheres on TRAPPIST-1 b and c, we employed both a day-night climate-photochemical model and a 3-D global climate model (GCM). The day-night climate-photochemical model provides the speed and versatility to model a broad range of potential atmospheric compositions to identify the suite of atmospheres that best fit the phase curves, and the 3-D GCM provides superior

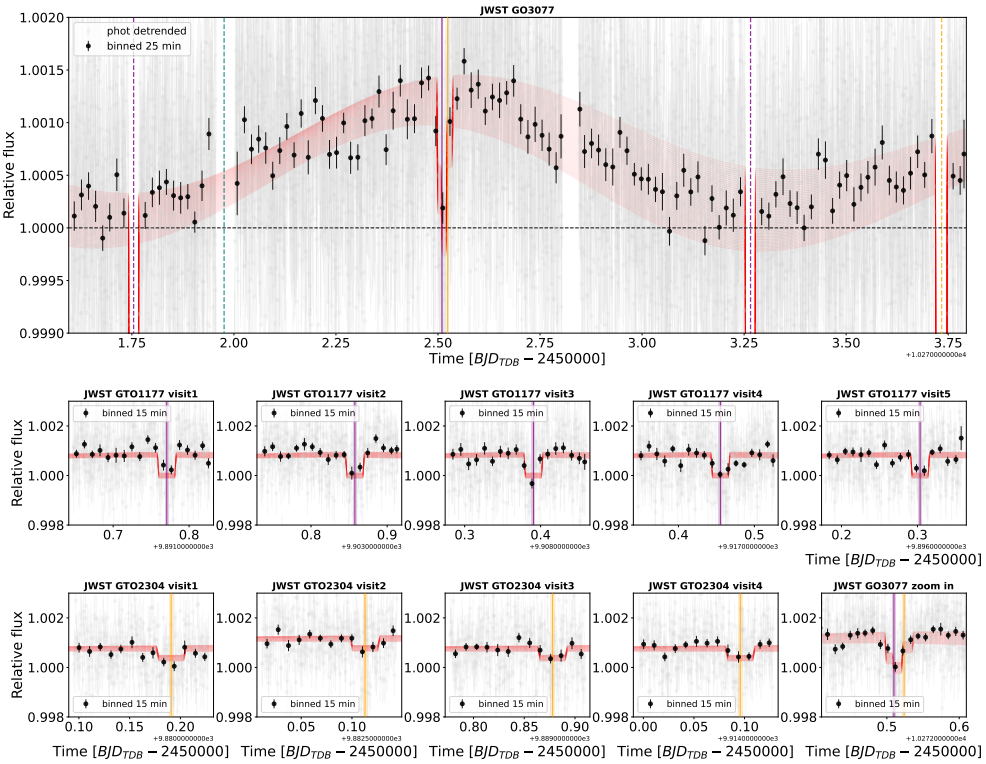

Fig. 2 | Range of best-fit phase curve and eclipse models for TRAPPIST-1 b and c. The detrended data are shown with gray dots and binned data with black dots. Red curves show the light curve model for each JWST program that observed TRAPPIST-1 b and c at 15μm using MIRI F1500W; the shading spans the range of models drawn from the posterior distribution of the day flux, night flux and phase offset for planets b and c from Analysis # 1 at 2-σ. The top panel shows the phase curve from GO 3077; the second row displays the five visits from GO 1177 (PI: Greene); and the third row presents the four visits from GO 2304 (PI: Kreidberg), along with a zoom-in on the double occultation observed in GO 3077. The expected transit and eclipse timings for each planet from [19] are shown in vertical dashed and plain lines respectively (purple for b, orange for c, and green for g).

modeling of the spatial dependence of temperature, which is particularly useful in reproducing the hot substellar region which dominates the dayside phase curve.

Fig. 3 presents the corrected, phase-folded light curves of TRAPPIST-1 b and c. These curves were derived using models that account for both astrophysical signals and instrumental systematics, employing either MCMC or nested sampling methods, in line with standard practice in the field [20–23]. In addition, to isolate each planet's signal, we subtract the contribution of the other planet from the data. The figure also shows the emission spectra of TRAPPIST-1 b and TRAPPIST-1 c. Panel a) highlights scenarios that were previously consistent with broadband dayside measurements but are now ruled out by the phase curve for TRAPPIST-1 b, and panel b) shows those that remain viable. Panel c shows the suite of surface and atmospheric scenarios that are still consistent with the data for TRAPPIST-1 c. We present results from Analysis

#1, which models the phase curves of both planets with sinusoidal shapes. We note that the different analyses (#1, #2, and #3) retrieve slightly different light curve shapes due to differences in model assumptions and parameterizations. For example, Analysis #1 fits six parameters to model the phase variations—$F_{b,\mathrm{day}}$, $F_{c,\mathrm{day}}$, $F_{b,\mathrm{night}}$, $F_{c,\mathrm{night}}$, δ_b, and δ_c—while Analysis #2 fits only four: $F_{b,\mathrm{day}}$, $F_{c,\mathrm{day}}$, γ_b, and γ_c. We emphasize that the suitability of atmospheric or surface models to the observed phase curves should not be assessed based on qualitative fits—such as sigma differences in the light curve shape—because such metrics are highly sensitive to the specific modeling framework. The shape of the phase curve alone is not a robust basis for comparison. Instead, meaningful evaluation should rely on the posteriors of the physical parameters sampled in the MCMC analysis. Accordingly, the sigma values shown in Fig. 3 reflect differences between the inferred dayside flux, nightside flux, and offset relative to various atmospheric models.

Fig. 3 shows the results of self consistent, day–night climate-photochemical-equilibrium atmospheres of a broad range of atmospheric types for TRAPPIST-1 b and c, with layer-by-layer day–night advection using the VPL Climate model in two-column mode (the 1.5D model) [8, 24]. We computed thermal phase curves (see Fig. 3) and occultation spectra for comparison to the data. In panel a, we show that although several 1.5D modeled atmospheres fit the combined 12.8μm and 15μm secondary eclipse measurements to within 2.4σ, they are now ruled out by the day- and night-side measurements of the thermal phase curve, due to excess heat transport to the nightside. These discarded scenarios include N_2 atmospheres of $\geq$ 1 bar (and with 1 ppm CO_2), pure O_2 atmospheres of $\geq$ 10 bar with no extra greenhouse gases, and 0.1 bar O_2 atmospheres containing 100ppm or more of CO_2. For the remaining 1.5D cases we examined (panel b), we find that several of our modeled atmospheres are consistent within 1.5σ of the combined 12.8μm and 15μm secondary eclipse measurements, and also fit the TRAPPIST-1 b phase curves. Notably, largely transparent atmospheres consisting of 1 bar or less of O_2 produce fits to the phase curves at $\leq$ 1.9σ, and a 0.1 bar O_2 atmosphere with greenhouse gases, in this case 0.1% H_2O (with photochemical ozone) fits within $\leq$ 1.6σ. Extremely tenuous 0.01 bar N_2 atmospheres with 100ppm of CO_2 also fit to within 1.8σ. However, this atmosphere is discarded as it is not stable against collapse on the nightside (see 3D results discussion below). For TRAPPIST-1 c, the uncertainty on the data preclude conclusively ruling out any of the 1.5D model atmospheres, although some scenarios appear to provide a better fit than others (Fig. 3 panel c). Similarly to TRAPPIST-1 b, atmospheres with small but non-zero atmospheric opacity and weak day-night heat transport provide better fits. As is the case for TRAPPIST-1 b, the best fits to the TRAPPIST-1 c thermal phase curve come from atmospheres with minimal greenhouse gases: in this case 1 bar pure O_2 (with photochemical ozone), or 0.1 bar O_2 with 1% or less H_2O, or less than 100ppm of CO_2. A steam atmosphere up to 0.1 bar is also not currently ruled out by these data. See Methods for more details about these models and their specific results. For our $\leq$ 2.5σ atmosphere fits, the corresponding transit spectral features (Extended Data Fig. 12) from O_3 and H_2O reach up to 80 ppm for TRAPPIST-1 b. These features are not yet ruled out by the currently available precision of the JWST transit transmission spectra for TRAPPIST-1 b [25].

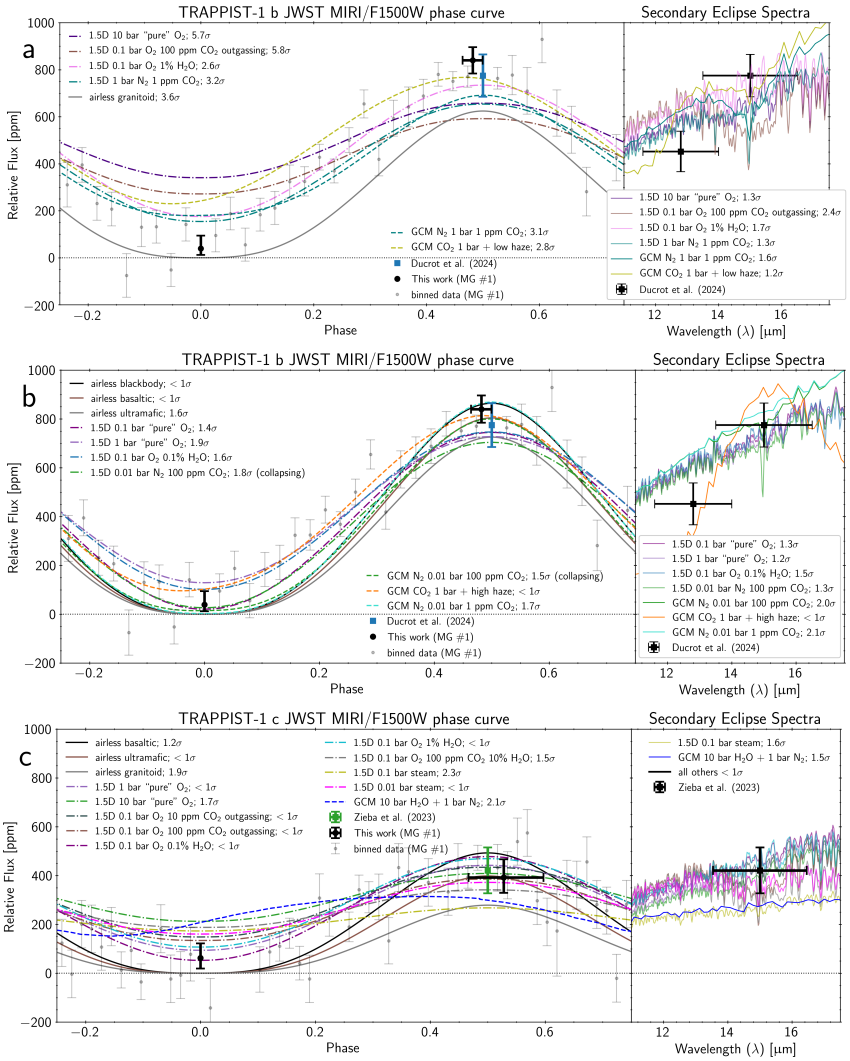

Fig. 3 | Phase-folded phase curves and emission spectra of TRAPPIST-1 b and c. (a) *Right panel:* Secondary eclipse depth measurements of TRAPPIST-1 b from [6], shown alongside a set of atmospheric models that were previously consistent with the data. *Left panel:* The phase curve of TRAPPIST-1 b from this work, with the corresponding dayside flux, nightside flux, and phase offset, all shown with their 1σ error bars. Goodness of fit reported in σ is a joint fit to the day/night phasecurve points, offset, and both data points from [6]. The models on the right that fit the secondary eclipse data are no longer favored once the phase curve data are taken into account. **(b)** Same layout as in (a), but showing models that remain consistent with both the secondary eclipse and the phase curve data. The TRAPPIST-1 b phase curve measurements are consistent with either a thin oxygen atmosphere with a small amount of water vapor (e.g., 1% H_2O), or a thicker atmosphere largely devoid of greenhouse gases (e.g., a 0.1-bar "pure" O_2 atmosphere). **(c)** Same format as above, but for TRAPPIST-1 c. *Right panel:* Secondary eclipse depth measurements from [7], along with atmospheric models that are still consistent with the data. *Left panel:* Phase curve of TRAPPIST-1 c from this work, with the derived dayside flux, nightside flux, and offset, all with 1σ error bars. The signal-to-noise ratio is lower for TRAPPIST-1 c, which makes it difficult to conclusively rule out any of these cases, although several of them appear to produce better fits including 0.1–1 bar "pure" O_2 atmospheres with photochemically generated O_3, and a 0.1 bar O_2-dominated atmosphere containing 1% H_2O and 100 ppm CO_2 (see Table Extended Data Table 6). For all panels, the data shown correspond to the nominal reduction (Analysis #1) by MG, binned at ∼60-minute intervals.

We then performed 3-D Global Climate Model (GCM) simulations of TRAPPIST-1b and c with the `Generic PCM` [9, 26] in order to assess whether phase curves could be used to constrain the atmospheres that are still plausible based on occultations alone [4, 6, 7] (see details of the calculations in the Methods). For TRAPPIST-1b, this includes thin, residual atmospheres [5] as well as CO_2-rich atmospheres with a hot, hazy stratosphere [6]. We represented here two end-member cases (*Haze high* and *Haze low*) of CO_2 atmospheres with maximal and minimal amounts of haze, respectively. Resolving the 3-D structure of the atmosphere is necessary to accurately represent the energy transport and phase offsets in all atmospheric layers. Fig. 3 a. and b. (right panels) shows the comparison between the observed phase curve and the synthetic phase curves computed from GCM simulations, carefully selected so that they match the available occultation measurements within 2.4σ [4, 6, 7]. We find that, for TRAPPIST-1 b, among the atmospheric cases still compatible with the occultations (see Extended Data Fig. 13), the values of the dayside flux, nightside flux and peak offset of the phase curves can be used to rule out atmospheric scenarios that produce non-negligible horizontal transport, which includes scenarios with a thick atmosphere (e.g., the 1 bar N_2 1 ppm CO_2 case) and CO_2-rich atmospheres with hazes that absorbs too deep in the atmosphere (e.g., the *Haze low* scenario, for which we also predict a significant phase curve offset). Some cases can also be discarded (e.g., the N_2 0.01 bar 100 ppm CO_2 case) because the GCM predicts CO_2 to collapse on the surface [26, 27]. Although not all atmospheric scenarios can be theoretically ruled out with all data now available (see Fig. 3a. and Fig. 3b.), those that remain (CO_2 1 bar + *Haze high*, N_2 0.01 bar 1ppm CO_2) appear to be very fine-tuned, and the most likely hypothesis is that TRAPPIST-1 b has no atmosphere, which is consistent with the prediction from the theoretical study of secondary atmospheric escape [28] (not considering possible replenishment via out-gassing). For TRAPPIST-1 c, the amplitude of the phase curve can be used to rule out atmospheric scenarios involving efficient heat redistribution as well, including the case of steam atmospheres [8, 9] which were compatible with the secondary eclipses of ref. [7] (see Methods), but also a possible outcome of atmospheric evolution. Additionally, we computed transit spectra (see Methods, Extended Data Fig. 13) for the atmospheres of TRAPPIST-1 b which are still compatible with all MIRI datasets (GTO 1177, GO 2304, GTO 1279,GO 3077) to assess the impact of using innermost planets (e.g. TRAPPIST-1b) to remove stellar contamination from the transit spectra of other, outer planets [29] as recently demonstrated by ref. [30]. We found that the amplitude of absorption features in TRAPPIST-1 b transit spectra (see Extended Data Fig. 13) is low but non-negligible, in particular for the (unlikely) CO_2-rich hazy atmospheric scenario.

Comparing the two sets of modeling results for TRAPPIST-1 b, both the day-night climate-photochemical and 3D GCM models are ruled out by the data for the proposed 1 bar N_2 or O_2 atmospheres with trace ($\leq$1 ppm) greenhouse gases (CO_2 and O_3). The data do not reject models with 0.01 bar N_2 and 100 ppm CO_2; however, the 3D GCM shows that this atmosphere is unstable to collapse, and therefore not a viable scenario. The self-consistent photochemically-generated hazy atmospheres did not fit the phase curves, and to fit both the phase curve and the 12.8 and 15μm secondary eclipse data, the 3D GCMs showed that unlikely densities of hydrocarbon

haze particles would be required. For TRAPPIST-1 c, the day-night model showed good fits for 0.1-1 bar pure O_2 and 0.1 bars of O_2 with small amounts of greenhouse gases (photochemical O_3 and 0.1% H_2O). The combined (two-column and 3D GCM) model results disfavor steam-dominated atmospheres from 1 bar to 10 bars.

Next, because the data for TRAPPIST-1 b are consistent with no atmosphere whatsoever, we model TRAPPIST-1 b's thermal phase curve using a bare rock model and a database of seven geologically fresh surface materials [31]. Note that our models produce noticeably higher albedos than previous surface models published for TRAPPIST-1 b based on the same database [5, 6], largely because these previous models were based on [32] which used an erroneous albedo conversion between spherical albedo and geometric albedo [33].

Overall, we find that TRAPPIST-1 b's phase curve indicates the surface should not be very dark, while the planet's secondary eclipse spectrum is able to rule out the blackbody surface. For the eclipse spectrum we combine the 15μm eclipse depth from analysis # 2 with the reported secondary eclipse at 12.8μm from [6]. We find that the spectrum is best fit by ultramafic albedo surfaces(see Extended Data Fig. 18). Moreover, the planet's phase curve also suggests the planet's surface is likely to be fresh ultramafic (see Extended Data Fig. 17). Although secondary eclipse spectrum doesn't prefer ultramafic over other materials by 3σ, the fitting is well enough which makes ultramafic most likely to be TRAPPIST-1 b's composition. One hypothesis to affect the fitting is space weathering, which in the Solar System acts to darken and redden the surface spectra of airless bodies like the Moon and Mercury [34], and which is likely even more efficient for the inner TRAPPIST-1 planets than in the Solar System [7]. We find that moderate amounts of space weathering significantly reduce the planet's albedo and warm the dayside surface, thus increasing its phase curve amplitude (see Extended Data Fig. 18). In this case, adding a few amount of space weathering material on planetary surface, feldspathic and granitoid could also be a good fit on TRAPPIST-1 b.

This work demonstrates the potential of JWST to assess the presence of dense secondary atmospheres around temperate ($T_{eq} < 400$ K) Earth-sized planets transiting nearby ultracool dwarf stars using thermal phase curves. It shows that it is highly unlikely that TRAPPIST-1 b has a significant atmosphere. The case of TRAPPIST-1 c is more ambiguous. On one hand, a full heat redistribution is discarded by the data, and most dense atmosphere ($> 1bar$) scenarios [8] consistent with the 15 μm occultation measurement [7] are now disfavored, leaving room only for a low opacity atmosphere of 1 bar of pure O_2, or thin atmospheres with pressures < 0.1 bar and traces of CO_2 and water. On the other hand, assuming both planets are airless leads to the conclusion that the surface properties of planet c must differ from those of planet b (which is not unexpected when compared to the variety of planetary surface types observed in the solar system). Indeed, the dayside brightness temperature inferred from analysis #1 is significantly larger than the equilibrium temperature (assuming a full heat distribution and a null Bond Albedo) for planet b (490 ± 17 K vs 398$\pm$4 K [35]), but not for planet c (369 ± 23 K vs 340$\pm$3 K [35]). This difference could be explained by a larger surface albedo for c, but also by a poor but non-null heat redistribution consistent with a thin atmosphere. This difference justifies the need to

further characterize TRAPPIST-1 c with JWST. Upcoming observations of its thermal emission at 12.8 μm (program GO 5191) will make it possible to discriminate between more scenarios. In parallel, transmission spectroscopy observations (GO 2589 + GO 2420) will provide additional constraints on the presence of molecules such as CO_2 in a putative atmosphere.

References

[1] Ment, K. & Charbonneau, D. The Occurrence Rate of Terrestrial Planets Orbiting Nearby Mid-to-late M Dwarfs from TESS Sectors 1-42. *Astron. J.* **165**, 265 (2023).

[2] Gillon, M. *et al.* The trappist-1 jwst community initiative. *Bulletin of the AAS* **52** (2020). URL http://dx.doi.org/10.3847/25c2cfeb.afbf0205.

[3] Lustig-Yaeger, J., Meadows, V. S. & Lincowski, A. P. The Detectability and Characterization of the TRAPPIST-1 Exoplanet Atmospheres with JWST. *Astron. J.* **158**, 27 (2019).

[4] Greene, T. P. *et al.* Thermal emission from the Earth-sized exoplanet TRAPPIST-1 b using JWST. *Nature* **618**, 39–42 (2023).

[5] Ih, J., Kempton, E. M. R., Whittaker, E. A. & Lessard, M. Constraining the Thickness of TRAPPIST-1 b's Atmosphere from Its JWST Secondary Eclipse Observation at 15 μm. *Astrophys. J. Lett.* **952**, L4 (2023).

[6] Ducrot, E. *et al.* Combined analysis of the 12.8 and 15 μm JWST/MIRI eclipse observations of TRAPPIST-1 b. *Nature Astronomy* (2024).

[7] Zieba, S. *et al.* No thick carbon dioxide atmosphere on the rocky exoplanet TRAPPIST-1 c. *Nature* **620**, 746–749 (2023).

[8] Lincowski, A. P. *et al.* Potential Atmospheric Compositions of TRAPPIST-1 c Constrained by JWST/MIRI Observations at 15 μm. *Astrophys. J. Lett.* **955**, L7 (2023).

[9] Turbet, M. *et al.* Water condensation zones around main sequence stars. *Astron. Astrophys.* **679**, A126 (2023).

[10] Hammond, M. *et al.* Reliable Detections of Atmospheres on Rocky Exoplanets with Photometric JWST Phase Curves. *Astrophys. J. Lett.* **978**, L40 (2025).

[11] Bell, T. *et al.* Eureka!: An End-to-End Pipeline for JWST Time-Series Observations. *The Journal of Open Source Software* **7**, 4503 (2022).

[12] Stetson, P. B. DAOPHOT: A Computer Program for Crowded-Field Stellar Photometry. *Publ. Astron. Soc. Pac.* **99**, 191 (1987).

[13] Gillon, M. *et al.* The Spitzer search for the transits of HARPS low-mass planets. I. No transit for the super-Earth HD 40307b. *Astron. Astrophys.* **518**, A25 (2010).

[14] Gillon, M. *et al.* The TRAPPIST survey of southern transiting planets. I. Thirty eclipses of the ultra-short period planet WASP-43 b. *Astron. Astrophys.* **542**, A4 (2012).

[15] Mandel, K. & Agol, E. Analytic Light Curves for Planetary Transit Searches. *Astrophys. J. Lett.* **580**, L171–L175 (2002).

[16] Placek, B., Knuth, K. H. & Angerhausen, D. Exonest: Bayesian model selection applied to the detection and characterization of exoplanets via photometric variations. *Astrophys. J.* **795**, 112 (2014). URL https://dx.doi.org/10.1088/0004-637X/795/2/112.

[17] Agol, E. Rounding up the wanderers: optimizing coronagraphic searches for extrasolar planets. *Mon. Not. R. Astron. Soc.* **374**, 1271–1289 (2007).

[18] Gelman, A. & Rubin, D. B. Inference from Iterative Simulation Using Multiple Sequences. *Statistical Science* **7**, 457–472 (1992).

[19] Agol, E. *et al.* Refining the Transit-timing and Photometric Analysis of TRAPPIST-1: Masses, Radii, Densities, Dynamics, and Ephemerides. *Planet. Sci. J.* **2**, 1 (2021).

[20] Mikal-Evans, T. *et al.* A JWST NIRSpec Phase Curve for WASP-121b: Dayside Emission Strongest Eastward of the Substellar Point and Nightside Conditions Conducive to Cloud Formation. *Astrophys. J. Lett.* **943**, L17 (2023).

[21] Kempton, E. M. R. *et al.* A reflective, metal-rich atmosphere for GJ 1214b from its JWST phase curve. *Nature* **620**, 67–71 (2023).

[22] Zhang, M. *et al.* GJ 367b Is a Dark, Hot, Airless Sub-Earth. *Astrophys. J. Lett.* **961**, L44 (2024).

[23] Bell, T. J. *et al.* Nightside clouds and disequilibrium chemistry on the hot Jupiter WASP-43b. *arXiv e-prints* arXiv:2401.13027 (2024).

[24] Lincowski, A. P. *et al.* Evolved Climates and Observational Discriminants for the TRAPPIST-1 Planetary System. *Astrophys. J.* **867**, 76 (2018).

[25] Lim, O. *et al.* Atmospheric Reconnaissance of TRAPPIST-1 b with JWST/NIRISS: Evidence for Strong Stellar Contamination in the Transmission Spectra. *arXiv e-prints* arXiv:2309.07047 (2023).

[26] Turbet, M. *et al.* Modeling climate diversity, tidal dynamics and the fate of volatiles on TRAPPIST-1 planets. *Astron. Astrophys.* **612**, A86 (2018).

[27] Turbet, M. *et al.* A Review of Possible Planetary Atmospheres in the TRAPPIST-1 System. *Space Sci. Rev.* **216**, 100 (2020).

[28] Dong, C. *et al.* Atmospheric escape from the TRAPPIST-1 planets and implications for habitability. *Proc. Natl Acad. Sci. USA* **115**, 260–265 (2018).

[29] TRAPPIST-1 JWST Community Initiative *et al.* A roadmap to the efficient and robust characterization of temperate terrestrial planet atmospheres with JWST. *arXiv e-prints* arXiv:2310.15895 (2023).

[30] Rathcke, A. D. *et al.* Stellar contamination correction using back-to-back transits of trappist-1 b and c (2024). URL https://arxiv.org/abs/2412.16541. 2412.16541.

[31] Lyu, X. *et al.* Super-earth lhs3844b is tidally locked. *Astrophys. J.* **964**, 152 (2024). URL http://dx.doi.org/10.3847/1538-4357/ad2077.

[32] Mansfield, M. *et al.* Identifying Atmospheres on Rocky Exoplanets through Inferred High Albedo. *Astrophys. J.* **886**, 141 (2019).

[33] Coy, B. P. *et al.* Population-level Hypothesis Testing with Rocky Planet Emission Data: A Tentative Trend in the Brightness Temperatures of M-Earths (2025).

[34] Pieters, C. M. & Noble, S. K. Space weathering on airless bodies. *J. Geophys. Res.: Planets* **121**, 1865–1884 (2016).

[35] Ducrot, E. *et al.* TRAPPIST-1: Global results of the Spitzer Exploration Science Program Red Worlds. *Astron. Astrophys.* **640**, A112 (2020).

[36] Gillon, M. *et al.* Temperate Earth-sized planets transiting a nearby ultracool dwarf star. *Nature* **533**, 221–224 (2016).

[37] Fauchez, T. J., Rackham, B. V., Ducrot, E., Stevenson, K. B. & de Wit, J. Stellar Models Also Limit Exoplanet Atmosphere Studies in Emission. *arXiv e-prints* arXiv:2502.19585 (2025).

Parameter	Analysis #1	Analysis #2	Analysis #3
Planet b			
Mid-transit timing (transit 1)	271.754380 ± 0.000088	271.754375 ± 0.000088	271.754377 ± 0.000088
Mid-transit timing (transit 2)	273.265974 ± 0.000084	273.265972 ± 0.000084	273.265974 ± 0.000084
Semi-major axis a	0.011513 ± 0.000078 au	0.0115256 ± 0.000081 au	0.0115185 ± 0.000086 au
Orbital inclination i	89.70 ± 0.13 deg	89.72 ± 0.13 deg	89.71 ± 0.14 deg
Impact parameter b	0.107 ± 0.047 R_*	$0.103^{+0.044}_{-0.050}$ R_*	$0.106^{+0.47}_{-0.50}$ R_*
Transit depth $dF = (Rp/R_*)^2$	7316 ± 117 ppm	7338 ± 112 ppm	7358^{+109}_{-114} ppm
Eccentricity e	$0.0008^{+0.0022}_{-0.0006}$	$0.0008^{+0.0020}_{-0.0006}$	$0.0008^{+0.0021}_{-0.0006}$
Argument of pericenter ω	203^{+68}_{-114} deg	181 ± 90 deg	200^{+71}_{-108} deg
$A = F_{\mathrm{b,D,max}}$	840 ± 56 ppm	751 ± 53 ppm	778 ± 64 ppm
$B = F_{\mathrm{b,N,max}}$	39^{+55}_{-27} ppm	0 ppm (fixed)	0 ppm (fixed)
Peak offset δ	-6.5 ± 6.4 deg	0 deg (fixed)	0 deg (fixed)
γ	-	2.44 ± 0.37	$2.61^{+0.41}_{-0.33}$
$T_{\mathrm{brightness,D}}$	490 ± 17 K	469 ± 17 K	473 ± 19 K
$T_{\mathrm{brightness,N}}$	197 ± 41 K	0 K (fixed)	0 K (fixed)
Planet c			
Mid-transit timing (BJD_{TDB} - 2460000)	273.733263 ± 0.000096	273.733264 ± 0.000096	273.733269 ± 0.000096
Semi-major axis a	0.01577 ± 0.00011 au	0.01579 ± 0.00012 au	0.01578 ± 0.00012 au
Orbital inclination i	89.813 ± 0.092 deg	89.798 ± 0.087 deg	89.793 ± 0.099 deg
Impact parameter b	0.092 ± 0.046 R_*	0.100 ± 0.043 R_*	0.102 ± 0.048 R_*
Transit depth $dF = Rp/R_*$	7098^{+133}_{-149} ppm	7146 ± 131 ppm	7134^{+124}_{-141} ppm
Eccentricity e	$0.0011^{+0.0013}_{-0.0007}$	$0.0012^{+0.0016}_{-0.0008}$	$0.0012^{+0.0014}_{-0.0008}$
Argument of pericenter ω	161^{+85}_{-61} deg	178 ± 76 deg	160^{+86}_{-59} deg
$A = F_{\mathrm{c,D,max}}$	392^{+75}_{-63} ppm	359^{+68}_{-55} ppm	413^{+66}_{-72} ppm
$B = F_{\mathrm{c,N,max}}$	62^{+60}_{-43} ppm	0 ppm (fixed)	102^{+97}_{-73} ppm
Peak offset δ	10^{+25}_{-22} deg	0 deg (fixed)	-12^{+20}_{-15} deg
γ	-	3.34 ± 0.46	-
$T_{\mathrm{brightness,D}}$	369 ± 23 K	357 ± 21 K	374 ± 25 K
$T_{\mathrm{brightness,N}}$	220^{+38}_{-47} K	0 K (fixed)	247^{+48}_{-60} K
Planet b + c			
$A = F_{\mathrm{b+c,D,max}}$	1231^{+93}_{-70} ppm	1117^{+66}_{-72} ppm	1189 ± 81
$B = F_{\mathrm{b+c,N,max}}$	116^{+70}_{-57} ppm	0 ppm (fixed)	102^{+97}_{-73} ppm
Planet g			
Mid-transit timing	271.97948 ± 0.00013	271.97955 ± 0.00011	271.97954 ± 0.00012
Semi-major axis a	0.04673 ± 0.00032 au	0.04678 ± 0.00033 au	0.04675 ± 0.00035 au
Orbital inclination i	89.7459 ± 0.0087 deg	89.7464 ± 0.0091 deg	89.745 ± 0.010 deg
Impact parameter b	0.373 ± 0.012 R_*	0.373 ± 0.012 R_*	0.374 ± 0.014 R_*
Transit depth $dF = Rp/R_*$	7563^{+138}_{-124} ppm	7726^{+185}_{-137} ppm	7680^{+129}_{-128} ppm
Eccentricity e	$0.00092^{+0.00099}_{-0.00065}$	$0.0009^{+0.0010}_{-0.0006}$	$0.0009^{+0.0010}_{-0.0007}$
Argument of pericenter ω	184^{+114}_{-121} deg	196^{+109}_{-128} deg	181 ± 120 deg
Candidate planet i			
Mid-transit timing (BJD_{TDB} - 2460000)	$272.2928^{+0.0038}_{-0.0054}$	$272.289^{+0.015}_{-0.011}$	$272.2921^{+0.0050}_{-0.0066}$
Semi-major axis a	0.081 ± 0.010 au	0.082 ± 0.010au	0.081 ± 0.011 au
Orbital inclination i	$89.79^{+0.12}_{-0.08}$	$89.78^{+0.13}_{-0.20}$	89.77 ± 0.12
Impact parameter b	$0.57^{+0.20}_{-0.31}$ R_*	$0.57^{+0.41}_{-0.35}$ R_*	0.61 ± 0.33 R_*
Period P	28.1 ± 5.0 d	28.5 ± 5.2	$28.4^{+5.1}_{-6.1}$
Transit depth $dF = Rp/R_*$	305^{+70}_{-80} ppm	289^{+326}_{-117} ppm	285^{+210}_{-109} ppm
Radius R_p	$0.228^{+0.025}_{-0.032} R_\oplus$	$0.22^{+0.10}_{-0.51} R_\oplus$	$0.220^{+0.070}_{-0.047} R_\oplus$

Table 1 | Resulting planetary parameters from the global MCMC analyses of data of programs 1177, 2305, and 3077. Analysis # 1: nominal analysis assuming a phase curve model allowing for the possible presence of an atmosphere for both planets. Analysis #2: airless model for both planets. Analysis #3: atmosphere model for c, airless model for b. Transit timings unit = BJD_{TDB}-2460000.

2 Methods

Observations

The observations of program 3077 consisted in the continuous observation of TRAPPIST-1 by the MIRI instrument aboard JWST from Nov 22, 2023 19h45 UT to Nov 25 2023 07h02 UT. These observations were obtained in imaging mode within the F1500W filter ($\lambda_{\text{effective}} = 15.1\mu m$, width = 3.1 μm). Unlike for programs GTO 1177 and GO 2304 that used the FULL array of MIRI (1024 × 1032 pixels), program 3077 used the BRIGHTSKY array (512 pixels × 512 pixels). The target was put on the center of the array. Because of the smaller group time of the BRIGHTSKY array (0.865s *vs* 2.775s for the FULL array), 45 groups could be gathered per integration for a similar signal-to-noise (SNR ∼840) and cadence (∼39s) than programs 1177 and 2304, resulting in a better sampling of the 'ramp' of the detector. JWST detectors are indeed read out using a non-destructive 'up-the-ramp' read-out technique, with the read out divided in several groups composing an integration [39]. For a given integration, a slope is fitted in the counts recorded for all groups to measure the flux of the star in counts per second. The accuracy of this ramp-fitting step depends on the number of groups in the integration, giving a benefit to the selection of the BRIGHTSKY array for the observations. Another benefit is that using a smaller array decreased significantly the data volume, which was convenient for such a long time-series observation. Finally, an extra-benefit of this strategy was a gain of 2.5 hours of overhead time, which allowed more time for the instrument to settle and to maximize the scientific potential of the program.

The start and the end of the observations were based on transit and occultation ephemeris from ref. [19], which successfully predicted a double occultation of planets *b* and *c* around Nov 24, 2023 00h15 UT. The goal was to observe a full phase curve of planet *b*, including two consecutive transits, in phase with a partial phase curve of planet *c* (i.e. with concomitant occultations of both planets), including one of its transits. This program was designed based on the analysis of simulated light curves that confirmed its potential to firmly constrain the heat distribution efficiency of both planets and the absence/presence of an atmosphere around them.

Currently, a single JWST exposure (i.e. a block of integrations in JWST jargon) cannot exceed 48 hours. For that reason, we had to cut the observation into two visits of one exposure each. At the start of the second visit, the telescope had to reacquire the target, resulting in a 5 minute and 45 second gap and a small shift of the target on the detector (see Supplementary Fig. 1). We selected the number of integrations for both visits to ensure that this gap occurs well away from the double occultation, potential planet-planet occultations, and transits. We thus decided to have one first visit of 1 exposure of 3473 integrations, followed by a shorter visit of 1 exposure of 1863 integrations. Doing so, the gap between visits fell within a relatively signal-free part of the light curve (see Supplementary Fig. 1).

Data reduction and analysis (MG)

As in ref. [7], we started the reduction of the data of program 3077 from the raw uncal.fits files available on the MAST website (https://mast.stsci.edu). We first calibrated the data using the first stage (going from groups to slopes and applying basic detector-level corrections) of the `Eureka!` pipeline [11] and the second stage (flat-fielding, unit conversion to MJy.sr^{-1}) of the JWST pipeline, resulting in calibrated calints.fits files. We used a new branch of `Eureka!` (version 0.11.dev77+g1e43198f.d20240130) developed by co-author TJB and using the version 1.13.4 of the JWST pipeline that included the correction of the 10Hz and 390Hz electromagnetic interference (EMI) pattern noise [39]. For stage 1, as in ref. [7], we used the default JWST pipeline settings, except for (1) the ramp-fitting weighting parameter set to `uniform` and (2) the deactivation of the jump correction. We also tested starting directly from the calints.fits files processed by the standard JWST pipeline, but the resulting light curves had lower photometric precision. The rest of the reduction was done using a pipeline coded in `IRAF` and Fortran 2003. It included for each calibrated image (1) a change of unit from MJy.sr^{-1} to recorded electrons, assuming a gain of 3.3 el.s^{-1} (P.-O. Lagage, private comm.), (2) the fit of 1D and 2D Gaussian functions to the point-spread function (PSF) of the star to measure the subpixel position of its centroid and its full width at half maximum (FWHM) in both directions, (3) the measurement of the noise-pixel (as defined in ref. [41]) within a circle of 4 pixels radius, and (4) the measurement of the stellar and background fluxes using circular and annular apertures, respectively, with `IRAF/DAOPHOT` [12]. Finally, the resulting light curve was normalized and outliers were discarded using a 4-σ clipping algorithm with a 20-min moving median on the fluxes, and a 5–σ clipping on the x- and y-positions, FWHM along the x and y directions, noise-pixels, and background measurements. In total, 2.9% of the measurements were flagged as outliers and discarded. The light curves obtained with different photometric apertures were compared, and we selected the one obtained with an aperture radius of 4 pixels as it minimized the errors of the measurements. The background was measured in an annulus extending from 30 to 45 pixels from the center of the PSF. For each stellar flux measurement, the corresponding error was computed taking into account the star and background photon noise, the readout noise and the dark noise.

Supplementary Fig. 1a shows the resulting raw light curve. Its first ∼4 hours contains significant structure. It is concomitant to a ramp-like increase of the background (see Supplementary Fig. 1b top-right panel) extending to BJD ∼2460271.6. After that time, the background shows a linear increase along the whole run. Based on this behavior of the background, we interpret this initial structure as an instrumental effect due to the stabilization of the detector. We thus discarded this initial part of the light curve in our analysis. The light curve shows also the signature of a double flare-like event between BJD 2460272.805 and 2460272.845 (Supplementary Fig. 2a). We discarded the corresponding data points. In the end, we discarded 834 points (including 155 outliers) out of the 5336 points of the raw light curve, i.e. 15%.

The light curve contains transits of planets b (2 transits), c (one transit), and g (one transit), in addition to a double occultation of planets b and c, an occultation of d (which is very shallow and therefore undetected) and some occultations of planet c by

planet b (Fig. 1). Its visual inspection also reveals a low-frequency signal that appears to be consistent with the combined phase-curve variations of the two inner planets.

Our data-analysis methodology used the Fortran 2003 code `Trafit` that includes a revised version of the adaptive Markov chain Monte Carlo code presented in refs. [13, 14] and ref. [42], to perform a global analysis of all available eclipse and phase curve data at 15 μm (GTO 1177, GO 2304, GO 3077), adopting the Metropolis-Hasting algorithm [43] to sample the posterior probability distributions of the system's parameters. The assumed model was composed of the eclipse model from ref. [15] to represent the transits of planets b, c and g, and the double occultation of b and c, a phase curve model for planet b and c, and a baseline model aiming to represent the other astrophysical and instrumental mechanisms able to produce photometric variations. We tested a large range of baseline models and we adopted the one minimizing the Bayesian Information Criterion (BIC, [44]). It was composed of the slope, the sum of second-order polynomials of the x and y position of the PSF's center, an initial decreasing ramp modeled as a linear function of the difference in time relative to the first point of the light curve, and a similar ramp model for points taken during the second visit. Our global model also included planet-planet occultations, using the model of ref. [15] to compute the fraction of each planet occulted by another one at any given time. Our planet occultation models assumed uniform disks for the occulted planets.

For the phase curve model, our nominal analysis (analysis # 1) adopted the one of ref. [16] based on the following formula that assumes that the planets are tidally locked and may have some significant heat distribution, as expected in the presence of an atmosphere:

$$\frac{F_{i,D}(t)}{F_*} = \frac{1}{2}(1 + cos(\theta(i,t) - \delta(i)))\frac{F_{i,D,max}}{F_*}\Omega(i,t) \quad (1)$$

$$\frac{F_{i,N}(t)}{F_*} = \frac{1}{2}(1 + cos(\theta(i,t) - \delta(i) - \pi))\frac{F_{i,N,max}}{F_*}\Omega(i,t) \quad (2)$$

$$\frac{F_i(t)}{F_*} = \frac{F_{i,D}(t)}{F_*} + \frac{F_{i,N}(t)}{F_*} \quad (3)$$

where i represents planet i, with $\theta(i,t)$ its phase angle at time t, $\gamma(i,t)$ its unocculted fraction at time t, $F_{i,D}(t)$ the flux contribution of its day side at time t, $F_{i,N}(t)$ the one of its night side, F_* the average flux of the star, and $\delta(i)$ is an angle offset to take into account a possible West or East shift of the planet's flux peak relative to the substellar point. $F_{i,N,max}$ and $F_{i,D,max}$ are the maxima of the fluxes for the planet's night and day sides. For each time t, the occulted (by the star or another planet) fraction of the planet $\Omega(i,t)$ is computed using the eclipse model of ref. [15].
In a second analysis (analysis # 2), we assumed that both planets were airless and adopted the following model from ref. [17] for their phase curves:

$$\frac{F_i(t)}{F_*} = \frac{F_{i,D,max}}{F_*} \times \cos(\theta(i,t)/2)^{\gamma(i)} \quad (4)$$

where $\gamma(i)$ is a free parameter. Assuming $\gamma(i) \sim 3$, this analytical function was shown to be a good approximation for the phase function of a Lambert sphere by ref. [17]. As analysis #1 led to the firm conclusion that b shows no significant heat redistribution

(see below) but to more ambiguous results for planet c, we performed a third analysis for which we assumed the 'airless' model from eq. (4) for planet b only. In all three analyses, the global model for the light curve was then:

$$F(t) = B(t, X) \times \left(1 + \Sigma_{i=1}^{N} \frac{F_i(t)}{F_*} - E(i, t)\right) \quad (5)$$

where $B(t, X)$ represents the baseline model depending on time t and on an array X of external parameters, N is the number of planets considered, and $E(i, t)$ is the fraction of the star occulted by planet i, taking into account limb-darkening (as computed under the formalism of ref. [15]). In other words, the light curve model is computed as the sum of the flux of the star (taking into account the transits) and the fluxes of the planets (taking into account their occultations) multiplied by a baseline + normalisation model $B(t, X)$. In our analysis, only planets b, c and g were considered. We did some test analyses including the flux contribution of the other planets assuming the extreme case of airless null albedo bodies for all of them, and the results were consistent with the ones obtained from our nominal analysis.

For analysis #1, we performed a preliminary Markov Chain of 20,000 steps to assess the need to rescale the photometric errors for white and red noise (e.g. [14]). The level of red noise of the residuals was anomalously high (see modified Allan's diagram in Extended Data Fig. 3c, black line). A visual examination of the residuals binned to different samplings showed four structures consistent with low-amplitude flare-like structures with decay times of a few dozens of minutes (Extended Data Fig. 3a). As the raw light curve showed a clear double flare (Supplementary Fig. 2a) with a similar exponential decay time, it is reasonable to assume that it also contain lower-amplitude 'mini-flares' responsible for a part of the red noise. Furthermore, using spectroscopic time-series observations taken by the Near-InfraRed Imager and Slitless Spectrograph (NIRISS) and Near-InfraRed SPECtrograph (NIRSPEC) instruments aboard JWST, [45] revealed a frequency of ∼3 low-energy ($\sim 10^{30}$ erg) flares per day for TRAPPIST-1, and that the continuum of these flares was well described by black body emission with an effective temperature below 5300 K. Assuming a black body temperature of 5000K, we computed that the amplitudes of the four low-amplitude flare-like structures in our MIRI light curves are also consistent with energies $\sim 10^{30}$ erg. Based on these considerations, we modeled these four structures (see Supplementary Fig. 2b) with a simple flare-model composed of an instant flux increase followed by an exponential decrease (3 parameters per flare: time and amplitude of the flux increase + exponential decay constant).

The residuals also showed a ∼2hr transit-like structure centered on 2460272.26 JD and with an amplitude ∼ 200 ppm (Fig. 1b). To represent this structure, we added to our global model the transit of a putative planet i (eighth planet) with an orbital period ∼30d and a size ∼0.2 $R_\oplus$. As can be seen in Extended Data Fig. 3, adding this transit to our global model drastically reduces the red noise level of the residuals. Given the very low amplitude of this potential transit, we used informative prior PDFs on the impact parameter and orbital period to ensure the MCMC convergence (see Extended Data Table 1).

Parameter	Prior PDF	Source
Star		
M_*	$\mathcal{N}(0.0898, 0.0023^2) M_\odot$	[19]
R_*	$\mathcal{N}(0.1192, 0.0013^2) R_\odot$	[19]
T_{eff}	$\mathcal{N}(2566, 26^2) K$	[19]
$[Fe/H]$	$\mathcal{N}(0.04, 0.08^2)$ dex	[36]
π_*	$\mathcal{N}(80.2123, 0.0716^2)$ mas	[46]
$u_{1,\mathrm{F1500W}}$	$\mathcal{N}(0.019, 0.035^2)$	[47]
$u_{2,\mathrm{F1500W}}$	$\mathcal{N}(0.095, 0.05^2)$	[47]
$F_{*,15\mu\mathrm{m}}$	$\mathcal{N}(2.496, 0.080^2)$ mJy	this work
Planet b		
Impact parameter b	$\mathcal{N}(0.095, 0.065^2)$ R_*	[19]
Orbital period P	$\mathcal{N}(1.51088432, 0.00000015^2)$ d	[35]
Orbital eccentricity e	$\mathcal{N}(0, 0.005^2)$	[19]
Phase curve offset δ	$\mathcal{N}(0, 45^2)$ deg (analyses #1)	
Phase curve parameter γ	$\mathcal{N}(3.3, 0.5^2)$ (analysis #2 and #3)	[17]
Planet c		
Impact parameter b	$\mathcal{N}(0.109, 0.061^2)$ R_*	[19]
Orbital period P	$\mathcal{N}(2.42179346, 0.00000023^2)$ d	[35]
Orbital eccentricity e	$\mathcal{N}(0, 0.003^2)$	[19]
Phase curve offset δ	$\mathcal{N}(0, 45^2)$ deg (analyses #1 and #3)	
Phase curve parameter γ	$\mathcal{N}(3.3, 0.5^2)$ (analysis #2)	[17]
Planet g		
Impact parameter	$\mathcal{N}(0.379, 0.018^2)$ R_*	[19]
Orbital period P	$\mathcal{N}(12.353556, 0.0000034^2)$ d	[35]
Orbital eccentricity	$N_p(0, 0.0013^2)$	[19]
Candidate Planet i		
Impact parameter	$\mathcal{N}(0.5, 0.5^2)$ R_*	
Orbital period P	$\mathcal{N}(30, 5^2)$ d	

Extended Data Table 1 | Prior probability distribution functions (PDFs) used in the MCMC analyses of MG. $\mathcal{N}(a, b^2)$ = normal distribution of mean a and standard deviation b. N_p = normal distribution discarding negative values.

We relaunched a Markov Chain of 20,000 steps that resulted in a drastic decrease in the level of red noise in the data (Extended Data Fig. 3). We then rescaled the photometric errors for white and red noise as described in ref. [14], and performed two chains of 100,000 steps each (with the first 20% as burn-in). The convergence of the analysis was checked using the Gelman and Rubin statistical test [18]. For the other analyses, we used the same rescaling factors than for analysis #1, which made possible to estimate their relative probability using their best-fit BIC as a proxy for the marginal likelihood of their models. This methodology is justified by the fact that all three analyses led to the same standard deviations of the residuals, i.e. the three models fitted equally well the data.

A quadratic limb-darkening law [15] was assumed for the star. We assumed normal prior probability distribution functions (PDFs) for the linear and quadratic coefficient u_1 and u_2 based on the output of the `ExoCTK` limb-darkening calculator [47] for a

star of T_{eff} = 3500K and $\log_{10}(g_*$ [cm/s^{-2}]) = 5 dex. As these values correspond to a M-dwarf of earlier-type than TRAPPIST-1, we adopted for the PDFs standard deviations ten times larger than the internal errors of `ExoCTK`.

The jump parameters of the analyses, that is, the parameters perturbed at each step of the MCMC chains, included (1) for the star, the logarithm of the mass, the logarithm of the density, the effective temperature and the metallicity, the combinations $q_1 = (u_1 + u_2)^2$ and $q_2 = 0.5u_1(u_1 + u_2)^{-1}$ of its quadratic limb-darkening coefficients u_1 and u_2 [48], the absolute stellar flux at 15 μm F_*, and (2) for planets, the square of the planet-to-star radius ratio (for planets b, c, and g), the maximal dayside planet-to-star flux ratio (only for planets b and c), the maximal nightside planet-to-star flux ratio (only for planets b and c, and only for the 'atmosphere' model), the phase curve offset δ (only for planet b and c, and only for the atmosphere model), the cosine of the orbital inclination (for the three planets), the mid-transit timing(s) (for all planets), and the Lagrangian parameters $e\cos\omega$ and $e\sin\omega$ (with e the orbital eccentricity and ω the argument of pericenter). Informative normal prior distributions were assumed for some physical parameters (see Extended Data Table 1).

To maximize the constraints on the planets' dayside emissions at 15 μm, we decided to globally analyze the data of programs 3077, 1177 (five occultations of planet b), and 2304 (four occultations of planet c). The data of programs 1177 and 2304 are described in ref. [4] and ref. [7], respectively. Our reductions of the data of these two programs were similar in all respects to the one of the data of program 3077 described above, using the same version of `Eureka!` than used for the double phase curve data. Supplementary Table 1 shows the baseline function and the photometric aperture selected for each light curve. For each occultation light curve of program 1177 and 2304, we also assumed priors on the timings of the surrounding transits based on the transit timing forecasts of ref. [19]. We did not use any priors on the transit timings for program 3077, as the light curve include two transits of planet b and one transit of planet c. The resulting fits are shown on Extended Data Fig. 1.

Results of analysis #1. Table 1 shows the median and 1-σ errors of the posterior PDFs of the parameters derived in analysis #1. Fig. 1 shows the detrended program 3077 light curves with the best-fit model as obtained in analysis #1. Extended Data Fig. 1 (top panels) shows for planet b and c the phase-folded light curve corrected from systematics and from the contribution of the other planets, binned per 60 min, with the best-fit phase curve model. Supplementary Fig. 3 shows the corner plot of the phase curve parameters of both planets, and the posterior PDFs for the sum of their day- and night-side fluxes. Extended Data Fig. 2 compares for each planet and for their sum the posterior PDF for the day- and night-side fluxes.

This analysis leads for planet b to a night-side flux consistent with zero, and significantly smaller than the day-side flux. For none of the accepted MCMC steps was the night-side flux larger or equal to the dayside flux, leading to a full heat redistribution probability lower than 0.0006%. The phase curve peak offset is very well constrained and consistent with zero (-6.5 ± 6.4 deg). The phase curve parameters inferred for planet b are thus fully consistent with an airless planet scenario. The inferred brightness temperatures of the day- and night-sides are, respectively, 490 ± 17

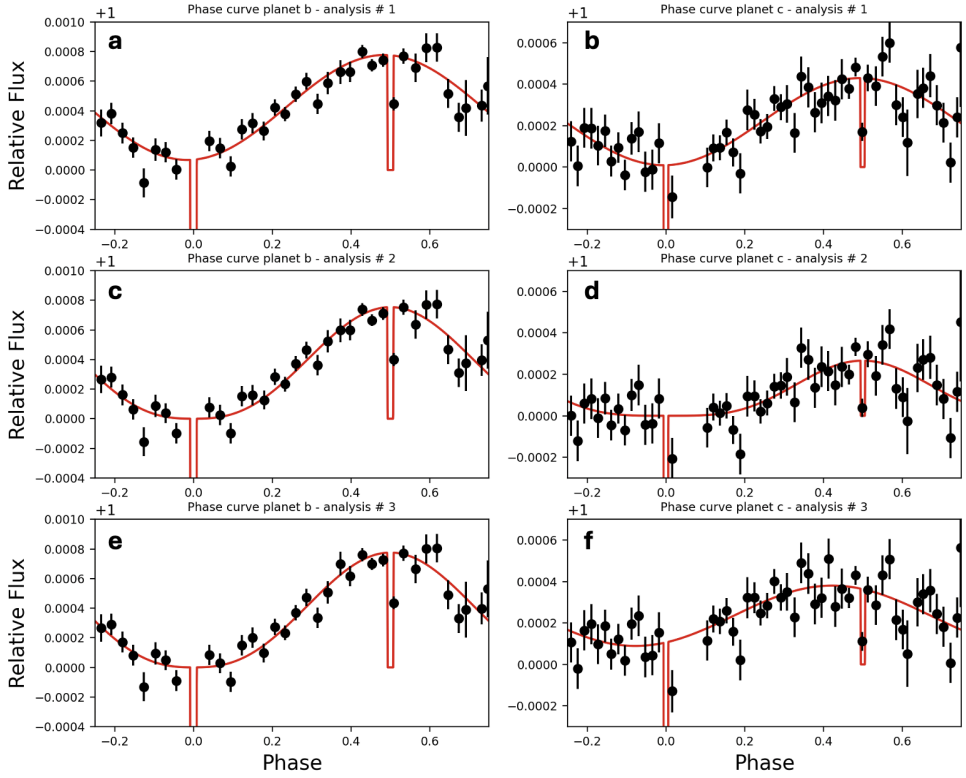

Extended Data Fig. 1 | Best-fit phase curve models for TRAPPIST-1 b and c. Phase-curve models for planets b (panels **a**, **c**, and **e**) and c (panels **b**, **d**, and **f**) from analysis #1 -assuming planet may have some heat redistribution- (panels **a** and **b**), #2 -assuming both planets are airless- (panels **c** and **d**), and #3 -assuming b only is airless- (panels **e** and **f**). The data points are the light curves corrected from the systematics and the contribution of the other planets, phase-folded, and binned per 60 minutes. Each binned point is the average value of the individual points within the bin, and the error bar is the average of the individual errors divided by the square root of the number of points within the bin.

K and 197 ± 41 K. On its side, the measured 15 μm transit depth for b, 7316 ± 117 ppm, is fully consistent with the ones measured by *Spitzer* at 3.6 and 4.5 μm (7236 ± 72 ppm and 7206 ± 77 ppm respectively, [35]).

The results for c are more ambiguous, even if they decisively discard a full heat redistribution (<0.0006% probability). The night side flux of the planet is consistent with zero but also (at 3-σ) with values as large as 232 ppm. The phase curve peak offset, is consistent with zero (10^{+25}_{-22} deg), but also with values as large as +76 deg (at 3-σ). The inferred brightness temperatures of the day and night sides are, respectively, 369 ± 23 K and 220^{+38}_{-47} K. Here again, the measured 15μm transit depth, 7098^{+133}_{-149} ppm, is fully consistent with the ones measured by *Spitzer* at 3.6 and 4.5 μm (7210 ± 140 ppm and 7027 ± 68 ppm respectively, [35]). The posterior PDFs of the sum of

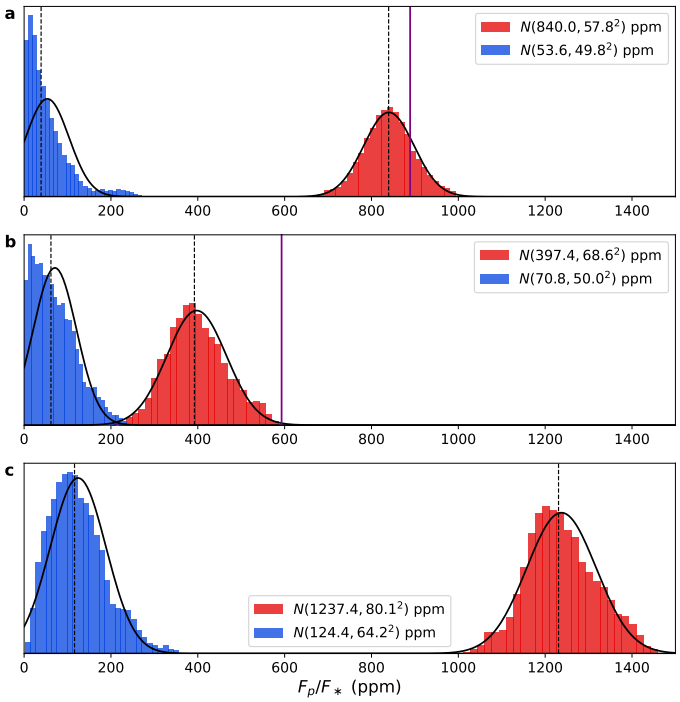

Extended Data Fig. 2 | Posterior probability distribution functions (PDFs) for the day- and night-side fluxes. Analysis #1 posterior PDFs for the relative fluxes of the day (red) and night (blue) sides of TRAPPIST-1 b (panel **a**), c (panel **b**), and the sum of the two planets (panel **c**). The symbol $\mathcal{N}(\mu, \sigma^2)$ stands for normal centered on μ with variance σ. The median of the distributions are shown as vertical dashed lines. The best-fit normal distributions are shown as dark solid lines. For both planets (panels a and b), the relative dayside flux for an airless null-albedo planet is shown as a purple vertical line (889ppm for b and 593ppm for c).

their day- and night-side fluxes strongly reveal a poor heat distribution efficiency (see Table 1, Extended Data Fig. 2 and Supplementary Fig. 3). The sum of the night-side fluxes is consistent with zero at the 2-σ confidence level (Extended Data Fig. 2) The transit depth measured at 15 μm for planet g, 7563^{+138}_{-124} ppm, is also consistent with those measured at 3.6 and 4.5 μm by *Spitzer*: 7240 ± 240 ppm and 7450 ± 110 ppm, respectively [35].

As can be seen in Fig. 1, two planet-planet occultations (PPOs) [49] were adjusted by the global model before the double b+c occultation. To assess the significance of the detection of these PPOs, we performed the very same analysis except that the option to include PPOs in the global model was turned off. It led to a BIC of 7792.4 *vs* 7787.3 with the PPOs. It corresponds to a Bayes factor of 12.8 in favor of the model with PPOs, which corresponds to a strong but far from decisive strength of

evidence [38]. We cannot thus conclude to a robust detection of PPOs in our program 3077 light curve. The transit depth measured for the candidate planet i is 306^{+70}_{-80} ppm, i.e. its significance level is $\sim 4\sigma$. If real, this planet would have a radius $\sim 0.2\ R_\oplus$, similar to Triton. From the delays between its transit and the one of g, we compute that, if this planet had the same orbital period than g, the distance between both planets would be $\sim$6 times g's Hill radius, i.e. it couldn't be a moon of g.

Results of analysis #2. This test analysis assuming airless models for both planets leads to a standard deviation of 862 ppm for the residuals of 3077 program's light curve, the exact same value than for analysis # 1. The resulting day-side fluxes are lower than those derived in analysis #1, but they are consistent with them at the $\sim$1-σ level. The best-fit BIC of analysis #2 is 7773.3 *vs* 7787.4 for analysis #1, which corresponds to a Bayes factor > 1152, decisively [38] in favor of the airless model for both planets. Nevertheless, cautions in the conclusions is advised, as there is no guarantee that the whole set of values derived for the parameter γ of eq. (4) correspond to physical solutions for the surface of a rocky planet. We thus limit to the conclusion that the data are well represented by a model assuming two airless planets. The transit depth measured for the candidate planet i is here 289^{+326}_{-117} ppm, i.e. its significance level is less than 3σ.

We also performed a variant of analysis #2 assuming a non-zero night-side flux that was let free in the MCMC. The resulting values were 67^{+74}_{-48} ppm for b and 72^{+60}_{-48} ppm. In other words, the analysis did not reveal any significant night-side flux for both planets. For the sum of both planets, the inferred night-side flux was 147^{+84}_{-63} ppm, which is not significantly larger than zero.

Results of analysis #3. This analysis leads again to a standard deviation of 862 ppm for the residuals of 3077 program's light curve. The derived day-side flux of planet b is consistent with those derived in analyses #1 and #2. On their side, the phase curve parameters derived for planet c are consistent with those derived in analysis #1. A full heat redistribution is again disfavored, but much less decisively than for analysis #1 (0.4% probability *vs* $< 0.0006\%$). The BIC of this analysis is 7780.1, which, when compared to analysis #2, leads to a Bayes ratio of 30 in favor of the double airless scenario, strongly supporting this latter [38]. But here again, caution in the conclusions is required, for the reasons mentioned above.

The transit depth measured for the candidate planet i is here 285^{+210}_{-109} ppm, i.e. its significance level is again less than 3σ, as in analysis #2. Considering the results of three analyses, the significance of this putative transit appears too low to claim a detection.

MG's nominal analysis (#1) and test analyses (#2 and #3) yield consistent results, leading to the conclusion that efficient heat redistribution is firmly ruled out for TRAPPIST-1 b and appears unlikely for TRAPPIST-1 c.

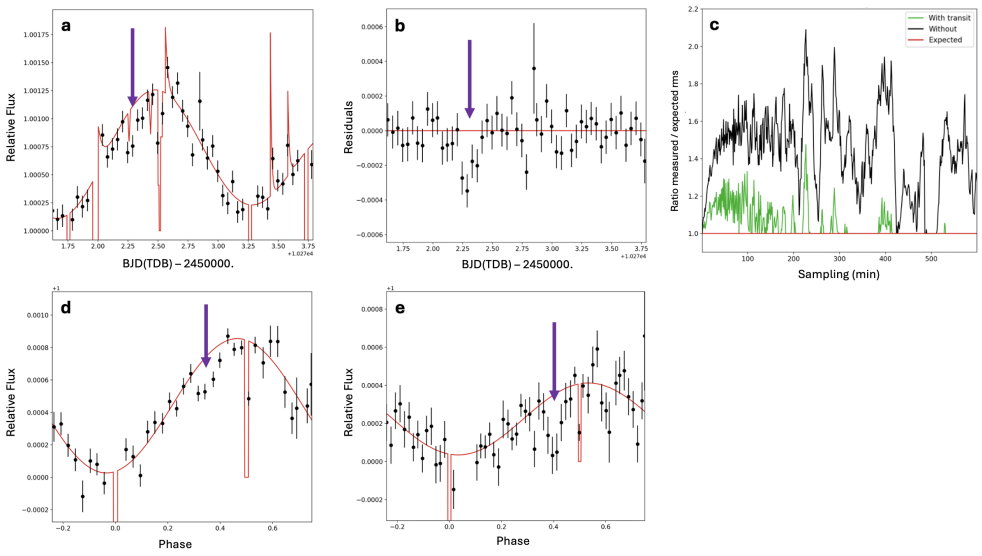

Extended Data Fig. 3 | Additional transit-like structure in the light curve of Program 3077. a, detrended 3077 program light curve obtained by MG in a version of analysis #1 not assuming the transit of a putative planet i, with the best-fit planet model deduced from the same analysis superimposed in red. **b**, residuals of that version of analysis #1. **c**, modified Allan diagram showing the ratio of the measured standard deviations of the residuals of the best-fit model and of the one expected for a fully white noise as a function of the sampling (i.e. for different binnings), without (black) and with the inclusion of a low-amplitude transit in the global model (green). The red line shows what the ratio should be for a fully white noise, i.e. 1. **d**, Best-fit phase curve for planet *b* from that version of analysis #1. The data points are phase-folded and corrected from the systematics and the contribution of the other planets. The best-fit phase curve model is superimposed in red. **e**, same for planet *c*. For panels **a**, **b**, **d** and **e**, the data points are binned per 60 minutes, each binned point is the average value of the individual points within the bin, and the error bar is the average of the individual errors divided by the square root of the number of points within the bin. The purple arrows show the location of the putative transit of a putative planet i.

Data reduction and analysis (ED)

For this second reduction, we employed the `Eureka!` pipeline [11] starting from the calints.fits files. In that context, we started using `Eureka!` from Stage 3 which corresponds to the aperture photometry extraction step. We used a subarray region for of [186, 326] in the x and y directions. We masked pixels flagged in the data quality flags array (DQ array[1]), interpolated defective pixels, and conducted aperture photometry on the star. We choose an aperture of 11 pixels and for each integration, we recorded the center and width of the point spread function (PSF) in the x and y directions by fitting a 2D Gaussian. Background computation involved an annulus of 40 to 60 pixels (centered on the target), with the result subtracted. We identified a bright group of pixels at 20 pixels from the center of the target which is why we started our background annulus only at 40 pixels. Once the flux was extracted we processed to stage 4, we applied a 4σ sigma-clip to identify outliers deviating from the median flux, calculated using a 100-integrations-width boxcar filter. In the final light curve we identified by eye five transits (partial c, b, g, b and c), the double eclipse (b+c) and two consecutive high energy flares. The planet-planet occultations and the eclipse of d are too shallow to be seen by eye in the light curve.

For the analysis of the phase curve we also used `trafit`. In order to maximize the observational constraints on planet b and c, we proceeded to a global analysis of all MIRI observations of TRAPPIST-1 b and c at 15 μm. This included 5 eclipses of planet b (GTO 1177) and 4 eclipses of planet c (GO 2305) and the double phase curve presented in this work. We used the light curves from the ED reductions in ref. [4] and ref. [7]. The eclipse model from ref. [15] was employed to depict photometric time series, and it was multiplied by a baseline model to account for additional astrophysical and instrumental factors contributing to photometric fluctuations. The other astrophysical model included stellar photometric activity such as flares. The instrumental systematics model included PSF width (PSF_{sx}, PSF_{sy}), PSF position (PSF_x, PSF_y) and background. Initially, baselines were chosen for each light curve by running one chain with all possible polynomial combinations for PSF_{sx}, PSF_{sy}, PSF_x, PSF_y, and background, we then chose the one minimizing the BIC. In all the different analyses, described below, orders of the polynomial were all inferiors to 3. We also modeled the expected persistent effect on MIRI [50] using two ramp models (we modeled these ramp as a quadratic function of $ln(dt)$ like in ref. [51]) at the beginning of each exposure, as the phase curve was divided in two exposures (see section 2). Once the baselines have been selected, we run one chain of 50000 steps to derive the errors correction factor of each light curves. These correction factors are a way to evaluate the need for re-scaling of the photometric errors through the consideration of a potential under- or over-estimation of the white noise of each measurement and the presence of time-correlated (red) noise in the light curve, more details in ref. [14]. A large set of jump parameters are randomly perturbed at each step, and a model is derived from their values and compared with the data. In our global analysis the jump parameters for the star were:

[1]Data Quality flags in details here https://jwst-pipeline.readthedocs.io/en/latest/jwst/dq_init/index.html

- the log of the mass, the stellar effective temperature, the log of the density, and the metallicity [Fe/H]. For each parameter we assumed a normal prior based on the value from ref. [19] (see Extended Data Table 1). We also fitted for the limb darkening coefficients with priors $\mathcal{N}(0.019, 0.07^2)$ and $\mathcal{N}(0.095, 0.1^2)$ for u_1 and u_2 respectively.
For the planets we used the following jump parameters:
- the radius ratios $R_p/R_\star$, the eccentricity e, and the impact parameter b, with priors from ref. [19].
- the TTVs (with fix T_0 and P), with a prior centered at 0.0 with an error of 3 min, 5 min, and 8 min for planets b, c and g respectively.
- the day and night flux ratios of planet b and c at $15\mu m$, with priors $\mathcal{N}(863, 90^2)$ ppm and $\mathcal{N}(45, 500^2)$ ppm for $F_{b,\ D,\ 15\mu m}$ and $F_{b,\ N,\ 15\mu m}$ respectively; and priors $\mathcal{N}(421, 90^2)$ ppm and $\mathcal{N}(45, 500^2)$ ppm for $F_{c,\ D,\ 15\mu m}$ and $F_{c,\ N,\ 15\mu m}$ respectively.
- Finally our last jump parameter was the phase curve offset for b ($\delta_{PC,\ b}$) and c ($\delta_{PC,c}$) with broad priors, $\mathcal{N}(0, 30^2)^\circ$, for both planet.
We fit for the eclipse timing variations (ETVs) in addition to TTVs and fix the periods and reference transit timings of the planets to the predictions by ref. [19]. The results from this global analysis are presented in Extended Data Table 2 under the name "Analysis 7 planets #1", the light curves and their best-fit model are shown on Extended Data Fig. 4. and the resulting phase-folded eclipse and transit light curves are shown in Extended Data Fig. 5.

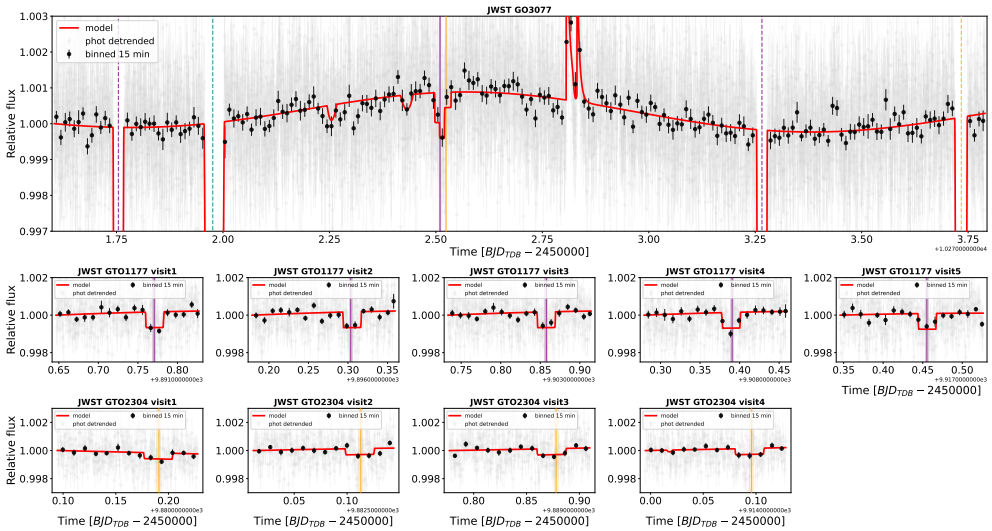

Extended Data Fig. 4 | Detrended light curves from ED's analysis #1. Detrended light curves for each JWST program that observed TRAPPIST-1 b and c at $15\mu m$ using MIRI F1500W. The top panel is the phase curve from GO 3077, second row of panels are the 5 visits from GO 1177 (PI: Greene) and the third row are the 4 visits from GO 2304 (PI: Kreidberg). The best fit from "Analysis 7 planets #1" is shown with a red curve. The expected transit and eclipse timings for each planet from [19] are shown in vertical dashed and plain lines respectively (purple for b, orange for c, and green for g).

Then, we performed two additional global analyses where we changed a couple of parameters. First, we proceeded similarly to MG and assumed that planet b is an airless planet that we can model with a quasi-Lambertian phase curve model from ref. [17], with a restricted normal prior for γ, $\mathcal{N}(2.95, 0.1^2)$. We used a restrictive prior centered on 2.95 because it is the value of γ that provides the closest approximation to the Bidirectional Reflectance Distribution Function (BRDF), and therefore the most suited way to model planet b as an airless planet. The results from this second global analysis are presented in Extended Data Table 2 under the name "Analysis 7 planets #2". Second, as we identified a structure that we could not associate to any instrumental systematic origin we tried to model it as a smaller outer 8th planet that we named planet i (similarly to MG analyses). For this planet we fitted for the following parameters : the transit depth with a wide prior $\mathcal{N}(500, 400^2)$ ppm, the impact parameter with $\mathcal{N}(0.5, 0.1^2)$, the transit mid-time with $\mathcal{N}(246\ 0272.277, 0.02^2)$ BJD_{TDB}, and the period with a wide prior $\mathcal{N}(30, 10^2)$ days. In this analysis we also assumed that planet b was an airless planet that we modeled with a quasi-Lambertian phase curve. The results from this second global analysis are presented in Extended Data Table 2 under the name "Analysis 8 planets".

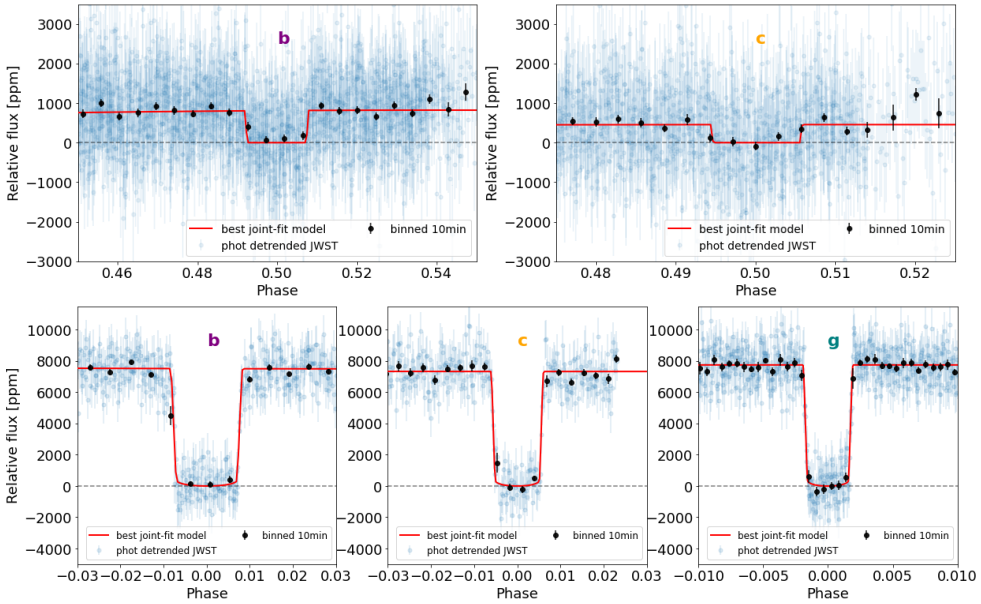

Extended Data Fig. 5 | Phase folded eclipse and transit light curves for planet b, c and g. These phase folded light curve result from the best fit analysis "Analysis 7 planets #1" by ED.

Results from the three global analyses

"Analysis 7 planets #1" favours a large flux contrast between the day and the night side of TRAPPIST-1b and almost no offset of the phase curve, very similar to what we expect for a bare-rock planet. For TRAPPIST-1 c we measured a larger day-side

Analyse	Analysis 7 planets #1	Analysis 7 planets #2	Analysis 8 planets
Planet b			
Mid-transit timing (# 1) (BJD_{TDB} - 2460000)	271.75438 ± 1.23E-04	271.75438 ± 8.69E-05	271.75438 ± 1.12E-04
Mid-transit timing (# 2) (BJD_{TDB} - 2460000)	273.26591 ± 1.11E-04	273.26591 ± 8.11E-05	273.26590 ± 9.83E-05
Impact parameter b	$0.1037^{+0.05}_{-0.07}$ R_*	$0.086^{+0.004}_{-0.003}$ R_*	$0.095^{+0.004}_{-0.008}$ R_*
Inclination i	89.7125 ± 0.0215 ^{o}	89.7608 ± 0.0124 ^{o}	89.7368 ± 0.0217 ^{o}
Semi-major axis a	0.011526 ± 7.1E-05 au	0.011600 ± 6.4E-05 au	0.011465 ± 6.0E-05 au
Transit depth dF	7271 ± 140 ppm	7334 ± 90 ppm	7315 ± 128 ppm
Eccentricity e	0.0003 ± 2.67E-04	0.00015 ± 4.44E-04	0.00075 ± 2.35E-03
$F_{b,D,max}$	791 ± 68 ppm	788^{+65}_{-41} ppm	810 ± 40 ppm
$F_{b,N,max}$	62^{+78}_{-45} ppm	0 ppm (fixed)	0 ppm (fixed)
Peak offset $\delta_{PC,\ b}$	8 ± 12 deg	0 deg (fixed)	0 deg (fixed)
γ	–	2.61 ± 0.15	2.99 ± 0.075
$T_{brightness,D}$	479 ± 22 K	472 ± 20 K	486 ± 32 K
$T_{brightness,N}$	217 ± 50 K	0 K (fixed)	0 K (fixed)
Planet c			
Mid-transit timing (BJD_{TDB} - 2460000)	273.73336 ± 1.35E-04	273.73335 ± 1.03E-04	273.73336± 1.23E-04
Impact parameter b	0.104 ± 0.075 R_*	0.08 ± 0.065 R_*	0.103 ± 0.010 R_*
Inclination i	89.7881 ± 0.0153 ^{o}	89.8283 ± 0.0134 ^{o}	89.7921 ± 0.0192 ^{o}
Semi-major axis a	0.01578 ± 9.7E-05 au	0.01588 ± 7.7E-05 au	0.01570 ± 8.2E-05 au
Transit depth dF	7098 ± 149 ppm	7122 ± 109 ppm	7077 ± 125 ppm
Eccentricity e	0.00024 ± 1.74E-04	0.00001 ± 2.54E-04	0.00018 ± 6.10E-04
$F_{c,D,max}$	405 ± 71 ppm	465 ± 74 ppm	473^{+40}_{-45} ppm
$F_{c,N,max}$	125 ± 90 ppm	92^{+93}_{-64} ppm	138^{+129}_{-193} ppm
Peak offset $\delta_{PC,\ c}$	-1^{+32}_{-28} deg	14^{+13}_{-14} deg	-31^{+27}_{-21} deg
γ	-	-	-
$T_{brightness,D}$	372 ± 21 K	388 ± 25 K	395 ± 36 K
$T_{brightness,N}$	258 ± 79 K	239 ± 102 K	267 ± 169 K
Planet g			
Mid-transit timing (BJD_{TDB} - 2460000)	271.97933 ± 0.00015	271.97934 ± 0.00011	271.97935 ± 0.00011
Impact parameter b	0.378 ± 0.021 R_*	0.355 ± 0.014 R_*	0.379 ± 0.0137 R_*
Inclination i	89.7420 ± 0.0155 ^{o}	89.7591 ± 0.0408 ^{o}	89.7453 ± 0.0127 ^{o}
Semi-major axis a	0.04678 ± 2.9E-04 au	0.04708 ± 2.6E-04 au	0.04653 ± 2.4E-04 au
Transit depth dF	7680 ± 146 ppm	7615^{+82}_{-90} ppm	7739^{+95}_{-122} ppm
Eccentricity e	0.000017± 1.66E-04	0.0000459± 1.54E-04	0.0001786± 1.54E-04
Candidate planet i			
Mid-transit timing (BJD_{TDB} - 2460000)	-	-	272.289611± 3.50E-02
Impact parameter b	-	-	0.50 ± 0.12 R_*
Orbital inclination i	-	-	89.80 ± 0.18
Period P	-	-	25 ± 1.3 d
Transit depth dF	-	-	340^{+111}_{-118} ppm
Radius R_p	-	-	$0.239^{+0.036}_{-0.046}$ $R_\oplus$

Extended Data Table 2 | Resulting planetary parameters from the global MCMC analyses done by ED

temperature than night-side, however considering the still low SNR on the later it is not possible to confirm whether the heat redistribution is fully inefficient or not on this planet. Similarly, the offset of TRAPPIST-1c's phase curve can vary between 1 and 30 degrees from one analysis to another, but the associated error bars are large such that it is always consistent with zero. Our best-fits for each analysis favor planet-planet occultations between planet b and c, however the detection is not at the 3-σ level, and therefore not significant yet. Finally, the transit depth that we derive for planet b, c

and g are all consistent with the values obtained from Spitzer IRAC observations at 3.6 μm and 4.5 μm [35]. Our conclusions concerning the fitting the double-flare event can be found in section 2.

Data reduction and analysis (TJB)

Our third independent reduction followed a similar process as that described by ref. [4]. We re-reduced all MIRI F1500W eclipse observations of TRAPPIST-1 b and c and reduced the novel phase curve observation using the same reduction procedure. Specifically, we used version 0.11.dev77+g1e43198f.d20240130 of the `Eureka!` data analysis pipeline [11], with `jwst` version 1.13.4 [39], CRDS version 11.17.19 [52], and using the 'jwst_1188.pmap' CRDS context. The `Eureka!` Control Files and `Eureka!` Parameter Files we used are available for download on Zenodo (https://zenodo.org/uploads/15005073). We began with the uncalibrated FITS files and ran `Eureka!`'s Stages 1–2 with the default `jwst` settings with the exception of turning off the Stage 1 EMI correction step (since initial experimentation showed that this time-consuming step offered little-to-no benefit for these data), turning on the Stage 1 'firstframe' and 'lastframe' steps (which discard the first and last groups of each integration, respectively), setting the Stage 1 jump rejection threshold to 10σ, and turning off the Stage 2 'photom' step.

In `Eureka!`'s Stage 3, we first masked pixels marked as 'DO_NOT_USE' in the data quality array, converted the data units from data number per second to electrons, masked outlier pixels in the background region using a double-iteration 5σ clipping procedure, and interpolated bad pixel values using a bilinear interpolation. We performed centroiding on each integration using `Eureka!`'s 'fgc' method on the 10 pixels surrounding the manually selected initial centroid guess for later use as covariates in Stage 5. We then performed a multi-step aperture optimization process on the phase curve observations using the median absolute deviation of the resulting lightcurves as a metric to select the lightcurve with the lowest noise before fitting. We first varied the photometric aperture radius from 3 to 11 pixels in 1-pixel steps and chose an aperture radius of 5-pixels, varied the sky annulus inner-radius from 10 to 24 pixels in 2-pixel steps and chose an inner-radius of 16 pixels, and finally varied the sky annulus width from 10 to 40 pixels in steps of 2-pixels before choosing a width of 30 pixels. Repeating the aperture and annulus selection process did not result in any changes. We then used these same aperture and annulus parameters for all nine eclipse-only observations. Finally, in `Eureka!`'s Stage 4 we performed sigma clipping on the time-series by iteratively replacing 3.5σ outliers compared to a smoothed version of the signal computed using a 20-integration wide boxcar filter, with a maximum of 20 iterations.

We then proceeded to simultaneously fit all nine eclipse-only lightcurves and the phase curve with `Eureka!`'s Stage 5. To model the transits of TRAPPIST-1 b, c, and g and the eclipse signals of TRAPPIST-1 b and c, we used the `batman` package [53] to compute light curves with quadratic limb-darkening using formulae from ref. [15]. We neglected the planet-planet occultations expected to be present in the phase curve observation; numerous attempts at fitting all ten lightcurves with the `starry` package [54, 55] (which models the planet-planet occultations) and `PyMC3`'s No U-Turns Sampler [56] failed to converge, perhaps due to very high dimensionality of the fit. For

the stellar limb-darkening, we freely fit the reparameterized quadratic limb-darkening coefficients (q_1, q_2) of ref. [48] assuming that the coefficients were consistent between the transits of TRAPPIST-1 b, c, and g. We used broad, minimally informative Gaussian priors on the planetary radii (R_p/R_*) and eclipse depths ($F_{p,day}/F_*$). For both TRAPPIST-1 b and c, we assumed the planets' orbital period (P), inclination (i), and semi-major axes (a/R_*) were sufficiently constant across all epochs and shared each of these parameters between the different epochs, using Gaussian priors based on ref. [19]. However, the gravitational effects of the other planets in the system are not negligible and result in transit timing variations (TTVs) as well as eclipse timing variations (ETVs); to model these variations in the eclipse timing, we used a different mid-eclipse time parameter for each epoch using the predictions of ref. [19] as Gaussian priors (see Extended Data Table 3). For the transits present in the phase curve observation, we also adopted Gaussian priors based on the predictions of ref. [19], with the exception of assuming that the change in orbital period was small enough over the phase curve observation that we could assume that the two TRAPPIST-1 b transits were separated by one orbital period. We estimate that the light travel time difference between transit and eclipse is only ∼11 seconds for TRAPPIST-1 b and ∼16 seconds for TRAPPIST-1 c [19], so we neglect this effect in our modelling.

For our phase variation model, we considered combinations of two different models. One model was the standard first-order sinusoidal phase variation model (with free parameters 'AmpCos1' and 'AmpSin1' as described by ref. [23]) which is the result of a first-order Fourier series decomposition of any planetary map [58]. The second model was the quasi-Lambertian model described above (ref. [17] and Equation 4; with the free parameter γ) which assumes an airless planet. We performed one fit using the quasi-Lambertian model for both TRAPPIST-1 b and c (Setup #1), one fit using the quasi-Lambertian model for TRAPPIST-1 b and the sinusoidal model for TRAPPIST-1 c (Setup #2), and one fit with sinusoidal phase variations for both TRAPPIST-1 b and c (Setup #3). For cases where we used the sinusoidal phase variation model, we imposed a prior that each planet's phase variations remained positive. For all other TRAPPIST-1 planets (including TRAPPIST-1 g which transits during the observations), we assumed there was negligible thermal emission.

Beyond the planetary signals in the data, there were also numerous obvious stellar and instrumental noise sources present in the lightcurves. To remove the initial settling ramp seen at the beginning of most MIRI observations, we trimmed the first 100 integrations from all ten lightcurves; for the phase curve observation, we removed an additional 700 integrations (800 in total) as there was an unusually strong ramp at the start of these observations and we wanted to limit any correlations between the initial ramp and the phase variations of TRAPPIST-1 b and c. For the phase curve observation, we also removed integrations 3160–3300 as these were affected by a pair of what appeared to be stellar flares. To capture the impact of red noise in the observations on our astrophysical parameters of interest, we simultaneously fitted the astrophysical model along with a polynomial in time (with a constant term and a linear slope term), a linear decorrelation against the PSF's position and width in both the x and y directions, and a Gaussian Process (GP; as implemented in `celerite2` [59, 60]) as a function of time using a Matérn-3/2 kernel [61] with fitted coefficients

of $\ln A$ (which controls the correlation strength and is unitless) uniformly constrained between -24 and -10 and $\ln \tau$ (which controls the correlation lengthscale, where τ has units of days^{-1}) uniformly constrained to be within -7 and 0. The systematic models for each lightcurve were treated independently. To evaluate the importance of the GP, we also performed an additional fit using Setup #3 without using a GP during fitting. With this test, we found that the residual white noise and red noise was greatly increased without the inclusion of the GP (e.g., see Extended Data Fig. 7), and several key parameters of interest appeared to be overly constrained without accounting for the presence of this red noise. To demonstrate what impact the GP had on our fitted and computed astrophysical parameters, we tabulate the results of this fit along with our other fits, although we emphasize that this is only for demonstrative purposes and the results of this particular no-GP fit should not be trusted as there is significant red noise which is unaccounted for in the statistical model. Finally, we also allowed for a white-noise multiplier for each lightcurve to account for background noise (which was not included in the initial estimates of the uncertainties), an incorrect assumption for the gain in Stage 3, and any other white noise term.

We performed sampling using the `emcee` Affine Invariant Markov chain Monte Carlo (MCMC) Ensemble sampler [62, 63] to obtain estimates for the best-fit values and uncertainties for each fitted parameter. In total, we had between 122 and 124 free parameters for each of our fits, as is documented in Extended Data Table 4. We used 500 walkers, each of which repeatedly took 20,000 steps (10 million total samples) until the chain had visually converged and the results from the first 5 million and last 5 million samples gave the same best-fit values and uncertainties. This required 70 million total posterior samples for Setup #1, 40 million total posterior samples for Setup #2, 30 million total posterior samples for Setup #3 with the GP, and 20 million total posterior samples for Setup #3 without the GP. We then used the median of the final 5 million samples as our best-fit estimate and the 16th and 84th percentiles as our uncertainty estimates. We had hoped to use the `dynesty` nested sampling algorithm [64] to enable more robust statistical model comparisons using the computed Bayesian evidence, but an initial attempt at fitting Setup #3 with the GP using `dynesty` had still not converged after 300 million posterior evaluations over 20 days of wall-clock runtime on 28 CPU threads (with $d \log z = 578$, still far from the stopping criteria of $d \log z < 0.1$). As a result, we have to resort to computing the Bayesian Information Criterion (BIC) for all four of our `emcee` fits following the methods of ref. [65].

The results of our fits are summarized in Extended Data Table 4, Extended Data Fig. 6 and Supplementary Fig. 4. As shown in Supplementary Fig. 5, our residuals (after having removed the red noise component modelled with our simultaneously fitted GP) show no unmodelled red noise. Based on the ΔBIC between our different fits we find that our significantly preferred model from the TJB suite was Setup #1 which used the quasi-Lambertian (airless) model for the phase variations of both TRAPPIST-1 b and c. Our measured eclipse depths ($F_{\rm p,day,T\text{-}1b}/F_*$=796$\pm$77 ppm, $F_{\rm p,day,T\text{-}1c}/F_*$=472$\pm$85 ppm) are consistent to within 1σ with previously published values ($F_{\rm p,day,T\text{-}1b}/F_*$=861$\pm$99 ppm, ref. [4]; $F_{\rm p,day,T\text{-}1c}/F_*$=421$\pm$91 ppm, ref. [7]). While the quasi-Lambertian (airless) model assumes zero-nightside flux, those fits which used the sinusoidal phase variation model found nightside flux values that were

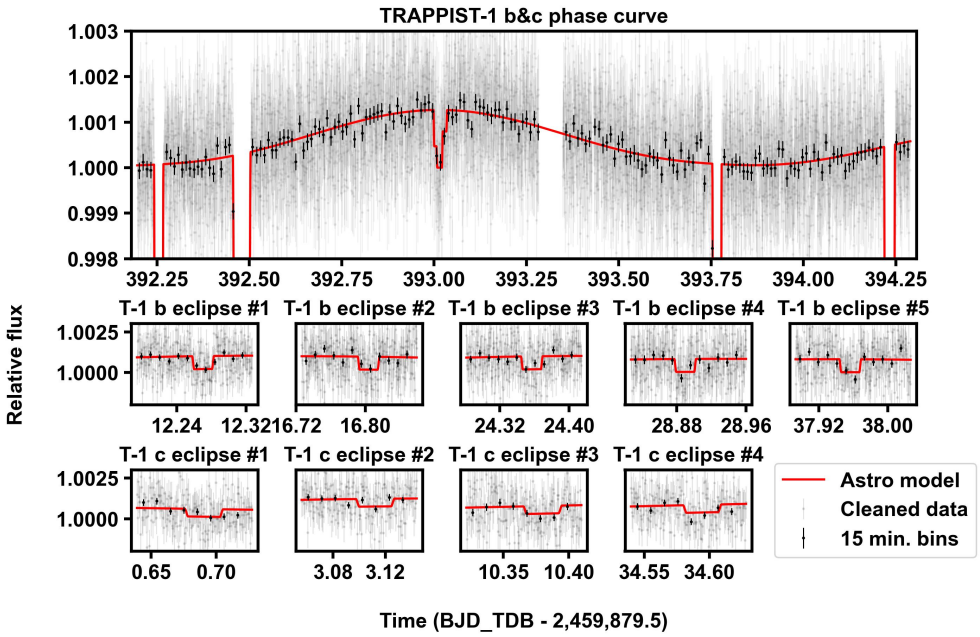

Extended Data Fig. 6 | Cleaned lightcurves and fitted models from TJB's reduction and analysis with Setup #1.

generally consistent with 0 ppm for both TRAPPIST-1 b and c. Similarly, while the quasi-Lambertian (airless) model assumes the phase variations are symmetric about the eclipse, those fits with sinusoidal phase variations were consistent with no phase curve offset. Together, these findings favour the scenario where neither TRAPPIST-1 b nor c have an atmosphere that transports appreciable amounts of heat to the nightside.

Finally, to assess the evidence for the potential new candidate identified in MG's analyses, we repeated a fit built upon our fiducial Setup #1 (with GP) with the addition of an additional transiting body. For this candidate, we adopted the following minimally informative priors: $Rp/R_* = \mathcal{N}(0.01414, 0.1^2)$, $P = \mathcal{N}(30, 10^2)$ days, $t_0 = \mathcal{N}(60271.76, 0.1^2)$ (in units of BJD_TDB - 2,400,000.5), $i = \mathcal{U}(85, 90)$ degrees, $a/R_* = \mathcal{N}(100, 10000^2)$, and $e = 0$, where $\mathcal{N}(\mu, \sigma^2)$ is a Normal prior with mean μ and standard deviation σ and $\mathcal{U}(\ell_1, \ell_2)$ is a Uniform prior with a lower bound of ℓ_1 and an upper bound of ℓ_2. Our posteriors closely matched our priors, and the BIC test significantly prefers the *exclusion* of the potential candidate with a ΔBIC of 67. As a result, with the reduction and analysis methods described in this subsection, there is no clear evidence for the inclusion of a new transiting exoplanet.

Data reduction and analysis (ZH)

Data Reduction (Stage 1-3) We carried out the data reduction and analysis starting from *_uncal.fits* files. We used the `JWST pipeline` (version 1.13.0) and `Eureka!`

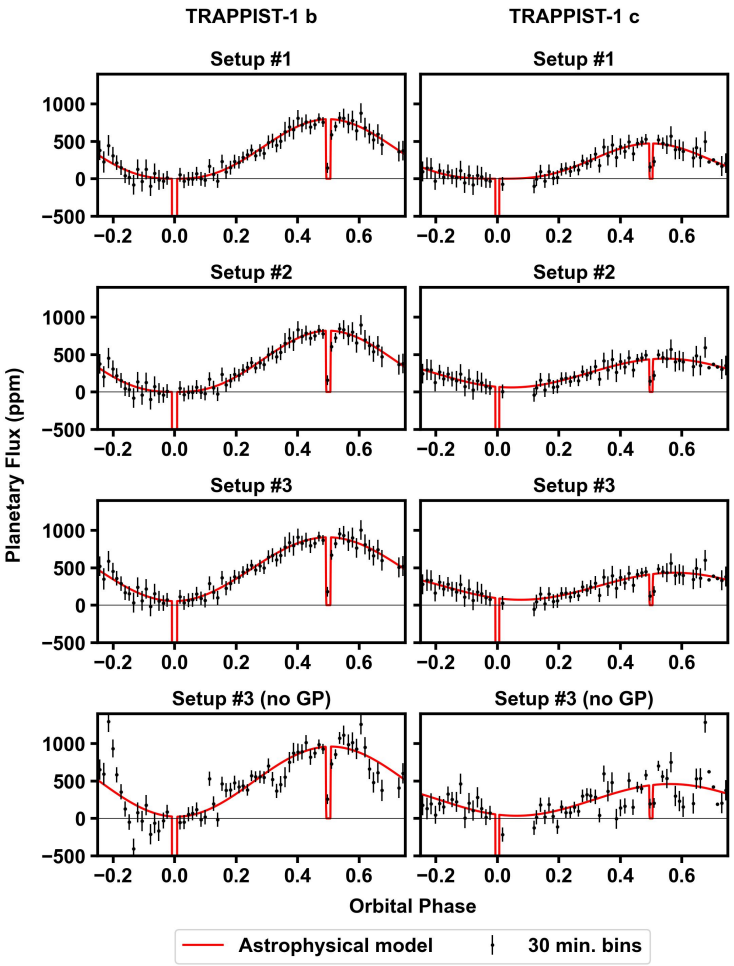

Extended Data Fig. 7 | Separated phase variations from TRAPPIST-1 b and c from TJB's reduction and analysis with Setup #1. The small cluster of points with small uncertainties around phase 0.7 on the TRAPPIST-1 c panels are caused by the many repeated TRAPPIST-1 b eclipse observations which happened to mostly occur at this particular orbital phase of TRAPPIST-1. Note that in the top 3 rows, correlated variations have been subtracted from the phase curve, as estimated by a maximum-likelihood prediction from the Gaussian process.

(version v0.10-696df7c) pipeline to include correction for noise appearing around 390 Hz and 10 Hz which was reported to potentially affect the MIRI detectors. The configuration of Stage 1 and Stage 2 are following the default settings except that we turned off the jump correction. The Stage 2 of `JWST` also includes converting lightcurves into $MJy.sr^{-1}$. Starting from Stage 3, the pipeline is used for aperture photometry and light curve fitting including phase curve, eclipse model and transit model. We first selected a window range of [200, 300] for x and [200, 300] for y that contains the source. We then used a 2D Gaussian model to estimate the position of the centroid and experimented with various source radii. Observations of the combined phase curve

Epoch	Predicted Timing [19] ($BMJD_{TDB}$)	TJB Fitted Timing ($BMJD_{TDB}$)
TRAPPIST-1 b		
Eclipse #1	59891.2730±0.0031	$59891.27049^{+0.00100}_{-0.00081}$
Eclipse #2	59895.8051±0.0031	$59895.80380^{+0.00170}_{-0.00083}$
Eclipse #3	59903.3600±0.0031	$59903.35691^{+0.00074}_{-0.00100}$
Eclipse #4	59907.8922±0.0031	$59907.88971^{+0.00100}_{-0.00099}$
Eclipse #5	59916.9579±0.0031	$59916.95650^{+0.00090}_{-0.00076}$
Phase Curve Eclipse	60272.0120±0.0031	$60272.01087^{+0.00190}_{-0.00069}$
Phase Curve Transits	60271.25424±0.00089	$60271.254440^{+0.000076}_{-0.000077}$
TRAPPIST-1 c		
Eclipse #1	59879.6903±0.0036	$59879.6906^{+0.0025}_{-0.0026}$
Eclipse #2	59882.1125±0.0036	$59882.1122^{+0.0074}_{-0.0019}$
Eclipse #3	59889.3781±0.0036	$59889.3801^{+0.0016}_{-0.0056}$
Eclipse #4	59913.5960±0.0036	$59913.5945^{+0.0019}_{-0.0015}$
Phase Curve Eclipse	60272.0236±0.0037	$60272.0210^{+0.0033}_{-0.0022}$
Phase Curve Transit	60273.23403±0.00085	$60273.23311^{+0.00012}_{-0.00012}$
TRAPPIST-1 g		
Phase Curve Transit	60271.4761±0.0015	$60271.47926^{+0.00013}_{-0.00013}$

Extended Data Table 3 | Predicted and fitted mid-occultation times for the transits and eclipses of TRAPPIST-1 b, c, and g. Predicted mid-eclipse and mid-transit times from ref. [19] are compared to the fitted timings from TJB's joint fit using Setup #1. $BMJD_{TDB}$ is the date in the Barycentric Julian Date in the Barycentric Dynamical Time system minus 2,400,000.5 days. Note that both the predicted and fitted timings neglect the light travel time effect which is only ∼11 seconds and ∼16 seconds for TRAPPIST-1 b and c, respectively.

of TRAPPIST-1 b and TRAPPIST-1 c lasted about 59 hrs and were taken in two exposures. Between the two observations, we notice a drift of the centroid which could possibly alter the data analysis with different radii used in this stage. As a result, we selected a range of the radii sizes from 5 to 12 pixels, incrementing in a step of 1 pixel. The ideal size for minimizing the phase curve fitting is a 9-pixel aperture, together with a background annulus ranging from 16 to 36 pixels away from the centroid. It's worth mentioning that the selection of the background annulus had minimal influence on the resulting light curve, indicating its robustness to variations in this parameter. The resulting lightcurve is shown in Extended Data Fig. 8

Data Analysis (Stage 4-5) The stage 4 and stage 5 fitting of the light curves are also done by `Eureka!` with a slight modification to enable the modeling of double phase curves. In stage 4, the obtained light curves are normalized, and an iterative 4-σ outlier clipping process is applied to identify significant outliers using a 10-minute moving median algorithm. Note that the normalized light curves show a large jump at the beginning and two flares around BJD 2460272.805 and BJD 2460272.905. We removed those data points before the phase curve fitting process. In the initial double phase curve fitting in stage 5, the forward model of the planet flux is described as

	Setup #1 (with GP)	Setup #2 (with GP)	Setup #3 (with GP)	Setup #3 (without GP)
TRAPPIST-1 (star)				
Limb darkening; q_1	$\mathbf{0.036}^{+0.034}_{-0.021}$	$0.036^{+0.034}_{-0.021}$	$0.035^{+0.033}_{-0.021}$	$0.035^{+0.034}_{-0.021}$
Limb darkening; q_2	$\mathbf{0.19}^{+0.29}_{-0.14}$	$0.19^{+0.31}_{-0.14}$	$0.20^{+0.34}_{-0.15}$	$0.19^{+0.33}_{-0.14}$
TRAPPIST-1 b				
P.C. Model	**Quasi-Lambertian**	Quasi-Lambertian	Sinusoidal	Sinusoidal
R_p/R_*	$\mathbf{0.08355}^{+0.00086}_{-0.00087}$	$0.083584^{+0.00087}_{-0.00090}$	$0.08357^{+0.00082}_{-0.00086}$	$0.08466^{+0.00063}_{-0.00067}$
P (days)	$\mathbf{1.511536}^{+0.000072}_{-0.000110}$	$1.511538^{+0.000070}_{-0.000100}$	$1.511547^{+0.000066}_{-0.000092}$	$1.511563^{+0.000055}_{-0.000084}$
a/R_*	**20.81±0.12**	20.81±0.12	20.82±0.11	20.79±0.11
i (degrees)	**89.74±0.12**	89.75±0.13	89.75±0.13	89.77±0.13
$F_{p,day}/F_*$ (ppm)	**796±77**	819±80	907±94	959±65
$F_{p,night}/F_*$ (ppm)	**≡0**	≡0	53±59	23±24
Phase Offset (°E)	**≡0**	≡0	1±10	-2.5±4.6
Quasi-Lambertian γ	$\mathbf{2.61}^{+0.53}_{-0.47}$	$2.62^{+0.51}_{-0.48}$	—	—
TRAPPIST-1 c				
P.C. Model	**Quasi-Lambertian**	Sinusoidal	Sinusoidal	Sinusoidal
R_p/R_*	**0.0839±0.0011**	$0.0836^{+0.0011}_{-0.0012}$	$0.0836^{+0.0011}_{-0.0012}$	0.08411±0.00082
P (days)	$\mathbf{2.42138}^{+0.00091}_{-0.00092}$	$2.42130^{+0.00096}_{-0.00080}$	$2.42136^{+0.00089}_{-0.00081}$	$2.42189^{+0.00074}_{-0.00087}$
a/R_*	**28.44±0.17**	28.44±0.17	28.46±0.17	28.44±0.17
i (degrees)	**89.806±0.093**	89.813±0.096	89.798±0.094	89.812±0.094
$F_{p,day}/F_*$ (ppm)	**472±85**	437±94	410±110	443±61
$F_{p,night}/F_*$ (ppm)	**≡0**	66±57	89±91	50±45
Phase Offset (°E)	**≡0**	-16±24	-27±31	-22±19
Quasi-Lambertian γ	$\mathbf{3.13}^{+0.46}_{-0.44}$	—	—	—
TRAPPIST-1 g				
R_p/R_*	**0.0872±0.0011**	0.0873±0.0011	0.0874±0.0011	$0.08691^{+0.00065}_{-0.00063}$
P (days)	**12.3557±0.0020**	$12.3556^{+0.0021}_{-0.0022}$	$12.3557^{+0.0020}_{-0.0021}$	$12.3556^{+0.0021}_{-0.0020}$
a/R_*	**84.21±0.48**	84.22±0.46	84.23±0.45	84.26±0.48
i (degrees)	**89.7465±0.0096**	89.7482±0.0096	89.7472±0.0097	89.7468±0.0099
Gaussian Process				
ln A (Amplitude)	**-16.72±0.24**	$-16.64^{+0.28}_{-0.25}$	$-16.63^{+0.42}_{-0.28}$	—
ln τ (Lengthscale)	$\mathbf{-3.87}^{+0.47}_{-0.36}$	$-3.78^{+0.59}_{-0.40}$	$-3.79^{+1.00}_{-0.44}$	—
# Free Parameters	**122**	123	124	122
Residual Std. Dev. (ppm)	**883**	883	884	907
ΔBIC (N_{data}=6571)	**0**	12.3	17.4	136.8

Extended Data Table 4 | Fitted and inferred parameters from TJB's fits using Setup #1.

follows:

$$F_{pi} = E_i + C_{1i}(\cos^2((\omega_i t - \delta_i)/2) - 1) \quad (6)$$

where E_i is the occultation depth of the planet and nightside flux can be calculated by $F_{nighside} = E_i - C_{1i}$. Furthermore, we also introduced an angle δ_i for each planet to explore possible peak offset due to atmosphere circulation. The phase curve, occultations, transits and planet-planet occultations are captured by using the `starry` package [54, 55]. The total number of free parameters in the analysis is 22, including phase curve parameters and orbital parameters (r_{pi},P_i, ω_i, ecc_i and i_i), several observational parameters such as limb-darkening coefficients u_1, u_2 (fitted by the quadratic law) and systematic variables c_0 and c_1. The priors of orbital parameters for TRAPPIST-1 b and TRAPPIST-1 c are taken from ref. [19] (details can be found in Extended Data Table 1). We also took secondary occultation depth of 861 ± 99 ppm for TRAPPIST-1 b and 421 ± 94 ppm for TRAPPIST-1 c as priors for our analysis taken from [4] and [7], respectively. The phase curve parameter A_b for both planets

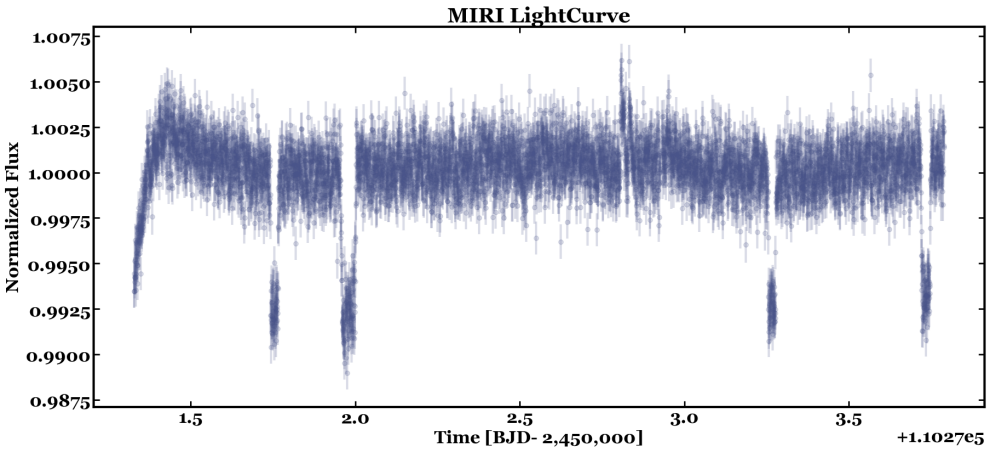

Extended Data Fig. 8 | Raw light curve from ZH analysis. Raw data from Stage 3, source radii = 9.0 pixels, background annulus from 16 to 36 pixels, from ZH Analysis

follows the prior of $A_b \sim \mathcal{N}(0.5, 0.1^2)$. In addition, we also added physical constraints for A_b to ensure positive emission for both dayside and nightside. For both planet, the offset angle δ_i is sampled using $\mathcal{N}(0, 45°)$ The `PyMC3` No-U-Turn Sampler(NUTS) is used to sample parameter space and explore the optimal fit. We ran 6 chains of 6000 tuning steps and 6000 production draws for the retrieval. We used the chi-square to compute the likelihood and used the 16th, 50th, and 84th percentiles from the samples to determine the best-fit values and their associated uncertainties.

The best fit parameters are listed in Extended Data Table 5 and the fitted combined phase curve is shown in Extended Data Fig. 9. We obtained a dayside flux of 835^{+75}_{-71} ppm and nightside flux of 100^{+66}_{-57} ppm for TRAPPIST-1 b with a shifted angle of $-2.02^{+6.14}_{-5.70}$ degree, which indicates an extremely poor heat-redistribution. For TRAPPIST-1 c, the dayside and nightside fluxes are 334^{+79}_{-78} ppm and 170^{+31}_{-92} ppm respectively with a shifted angle of $8.98^{+22.86}_{-37.07}$ degree. The best fit flux and shifted angle point to the possible existence of an atmosphere that re-distribute heat; however, the values are poorly constrained since the contribution of TRAPPIST-1 c's light curve to the total light curve is relative small. This leaves the existence of an atmosphere and the atmospheric composition of TRAPPIST-1 c still unclear based on the double phase curve retrieval but combined with previous eclipse depth of TRAPPIST-1 c, a thin atmosphere is favored (see atmospheric modeling below).

Quasi-Lambertian Phase Curve Fitting Alternatively, the phase variation is found to be consistent with high order cosine functions with a form similar to equation 4]:

$$\Phi(\alpha) = \cos^{\gamma}((\omega_i t - \delta_i)/2). \quad (7)$$

Here the γ is the Quasi-Lambertian parameter from ref. [17]. In the retrevial, we adopted a prior of $\gamma_i \sim N\left(2.0, 2.0^2\right)$. The combined phase curve can be derived similarly as:

$$F_{pi} = E_i + \Sigma_i C_{1i}(\Phi_i - 1) \quad (8)$$

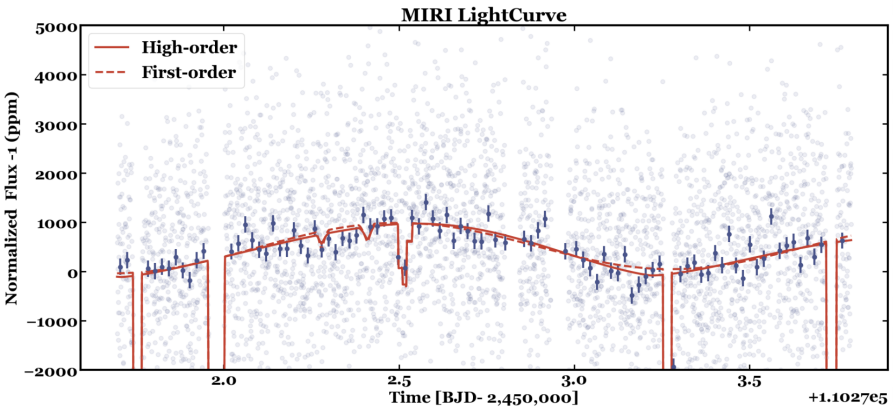

Extended Data Fig. 9 | Combined phase curve of TRAPPIST-1 b and TRAPPIST-1 c fitting (High-order : quasi-lambertian, First-order : sinusoidal from ZH data reduction in Extended Data Fig. 8

The best fit results are listed in Extended Data Table 5 with TRAPPIST-1 b has the order of $\gamma_b = 2.82^{+0.64}_{-0.56}$ and $\gamma_c = 3.92^{+1.89}_{-1.88}$. The newly retrieved dayside flux of TRAPPIST-1 b is 909^{+72}_{-73} ppm and the nightside flux is 65^{+56}_{-34} ppm with a shifted angle of $6.71^{+10.09}_{-7.14}$ degree. For TRAPPIST-1 c, the dayside and nightside fluxes are 356^{+82}_{-82} ppm and 135^{+57}_{-72} ppm respectively with a shifted angle of $-8.23^{+33.27}_{-20.09}$ degree. To calculate the brightness temperature, we use the stellar flux of 2.496 ± 0.080 mJy at 14.87 μm (see below) and retrieved parameters from MCMC results. Applying Planck's law, the brightness temperature of TRAPPIST-1 b and TRAPPIST-1 c are shown in Extended Data Table 5.

Free Parameter	PC model: Sinusoidal	PC model: Quasi-Lambert
Trappist-1 b		
A_b	$0.880^{+0.072}_{-0.098}$	$0.929^{+0.040}_{-0.074}$
δ_b (degree)	$-2.0^{+6.1}_{-5.7}$	$6.7^{+10.1}_{-7.1}$
γ_b	-	$2.82^{+0.64}_{-0.55}$
F_b (ppm)	835^{+75}_{-71}	909^{+72}_{-73}
P_b (days)	$1.510884^{+1.50e-07}_{-1.51e-07}$	$1.510884^{+1.50-07}_{-1.51e-07}$
T_{b-day} (K)	489 ± 18	508 ± 18
$T_{b-night}$ (K)	243 ± 40	220 ± 35
Trappist-1 c		
A_c	$0.49^{+0.32}_{-0.30}$	$0.62^{+0.24}_{-0.32}$
δ_c (degree)	9.0^{+23}_{-37}	-8.0^{+33}_{-20}
γ_c	-	3.9 ± 1.9
F_c (ppm)	334^{+79}_{-78}	356 ± 82
P_c (days)	$2.421793 \pm 2.3e-07$	$2.421793 \pm 2.3e-07$
T_{c-day} (K)	349 ± 28	356 ± 28
$T_{c-night}$ (K)	283 ± 43	266 ± 36
u_1	0.107 ± 0.062	0.142 ± 0.062
u_2	0.236 ± 0.083	0.210 ± 0.082

Extended Data Table 5 | Summary of MCMC derived physical parameters including brightness temperature from ZH analysis.

Comparison of the different reductions

We compared the different reductions and found good agreement between the four approaches. Extended Data Fig. 10 shows the detrended light curves obtained from four distinct analyses with their best-fit phase curve model. The analyses shown are (1) Analysis #1 for MG, (2) Analysis 7-planet #1 for ED, (3) Setup # 3 for TJB, and (4) the Sinusoidal analysis for ZH. Extended Data Fig. 11 shows the posterior distribution functions for the dayside flux ratio $F_{p,day}/F_\star$, the nightside flux ratio $F_{p,night}/F_\star$ and the phase curve offset δ from the same four analyses.

We note that all reductions and analyses yield results that are consistent with each other within 1-σ.

Calibrated stellar flux (MG + TJB)

As emphasized in ref. [37], translating our measured planet-to-star flux ratios into absolute planet fluxes and brightness temperatures required measurements of the absolute stellar flux $F_{*,15\mu m}$ and the effective wavelength of the observations. We performed the absolute flux measurement in the calibrated images of programs 1177, 2304, and 3077, using an aperture of 25 pixels, large enough to encompass 99.9% of the star's PSF [66]. An annulus extending from 30 to 45 pixels from the measured PSF's center was used to measure the background. We performed this flux measurement independently for the ten data sets, discarding images taken during transit or occultation, and the images of program 3077 affected by the initial large systematic effect and by a flare. Combining the ten measurements led to a mean stellar flux $F_{*,15\mu m}$ of 2.448 ± 0.040 mJy, the error bar being the standard deviation of the ten measurements. We added

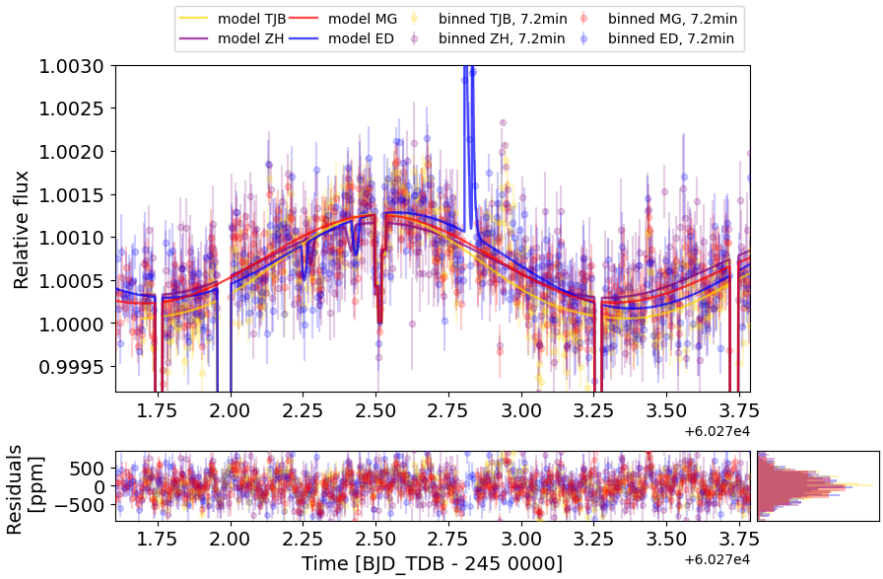

Extended Data Fig. 10 | Comparison of the light curves obtained from the four different data reductions. The top panel shows the raw light curves (MG analysis #1 in orange, ED analysis 7-planets #1 in green, TJB setup #1 in red, ZH quasi-Lambert in blue). The data are binned per 14.4 minutes. Each binned point is the average value of the individual points within the bin, with error bars equal to the standard deviation of the points within the bin. The solid line represent the best fit models from each analysis. The bottom panel shows the residuals for each light curve (raw minus best-fit).

quadratically a systematic error of 3%, which corresponds to the estimated absolute photometric precision of MIRI (P.-O. Lagage, private communication). It resulted in $F_{*,15\mu m}$ of 2.448 ± 0.083 mJy. We note that measurements' standard deviation is only 1.6%, nearly twice smaller than the instrument systematic error, which demonstrates the photometric stability of the star at 15 μm.

We then performed a similar independent measurement of the absolute stellar flux using TJB Stage 1 outputs. After photometric calibration and aperture extraction using the same aperture and annuli as in the first approach, we removed the astrophysical variations in the data caused by the planets (transits, eclipses, and phase variations) using the best-fit model from TJB's analysis described below. The median and standard error were then calculated for each visit, and then a final value was computed using the error-weighted mean of each of the different visits giving a value of 2.54314 ± 0.00011 mJy (where the uncertainty is the error-weighted standard error). After adding in quadrature the systematic error of 3%, this gives an absolute stellar flux of 2.543 ± 0.076 mJy. Both measurements are thus consistent with each other. We ultimately adopted the average of their values and errors - 2.496 ± 0.080 mJy - in our analyses. For the effective wavelength of the observations, we followed ref. [7] and adopted 14.87 μm.

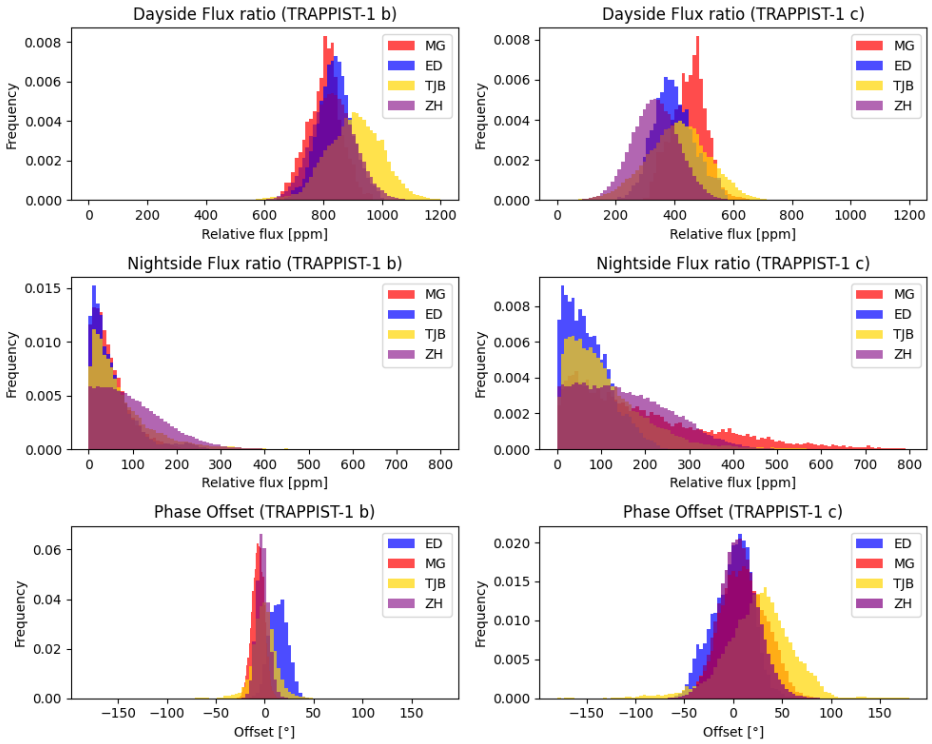

Extended Data Fig. 11 | Comparison of the posterior distribution functions for the dayside flux ratio $F_{p,day}/F_\star$, the nightside flux ratio $F_{p,night}/F_\star$ and the phase curve offset δ.

Day-Night Atmospheric Phase Curve Modeling (VM/AL)

To bridge the radiative and compositional versatility advantages of 1D climate-photochemical models, and the spatial and heat redistribution capabilities of 3D models, we use the Virtual Planetary Laboratory (VPL) 1D climate-photochemical model framework [24, 68] upgraded with a new two-column (day–night) climate mode [8], to model the thermal phase curves of TRAPPIST-1 b and c. The new two-column climate mode explicitly calculates day and night hemispheres with layer-by-layer, day-night advective heat transport driven by simplified versions of the 3D primitive equations for atmospheric transport. The geopotential gradient and convection/advection parameters were taken from ref. [8]. Comparison with ExoCAM 3D GCM results show that this model can adequately reproduce the day-night contrast of 3D GCM phase curves [8], from radiatively thin (N_2/O_2) to radiatively thick (CO_2) atmospheres, which are comparable to the types of atmospheres modeled here. VPL Climate uses SMART [70] with DISORT [71, 72] for spectrum-resolving radiative transfer for both climate modeling and planetary spectra generation. We adjust the stellar flux in our model for spectral simulations to match the observed stellar flux in the MIRI 15μm bandpass [8]. To generate the thermal phase curves, phase-dependent hemispherically-averaged, day–night weighted thermal flux spectra are calculated for each atmosphere,

assuming either a basaltic surface [73] or fixed albedo, and then convolved with the MIRI 1500W filter bandpass. We then generate thermal phase curves for post- or ongoing-water-loss atmospheres from 0.01 to 10 bar to compare with the observations (Extended Data Table 6).

To identify the most plausible planetary environments that fit the observed phase curves, we compare to the day and night data points assuming both b and c can have atmospheres, and hence a non-zero night-side flux for both planet (using secondary eclipse analyses from ref. [6, 7] and the nominal MG #1, this work). We use the following process to quantify the data/model goodness of fits. We first calculate the χ^2 between data and model. To determine the goodness of fit, we then calculate the confidence interval Z (in units of σ) as:

$$Z = \Phi^{-1}(1 - p/2), \tag{9}$$

where p is the upper-tail p-value for the cumulative distribution function for χ^2 given the number of degrees of freedom for comparing our forward models (with no fit parameters). We list these confidence intervals in Extended Data Table 6, along with the best-fit phase offset for each atmosphere model.

For TRAPPIST-1 b, we model two different surfaces. The primary surface was guided by the bare rock models in this work. We halve the albedo of our basalt surface to approximate the bond albedo of Mercury, and similar to the Fe-oxidized surface, the darkest mineral surface from the bare rock models. The modeled N_2 atmospheres are for comparison with the GCM results, and use a fixed grey albedo of 0.1. For TRAPPIST-1 b, a tenuous (0.1 bar) pure O_2 atmosphere or with 0.1% H_2O, both with photochemically generated ozone, provide the best joint fits (within 1.9σ) to the data of the models we considered (see Fig. 3). Our 0.01 bar N_2, 100 ppm CO_2 GCM comparison case also fits at 1.8σ. A pure 10 bar or greater oxygen atmosphere is ruled out at $> 5\sigma$. A 0.1 bar O_2 atmosphere with 1% H_2O is disfavored at 2.6σ. Adding O_2 or 100 ppm or more of CO_2 (in 0.1 bar or greater) redistributes too much energy (Extended Data Table 6). Our modeled 1 bar N_2 with 1 ppm atmosphere for comparison with the GCM is ruled out at 3.2σ.

We note in our phase curve modeling that our thin O_2 and N_2 models with the hottest day sides fail to reach the observed peak flux on the day side. This may have less to do with the atmospheric environments and is more likely to be a limitation of the two-column model, which may fail to resolve the sharp peak substellar temperature with thin atmospheres. This effect can be seen in the comparison of the 0.01 bar N_2 atmosphere modeled phase curves modeled by both the day–night model and the GCM (Fig. 3).

For TRAPPIST-1 c, the data quality make it impossible at this stage to discriminate between atmosphere fits. None of our atmospheres, which all fit the data point from [7], are ruled out by the phasecurve. The flattest modeled phase curve, the 0.1 bar steam atmosphere, is disfavored at only 2.3σ.

Although several tenuous atmospheres plausibly fit for TRAPPIST-1 b, and denser atmospheres are ruled out, even tenuous atmospheres may still produce relatively large transmission features (50–60 ppm), as shown in Extended Data Fig. 12. Additionally, the compositional constraints on the atmospheres for both planets are not sufficiently

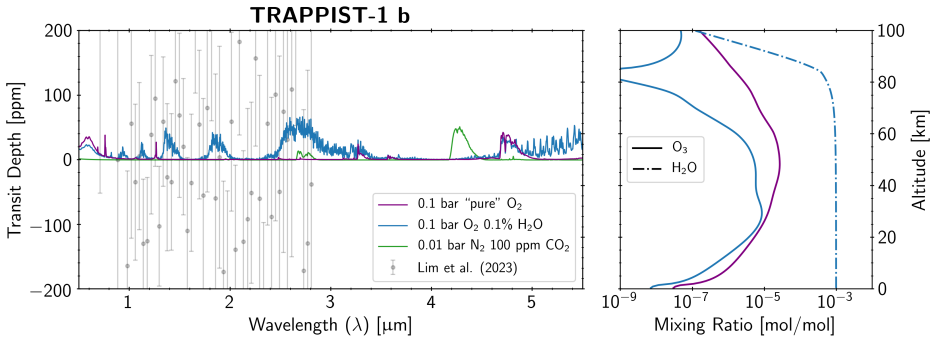

Extended Data Fig. 12 | Transit spectra and key gas profiles of 1.5D atmospheric models that fit the TRAPPIST-1 b phase curve measurements within 3σ. All features shown here are significantly smaller than the 1σ ($\sim$100 ppm) error bars from currently observed spectra, due to the stellar source noise issues. Shown are model transit spectra and gas profiles for TRAPPIST-1 b. The zero point for the transit depth is the planetary surface. The spectra demonstrate the potential for water vapor absorption at relative transit depths of 50–60 ppm. TRAPPIST-1 b may also exhibit ozone or CO_2 NIR features up to $\sim$50 ppm. These potential features should be taken into account if using either TRAPPIST-1 b in analyses for stellar contamination.

conclusive to categorically rule out even larger features in transit transmission observations, which may complicate attempts to use TRAPPIST-1 b to remove stellar contamination from the spectra of other TRAPPIST-1 planets [29], though work is underway to do so [30].

Environment	Surface	Surface Pressure	Day / Night Surf. Temp. [K]	Key Gases	Std. dev. [σ]
TRAPPIST-1 b					
O_2 pure	dark basalt	0.1 bar	456 / 165	O_2, O_3	1.4
O_2 pure	dark basalt	1 bar	461 / 252	O_2, O_3	1.9
O_2 pure	dark basalt	10 bar	468 / 340	O_2, O_3	5.7
O_2 outgassing	dark basalt	0.1 bar	493 / 288	O_2, 2% H_2O, 100 ppm CO_2, O_3, CO	5.8
O_2-H_2O (0.1%)	dark basalt	0.1 bar	474 / 234	O_2, 0.1% H_2O, O_3	1.6
O_2-H_2O (1%)	dark basalt	0.1 bar	483 / 267	O_2, 1% H_2O, O_3	2.6
N_2	$A = 0.1$	0.01 bar	463 / 132	N_2, 100 ppm CO_2	1.8
N_2	$A = 0.1$	1 bar	455 / 245	N_2, 1 ppm CO_2	3.2
TRAPPIST-1 c					
O_2 pure	basalt	0.1 bar	395 / 156	O_2, O_3	<1
O_2 pure	basalt	1 bar	388 / 237	O_2, O_3	<1
O_2 pure	basalt	10 bar	383 / 300	O_2, O_3	1.7
O_2 outgassing	basalt	0.1 bar	410 / 250	O_2, 2% H_2O, 10 ppm CO_2, CO, O_3	<1
O_2 outgassing	basalt	0.1 bar	419 / 235	O_2, 2% H_2O, 100 ppm CO_2, CO, O_3	<1
O_2-H_2O (0.1%)	basalt	0.1 bar	400 / 203	O_2, 0.1% H_2O, O_3	<1
O_2-H_2O (1%)	basalt	0.1 bar	405 / 236	O_2, 1% H_2O, CO, O_3	<1
O_2-H_2O (10%)	basalt	0.1 bar	433 / 267	O_2, 10% H_2O, 100 ppm CO_2, CO, O_3	1.5
Steam	basalt	0.01 bar	437 / 277	H_2O, 0.1% CO_2, CO, O_3	<1
Steam	basalt	0.1 bar	547 / 433	H_2O, 0.1% CO_2, CO, O_3	2.3

Extended Data Table 6 | VPL Climate Day-Night Model Planetary States and Results Table showing day-night model results for a broad sweep of atmosphere types, which include different surface pressures and key gases. Calculated day/night surface temperatures and standard deviation to combined day/night goodness of fit to [6] and day/night points of nominal analysis MG #1 are shown.

3-D Global Climate Modeling of TRAPPIST-1b and c and associated synthetic observables

We performed 3-D Global Climate Model (GCM) simulations of TRAPPIST-1b and c using the state-of-the-art `Generic PCM` (Generic Planetary Climate Model), extensively described in refs. [9, 26] in the context of the TRAPPIST-1 planets. GCM simulations enable resolving the 3-D structure of the atmosphere necessary to capture the day-night temperature contrast and to compute physically-consistent thermal phase curves.

The model includes self-consistent treatment of radiation, convection and clouds. Parameterizations of these processes are detailed in ref. [9] (and references therein). In short, radiation is computed using the correlated-k approach, using opacity tables based on HITRAN and HITEMP; convection is represented through dry and moist adjustment schemes; H_2O and CO_2 cloud formation is treated using a prognostic scheme, and assumes a fixed amount of cloud condensation nuclei (CCN). TRAPPIST-1b and c are in fact hot enough that water condensation is very limited and therefore that only a tiny amount of clouds form in the simulations.

We performed GCM simulations of TRAPPIST-1b and c to assess whether phase curves could be used to identify the atmospheric scenarios that are still plausible based on constraints from occultations alone [4, 6, 7]. For TRAPPIST-1b, this includes thin, residual atmospheres [5] as well as CO_2-rich atmospheres with a hot stratosphere [6], induced by absorption of high-altitude hazes. For TRAPPIST-1c, we investigated the specific case of a H_2O-dominated atmosphere using the simulations of ref. [9], which was shown to be roughly compatible with occultation measurements in two independent analyses [8, 9]. All simulations were performed assuming synchronous rotation. All planetary parameters (masses, radii, insolations) were taken from ref [19]. For the TRAPPIST-1 stellar spectrum, we used a PHOENIX BT-Settl spectrum as in ref. [26]. The surface albedo was set to 0.1 in all simulations. This choice is motivated by the fact that in most scenarios (except cases with hazes where the emission comes from very high in the atmosphere) a low surface albedo is necessary to match the measured occultations. A much wider range of 3-D GCM simulations will be presented in a follow-up paper (Maurel et al., submitted).

In the hazy TRAPPIST-1b simulations (*Haze high* and *Haze low*), we followed an approach very similar to the one used in ref. [6], which consisted in adding an extra source term of haze-induced opacity to the (correlated-k) CO_2 opacity tables in the GCM: $\sigma = f_{\rm haze}\ \kappa\ (\lambda_0/\lambda)^2\ (M_{\rm CO_2}/N_a)$, with $\kappa = 0.5$ cm$^2/g$ and $\lambda_0 = 1$ μm. In the *Haze high* case, we used exactly the same parameters as in ref. [6] ($f_{\rm haze} = 7.0 \times 10^{-4}$), but used a single-scattering albedo of 0.5 by artificially decreasing the incoming stellar flux accordingly. This artificial increase in albedo is necessary – compared to [6], which used 1-D atmospheric simulations with higher heat redistribution than predicted by the GCM – to prevent the dayside emission to be higher than the constraints given from the occultation observations. In the *Haze low* case, we used $f_{\rm haze} = 3.0 \times 10^{-5}$ and a single-scattering albedo of 0.2. In this case, the amount of hazes is so large that absorption of incoming stellar radiation takes place in the uppermost layers of the atmosphere.

Our strategy was the following: (1) we performed a grid of GCM simulations for both thin atmospheres and CO_2-rich atmospheres with high-altitude hazes (for TRAPPIST-1b) and of an H_2O-rich atmosphere for TRAPPIST-1c; (2) we computed occultations in the MIRI F1280W and F1500W filters, using the `Pythmosph3R` 3-D radiative transfer package [81]; (3) we selected the GCM simulations that best fit the MIRI observations [4, 7] (see Extended Data Fig. 13); (4) we computed thermal phase curves in the MIRI F1500W filter, using again `Pythmosph3R` (see Fig. 3). The sigma values can be found in the legend of Fig. 3. However, due to the complexity of the GCM simulations, the sigma values can not be used to compare GCM simulations to 1-D simulations, since they correspond to a very different modeling approach. We refer to Maurel et al., submitted, for more details.

For the post-processing, we used a stellar spectrum from the SPHINX model grid [82] interpolated to TRAPPIST-1's parameters. This whole spectrum was normalized by the measured flux at 15 μm. We checked the consistence with the measured flux at 12.8 μm from ref. [6], and found a difference of only 1.3% between our flux integrated at 12.8 μm and the one measured. Note that sensitivity tests were performed by comparing the outputs of `Pythmosph3R` with the `Planetary Spectrum Generator (PSG)` [83, 84] for airless and CO_2 dominated scenarios. The two codes show a good agreement, but we note that the amplitude of the synthetized phase curve is very sensitive to the opacity tables used. A more detailed comparison is out of the scope of this paper and will be carried on as part of the MALBEC model intercomparison project [85].

Extended Data Fig. 13 shows the results of TRAPPIST-1b occultations computed for five different GCM simulations that fit relatively well the measurements of ref. [4, 6], compared with the flux emitted by a low albedo (0.1), airless planet. At least two types of atmospheric scenarios are compatible with the data. This is the case for (1) thin and/or transparent atmospheres, in agreement with [5]; (2) CO_2-rich atmospheres with a fine-tuned upper-atmosphere haze layer, in agreement with [6]. While in the former cases most of the thermal emission comes from the surface, in the latter cases it comes from the upper-atmosphere layers (see Extended Data Fig. 13). In this case, CO_2 is seen in emission due to the strong near-infrared absorption by the haze layer. For this mechanism to work though, the optical properties of the hazes need to be fine-tuned (see above).

Extended Data Fig. 13 also shows that all five cases have a dayside temperature (weighted by the 15 μm emission contribution function) which is very close to the brightness temperature measured in the JWST MIRI occultation observations. However, they also show that as a result of non-negligible atmospheric heat transport, the nightside temperatures can vary significantly compared to the low-albedo, airless case (see temperature maps in Extended Data Fig. 14), leaving distinct features on the thermal phase curves (see Fig. 3). In the case of thin N_2+CO_2 atmospheres, a too high N_2 partial pressure and/or a too high a CO_2 mixing ratio increase heat redistribution, which can be discarded by the phase curve observations (see e.g. the N_2 1bar + 1ppm CO_2 case). GCM simulations also show that, in some working cases, CO_2 can collapse on the nightside (e.g. the N_2 0.01bar + 100ppm CO_2 case, which, after complete condensation of the CO_2, ends up on the N_2 0.01bar + 1ppm CO_2

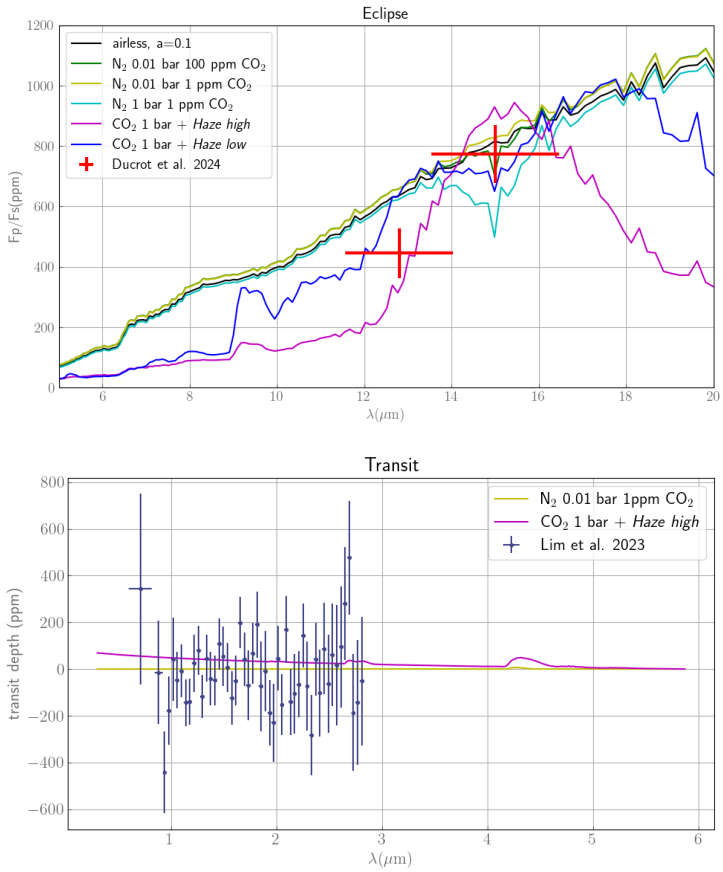

Extended Data Fig. 13 | Upper panel : Occultation depth measurements compared to models of TRAPPIST-1 b occultation depth spectra computed for five distinct GCM simulations along with a low albedo, airless planet case. Data points (in red) were taken from ref. [4, 6]. The six spectra have been selected here for their good agreement with the observed occultations at 12.8 and 15 μm. Lower panel : Transit spectra computed for the TRAPPIST-1b atmospheric scenarios fitting all available infrared MIRI data points (0.01 bar N_2 with 1 ppm of CO_2 and *Haze high* cases). The transit spectrum has been offset by 103 ppm for the *Haze high* case so that the minimum value is zero. For comparison, we added the transmission spectrum from ref. [25], not corrected from stellar contamination, with an offset of 7150 ppm.

case). In the case of thick CO_2 atmospheres with hazes, GCM simulations show that the amount of hazes and their optical properties need to be fine-tuned to fit both the occultations and the phase curve. In particular, as soon as the hazes absorb too low in the atmosphere, strong super-rotating winds in the atmosphere are enough to flatten the phase curve and generate an offset (see e.g., the *Haze low* case). For this scenario to work (see e.g., the *Haze high* case), the atmosphere must emit and therefore the hazes absorb high enough that the radiative timescale is much less than the advective timescale (by winds), thus limiting heat redistribution. The difference in altitude at which thermal emission occurs (*Haze high* vs *Haze low* cases) is clearly visible on

the pressure-temperature profiles of Extended Data Fig. 14. Consequences on the difference in nightside emission temperatures are also clearly visible on the associated temperature maps.

We did a similar exercise for TRAPPIST-1c, but focusing now on the H_2O-dominated atmospheric scenarios using the GCM simulations of ref. [9]. The case of a H_2O-dominated atmosphere is particularly interesting, as it had been proposed as being compatible within less than 2σ to occultations [8, 9]. GCM simulations show that H_2O-dominated atmospheres are in fact very effective at flattening the phase curve and generating a strong offset (see Fig. 3, bottom panel). Phase-curve observations therefore discard the cases of H_2O-dominated atmospheres. Given the past and present insolation on TRAPPIST-1c, which places it outside the water condensation zone [9], this result suggests that TRAPPIST-1c, like TRAPPIST-1b, started out with a relatively limited amount of water [86].

Finally, we computed transit spectra of TRAPPIST-1b with `Pythmosph3R` employing the same GCM simulations. The aim is to assess (1) the amplitude of transit spectra features produced by the different types of atmospheres which are still compatible with the different MIRI datasets (0.01 bar N_2 with 100 ppm of CO_2 and *Haze high* cases), (2) the impact of using planets b to remove stellar contamination from the transit spectra of other, outer planets [29, 30]. This is an essential prerequisite for the success of the JWST GO 6456 program [88], whose aim is to use consecutive transits of TRAPPIST-1b and e to correct for the stellar contamination of planet e using planet b. This method assumes, however, that planet b has no atmosphere, otherwise it risks introducing a new source of contamination. We find that the amplitude of transit spectra (see Extended Data Fig. 13) is low but non-negligible, in particular for the CO_2-rich hazy atmospheric scenario. This is because the presence of hazes produces a significant slope in the spectrum (in the visible and near-infrared wavelengths covered by NIRSpec and NIRISS instruments), and the heating produced by this haze increases the scale height of the atmosphere, which makes CO_2 feature prominent – although not as strong as the clear-sky case, due to blanketing by hazes [3] – in particular at 4.3 μm. Thin atmosphere scenarios produce absorption features with low amplitudes as expected [90]. For the TRAPPIST-1b transit spectra we have computed, in all cases the amplitude of the molecular features is well below the precision of the JWST NIRISS observations of ref. [25] (see Extended Data Fig. 13).

Tidal heating and constraints from observations

Here we present potential observational constraints on the rotation and the obliquity states of the planet b considering the effect of tidal heating. Deviations from a circular orbit, a synchronized rotation and a null obliquity result in tidal dissipation. According to posterior distributions, the maximum nightside fluxes at 2σ and 3σ are 196 ppm and 270 ppm, respectively, which correspond to brightness temperatures of 291K and 322K, respectively. These upper limits on the nightside temperature allows to put an upper limit on the actual tidal heating and therefore to constrain the domain of possible rotation rate - obliquity - the eccentricity being constrained independently by transit and eclipse timing/durations. The tidal heat flux also depends, however, on the internal structure of the planet (Bolmont et al. in prep).

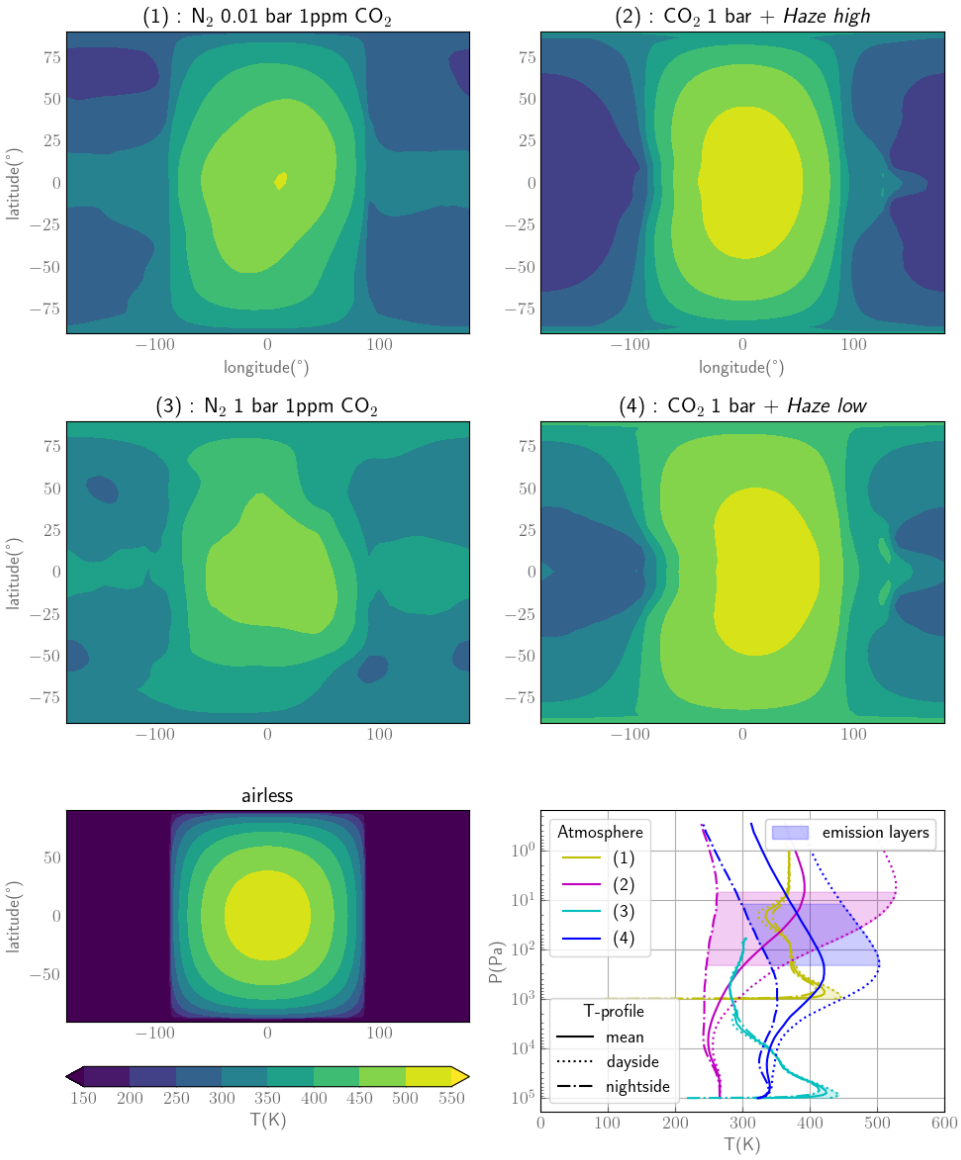

Extended Data Fig. 14 | Temperature maps computed for four distinct GCM simulations along with a low albedo, airless planet case. The maps were computed by weighting vertically the 3-D field of atmospheric temperatures by their contribution to the thermal emission at 15 μm. The figure also shows the vertical temperature profiles for each case, as well as the vertical region of contribution to thermal emission. All five cases have a dayside temperature very close to the brightness temperature measured by the JWST MIRI occultation observations.

Usually, the computation of tidal heating uses a simple prescription of tides, based on an equilibrium model, such as the constant time lag model (i.e. CTL, [92, 93]). But such a model does not take into account the complex response of a rocky planet to the tidal forcing [94]. Here, we use a frequency-dependent tidal response following the method of refs. [95, 96], computed with an Andrade rheology [97]. The tidal heating is computed using the method of ref. [98] (Eq 4.)

$$\dot{E}_{\rm tidal} = -\frac{{\rm d}E}{{\rm d}t} = -C\Omega \times \frac{{\rm d}\Omega}{{\rm d}t} - \frac{GM_pM_\star}{2a^2} \times \frac{{\rm d}a}{{\rm d}t}, \tag{10}$$

where E is the total energy of the system, M_p and $M_\star$ the masses of the planet and star respectively, Ω the rotation rate of the planet, C its moment of inertia and a its semi-major axis. We use the equations for the derivative of a and of Ω of ref. [99] (Eq. 116 and 123).

We calculate the dissipation assuming a multi-layered internal structure, based on masses and radii from ref. [19], with a silicate mantle and a liquid metallic core. The internal structures are computed using the `BurnMan` code [100, 101], which enables us to explore the effects of degeneracy in possible planetary structures by testing three different scenarios (Bolmont et al., in prep). We consider three different core sizes by varying their composition, in percentage of iron, silicium and sulfur. The smallest core we consider has an Earth-like composition, comprising approximately 57% of the planet's total radius. The biggest core we consider has a much lighter composition, comprising approximately 84% of the planet's total radius. The different relative core sizes considered are listed in Extended Data Table 7. The mantle is assumed to be

Extended Data Table 7 | Relative size of the core to the total radius of each planet (%)

Planet	Big core	Intermediate core	Small core
T1-b	84.3	70.3	57.0
T1-c	85.7	71.6	57.8

silicate with pyrolitic composition. The bulk dissipation is neglected, assuming only the dissipation associated with shear deformation [95, 102]. As shown below, a bigger core corresponds to a higher dissipation than a smaller core. It is important to keep in mind that the retroaction of the tidal heating on the internal structure is not taken into account here.

Extended Data Fig. 15 shows color maps of the tidal temperature (given by $(\Phi_{\rm tides}/\sigma)^{1/4}$, where $\Phi_{\rm tides}$ is the tidal heat flux and σ the Boltzmann constant) as a function of the rotational and obliquity state, for the three internal structures, that correspond to high to low dissipation cases, and for the upper and lower limit in eccentricities given in Table 1. The maximum night side temperatures measured at 291K and 322K constrain the obliquity to be up to 2° for the high dissipation case and to 3.5° for the low dissipation case. The rotation state can be constrained within about 0.02% and 0.06% of the orbital period, i.e. $0.99979 < \Omega/n < 1.00058$.

Planet-planet interactions induce short-time scale variations in the mean motion of each planet. For planet b, the mean motion variations are strong enough to take the spin out of the synchronization, i.e., the spin rate does not stay strictly equal to the mean motion [103]. Ref. [103] used the N-body code `osidonius` to compute the spin of the TRAPPIST-1 planet using a tidal model which allows to correctly descrive the response of rocky planets. They found that the spin oscillates around the synchronization state $\Omega/n = 1.0$, see Extended Data Fig. 16. The maximum and minimum deviation of that spin is represented in Extended Data Fig. 15 (vertical black dotted lines). The vertical black dashed-dotted lines correspond to the range within which the spin spends 70% of the simulation time. It is interesting to note that the limits of the spin oscillations are compatible with the observational constraints we get.

We compare tidal temperatures with nightside brightness temperatures, acknowledging that tidal temperatures may differ from nightside values in cases of non-purely synchronous rotation. For such rotations, planetary inertia must be considered to accurately determine nightside temperatures. However, in the narrow range of Ω/n (0.999 to 1.001) studied here, the departure from synchronization is negligible, allowing tidal temperatures to reliably approximate nightside brightness temperatures.

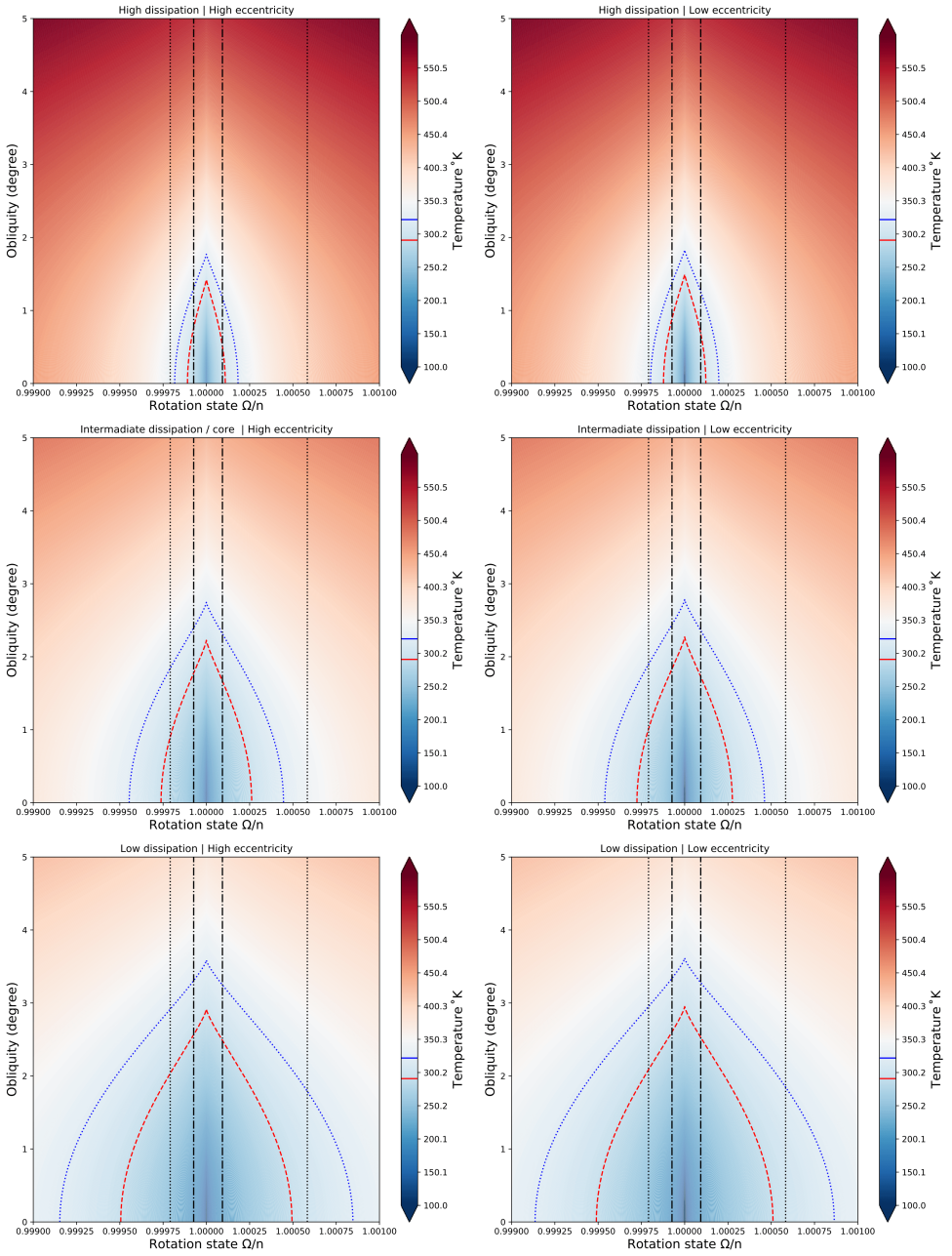

Extended Data Fig. 15 | Tidal temperature (in K) for the planet b. The red and blue curves represent the 196 and 270 ppm maximum emission from the night side of the planet, i.e. 291K and 322K. The black dash-dotted lines correspond to the maximum and minimum variations of the spin rate from the synchronization state $\Omega/n = 1.0$ from ref. [103]. The dash-dotted lines represent the range within which 70% of the spin variation occurs.

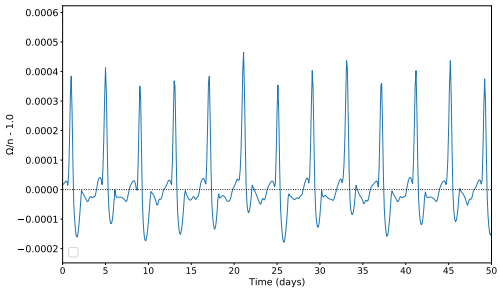

Extended Data Fig. 16 | Deviation of the spin state of planet b from the synchronization in $\Omega/n-1$, with Ω the spin rate, n the mean motion. The horizontal line at $\Omega/n-1=0$ represents the perfect synchronization state. The simulation was made with the N-body code Posidonius [103–105].

Bare rock simulations for TRAPPIST-1 b

Based on the phase curve of TRAPPIST-1 b, we performed simulations assuming the planet is an airless bare rock. We use the model developed in ref. [31], which simulates the 3D temperature profile (latitude, longitude, and depth) of an airless planet. The model takes into account instellation, reflection, thermal emission, and heat conduction in the subsurface. For the stellar spectrum we assume a Phoenix stellar model. For the planet's surface we assume it consists of regolith, like the Moon and Mercury. We then model the regolith's bi-directional reflectance and emission following [106]; this approach is motivated by laboratory measurements and solar system observations. We neglect horizontal heat conduction since heat redistribution via conduction is too small to influence a planet's phase curve [107]. In addition we assume both planets are in 1:1 synchronous rotation and ignore potential tidal heating (see 2).

First, we simulate different geologically fresh surfaces. The surfaces are based on reflectance spectroscopy measurements of different materials and were compiled in ref. [108]. For each material, we first find the planet's temperature distribution in local radiative equilibrium. We then compute phase curves in the MIRI-F1500W bandpass plus secondary eclipse spectra. Note that, since initial submission of this manuscript, other databases of surface materials have been published [109, 110]. For ease of comparing our results to previous models for TRAPPIST-1 b, here we only consider the materials from ref. [108].

The phase curves are shown in the left panel of Extended Data Fig. 17. The data are best fit by an ultramafic; all other surfaces considered here produce a higher χ^2 than an ultramafic. Even the second best-fitting fresh model, a Fe-oxidized surface made of hematite ($Fe2O_3$), produces a significantly worse fit than an ultramafic (χ^2=52.20 for an ultramafic versus χ^2=59.47 for a Fe-oxidized surface). Assigning confidence intervals based on $\Delta\chi^2$ relative to the best-fit model [111], suggests that any model with $\Delta\chi^2 > 6.63$ relative to the ultramafic can be ruled out at 3σ confidence. Applying this criterion to TRAPPIST-1 b's phase curve, we find that an ultramafic is preferred over all geologically fresh surfaces from ref. [108] at more than 3σ.

In contrast to the MIRI phase curve, which strongly indicates the planet's surface should be dark, we find that the secondary eclipse spectrum provides a much weaker constraint. The left panel of Extended Data Fig. 18 compares spectra of geologically fresh surfaces against the observed eclipse depth at 15μm (from Analysis #2; see main text) and the planet's published eclipse depth at 12.8μm from ref. [6]. We find that the observed secondary eclipse spectrum is best fit by an ultramafic surface (χ^2=2.86), similarly to [6]. This result corresponds to the phase curve fitting. However, most surfaces and even a blackbody match the observed eclipse spectrum within 3σ ($\Delta\chi^2 < 6.63$ relative to best-fit). Based solely on the eclipse measurements, the only fresh surfaces that are ruled out at more than 3σ relative to the best-fitting surface are those with very high albedo, namely feldspathic and granitoid surfaces. This highlights the valuable additional constraints provided by the phase curve.

Taking the phase curve at face value, the question is: what physical process could explain a low albedo for TRAPPIST-1 b? To address this question we simulate the potential impact of space weathering. In the Solar System, albedos and spectra of atmosphere-less bodies are modified and typically darkened by a range of processes

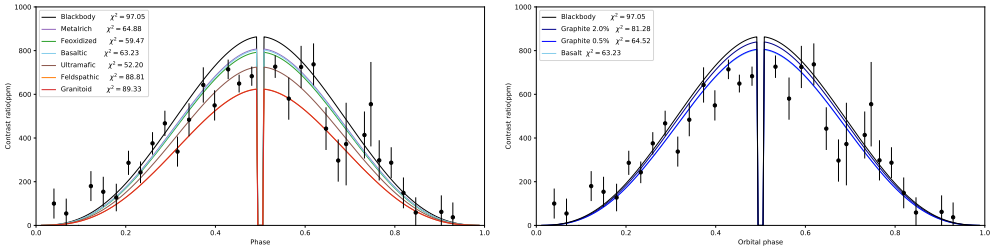

Extended Data Fig. 17 | TRAPPIST-1 b's phase curve for different geologically fresh surface materials (left) and a space weathered basalt surface (right) compared to data from MG Analysis #2. Left: Models for the planet's dayside emission spectrum based on geologically fresh materials (curves), compared to the 15μm phase curve from this work (black point). A blackbody is significantly preferred ($> 3\sigma$) over all geologically fresh materials shown here. Right: Space weathering improves the fit to observations, by reducing the planet's albedo at short wavelengths and increasing the phase curve amplitude at 15 μm.

called space weathering [34]. Here we investigate the impact of space weathering using the same approach that was previously applied to LHS-3844 b [31]. For simplicity we assume the planet's bulk surface consists of basalt. This assumption is reasonable, as basalt is a wide-spread material in the solar system. We then simulate the effects of space weathering by adding increasing amounts of graphite, which has been previously proposed to explain the low albedo of Mercury [113]. Note that we are not trying to constrain the exact space weathering mechanism, and space weathering via the formation of iron nanoparticles could similarly produce a low surface albedo [31].

The results are shown in the right panels of Extended Data Fig. 17 and Extended Data Fig. 18. We find that moderate space weathering weakens the fit to the observed phase curve (χ^2=81.28 for strongly weathered basalt versus χ^2=63.23 for fresh basalt), plus increasing the mismatch to the eclipse spectrum (χ^2=7.37 versus χ^2=5.92). With 2% graphite by volume added, TRAPPIST-1 b's albedo significantly decreases, and the surface becomes increasingly indistinguishable from a blackbody. For comparison, the 2% graphite considered here is less than the 3-6% invoked to explain Mercury's low surface albedo [113].

Assuming the planet is airless, consistent with previous atmospheric analyzes, we conclude that, based on the JWST 15 μm phase curve and the materials considered here, TRAPPIST-1 b's surface is most likely to be fresh ultramafic. However, current data are still insufficient to place strong constraints on TRAPPIST-1 b's bulk composition if taking account of 12.8 μm observation and potential space weathering effect. Although we only simulated space weathering for basalt, space weathering would similarly darken other materials. Taking into account the potential degeneracy due to space weathering, feldspathic and granitoid might thus produce a similarly good match to the observed phase curve amplitude.

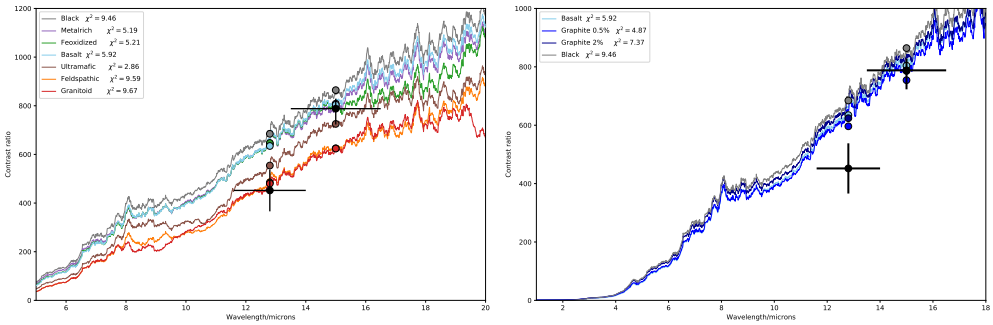

Extended Data Fig. 18 | TRAPPIST-1 b's dayside spectrum for different geologically fresh surface materials (left) and a space weathered basalt surface (right). Left: Models for the planet's dayside emission spectrum based on geologically fresh materials (curves), compared to the contrast ratio at 15μm from this work (black point) and the reported contrast ratio at 12.8μm (grey point, from ref. [6]). Right: Space weathering darkens the surface and improves the match to the observed flux at 15μm. Progressively darker curves correspond to increasing space weathering via the addition of graphite.

Flare characterization

During the $\simeq$ 60hours of observations of TRAPPIST-1 we observed a clear flares. In this section we discuss how these flares can be modeled and estimate the associated energy to compare it to existing studies on TRAPPIST-1 [35, 45, 116]. The flaring event and the best-fit model from this analysis is shown in Extended Data Fig. 19. The flares were fitted with a three-component model using the formalism from [117] described by equation (11) and fitted with `emcee` [63]:

$$F_{\mathrm{flare},t} = \frac{\sqrt{\pi}}{2} AC * \Big(F_1 h(t, A, B, C, D_1) + F_2 h(t, A, B, C, D_2) \Big) \tag{11}$$

with

$$h(t, B, C, D) = e^{-Dt + (\frac{B}{C} + \frac{DC}{2})^2} \mathrm{erfc}\left(\frac{B - t}{C} + \frac{CD}{2} \right) \tag{12}$$

where, t is the relative time; A is the amplitude; B is the position of the peak of the flare; C is the Gaussian heating timescale; D_1 is the rapid cooling phase timescale; D_2 is the slow cooling phase timescale; and $F_2 = 1–F_1$ describes the relative importance of the exponential cooling terms. The parameters resulting from this fit are presented in Extended Data Table 8.

Flare #	**Timing ± 1-σ [JD - 2460000] B in eq. (11)**		**Amplitude ± 1-σ [ppt] A in eq. (11)**		**Duration ± 1-σ (min) D1 in eq. (11)**		**Flare energy (erg)**
1	272.808004	4.44E-04	6.24	0.17	8.74	2.11	1.389047e+33
2	272.815411	9.6E-04	1.89	0.91	9.92	4.47	1.526377e+33
3	272.832834	3.93E-04	3.55	0.37	8.97	2.47	2.974541e+33

Extended Data Table 8 | Output flare parameters from fit using Mendoza et al. 2022. Timing, amplitudes, and duration of the flares are measured through a MCMC analysis of the light curve centered on the flaring events.

Assuming that the star is a blackbody radiator, the bolometric flare luminosity can be defined as equation:

$$L_{\mathrm{flare,bol}} = \sigma_{SB} T_{\mathrm{flare}}^4 A_{\mathrm{flare}}, \tag{13}$$

where σ_{SB} is the Stefan-Boltzmann constant, T_{flare} is the black-body temperature of the flare, and A_{flare} is the area of the flare. Then, to estimate A_{flare}, we use the observed luminosity of the star ($L_\star$) and the luminosity of the flare (L_{flare}) defined by equation (14), where the integration is made for the F1500W MIRI filter band.

$$L_{\mathrm{flare,F1500W}}(t) = A_{\mathrm{flare}}(t) \int_{F1500W} R_\lambda B_\lambda(T_{\mathrm{flare}}) d\lambda \tag{14}$$

and the flare amplitude in relative flux $\frac{\Delta F(t)}{F(t)}$ is defined as equation (15) :

$$\frac{\Delta F(t)}{F(t)} = \frac{L_{\mathrm{flare,F1500W}}(t)}{L_\star}. \tag{15}$$

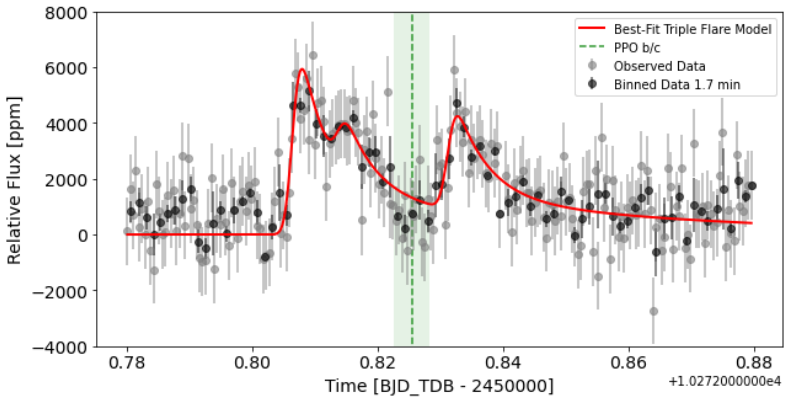

Extended Data Fig. 19 | Best fit triple-flare event caught during the observations. The three flares are modeled using eq. 11. We note that a planet-planet occultation (PPO) of planet b by planet c is also supposed to happen in between the two flares according to the parameters and ephemeris from ref. [19].

In equation (14), R_λ stands for the spectral response function of the F1500W filter and B_λ is the Planck function. From equations (14) and (15), we can derive A_{flare}, see equation (16) :

$$A_{\mathrm{flare}} = \frac{\Delta F(t)}{F(t)} \pi R_\star^2 \frac{\int R_\lambda B_\lambda(T_{\mathrm{eff}}) d\lambda}{\int R_\lambda B_\lambda(T_{\mathrm{flare}}) d\lambda} \tag{16}$$

Finally, the total bolometric energy of the flare ($E_{\mathrm{flare,bol}}$) is defined as the integral of $L_{\mathrm{flare,bol}}$ over the flare duration, equation (17) :

$$E_{\mathrm{flare,bol}} = \int L_{\mathrm{flare,bol}}(t) dt \tag{17}$$

From eq. (17) we derive the energy of the three flares, see Extended Data Table 8. We note that this energy is dependent on the temperature that we assume for the flare. It is common practice to assume a temperature of 9000 K in the literature [118, 119]. However, a recent study by refs. [45, 120] show that the spectra of the flares observed with MuSCAT1 and JWST/NIRISS instruments are well fitted with black body temperatures lower than the commonly used 9000K. Most recently, [45] shows that the flares are well-described by a blackbody emission with an effective temperature 5300 K. To address both of these scenarios we compute the flare energies and frequencies assuming first that the temperature of the flare is 9000 K and then assuming it is 5300 K. In Extended Data Fig. 20 we show the resulting flare frequency

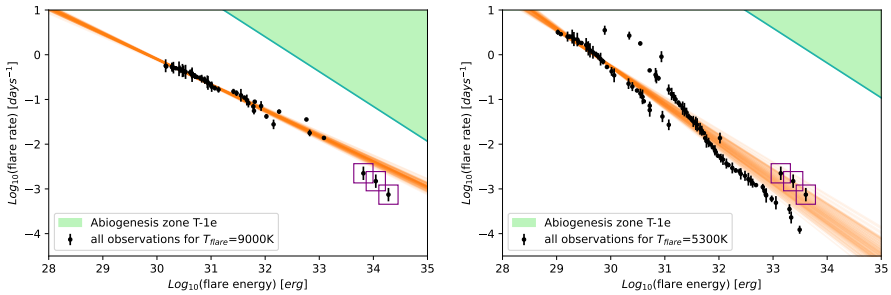

Extended Data Fig. 20 | Flare frequency distribution plot for TRAPPIST-1. *Left:* FFD using data from ref. [35] and refs. [116, 121] and the two newly observed flares from MIRI F1500W observations, assuming a 9000 K blackbody for the flares. Orange lines show the results from 200 best fit from the MCMC. *Right:* Same but using data from [45] and assuming a 5300 K blackbody for the flares.

distribution (FFD) for these two scenarios. In both cases the three flares that we detect with MIRI at 15μm are among the most energetic ever observed. These observations are remarkable but also highlight the possible presence of several "mini flares" in the data set, adding more red noise. Furthermore, having gained valuable insights from this experience, we highly recommend performing simultaneous observations of TRAPPIST-1 in a bluer band whenever possible, preferably from the ground, for all future JWST observations (GO 6456). This approach would enable the detection of lower energy flares that might not be significantly visible in the NIR light curve but which could introduce correlated noise into the observations. In addition these observations are underlining the important of programs such as GO 7068 that aim to provide a library of M-dwarfs flares[2].

Finally we run a MCMC analysis to derive that the occurrence rate as a function of flare energy can be described as:

$$\log(\nu) = \beta \log(E) + \alpha \tag{18}$$

Where $\beta = -0.8467 \pm 0.05$ for $T_{flare} = 9000$ K and $\beta = -0.84 \pm 0.04$ for $T_{flare} = 5300$ K. In comparison ref. [35] found $\beta = -0.63 \pm 0.14$, fitted from our measurements, ref. [121] found $\beta = -0.61 \pm 0.02$, ref. [120] found $\beta = -0.45 \pm 0.20$, and ref. [116] found $\beta = -0.59$.

Data availability

The program 3077 JWST data used in this work are available on the MAST online database (https://mast.stsci.edu/portal/Mashup/Clients/Mast/Portal.html).

[2] https://www.stsci.edu/jwst-program-info/download/jwst/pdf/7068/

Code availability

The code `TRAFIT` used to analyse the light curves is a `Fortran 2003` code that can be obtained from the first author on reasonable request. The `Generic PCM` (and documentation on how to use the model) can be downloaded from the SVN repository https://svn.lmd.jussieu.fr/Planeto/trunk/LMDZ.GENERIC/. More information and documentation on the model are available on http://www-planets.lmd.jussieu.fr. The N-body code `Posidonius` and its documentation are available from https://github.com/revolal/posidonius/tree/kaula_v2.

Authors' contributions

MG co-led the project with ED. Both of them wrote the JWST proposal of program 3077, interacted with STScI to set up observations, performed an analysis of the data, and wrote a significant part of the paper. T.J.B. contributed one of the independent analyses using the `Eureka!` pipeline and contributed significantly to the writing and editing of the paper. X.L. and D.D.B.K. designed the strategy and experiments for the bare rock models and space weathering simulations of TRAPPIST-1 b and c, and wrote the corresponding parts of the paper. V.S.M. and A.P.L. designed the strategy and experiments for day-night climate-photochemical-spectral modeling of the TRAPPIST-1 b and c planets. A.P.L. conducted the day-night climate-photochemical simulations, and prepared the associated secondary eclipse spectra and phase curves of TRAPPIST-1 b and c. V.S.M. and A.P.L. interpreted the results and wrote the corresponding parts of the paper. E.A., A.P.L., V.S.M., and J.L-Y. developed the calculation of the confidence of phase curve model fits to the data. A.M. and M.T. performed the 3D GCM simulations of TRAPPIST-1b and c for the JWST proposal of program 3077 and the present paper. A.M., M.T., T.F. and J.L. computed the associated eclipses, phase curves and transit spectra for the proposal and the present paper. A.M., M.T., F.S., J.L. and T.F. designed the strategy for 3D climate modeling of the TRAPPIST-1b and c planets, and wrote the corresponding parts of the paper. AH and DB performed a data reduction and analysis of the photometric time-series. BOD conducted an independent reduction of the data and analysed the photometric time-series. TG contributed to the design of the observations and contributed the JWST program 1177 observations used in the joint analyses. Z.H. and C.D. performed an independent data reduction and analysis of the JWST/MIRI data and wrote the corresponding part of the manuscript. AR performed N-body simulations of TRAPPIST-1 including tides with `Posidonius` to estimate the rotation of the planets. AR and EB performed estimations of the tidal heating that planets b and c are experiencing, within the framework of a realistic dissipation response. AR, EB and FS wrote the corresponding part of the paper.

Acknowledgments We thank Olivia Lim for sharing their transmission spectra of TRAPPIST-1 b obtained from the reduction and analysis of JWST/NIRISS data and published in their paper ref. [25]. This work is based on observations made with the NASA/ESA/CSA JWST. The data were obtained from the Mikulski Archive for Space Telescopes at the Space Telescope Science Institute, which is operated by the Association of Universities for

Research in Astronomy, Inc., under NASA contract NAS 5-03127 for JWST. These observations are associated with programs 1177, 1279, 2304 and 3077. MG is F.R.S-FNRS Research Director. His contribution to this work was done in the framework of the PORTAL project funded by the Federal Public Planning Service Science Policy (BELSPO) within its BRAIN-be: Belgian Research Action through Interdisciplinary Networks program. The authors thank the Belgian Federal Science Policy Office (BELSPO) for the provision of financial support in the framework of the PRODEX Programme of the European Space Agency (ESA) under contract number 4000142531. T.J.B. and T.P.G. acknowledge funding support from the NASA Next Generation Space Telescope Flight Investigations program (now JWST) via WBS 411672.07.05.05.03.02. T.J.B. also acknowledges funding support from STScI provided with GO 3077 through JWST-GO-03077.015-A. C.D. and Z.H. acknowledge funding support from NASA Exoplanets Research Program via Grant No. 80NSSC23K1115, STScI provided with GO 3077 through JWST-GO-03077.019-A, and Alfred P. Sloan Research Fellowship. X.L. and D.D.B.K. acknowledge support from the National Natural Science Foundation of China (NSFC) under grant 42250410318. M.T. acknowledges support from the Tremplin 2022 program of the Faculty of Science and Engineering of Sorbonne University. M.T., A.M. and J.L. thank the Generic PCM team for the teamwork development and improvement of the model. M.T. acknowledges support from the High-Performance Computing (HPC) resources of Centre Informatique National de l'Enseignement Supérieur (CINES) under the allocations No. A0120110391 and A0140110391 made by Grand Équipement National de Calcul Intensif (GENCI). V.S.M., A.P.L. and E.A. are part of the Virtual Planetary Laboratory Team, which is a member of the NASA Nexus for Exoplanet System Science, and financed through NASA Astrobiology Program grant 80NSSC18K0829. V.S.M. and A.P.L. made use of the advanced computational, storage, and networking infrastructure provided by the Hyak supercomputer system at the University of Washington. B.-O. D. acknowledges support from the Swiss State Secretariat for Education, Research and Innovation (SERI) under contract number MB22.00046. A.R. and E.B. acknowledge the financial support of the SNSF (grant number: 200021_197176 and 200020_215760). This work has been carried out within the framework of the NCCR PlanetS supported by the Swiss National Science Foundation under grants 51NF40_182901 and 51NF40_205606. The N-body computations including tides with `Posidonius` were performed at University of Geneva on the Baobab and Yggdrasil clusters. The GO 3077 team offers a special thanks to Sarah Kendrew and the JWST Science Operations' Planning and Scheduling Team at the Space Telescope Science Institute for their dedicated efforts to optimize and schedule the long MIRI observation that made the entirety of this work possible.

Methods References

[38] Kass, R. E. & Raftery, A. E. Bayes factors. *Journal of the American Statistical Association* **90** (430), 773–795 (1995). URL https://www.tandfonline.com/doi/abs/10.1080/01621459.1995.10476572. https://doi.org/10.1080/01621459.1995.10476572, https://www.tandfonline.com/doi/pdf/10.1080/01621459.1995.10476572 .

[39] Bushouse, H. *et al.* JWST Calibration Pipeline (2024).

[40] Agol, E. *et al.* Refining the Transit-timing and Photometric Analysis of TRAPPIST-1: Masses, Radii, Densities, Dynamics, and Ephemerides. *Planet. Sci. J.* **2** (1), 1 (2021). https://doi.org/10.3847/PSJ/abd022, arXiv:2010.01074 [astro-ph.EP].

[41] Deming, D. *et al.* Spitzer Secondary Eclipses of the Dense, Modestly-irradiated, Giant Exoplanet HAT-P-20b Using Pixel-level Decorrelation. *Astrophys. J.* **805** (2), 132 (2015). https://doi.org/10.1088/0004-637X/805/2/132, arXiv:1411.7404 [astro-ph.EP].

[42] Gillon, M. *et al.* Search for a habitable terrestrial planet transiting the nearby red dwarf GJ 1214. *Astron. Astrophys.* **563**, A21 (2014). https://doi.org/10.1051/0004-6361/201322362, arXiv:1307.6722 [astro-ph.EP].

[43] Hastings, W. K. Monte carlo sampling methods using markov chains and their applications. *Biometrika* **57** (1), 97–109 (1970). URL http://www.jstor.org/stable/2334940 .

[44] Schwarz, G. Estimating the Dimension of a Model. *Annals of Statistics* **6** (2), 461–464 (1978) .

[45] Howard, W. S. *et al.* Characterizing the Near-infrared Spectra of Flares from TRAPPIST-1 during JWST Transit Spectroscopy Observations. *Astrophys. J.* **959** (1), 64 (2023). https://doi.org/10.3847/1538-4357/acfe75, arXiv:2310.03792 [astro-ph.EP].

[46] Gaia Collaboration. VizieR Online Data Catalog: Gaia EDR3 (Gaia Collaboration, 2020). *VizieR Online Data Catalog* I/350 (2020). https://doi.org/10.26093/cds/vizier.1350 .

[47] Bourque, M. *et al.* ExoCTK: Exoplanet Characterization Tool Kit. Astrophysics Source Code Library, record ascl:2207.012 (2022). 2207.012.

[48] Kipping, D. M. Efficient, uninformative sampling of limb darkening coefficients for two-parameter laws. *Mon. Not. R. Astron. Soc.* **435** (3), 2152–2160 (2013). https://doi.org/10.1093/mnras/stt1435, arXiv:1308.0009 [astro-ph.SR].

[49] Luger, R., Lustig-Yaeger, J. & Agol, E. Planet-Planet Occultations in TRAPPIST-1 and Other Exoplanet Systems. *Astrophys. J.* **851** (2), 94 (2017). https://doi.org/10.3847/1538-4357/aa9c43, arXiv:1711.05739 [astro-ph.EP].

[50] Dyrek, A. *et al.* Transiting exoplanets with the Mid-InfraRed Instrument on board JWST: From simulations to observations. *Astron. Astrophys.* **683**, A212 (2024). https://doi.org/10.1051/0004-6361/202347127, arXiv:2403.00676 [astro-ph.EP].

[51] Charbonneau, D. *et al.* The Broadband Infrared Emission Spectrum of the Exoplanet HD 189733b. *Astrophys. J.* **686** (2), 1341–1348 (2008). https://doi.org/

10.1086/591635, arXiv:0802.0845 [astro-ph].

[52] CRDS developers. CRDS: Calibration Reference Data System for HST and JWST (2022). URL https://github.com/spacetelescope/crds.

[53] Kreidberg, L. batman: BAsic Transit Model cAlculatioN in Python. *Publ. Astron. Soc. Pac.* **127** (957), 1161 (2015). https://doi.org/10.1086/683602, arXiv:1507.08285 [astro-ph.EP].

[54] Luger, R. *et al.* starry: Analytic Occultation Light Curves. *Astron. J.* **157** (2), 64 (2019). https://doi.org/10.3847/1538-3881/aae8e5, arXiv:1810.06559 [astro-ph.IM].

[55] Luger, R. *et al.* rodluger/starry: v1.2.0 (2021).

[56] Salvatier, J., Wiecki, T. V. & Fonnesbeck, C. Probabilistic programming in python using pymc3. *PeerJ Computer Science* **2**, e55 (2016). URL https://doi.org/10.7717/peerj-cs.55. https://doi.org/10.7717/peerj-cs.55 .

[57] Bell, T. J. *et al.* Nightside clouds and disequilibrium chemistry on the hot Jupiter WASP-43b. *arXiv e-prints* arXiv:2401.13027 (2024). https://doi.org/10.48550/arXiv.2401.13027, arXiv:2401.13027 [astro-ph.EP].

[58] Cowan, N. B. & Agol, E. Inverting Phase Functions to Map Exoplanets. *Astrophys. J. Lett.* **678** (2), L129 (2008). https://doi.org/10.1086/588553, arXiv:0803.3622 [astro-ph].

[59] Foreman-Mackey, D., Agol, E., Ambikasaran, S. & Angus, R. Fast and Scalable Gaussian Process Modeling with Applications to Astronomical Time Series. *Astron. J.* **154**, 220 (2017). https://doi.org/10.3847/1538-3881/aa9332 .

[60] Foreman-Mackey, D. Scalable Backpropagation for Gaussian Processes using Celerite. *Research Notes of the American Astronomical Society* **2** (1), 31 (2018). https://doi.org/10.3847/2515-5172/aaaf6c .

[61] Rasmussen, C. E. & Williams, C. K. I. *Gaussian Processes for Machine Learning* (2006).

[62] Goodman, J. & Weare, J. Ensemble samplers with affine invariance. *Communications in Applied Mathematics and Computational Science* **5** (1), 65–80 (2010). URL http://dx.doi.org/10.2140/camcos.2010.5.65. https://doi.org/10.2140/camcos.2010.5.65 .

[63] Foreman-Mackey, D., Hogg, D. W., Lang, D. & Goodman, J. emcee: The MCMC Hammer. *Publ. Astron. Soc. Pac.* **125** (925), 306 (2013). https://doi.org/10.1086/670067, arXiv:1202.3665 [astro-ph.IM].

[64] Speagle, J. S. DYNESTY: a dynamic nested sampling package for estimating Bayesian posteriors and evidences. *Mon. Not. R. Astron. Soc.* **493**, 3132–3158 (2020). URL https://ui.adsabs.harvard.edu/abs/2020MNRAS.493.3132S. https://doi.org/10.1093/mnras/staa278, aDS Bibcode: 2020MNRAS.493.3132S .

[65] Bell, T. J. *et al.* Mass loss from the exoplanet WASP-12b inferred from Spitzer phase curves. *Mon. Not. R. Astron. Soc.* **489** (2), 1995–2013 (2019). https://doi.org/10.1093/mnras/stz2018, arXiv:1906.04742 [astro-ph.EP].

[66] Guillard, e. a., P. Miri point spread functions: Radial and encircled energy profiles (2023). URL https://jwst-docs.stsci.edu/jwst-mid-infrared-instrument/miri-performance/miri-point-spread-functions#MIRIPointSpreadFunctions-Radialandencircledenergyprofiles.

[67] Lincowski, A. P. *et al.* Evolved Climates and Observational Discriminants for the TRAPPIST-1 Planetary System. *Astrophys. J.* **867** (1), 76 (2018). https://doi.org/10.3847/1538-4357/aae36a, arXiv:1809.07498 [astro-ph.EP].

[68] Robinson, T. D. & Crisp, D. Linearized Flux Evolution (LiFE): A technique for rapidly adapting fluxes from full-physics radiative transfer models. *Journal of Quantitative Spectroscopy and Radiative Transfer* **211**, 78–95 (2018). https://doi.org/10.1016/j.jqsrt.2018.03.002 .

[69] Lincowski, A. P. *et al.* Potential Atmospheric Compositions of TRAPPIST-1 c Constrained by JWST/MIRI Observations at 15 μm. *Astrophys. J. Lett.* **955** (1), L7 (2023). https://doi.org/10.3847/2041-8213/acee02, arXiv:2308.05899 [astro-ph.EP].

[70] Meadows, V. S. & Crisp, D. Ground-based near-infrared observations of the Venus nightside: The thermal structure and water abundance near the surface. *J. Geophys. Res.* **101**, 4595–4622 (1996). https://doi.org/10.1029/95JE03567 .

[71] Stamnes, K., Tsay, S. C., Wiscombe, W. & Jayaweerz, K. Numerically stable algorithm for discrete-ordinate-method radiative transfer in multiple scattering and emitting layered media. *Appl. Opt.* **42** (15), 2502–2509 (1988). https://doi.org/10.1364/AO.27.002502 .

[72] Stamnes, K., Tsay, S. C., Wiscombe, W. & Laszlo, I. DISORT, a general-purpose Fortran program for discrete-ordinate-method radiative transfer in scattering and emitting layered media: documentation of methodology. ftp://climate.gsfc.nasa.gov/pub/wiscombe/MultipleScatt/ (2000).

[73] Kokaly, R. *et al.* Usgs spectral library version 7 data: Us geological survey data release. *United States Geological Survey (USGS): Reston, VA, USA* **61** (2017) .

[74] Ducrot, E. *et al.* Combined analysis of the 12.8 and 15 μm JWST/MIRI eclipse observations of TRAPPIST-1 b. *Nature Astronomy* (2024). https://doi.org/10.

1038/s41550-024-02428-z, arXiv:2412.11627 [astro-ph.EP].

[75] Zieba, S. *et al.* No thick carbon dioxide atmosphere on the rocky exoplanet TRAPPIST-1 c. *Nature* **620** (7975), 746–749 (2023). https://doi.org/10.1038/s41586-023-06232-z, arXiv:2306.10150 [astro-ph.EP].

[76] Rathcke, A. D. *et al.* Stellar contamination correction using back-to-back transits of trappist-1 b and c (2024). URL https://arxiv.org/abs/2412.16541. 2412.16541.

[77] Turbet, M. *et al.* Modeling climate diversity, tidal dynamics and the fate of volatiles on TRAPPIST-1 planets. *Astron. Astrophys.* **612**, A86 (2018). https://doi.org/10.1051/0004-6361/201731620, arXiv:1707.06927 [astro-ph.EP].

[78] Turbet, M. *et al.* Water condensation zones around main sequence stars. *Astron. Astrophys.* **679**, A126 (2023). https://doi.org/10.1051/0004-6361/202347539, arXiv:2308.15110 [astro-ph.EP].

[79] Greene, T. P. *et al.* Thermal emission from the Earth-sized exoplanet TRAPPIST-1 b using JWST. *Nature* **618** (7963), 39–42 (2023). https://doi.org/10.1038/s41586-023-05951-7, arXiv:2303.14849 [astro-ph.EP].

[80] Ih, J., Kempton, E. M. R., Whittaker, E. A. & Lessard, M. Constraining the Thickness of TRAPPIST-1 b's Atmosphere from Its JWST Secondary Eclipse Observation at 15 μm. *Astrophys. J. Lett.* **952** (1), L4 (2023). https://doi.org/10.3847/2041-8213/ace03b, arXiv:2305.10414 [astro-ph.EP].

[81] Falco, A., Zingales, T., Pluriel, W. & Leconte, J. Toward a multidimensional analysis of transmission spectroscopy. I. Computation of transmission spectra using a 1D, 2D, or 3D atmosphere structure. *Astron. Astrophys.* **658**, A41 (2022). https://doi.org/10.1051/0004-6361/202141940, arXiv:2110.11799 [astro-ph.EP].

[82] Iyer, A. R., Line, M. R., Muirhead, P. S., Fortney, J. J. & Gharib-Nezhad, E. The SPHINX M-dwarf Spectral Grid. I. Benchmarking New Model Atmospheres to Derive Fundamental M-dwarf Properties. *Astrophys. J.* **944** (1), 41 (2023). https://doi.org/10.3847/1538-4357/acabc2, arXiv:2206.12010 [astro-ph.SR].

[83] Villanueva, G. L., Smith, M. D., Protopapa, S., Faggi, S. & Mandell, A. M. Planetary Spectrum Generator: An accurate online radiative transfer suite for atmospheres, comets, small bodies and exoplanets. *J. Quant. Spectrosc. Radiat. Transf.* **217**, 86–104 (2018). https://doi.org/10.1016/j.jqsrt.2018.05.023, arXiv:1803.02008 [astro-ph.EP].

[84] Villanueva, G. L. *et al.* *Fundamentals of the Planetary Spectrum Generator* (https://psg.gsfc.nasa.gov/help.php, 2022).

[85] Villanueva, G. L. *et al.* Modeling atmospheric lines by the exoplanet community (malbec) version 1.0: A cuisines radiative transfer intercomparison project.

Planet. Sci. J. **5** (3), 64 (2024). URL https://dx.doi.org/10.3847/PSJ/ad2681. https://doi.org/10.3847/PSJ/ad2681 .

[86] Bolmont, E. *et al.* Water loss from terrestrial planets orbiting ultracool dwarfs: implications for the planets of TRAPPIST-1. *Mon. Not. R. Astron. Soc.* **464** (3), 3728–3741 (2017). https://doi.org/10.1093/mnras/stw2578, arXiv:1605.00616 [astro-ph.EP].

[87] TRAPPIST-1 JWST Community Initiative *et al.* A roadmap to the efficient and robust characterization of temperate terrestrial planet atmospheres with JWST. *arXiv e-prints* arXiv:2310.15895 (2023). https://doi.org/10.48550/arXiv.2310.15895, arXiv:2310.15895 [astro-ph.EP].

[88] Allen, N. *et al.* Using stellar contamination proxy TRAPPIST-1 b to search for an atmosphere on TRAPPIST-1 e. JWST Proposal. Cycle 3, ID. #6456 (2024).

[89] Lustig-Yaeger, J., Meadows, V. S. & Lincowski, A. P. The Detectability and Characterization of the TRAPPIST-1 Exoplanet Atmospheres with JWST. *Astron. J.* **158** (1), 27 (2019). https://doi.org/10.3847/1538-3881/ab21e0, arXiv:1905.07070 [astro-ph.EP].

[90] Morley, C. V., Kreidberg, L., Rustamkulov, Z., Robinson, T. & Fortney, J. J. Observing the Atmospheres of Known Temperate Earth-sized Planets with JWST. *Astrophys. J.* **850** (2), 121 (2017). https://doi.org/10.3847/1538-4357/aa927b, arXiv:1708.04239 [astro-ph.EP].

[91] Lim, O. *et al.* Atmospheric Reconnaissance of TRAPPIST-1 b with JWST/NIRISS: Evidence for Strong Stellar Contamination in the Transmission Spectra. *arXiv e-prints* arXiv:2309.07047 (2023). https://doi.org/10.48550/arXiv.2309.07047, arXiv:2309.07047 [astro-ph.EP].

[92] Goldreich, P. Final spin states of planets and satellites. *Astron. J.* **71**, 1 (1966). https://doi.org/10.1086/109844 .

[93] Mignard, F. The Evolution of the Lunar Orbit Revisited. I. *Moon and Planets* **20** (3), 301–315 (1979). https://doi.org/10.1007/BF00907581 .

[94] Makarov, V. V. & Efroimsky, M. No Pseudosynchronous Rotation for Terrestrial Planets and Moons. *Astrophys. J.* **764** (1), 27 (2013). https://doi.org/10.1088/0004-637X/764/1/27, arXiv:1209.1616 [astro-ph.EP].

[95] Tobie, G., Mocquet, A. & Sotin, C. Tidal dissipation within large icy satellites: Applications to Europa and Titan. *Icarus* **177** (2), 534–549 (2005). https://doi.org/10.1016/j.icarus.2005.04.006 .

[96] Tobie, G., Grasset, O., Dumoulin, C. & Mocquet, A. Tidal response of rocky and ice-rich exoplanets. *Astron. Astrophys.* **630**, A70 (2019). https://doi.org/10.

1051/0004-6361/201935297 .

[97] Andrade, E. N. D. C. On the Viscous Flow in Metals, and Allied Phenomena. *Proceedings of the Royal Society of London Series A* **84** (567), 1–12 (1910) .

[98] Levrard, B. A proof that tidal heating in a synchronous rotation is always larger than in an asymptotic nonsynchronous rotation state. *Icarus* **193** (2), 641–643 (2008). https://doi.org/10.1016/j.icarus.2007.10.003, arXiv:0710.5651 [astro-ph].

[99] Boué, G. & Efroimsky, M. Tidal evolution of the Keplerian elements. *Celestial Mechanics and Dynamical Astronomy* **131** (7), 30 (2019). https://doi.org/10.1007/s10569-019-9908-2, arXiv:1904.02253 [astro-ph.EP].

[100] Cottaar, S., Heister, T., Rose, I. & Unterborn, C. BurnMan: A lower mantle mineral physics toolkit. *Geochemistry, Geophysics, Geosystems* **15** (4), 1164–1179 (2014). https://doi.org/10.1002/2013GC005122 .

[101] Myhill, R., Cottaar, S., Heister, T., Rose, I. & Unterborn, C. BurnMan v1.0.1. Zenodo (2021).

[102] Kervazo, M., Tobie, G., Choblet, G., Dumoulin, C. & Behounková, M. Solid tides in io´s partially molten interior - contribution of bulk dissipation. *Astron. Astrophys.* **650**, A72 (2021). URL https://doi.org/10.1051/0004-6361/202039433. https://doi.org/10.1051/0004-6361/202039433 .

[103] Revol, A. *et al.* Drifts of the sub-stellar points of the TRAPPIST-1 planets. *arXiv e-prints* arXiv:2409.12065 (2024). https://doi.org/10.48550/arXiv.2409.12065, arXiv:2409.12065 [astro-ph.EP].

[104] Blanco-Cuaresma, S. & Bolmont, E. Studying Tidal Effects In Planetary Systems With Posidonius. A N-Body Simulator Written In Rust. (2017). 1712.01281.

[105] Bolmont, E. *et al.* Impact of tides on the transit-timing fits to the TRAPPIST-1 system. *Astron. Astrophys.* **635**, A117 (2020). https://doi.org/10.1051/0004-6361/202037546, arXiv:2002.02015 [astro-ph.EP].

[106] Hapke, B. *Theory of reflectance and emittance spectroscopy* (Cambridge university press, 2012).

[107] Seager, S. & Deming, D. On the method to infer an atmosphere on a tidally locked super earth exoplanet and upper limits to gj 876d. *Astrophys. J.* **703** (2), 1884 (2009) .

[108] Hu, R., Ehlmann, B. L. & Seager, S. Theoretical Spectra of Terrestrial Exoplanet Surfaces. *Astrophys. J.* **752** (1), 7 (2012). https://doi.org/10.1088/0004-637X/752/1/7 .

[109] Paragas, K. *et al.* A New Spectral Library for Modeling the Surfaces of Hot, Rocky Exoplanets (2025). URL http://arxiv.org/abs/2502.04433. https://doi.org/10.48550/arXiv.2502.04433 .

[110] First, E. C. *et al.* Potential for observing geological diversity from mid-infrared spectra of rocky exoplanets. *Nature Astronomy* **9** (3), 370–379 (2025). URL https://www.nature.com/articles/s41550-024-02412-7. https://doi.org/10.1038/s41550-024-02412-7, publisher: Nature Publishing Group .

[111] Avni, Y. Energy spectra of X-ray clusters of galaxies. *Astrophys. J.* **210**, 642–646 (1976). https://doi.org/10.1086/154870 .

[112] Pieters, C. M. & Noble, S. K. Space weathering on airless bodies. *J. Geophys. Res.: Planets* **121** (10), 1865–1884 (2016) .

[113] Syal, M. B., Schultz, P. H. & Riner, M. A. Darkening of Mercury's surface by cometary carbon. *Nature Geoscience* **8** (5), 352–356 (2015). https://doi.org/10.1038/ngeo2397 .

[114] Lyu, X. *et al.* Super-earth lhs3844b is tidally locked. *Astrophys. J.* **964** (2), 152 (2024). URL http://dx.doi.org/10.3847/1538-4357/ad2077. https://doi.org/10.3847/1538-4357/ad2077 .

[115] Ducrot, E. *et al.* TRAPPIST-1: Global results of the Spitzer Exploration Science Program Red Worlds. *Astron. Astrophys.* **640**, A112 (2020). https://doi.org/10.1051/0004-6361/201937392, arXiv:2006.13826 [astro-ph.EP].

[116] Vida, K., Kővári, Z., Pál, A., Oláh, K. & Kriskovics, L. Frequent flaring in the TRAPPIST-1 system—unsuited for life? *Astrophys. J.* **841** (2), 124 (2017). URL https://doi.org/10.3847%2F1538-4357%2Faa6f05. https://doi.org/10.3847/1538-4357/aa6f05 .

[117] Tovar Mendoza, G., Davenport, J. R. A., Agol, E., Jackman, J. A. G. & Hawley, S. L. Llamaradas Estelares: Modeling the Morphology of White-light Flares. *Astron. J.* **164** (1), 17 (2022). https://doi.org/10.3847/1538-3881/ac6fe6, arXiv:2205.05706 [astro-ph.SR].

[118] Günther, M. N. *et al.* Stellar Flares from the First TESS Data Release: Exploring a New Sample of M Dwarfs. *Astron. J.* **159** (2), 60 (2020). https://doi.org/10.3847/1538-3881/ab5d3a, arXiv:1901.00443 [astro-ph.EP].

[119] Howard, W. S. *et al.* The First Naked-eye Superflare Detected from Proxima Centauri. *Astrophys. J. Lett.* **860** (2), L30 (2018). https://doi.org/10.3847/2041-8213/aacaf3, arXiv:1804.02001 [astro-ph.EP].

[120] Maas, A. J. *et al.* Lower-than-expected flare temperatures for TRAPPIST-1. *Astron. Astrophys.* **668**, A111 (2022). https://doi.org/10.1051/0004-6361/

202243869, arXiv:2210.11103 [astro-ph.SR].

[121] Paudel, R. R. *et al.* K2 ultracool dwarfs survey – v. high superflare rates on rapidly rotating late-m dwarfs. *Mon. Not. R. Astron. Soc.* **486** (1), 1438–1447 (2019). URL https://doi.org/10.1093/mnras/stz886. https://doi.org/10.1093/mnras/stz886 .

[122] Foreman-Mackey, D. corner.py: Scatterplot matrices in python. *The Journal of Open Source Software* **1** (2), 24 (2016). URL https://doi.org/10.21105/joss.00024. https://doi.org/10.21105/joss.00024 .

Supplementary Figures

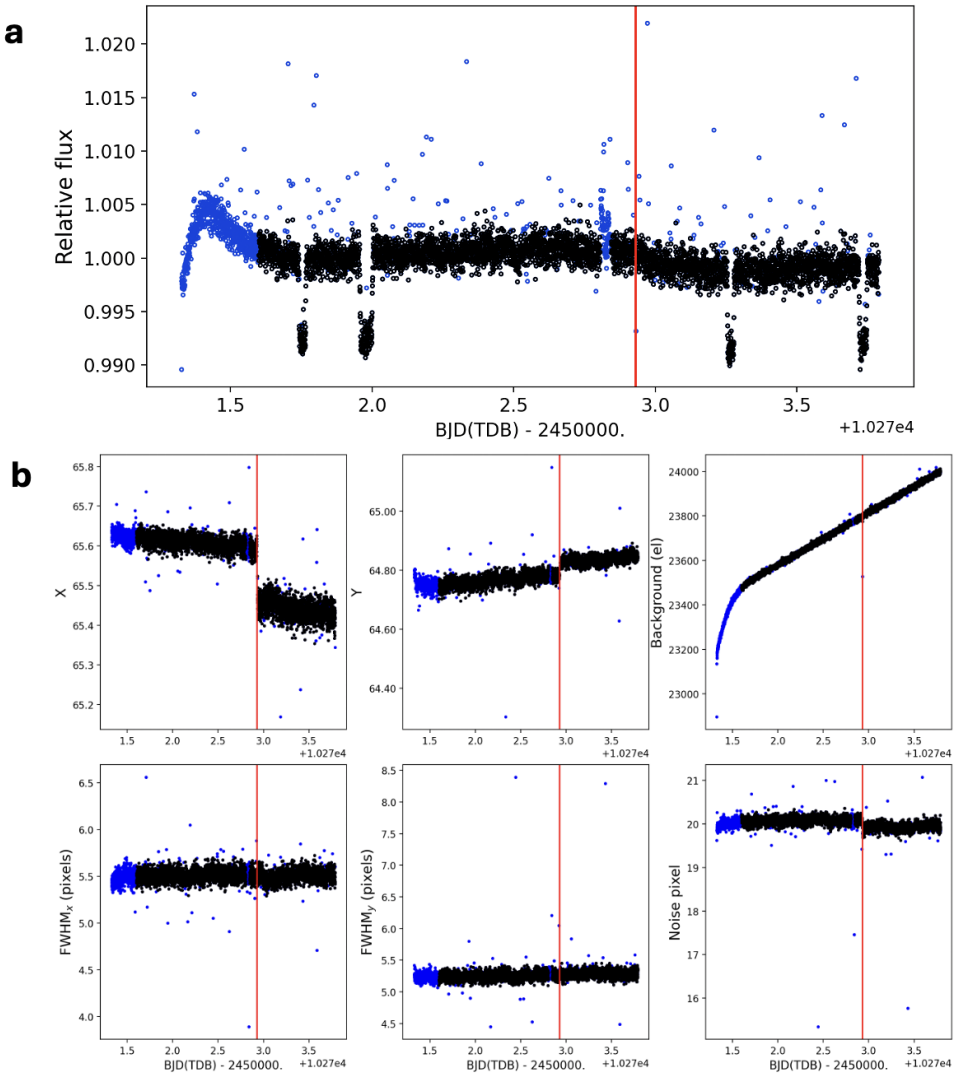

Supplementary Fig. 1 | Program 3077 raw light curve and external parameters evolution. **a**, raw light curve obtained by MG with a photometric aperture of 4 pixels radius (see text for details). **b**, evolution of the external parameters: x and y positions of the target's point-spread function (PSF) center, background, PSF's full-width at half-maximum in the x and y directions, and noise-pixel (as defined in [41]). Blue points are those discarded before the MCMC analysis. The vertical red line shows the gap between visit 1 and 2.

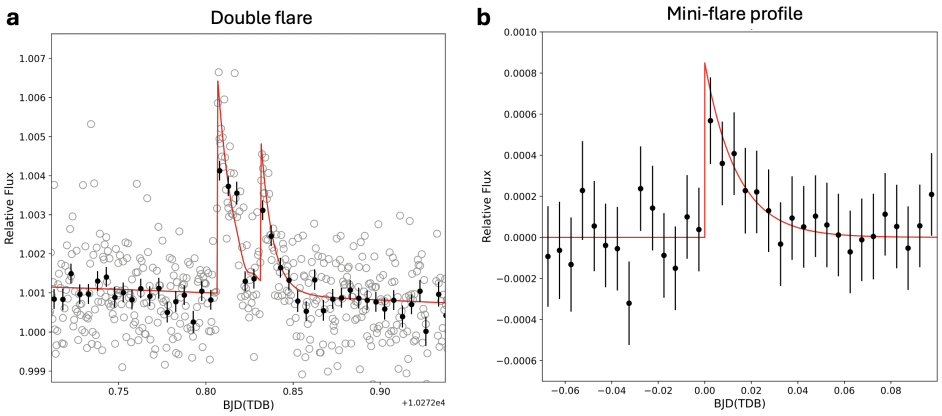

Supplementary Fig. 2 | Flares in the light curve of program 3077. a, double flare-like structure in the light curve of program 3077. The black points are flux measurements binned per 7.2 minutes. **b**, Stack of the four low-amplitude flare-like structures in the residuals of MG's analysis #1, binned per 7.2 minutes. For both panels, the error bars are the averages of the individual errors divided by the square root of the number of points within the bin, and the best-fit flare models are overimposed in red.

Light curve	Aperture (pixels)	Baseline function	σ (ppm)
3077 (23 Nov 2023)	4	2 ramps + $p(t) + p(x^2) + p(y^2)$	862
1177.1 (8 Nov 2022)	3.5	ramp + $p(t) + p(y)$	907
1177.2 (12 Nov 2022)	4	ramp + $p(t^2)$	865
1177.3 (20 Nov 2022)	3.5	ramp	876
1177.4 (24 Nov 2022)	4	ramp + $p(t)$	1040
1177.5 (3 Dec 2022)	4	ramp + $p(y)$	908
2304.1 (27 Oct 2022)	3.5	ramp + $p(t)$	954
2304.2 (30 Oct 2022)	3.5	ramp + $p(t) + p(x) + p(y)$	913
2304.3 (6 Nov 2022)	3.5	ramp	985
2304.4 (30 Nov 2022)	3.5	ramp + $p(t) + p(x^2)$	921

Supplementary Table 1 | Light curves used in this work. First column: light curve (program + date). Second column: photometric extraction aperture. Third column: baseline functions used for each light curve of program 3077, 1177, and 2304 in the global MCMC analysis of MG. The last column gives the standard deviation of the residuals of the best-fit model. $p(a^b)$ represents a polynomial of degree b of the parameter a. The ramp model used for all light curves of programs 1177 and 2304 is a quadratic function of the logarithm of the time difference between the considered data point and the first data point.

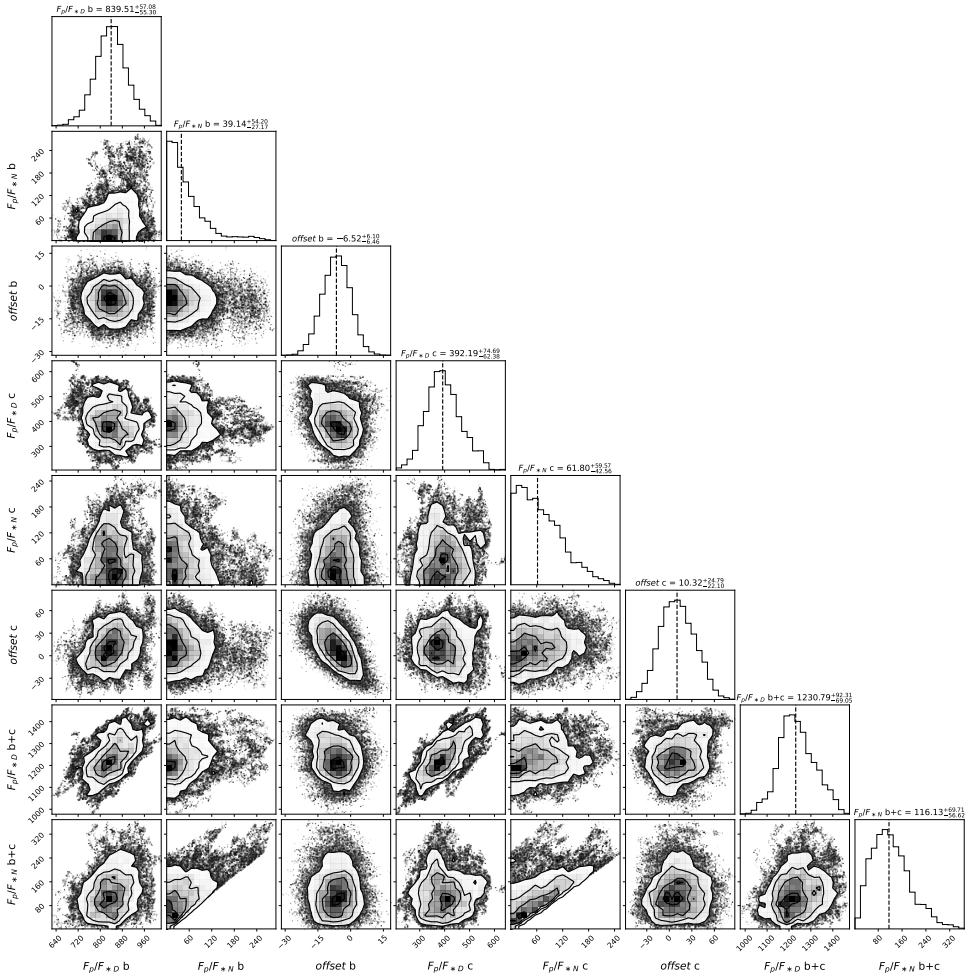

Supplementary Fig. 3 | Corner plot [122] for the phase curve parameters of planet b and c inferred from MG's analysis # 1. The posterior PDFs for the sum of the day- and night-side fluxes of planets b and c are also shown.

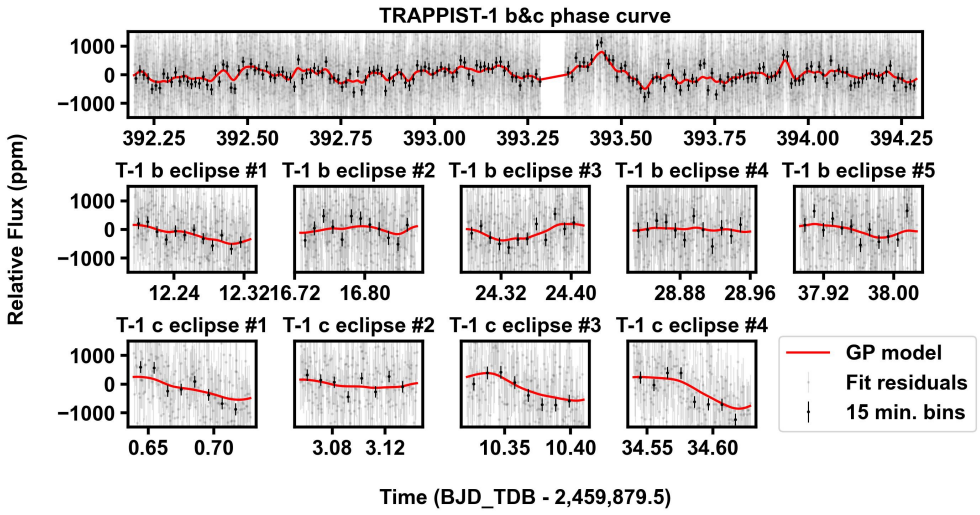

Supplementary Fig. 4 | Fitted GP time-series models from TJB's reduction and analysis with Setup #1.

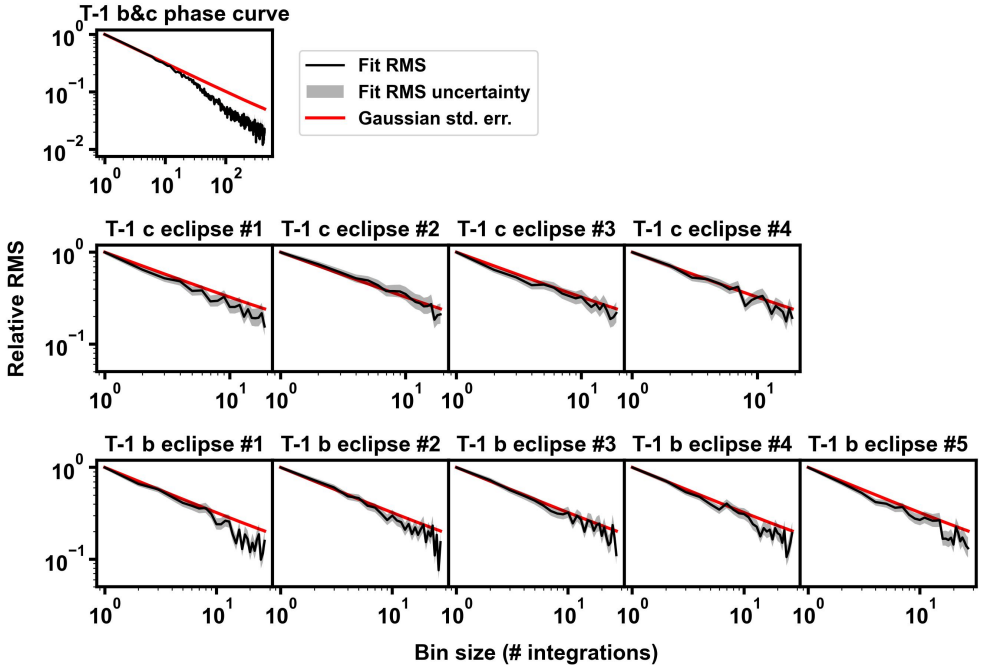

Supplementary Fig. 5 | Allan variance plots from TJB's reduction and analysis with Setup #1. Note that the reduction in RMS at long timescales (Bin size >20 integrations) in the phase curve panel is due to the subtraction of correlated variations as estimated from the GP.

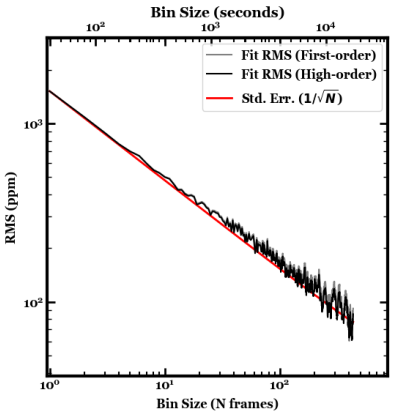

Supplementary Fig. 6 | Allan plot from ZH data analysis

B. Outreach

During my PhD, I was lucky to have a doctoral mission at the *Cité des Sciences et de l'Industrie*, a French science museum. For me, sharing my interest in science, discussing with a general audience about my work is an inseparable part of my job. I believe this is necessary -but I guess not sufficient- in order to honestly claim that this highly specialized and difficult-to-access fundamental science is something of general interest. I hope that my work as a science communicator has helped some children to appreciate science, some enthusiasts to learn more about exoplanets, and, finally, that I have been able to entertain as many people as possible.

In this appendix, you can find a document, in French, that contains the instructions for facilitating three outreach workshops that I developed and animated during my PhD and at the Cité des Sciences et de l'Industrie. *This document was originally created for the outreach team of the museum.*

Ce document est mis à disposition selon les termes de la licence
Creative Commons ‘‘Attribution - Pas d’utilisation commerciale -
Partage dans les mêmes conditions 4.0 International’’.

Médiations en Astronomie et Astrophysique

Alice Maurel

Contenu

1 Jeu Astronomie/Astrophysique **1**
1.1 Règles du jeu . . . 1
1.2 Erreurs communes . . . 2
1.3 Liste des cartes . . . 3

2 Placement dans la galaxie **5**
2.1 Principe . . . 5
2.2 Proposition de déroulé détaillé . . . 5
2.3 Matériel . . . 5

3 Atelier sur les transits **7**
3.1 Explication du transit . . . 7
3.2 Déroulé . . . 7
3.3 Matériel . . . 7
3.3.1 Courbes de transit . . . 7
3.3.2 Abaques . . . 10

Ces différentes animations peuvent se faire à la suite dans l’ordre proposé, ou de manière indépendante.

1 Jeu Astronomie/Astrophysique

Objectif pédagogique : Montrer le lien entre les objets observables dans le ciel à l’oeil nu ou un petit télescope (astronomie) et la réalité de l’objet correspondant (astrophysique). Faire prendre conscience des différentes échelles astronomiques.
Public cible : Tout public. L’animateur·ice peut adapter son discours et le niveau de détails de ses explications selon les connaissances et l’intérêt du public.
Format : Jeu collaboratif ou en deux équipes
Durée : 15 à 30 minutes
Origine : L’atelier a été originellement créé par Axel Lapel et Alice Maurel, doctorant·e·s à l’Institut d’Astrophysique de Paris, en 2023, pour un atelier au centre pénitentiaire de Bois d’Arcy dans le cadre de l’association Champs Libre. L’atelier a ensuite été utilisé à la Cité des Sciences et de l’Industrie.

1.1 Règles du jeu

Le jeu est constitué de quatorze cartes-images : sept avec encadrement orange, correspondant à des images d’ojets du ciel qu’on peut voir à l’oeil nu ou avec du matériel amateur, et sept avec encadrement bleu, correspondant aux mêmes objets, mais avec des vues beaucoup plus détaillées, correspondants à des images de grands télescopes, sondes, ou aux objets vus de plus près.

Le jeu est se déroule en deux manches :

1. Associer à chaque carte orange la carte bleue qui correspond au même objet
2. Trier toutes les cartes bleues dans l’ordre, du plus proche de la Terre au plus éloigné.

Le jeu peut se faire avec un seul set de cartes, sous forme de jeu collaboratif, ou deux, sous forme d’affrontement entre deux équipes. Tout au long du jeu, l’animateur·ice peut aider les joueur·euses en leur donnant des informations sur les images à leur demande.





Exemple de cartes à jouer : la Lune. La carte orange correspond à la Lune vue à l'oeil nu, la carte bleue à la Lune en détails, vue à travers un télescope. *Crédits : Guillaume Cannat (gauche), Gregory H. Revera (droite)*

1.2 Erreurs communes

Lors de l'atelier, nous avons remarqué que certaines confusions reviennent systématiquement et sont très utiles pour donner des explications. Voici donc une liste de celles-ci ainsi qu'une proposition de discours explicatif. Il est préférable d'insister auprès du public que ces objets sont en effet régulièrement confondus, et d'expliquer les raisons de ces confusions.

Étoile/Planète Les étoiles et planètes sont très similaires vues à l'oeil nu : ce sont des points lumineux dans le ciel. En théorie, une étoile scintille alors qu'une planète non, car l'étoile est très éloignée et c'est une source ponctuelle, et la planète est beaucoup plus proche, et n'est pas ponctuelle (avec des jumelles ou un télescope, on peut voir que c'est un disque). Mais cette différence est très discrète. Par ailleurs, le mot planète vient de "astre errant" en grec, car les planètes se déplacent dans le ciel tout au long de l'année par rapport aux étoiles, alors que les étoiles ne se déplacent pas les unes par rapport aux autres et forment des constellations. C'est la principale différence observationnelle.
Enfin, malgré leur ressemblance, ces objets sont très différents : les planètes tournent toutes autour du soleil, et la lumière qu'elles nous renvoient n'est que le reflet de celui-ci, alors que les étoiles sont chacune un soleil, qui produit sa propre lumière, et elles se situent donc en dehors du système solaire.

Comète/Étoile Filante En photo, les deux peuvent se confondre, ce sont des tracés dans le ciel, mais l'étoile filante ne dure que quelques instants alors que la comète reste visible souvent plusieurs nuits d'affilée, et ne se déplace que très lentement dans le ciel.
Ces deux objets, souvent confondus dans le langage, correspondent à des réalités très différentes : l'étoile filante est un débris spatial qui frotte contre l'atmosphère terrestre, produisant de la lumière, alors que la comète est beaucoup plus lointaine, on la voit lorsqu'elle se rapproche du soleil, ce qui la réchauffe au point de transformer la glace contenue dedans en vapeur d'eau, éjectant de la matière sur des millions de kilomètres. Ces jets, constituant la queue de la comète, sont visibles lorsque la comète est assez près du soleil.

Galaxie/Nébuleuse Les galaxies et nébuleuses étaient initialement confondues sous le nom de "nébuleuse", car ce sont des objets fous, comme des nuages lumineux. Au départ, les astronomes ne faisaient pas de différences entre ces objets car ils se ressemblaient beaucoup avec un télescope moyen.
Ce n'est qu'au vingtième siècle qu'on a pu mesurer les distances de ces objets, et se rendre compte que les galaxies sont des objets extrèmement éloignés, qui contiennent des milliards d'étoiles, qui chacune produit de la lumière, l'ensemble produisant une tache ovale floue. Notre système solaire est dans une galaxie, la Voie Lactée, qu'on peut observer par la tranche sous un beau ciel étoilé. Les nébuleuses, elles, ne sont que des nuages de gaz et de matière, qui peuvent être les restes d'une explosion d'étoile, et sont des zones de naissance d'étoiles. Dans une galaxie, il y a de nombreuses nébuleuses.

1.3 Liste des cartes

Liste des cartes, dans l'ordre de la plus proche à la plus lointaine de la Terre.



Une étoile filante/météorite. Elle arrive carrément sur Terre. *Crédits : Jared Tennant (gauche), Ludovic Godard (droite)*



La Lune. C'est le satellite de la Terre, et donc l'objet astronomique le plus proche. *Crédits : Guillaume Cannat (gauche), Gregory H. Revera (droite)*

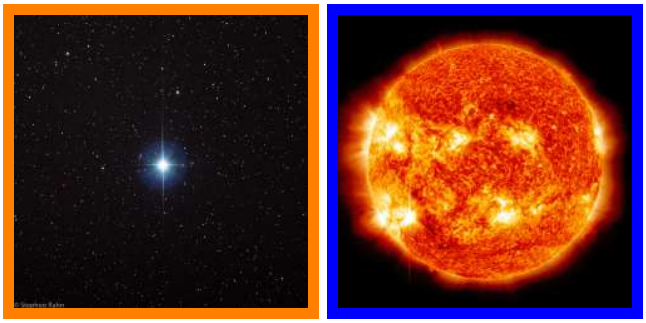

Une étoile/le Soleil. Question possible : Est-ce que le Soleil est une étoile spéciale ? (Voir animation "Placement dans la galaxie".) *Crédits: Stephen Rahn (gauche), NASA (droite)*



Une comète. Lorsqu'elle est visible, elle est proche du soleil, donc à peu près à même distance que le soleil. La comète vue de près est 67P/Tchourioumov-Guérassimenko, "Tchouri", la seule comète sur laquelle une mission spatiale est allée se poser. *Crédits : Flickr (gauche), ESA (droite)*



Une planète (Jupiter). Attention, Jupiter est bien plus éloignée du soleil que la Terre, et donc le Soleil est plus proche de la Terre que Jupiter, malgré l'intuition de certain·e·s. *Crédits : Paul Williams (gauche), ESA (droite)*

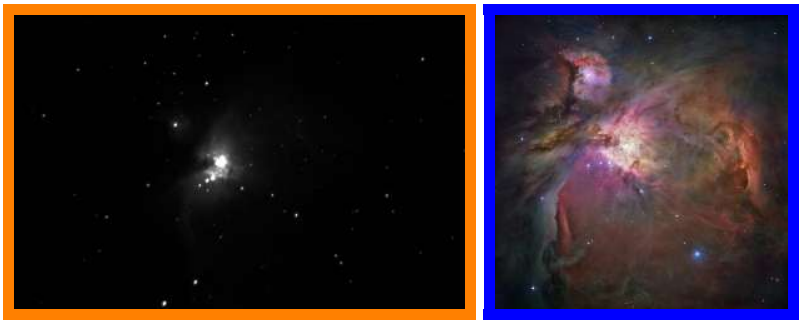

Une nébuleuse (Orion). Cet objet est en dehors du système solaire, mais dans notre galaxie. *Crédits : Forest - webastro.com (gauche), HST (droite)*



Une galaxie (Andromède). C'est la galaxie la plus proche de la Voie Lactée. *Crédits : Jean-Baptiste Feldmann (gauche), Adams Evans (droite)*

2 Placement dans la galaxie

Objectif pédagogique : Faire prendre consciences des échelles : il y a des milliards de systèmes solaires dans notre galaxies. Amener vers la possibilité de l'existence d'exoplanètes.
Public cible : Tout public. Adaptable.
Durée : 10 minutes
Format : Devinette, discussion
Origine : Animation originellement créée pour l'événement Science Infuse à la Cité des Sciences et de l'Industrie, pour servir d'introduction à l'atelier sur les transits.

2.1 Principe

Cette animation est très simple : sur un dessin de notre Galaxie, on demande au public de placer le système solaire, puis l'ensemble des exoplanètes découvertes.

2.2 Proposition de déroulé détaillé

L'anim. montre l'image de la Voie Lactée

Question : Voici une image d'artiste de la Voie Lactée. À votre avis, pourquoi je ne vous ai pas mis une photo ?
Réponse : Parce qu'on est dans la voie lactée, on ne peut pas en sortir pour prendre une photo, c'est beaucoup trop loin.

Question : Maintenant, à votre avis, où est-ce qu'on se situe dans la voie lactée ? *Variante : Où se situe le Système solaire/la Terre...*
Réponse : en périphérie. L'objectif est de faire la différence entre le système solaire et la voie lactée : sur cette image, le système solaire en entier tient dans un point. La voie lactée contient des milliards de milliards d'étoiles, qui sont chacune un soleil.

Question : Est-ce que le soleil est une étoile ? Est-ce que c'est une étoile spéciale ?
Le soleil n'est pas une étoile plus grosse, plus brillante ou plus chaude que les autres. Si elle nous *apparaît* beaucoup plus chaude/brillante/grosse, c'est uniquement parce que c'est notre étoile : nous sommes beaucoup plus près d'elle que de toutes les autres.

Question : Si le soleil est une étoile comme les autres, est-ce que les autres étoiles peuvent aussi avoir des planètes ? Est-ce qu'on en a découvertes ?
Réponse : oui, on en a découvert des milliers !

Question : Et à votre avis, où est-ce qu'elles se trouvent ? Dans notre voie lactée ? Si oui, où ?
Après leur avoir fait faire des propositions, montrer le calque. Expliquer la différence entre TESS et Kepler : TESS regarde partout dans le ciel, mais avec une moins bonne sensibilité, Kepler regarde uniquement une région, mais en profondeur. Cela permet d'avoir des informations complémentaires. Microlentilles gravitationnelles : ça permet de voir très loin, mais on ne voit la planète qu'une fois, donc on ne peut pas l'étudier en détails.

2.3 Matériel

- Une image d'artiste/simulation de la Voie Lactée
- Un calque avec un point placé à l'endroit du système solaire dans la galaxie
- Un calque avec les zones de découvertes de la majorité des exoplanètes (TESS, Kepler et microlentilles)

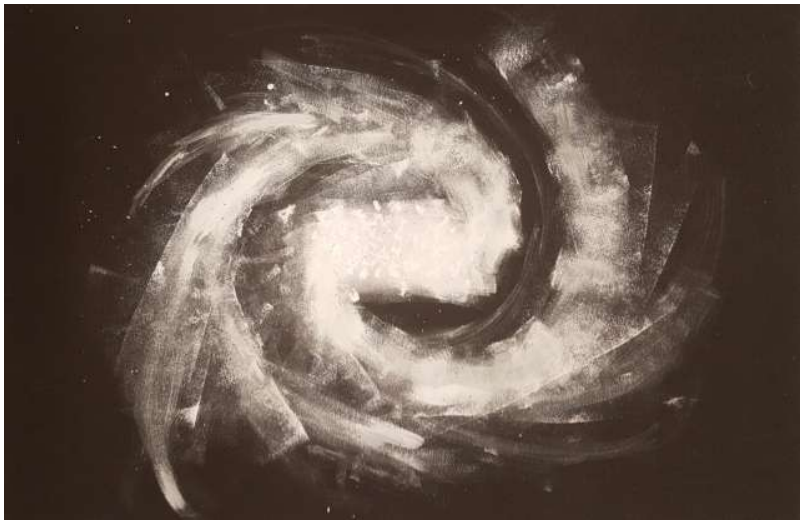

Image utilisée pour la galaxie (peinture blanche sur panneau noir)

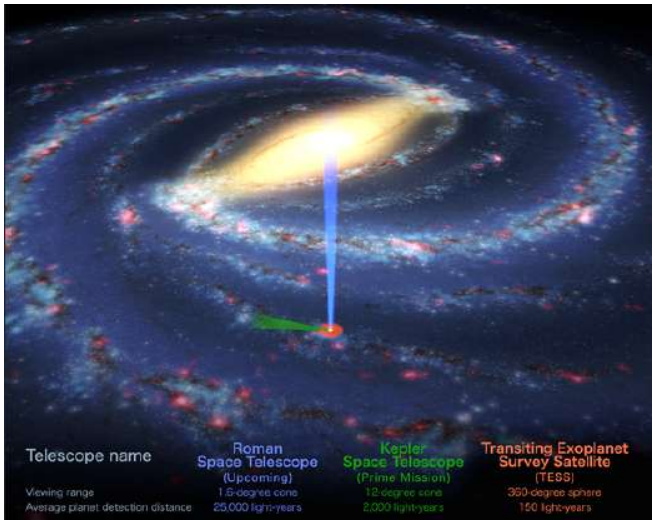

Zones de détection pour les télescopes TESS et Kepler. La Voie lactée faisant environ 100 000 années-lumères, la zone de Kepler doit faire environ 3% de la longueur totale de la galaxie : c'est très petit ! (TESS et Kepler utilisent la méthode des transits, le Roman Space Telescope la méthode des microlentilles gravitationnelles.) *Crédits : NASA's Goddard Space Flight Center*

3 Atelier sur les transits

Objectif pédagogique : Faire découvrir une méthode de détection d'exoplanètes. Montrer une application de compétences acquises à l'école : lire un graphe, faire des calculs.
Durée : 15 minutes à 1h
Format : Atelier d'initiation à la recherche
Public cible : Recommandée pour un public âgé de 15 ans ou plus. Particulièrement adapté dans le cadre d'un atelier en classe lycée.
Origine : Originellement créé pour l'événement Science Infuse à la Cité des Sciences et de l'Industrie.

3.1 Explication du transit

Les exoplanètes ne produisent pas leur propre lumière. Les planètes du système solaire, on les voit parce qu'elles reflètent la lumière du soleil. Mais pour une exoplanète à des années lumières, le système est trop loin (pour l'écrasante majorité des exoplanètes) pour qu'on distingue l'exoplanète de son étoile. De plus, le rapport de contraste est beaucoup trop élevé, la planète est invisible par rapport à l'étoile. Pour détecter la planète, une méthode consiste à détecter le transit : si le système a le bon alignement, la planète qui tourne autour de l'étoile passe entre l'étoile et nous. Si on mesure la lumière de l'étoile au cours du temps, on peut détecter ce transit car la planète cache une petite partie de la lumière, ce qui correspond à une petite baisse de luminosité. Si cette baisse de luminosité se répète régulièrement, c'est que c'est une planète, et la durée entre deux baisses de luminosité correspond à la durée d'une année sur cette exoplanète. Cette information, associée à la température de l'étoile, permet de déduire une estimation de la température de la planète. Une autre information que l'on peut déduire de la courbe de transit est la taille de la planète : en effet, la profondeur du transit (en % de la lumière de l'étoile) correspond au rapport entre la surface de l'étoile et celle de la planète, soit le rapport du rayon de la planète sur celui de l'étoile au carré.

3.2 Déroulé

L'anim. présente quelques vues d'artiste d'exoplanètes, L'anim. introduit la méthode du transit, de préférence avec des questions guidées, et les différentes informations que l'on peut avoir à partir de l'exemple le plus simple (HD-209458 b). Il ou elle explique comment on peut retrouver la taille et la température d'une planète avec la courbe ainsi que des calculs, puis présente les abaques qui permettent de retrouver sans calculs. Ensuite, le public peut chercher soi-même les caractéristiques de différentes exoplanètes, et retrouver auxquelles elles correspondent par rapport aux vues d'artistes. Les différents exemples permettent d'introduire notamment :

- Un système à plusieurs planètes
- Le fait que nous sommes incapables actuellement de repérer une exo-Terre
- L'influence de la température et taille de l'étoile, et donc qu'il est plus simple de chercher autour des naines rouges pour trouver des planètes rocheuses tempérées

Bonus/activité parallèle : Faire une vue d'artiste de notre exoplanète, à partir des caractéristiques qu'on a mesurées sur la courbe de transit... Ou juste de son imagination, pour les enfants plus jeunes !

3.3 Matériel

3.3.1 Courbes de transit

Le premier exemple correspond à des données réelles. Tous les transits proposés sont des transits simulés d'exoplanètes réelles. Les exemples sont présentés par ordre de difficulté/complexité.

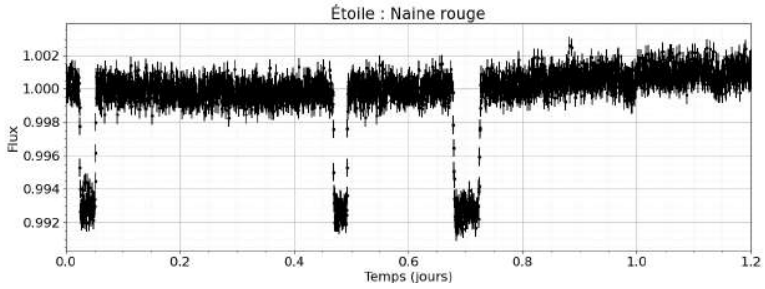

TRAPPIST-1, données réelles. Les incertitudes rendent difficile la détection de petites exoplanètes.

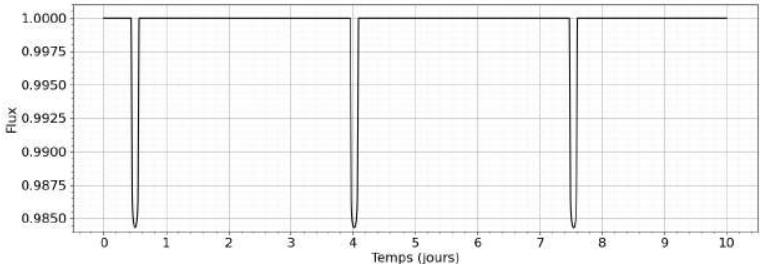



HD-209458 b. Un jupiter chaud. *Crédits : ESA, Alfred Vidal-Madjar (IAP, CNRS, France), NASA*

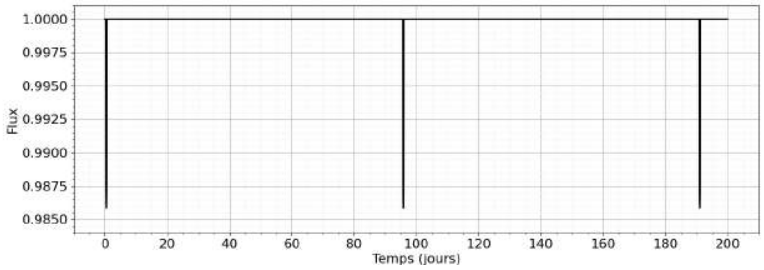

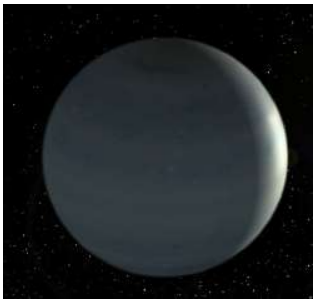

Corot-9 b. Une exoplanète avec une plus longue période, donc plus tiède. Plus difficile à détecter, car cela suppose de regarder l'étoile pendant longtemps. *Crédits : ESO/Instituto de Astrofísica de Canarias*

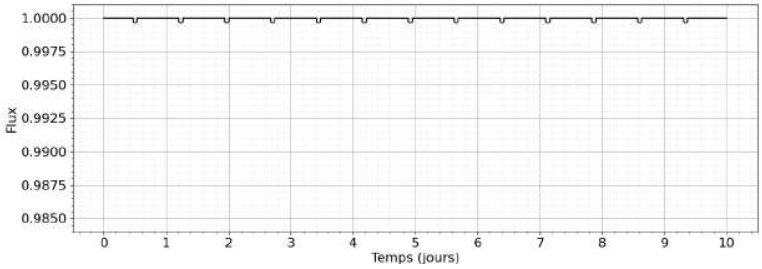



55-Cancri e. Une petite exoplanète extrêmement chaude, elle est composée de roche mais son côté qui fait face à l'étoile est sous forme de magma ! *Crédits : ESA/Hubble, M. Kornmesser*

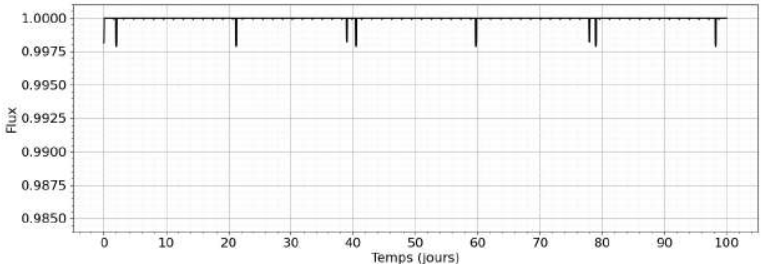



Kepler 9. Un système avec deux exoplanètes de taille et période différentes. *Crédits : NASA/Ames/JPL-Caltech/Ciel et Espace Photos*

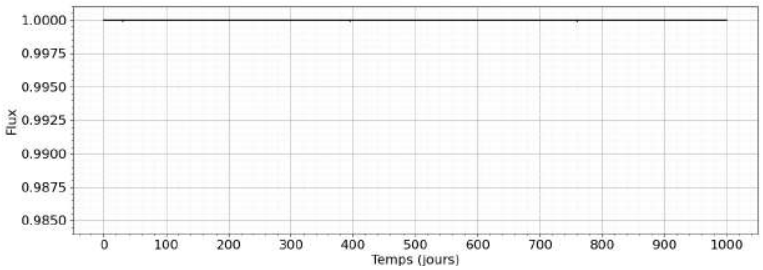

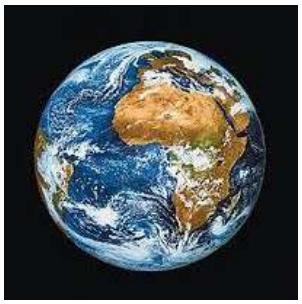

La Terre (si c'était une exoplanète) ! Son transit par rapport au soleil serait indétectable. *Crédits : ESA*

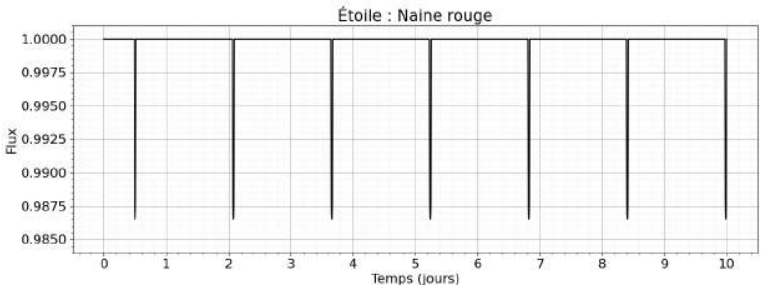

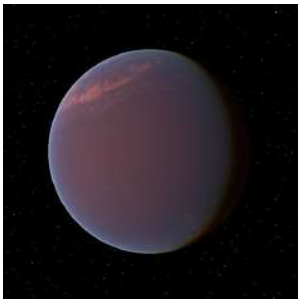

GJ 1214 b. Une exoplanète autour d'une naine rouge : son transit est plus grand, alors qu'elle est plus petite que certaines exoplanètes précédentes. *Crédits : DLR Institute of Planetary Research*

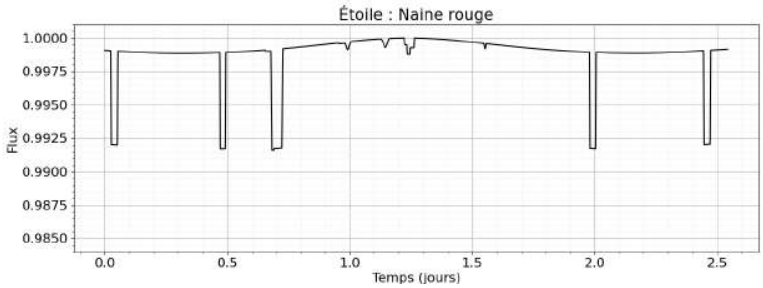

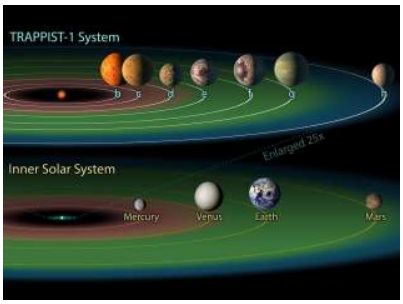

Le système TRAPPIST-1. Il y a tellement d'exoplanètes qu'on ne peut plus les distinguer ! *Crédits : NASA/JPL/Caltech*

3.3.2 Abaques

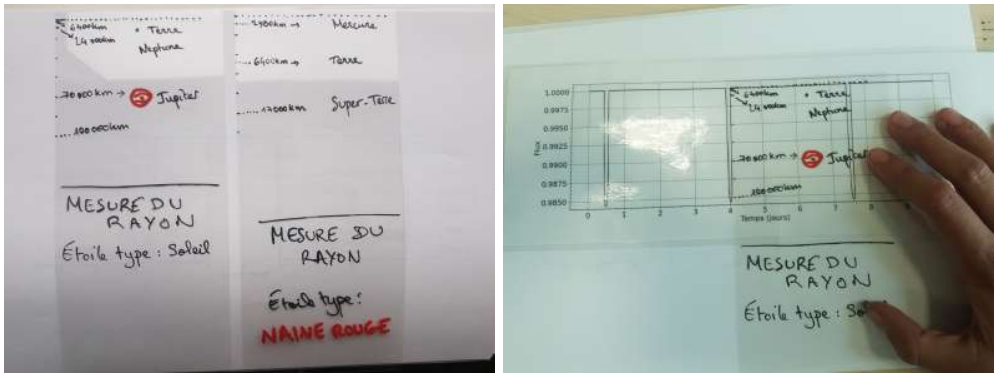

Abaque pour trouver la taille de l'exoplanète, avec un exemple d'utilisation.



Abaques pour trouver la température de l'exoplanète, pour une étoile tyle soleil ainsi que pour une naine rouge. À partir de la courbe de transit, on connaît la période, ces abaques permettent de relier la période à la distance à l'étoile, puis à la température d'équilibre.



Abaques pour trouver la température de l'exoplanète, comparaison des tailles

The idea is like grass. It craves light, likes crowds, thrives on crossbreeding, grows better for being stepped on.

Ursula Le Guin, *The Dispossessed: An Ambiguous Utopia*